Modeling the Regional and Global Climate Responses to Holocene Land Surface Change

by

Alexander James Thompson

A dissertation submitted in partial fulfillment
of the requirements for the degree of
Doctor of Philosophy
(Earth and Environmental Sciences)
in the University of Michigan
2021

Doctoral Committee:

Professor Christopher J. Poulsen, Chair
Professor Julia E. Cole
Associate Professor Naomi E. Levin
Professor Richard B. Rood
Assistant Professor Christopher B. Skinner, University of Massachusetts Lowell

Alexander J. Thompson

alexjt@umich.edu

ORCID iD: 0000-0002-8037-5990

Dedication

To my parents, Jim and Jane, who raised me to value the wonders of the natural world, and to my wife, Yasmeen, words cannot express how thankful I am to have you as my partner. The love and support from the three of you are the reason I am here today.

Acknowledgements

Scientific progress is only possible with the efforts of a large community and I have many people to thank for their support of my dissertation. First, to my advisor Chris Poulsen. Thank you for giving me the freedom and guidance to pursue both interesting and relevant research topics. Your trust and confidence in my ability to achieve a high standard of scientific work has allowed me to excel in graduate school. You have been an excellent mentor to me throughout the years and I am very fortunate you introduced me to the benefits of a Ph.D. back when I was an undergraduate. Thank you to my other dissertation committee members: Julie Cole, Naomi Levin, Richard Rood, and Chris Skinner. Your feedback and support of my dissertation has helped me grow as a scientist. I want to thank my co-authors: Jiang Zhu, Chris Poulsen, Chris Skinner, Clay Tabor, Jess Tierney. Your constructive feedback and edits to my constant drafts have helped elevate me as an early career scientist and I greatly enjoyed co-authoring these works with all of you. This dissertation was supported by the National Science Foundation award 1602956 and high-performance computing support from Cheyenne (doi:10.5065/D6RX99HX) provided by NCAR's Computational and Information Systems Laboratory, sponsored by the National Science Foundation, as well as through computational resources and services provided by Advanced Research Computing at the University of Michigan.

I feel very fortunate to have been a part of the Earth community at the University of Michigan and have many people to thank for making my time here so enjoyable. To my lab mates from the beginning to the end, Sophie and Phoebe, you two have been wonderful friends and colleagues over the years and I am lucky to have shared my graduate school experience with you. To the rest of the Poulsen Lab Group, past and present: Jeremy, Daeun, Emily, Paul, Dora, Andrew, Jiang, Chris, J.B., Clay, Ran, Rich, and Chana, I appreciate all of your encouragement and friendship. To my large cohort of the incoming Earth class of 2016: Sha, Alessio, Becca, Aaron, Sophie, Juliana, Billy, Nik, Kierstin, James, Bekah, Kirk, and Bian, as well as other friends in the department, you all have made graduate school so much fun and I want to thank you all for

creating such a wonderful community of graduate students. I also would like to thank Anne Hudon for always helping me navigate life as a graduate student.

I had the great fortune of learning from and teaching with a wonderful group of educators during my Ph.D. I want to thank my many professors and mentors for the great education I received at the University of Michigan. My co-GSIs, Sophie, Aaron, Rodrigo, Tonya, and Jacqueline, it was a pleasure to work with you all in a variety of fun teaching settings at Michigan. Also, to Jamie Gleason and my co-GSIs of Winter term 2020 Earth 120, Rodrigo and Tonya, it was quite the experience transitioning to online teaching during the start of the pandemic with you – thank you for making it a mostly positive and interesting time.

Many people at Michigan helped me highlight the importance of communication of science and engagement with the broader public. Thank you to Jenna Munson for your constant coordination of Earth Camp and providing such a unique experience for me to share my earth science passion with Michigan high schoolers. Thank you to Alicia Comer and Kira Berman with the Science Communication program at the Museum of Natural History for teaching me to effectively communicate my science to the public and for providing numerous opportunities to engage with the public in ways that were both fun and educational.

Lastly, I want to thank my wide support network of family and friends, who kept me going all these years. To my aunts, uncles, and cousins, you have always been there for me with love and encouragement. To my grandmother, Anne, thank you for teaching me to always have a curious mind. To my in-laws, especially Kristi and Bill, I greatly appreciate your unwavering support (and snickerdoodles!) for over a decade. I extend a big time thank you to all of my friends, especially the barn guys, who always keep me laughing, and Jeff, whose Green Sahara joke at my wedding is the best joke I have ever heard. To my parents, Jim and Jane, your unending love and support for all of my pursuits, both personal and professional, have made me the man I am today. And to my wife, Yasmeen, words simply cannot express how much your love and support means to me. You have been there by my side through this entire process, listening to every practice presentation, distracting me during work-from-home time, and helping keep me grounded as a human being. My achievement of this doctoral degree is in large part because of you.

Table of Contents

List of Tables

List of Figures

Abstract

Widespread land surface changes took place in the Northern Hemisphere throughout the Holocene epoch (11,700 years ago to the present). The most notable of these changes were large increases in vegetation cover that occurred throughout the African Sahara. Yet, the varied responses of regional and global climate to this land surface change are not well understood because few modeling studies have directly incorporated it in their experiments. This dissertation presents new Earth system modeling results that include land surface changes in the African Sahara and Northern Hemisphere mid- and high latitudes to directly identify the responses of regional and global climate to these changes. The chapters in this dissertation provide various resolutions to several challenges in reconciling Holocene model and proxy reconstructions of both hydroclimate and temperature.

Chapters 2 and 3 investigate challenges related to the impact of African Saharan greening, known as the "Green Sahara", on the West African monsoon during the mid-Holocene. Conclusions from these chapters better constrain the mid-Holocene response of African hydroclimate to a wide array of land surface processes associated with the Green Sahara. Chapter 2 explores the competing impacts of the direct radiative and indirect aerosol-cloud effects associated with the vegetation-induced reduction in dust aerosols, providing an improved understanding of the West African monsoon response to vegetation and dust forcing in the mid-Holocene. Chapter 3 examines how vegetation-induced changes in the isotopic composition of precipitation and soil water help to constrain estimates of the monsoon's northernmost limit. By showcasing a previously unknown positive anomaly in the isotopic composition of precipitation, this chapter suggests a mid-Holocene northernmost limit of ~23–28°N for the West African monsoon.

Chapters 4 and 5 expand the spatial and temporal scope of this dissertation and investigate external climate responses, both regional and global, to Holocene land surface change. Both of these chapters offer increased Northern Hemisphere vegetation as a resolution to challenges related to reconstructing Holocene climate with model simulations and geochemical proxies. Chapter 4

explores the opposing isotopic signature of the North American monsoon in comparison with other Northern Hemisphere land monsoons and shows that the Green Sahara is likely responsible for this opposing behavior by modulating the local Walker circulation. Seasonal exploration of hydroclimatic and stable water isotopic changes elucidates the factors contributing to the evolution of the North American monsoon. Chapter 5 investigates the controversial model-data disagreement in reconstruction of Holocene global temperatures known as the Holocene Temperature Conundrum. By inclusion of Holocene increases in vegetation in the African Sahara and Northern Hemisphere mid- and high latitudes, the results of this chapter suggest that vegetation change drives a mid-Holocene maximum in annual global mean temperatures and better aligns model simulations with proxy data.

Taken together, findings from this dissertation highlight the importance of vegetation in driving past climate change and in reconciling results from model simulations with geochemical proxy data.

Chapter 1 Introduction

1.1 Overview and motivation

During the early and mid-Holocene (~11–5 ka BP; thousand years before present), widespread increases in vegetation occurred throughout the Northern Hemisphere, most notably in the African Sahara (Binney et al., 2017; COHMAP Members, 1988; Hoelzmann et al., 1998; Jolly et al., 1998). These large-scale land surface changes influenced Earth's climate system through a variety of interactions and feedbacks at both the regional and global scale, highlighting the significance of the Saharan land surface on global climate (Pausata et al., 2016; Swann et al., 2014). While many studies have investigated other aspects of Holocene climate change (Brierley et al., 2020; Tierney et al., 2017), several questions remain regarding the direct impact of these land surface changes on regional and global climate. This dissertation investigates the regional and global hydroclimate and temperature responses to the widespread land surface changes that occurred throughout the Holocene epoch (~11.7 ka BP–present) by directly simulating these impacts with Earth system models. Given the prevalence of natural and anthropogenic land surface changes and their uncertain influence on modern climate (Drijfhout et al., 2015; Lejeune et al., 2018; Winkler et al., 2021), implications of this dissertation involve a better understanding of the broad impacts a changing land surface has on both past and future climate.

With the same background climate as the modern day, the Holocene represents an ideal time period for studying land surface-climate interactions with relevance for both past and future climate change. The Holocene consists of an interglacial climate, taking place after the last glaciation in the Pleistocene, that is relatively stable with only minor fluctuations in large-scale climate forcings (Dansgaard et al., 1993; Kaufman et al., 2020). Throughout the Holocene, global mean temperature remained within ~0.3°C of the Preindustrial (PI, 1850 CE) era (Kaufman et al., 2020). During this time, greenhouse gas concentrations were relatively stable with minor gradual increases (Brovkin et al., 2019; Indermühle et al., 1999; Sowers, 2010). Remnant Northern Hemisphere ice sheets from the last Pleistocene glaciation remained in the early Holocene and

roughly reached their modern day extent by the mid-Holocene (6 ka BP) (Peltier et al., 2015). Even orbitally-driven changes in insolation, generally thought of as a primary driver of Holocene changes in climate, were relatively small as Northern Hemisphere summer insolation during the early Holocene was ~7% higher than the modern day (Berger and Loutre, 1991).

Yet, despite these minor fluctuations in climate forcings, geochemical proxy and model evidence suggests large changes in both the land surface and climate system during the Holocene. In response to seasonal variations in orbitally-driven insolation, Northern Hemisphere rainfall, especially that related to the land monsoon system, was considerably enhanced (Bosmans et al., 2012; Braconnot et al., 2012; Brierley et al., 2020; Kutzbach, 1981; Sun et al., 2019). Through land-atmosphere feedbacks, these increases in rainfall prompted dramatic changes in the composition and extent of vegetation, producing the so-called "Green Sahara" and increasing vegetation cover throughout the Northern Hemisphere mid- and high latitudes (Binney et al., 2017; COHMAP Members, 1988; Hoelzmann et al., 1998; Jolly et al., 1998; Prentice et al., 1998; Tarasov et al., 1998). However, in their attempts to reconstruct these changes in Holocene climate, previous modeling studies have often failed to reproduce many of the proxy-inferred changes in rainfall and temperature (Braconnot et al., 2012; Liu et al., 2014; Tierney et al., 2017). Thus, several unanswered questions remain regarding the responses of regional and global climate to Holocene land surface changes, likely because few studies have directly explored their impacts on the climate system.

This dissertation presents new Earth system modeling results that directly incorporate Holocene land surface changes in the African Sahara and Northern Hemisphere mid- and high latitudes. In doing so, this research aims to better constrain the varied responses of regional and global climate to Holocene land surface change and resolve previous challenges related to reconciling model simulations with evidence from geochemical proxy data. The first half of this dissertation investigates how the Green Sahara impacts mid-Holocene African climate. Chapter 2 explores the effect of the vegetation-induced reduction in dust aerosols, and its subsequent impact on aerosol-cloud interactions, on the West African monsoon. Chapter 3 examines how vegetation-induced changes in the isotopic composition of precipitation and soil water helps us constrain estimates of the monsoon's northernmost limit. The second half of this dissertation investigates external climate responses, both regional and global, to Holocene land surface change. Chapter 4 explores how the Green Sahara may have impacted the evolution of the North American monsoon

and its recorded isotopic signature. Chapter 5 investigates how Northern Hemisphere vegetation change drives a Holocene temperature maximum and resolves a mismatch between model- and proxy-reconstructed global mean temperatures. Taken together, findings from this dissertation highlight the importance of the land surface in driving past climate change.

1.2 Land surface-climate interactions of the Green Sahara

Interactions between the land surface and climate system produced an early and mid-Holocene African Sahara that was much different than the modern-day desert. Variations in orbital precession triggered warmer summers and an enhanced West African monsoon that fostered vegetation growth throughout the Sahara (Hély et al., 2014; Kutzbach et al., 1996; Kutzbach, 1981). This "Green Sahara" consisted of a mixed environment of grass, shrub, and tree cover that may have extended as far north as 31°N (Hély et al., 2014; Hoelzmann et al., 1998; Tierney et al., 2017). The sandy soils of today's Sahara Desert were instead organic-rich loam, retaining more moisture and exhibiting lower surface albedo than the modern day (Levis et al., 2004; Vamborg et al., 2011). Evidence for these widespread changes to the Saharan land surface come from a host of geochemical proxy data, including dust flux, pollen, and leaf wax *n*-alkane records (Collins et al., 2017; deMenocal et al., 2000; Hoelzmann et al., 1998; Jolly et al., 1998; Tierney et al., 2017).

Complex feedbacks between the land surface and atmosphere led to a further enhancement of monsoonal rainfall driven by vegetation growth. By lowering the albedo of the surface, increases in vegetation cover and soil moisture enhanced absorption of radiative energy at the land surface, which resulted in increases in both moist static energy and local rainfall (Charney et al., 1975; Charney, 1975; Eltahir, 1998; Levis et al., 2004). Increased vegetation also reduced dust aerosol loading by as much as ~70% (Albani et al., 2015; Egerer et al., 2016), impacting hydroclimate through both direct radiative and indirect aerosol-cloud effects (Egerer et al., 2016; Ghan et al., 2013, 2012; McGee et al., 2013; Xie et al., 2017). Through remote teleconnections, the Green Sahara also impacted atmospheric circulation patterns across the globe (Griffiths et al., 2020; Pausata et al., 2017a, 2017b; Tabor et al., 2020).

Yet, the Green Sahara's broad impacts on regional and global climate are still relatively poorly understood because few modeling studies have directly incorporated these changes. In fact, Paleoclimate Model Intercomparison Project simulations have neglected Holocene land surface changes by design, instead specifying a PI vegetation extent in their experiments (Brierley et al.,

2020; Kageyama et al., 2016). Further, previous modeling studies using dynamic simulation of vegetation have failed to adequately capture the large-scale changes in vegetation and hydroclimate inferred from pollen data (Bartlein et al., 2011; Braconnot et al., 2012; He et al., 2013; Tierney et al., 2017). While some recent studies have explored the impact of the Green Sahara on climate change in Africa and a few other regions worldwide (Griffiths et al., 2020; Hopcroft et al., 2021; Pausata et al., 2017a, 2017b, 2016; Tabor et al., 2020), this field of research is still relatively new. Thus, many unknowns remain regarding reconstruction of the responses of regional and global climate to African Saharan and other Northern Hemisphere land surface changes during the Holocene. As a result, several known discrepancies exist between the reconstructions of Holocene climate from model simulations and geochemical proxy data.

1.3 Integrating Earth system models with proxy data

This dissertation aims to address these model-data disagreements through integration of new results from Earth system models with previous geochemical proxy data. Here, I use global simulations of NCAR's Community Earth System Model (CESM1), which is among the most realistic of IPCC-class models in its simulation of the global climate system (Knutti et al., 2013), to comprehensively address these challenges in reconstructing Holocene climate change. In these simulations, changes to the Holocene land surface are prescribed directly in the model. CESM1 consists of component models representing the atmosphere, land surface, ocean, and cryosphere, which are connected through a central coupler (Hurrell et al., 2013). In the chapters in this dissertation, I utilize a variety of CESM1 configurations, including full Earth system coupling (Hurrell et al., 2013) and stable water isotope-enabled (Brady et al., 2019) versions, to investigate hydroclimate and temperature changes through the Holocene. Specifically, I utilize fields of temperature, precipitation, winds, several variables related to atmospheric circulation and cloud dynamics, and the isotopic composition of precipitation, soil water, and water vapor. Simulation of stable water isotopes provide insight into changes in atmospheric and land surface dynamics that cannot otherwise be discerned from investigation of rainfall, temperature, or wind fields alone (Dansgaard, 1964; Konecky et al., 2019b; Rozanski et al., 1993).

Due to its comprehensive representation of the Earth system, CESM1 is a state-of-the-art scientific tool for simulating past climates (Kageyama et al., 2016; Skinner and Poulsen, 2016). CESM1 provides a robust, physically based depiction of the Earth system that can be used to

diagnose the processes and mechanisms, such as greening in the African Sahara, that are responsible for changes in regional and global climate (He et al., 2013; Kattsov et al., 2013; Liu et al., 2009; Pausata et al., 2016; Tierney et al., 2017). I employ these strengths of CESM1, mainly through sensitivity analysis, to systematically analyze the underlying mechanisms associated with large-scale Holocene climate change.

Yet, uncertainties do exist regarding the necessary simplification of climate in CESM1. The simulated climate system is represented by a specified finite grid (i.e., 1.9° latitude × 2.5° longitude) on which equations of fluid motion and thermodynamics are solved, resulting in a simplified depiction of climate that is largely dependent on the model's initial and boundary conditions (Kattsov et al., 2013). For example, I prescribe changes in Holocene vegetation extent that are derived from best-available information regarding the true extent. However, the composition and extent of vegetation used in my simulations are still simplified and lack the complexity of the real-world land surface, which could lead to over- or underestimation of the resulting Holocene climate response to these changes in vegetation.

To overcome these uncertainties inherent in Earth system models, I integrate and compare my simulated results with geochemical proxy data. Proxy data provide invaluable information regarding the chemical and sedimentological signatures of the past with numerous records that span the Holocene quantitatively measuring and integrating a variety of complex environmental and climatic processes (COHMAP Members, 1988; Hernández et al., 2020; Kaufman et al., 2020; Metcalfe et al., 2015). Additionally, proxies provide for realistic climate bounds with which to ground truth modeling results (Haywood et al., 2019). Models and proxies can also be integrated with proxy system models, as is done in Chapters 3 and 4, providing for an intermediary that allows for like-for-like comparisons between the two (Dee et al., 2015; Konecky et al., 2019a). However, uncertainties are also associated with proxies because they require interpretations, that often evolve as new findings emerge, to link their reconstructed changes to changes in climate and they do not allow for comprehensive analysis of the underlying mechanisms responsible for their reconstructed changes (Dansgaard, 1964; Kaufman et al., 2020; Konecky et al., 2019b; Rozanski et al., 1993; Tierney et al., 2017). Thus, in using an integrative approach between CESM1 and geochemical proxy data, I leverage the strengths of both to provide for robust, physically based analysis of the regional and global climate responses to Holocene land surface change.

1.5 Dissertation chapter summaries

This dissertation consists of four studies (Chapters 2–5) utilizing an integrative approach between CESM1 and geochemical proxy data to investigate the impact of Holocene land surface changes on African, North American, and global climate. These studies address several previously unsolved challenges in reconciling model-data disagreements related to Holocene land surface-climate interactions ranging from the regional to global scale. The conclusions from this dissertation help to better constrain and quantify the ways in which the Holocene land surface modulated regional and global climate and contribute to resolving several disagreements between Holocene model and proxy reconstructions.

Chapters 2 and 3 assess challenges related to the greening of the African Sahara and its impact on the West African monsoon during the mid-Holocene. In comparison to proxies, previous modeling studies have underestimated the enhancement of the West African monsoon during the mid-Holocene, likely because their experiments largely neglected changes in the African land surface (Braconnot et al., 2012; Brierley et al., 2020; Kageyama et al., 2016; Pausata et al., 2016; Tierney et al., 2017). A host of geochemical proxy data has indicated a mid-Holocene northernmost limit of the West African monsoon as far as ~31°N (Sha et al., 2019; Tierney et al., 2017), yet models that have accounted for climate forcings like orbital insolation and greenhouse gas concentrations but neglected land surface changes have failed to simulate a comparable monsoonal limit (Braconnot et al., 2012; Brierley et al., 2020; Joussaume et al., 1999; Perez-Sanz et al., 2014). These chapters address this discrepancy by utilizing Earth system model sensitivity experiments to investigate the hydroclimatic impacts directly associated with the greening of the African Sahara. Together, these chapters contribute to the growing body of knowledge aimed at improving model quantifications of the West African monsoon enhancement during the mid-Holocene and better understanding how this highly variable system may respond to land surface change in the modern day.

Chapter 2 (published in *Geophysical Research Letters*; Thompson et al., 2019) investigates how the vegetation-induced reduction in dust aerosol loading impacts the West African monsoon during the mid-Holocene via both direct and indirect aerosol effects. This study finds that the mid-Holocene reduction in dust has competing effects on the West African monsoon. The direct radiative effects of the dust reduction lead to increased convective rainfall and contribute to an overall increase in monsoonal rainfall as a result of combined greening and dust reduction.

However, the indirect aerosol-cloud effects decrease stratiform rainfall and dampen the overall increase from combined greening and dust reduction. This study concludes that monsoonal rainfall is directly impacted by vegetation to a greater degree than dust.

Chapter 3 (published in *Earth and Planetary Science Letters*; Thompson et al., 2021) investigates the water isotopic response, in both precipitation and soil water, to the greening of the Sahara. This study finds a previously unknown response in the isotopic composition of precipitation to Saharan greening, which is at odds with interpretations of past reconstructions from leaf wax *n*-alkanes. However, investigation of the isotopic composition of soil water instead reveals an alternative interpretation of these leaf wax *n*-alkane reconstructions. Results from this study suggest that the northernmost limit of the West African monsoon during the mid-Holocene was ~23–28°N, in agreement with many pollen and dust records and lower than the inferred limit from leaf wax *n*-alkane records. Through novel findings on the water isotopic response to Saharan greening and comparison of this response with several geochemical proxy reconstructions, this study provides useful information for improving constraints on the northernmost limit of the West African monsoon during the mid-Holocene.

Chapters 4 and 5 increase the spatial and temporal scale of this research and assess the impacts of greening throughout the Holocene on regional and global climate. These chapters further explore known model-data discrepancies in the Holocene, offering increased Northern Hemisphere vegetation as a resolution. Both Chapters 4 and 5 investigate these challenges using time slice simulations throughout the Holocene.

In the early and mid-Holocene, isotopic reconstructions of the North American monsoon exhibit a positive signature, in opposition to reconstructions from other Northern Hemisphere land monsoons (Asmerom et al., 2007; Cai et al., 2012; Dong et al., 2010; Tierney et al., 2017). The reasons for this opposing signature are poorly understood since, to date, comparisons with water isotope-enabled models have not been performed (Hermann et al., 2018; Metcalfe et al., 2015). Chapter 4 explores the evolution of the North American monsoon from the Last Glacial Maximum (~21 ka BP) to the PI and how this highly variable hydrologic system responds to a variety of orbital-scale climate forcings, including the early and mid-Holocene greening of the African Sahara. Remote teleconnections related to the Green Sahara have been established in other regions of the world (Griffiths et al., 2020; Pausata et al., 2017a, 2017b; Tabor et al., 2020) and this chapter demonstrates that they may also lead to a reduction in North American monsoon rainfall via

modulation of the local Walker circulation. Furthermore, this study aligns simulated water isotopic results from both Earth and proxy system models to understand the competing influences of winter and summer atmospheric dynamics on their reconstructed signatures from proxy records. Conclusions from this study help to constrain evolution of the poorly understood North American monsoon during the late Pleistocene and Holocene.

In attempts to simulate global mean temperature, previous climate modeling studies have failed to reproduce the Holocene thermal maximum and subsequent cooling thereafter that has appeared in proxy reconstructions, instead simulating a gradual warming (He et al., 2013; Kaufman et al., 2020). This disagreement is known as the "Holocene Temperature Conundrum" (Liu et al., 2014). Chapter 5 (submitted to *Science Advances*) investigates how increases in Northern Hemisphere vegetation during the early and mid-Holocene increase annual global mean temperatures and largely resolve the model-data discrepancy. This vegetation change is well-known from pollen records (Bartlein et al., 2011; Binney et al., 2017; COHMAP Members, 1988; Hoelzmann et al., 1998) but has not yet been explored for its direct impact on annual global mean temperatures. This study confirms that a robust maximum, which had previously been a controversial topic in the literature, appears in annual mid-Holocene temperatures and demonstrates that Northern Hemisphere vegetation change drives this maximum. Further analysis also shows resolution of the Holocene Temperature Conundrum in regional temperature, highlighting the importance of vegetation when simulating past climate change and its ability to resolve model-data disagreements in paleoclimate.

This dissertation concludes with a summary chapter (Chapter 6) that highlights the key findings and implications of this work. This concluding chapter then discusses several opportunities for future work related to yet unknown questions in the field of Holocene land surface-climate interactions.

1.6 References

Albani, S., Mahowald, N.M., Winckler, G., Anderson, R.F., Bradtmiller, L.I., Delmonte, B., François, R., Goman, M., Heavens, N.G., Hesse, P.P., Hovan, S.A., Kang, S.G., Kohfeld, K.E., Lu, H., Maggi, V., Mason, J.A., Mayewski, P.A., McGee, D., Miao, X., Otto-Bliesner, B.L., Perry, A.T., Pourmand, A., Roberts, H.M., Rosenbloom, N., Stevens, T., Sun, J., 2015. Twelve thousand years of dust: The Holocene global dust cycle constrained by

natural archives. Clim. Past 11, 869–903. https://doi.org/10.5194/cp-11-869-2015

Asmerom, Y., Polyak, V., Burns, S., Rassmssen, J., 2007. Solar forcing of Holocene climate: New insights from a speleothem record, southwestern United States. Geology 35, 1–4. https://doi.org/10.1130/G22865A.1

Bartlein, P.J., Harrison, S.P., Brewer, S., Connor, S., Davis, B.A.S., Gajewski, K., Guiot, J., Harrison-Prentice, T.I., Henderson, A., Peyron, O., Prentice, I.C., Scholze, M., Seppä, H., Shuman, B., Sugita, S., Thompson, R.S., Viau, A.E., Williams, J., Wu, H., 2011. Pollen-based continental climate reconstructions at 6 and 21 ka: a global synthesis. Clim. Dyn. 37, 775–802. https://doi.org/10.1007/s00382-010-0904-1

Berger, A., Loutre, M.F., 1991. Insolation values for the climate of the last 10 million years. Quat. Sci. Rev. 10, 297–317. https://doi.org/10.1016/0277-3791(91)90033-Q

Binney, H., Edwards, M., Macias-Fauria, M., Lozhkin, A., Anderson, P., Kaplan, J.O., Andreev, A., Bezrukova, E., Blyakharchuk, T., Jankovska, V., Khazina, I., Krivonogov, S., Kremenetski, K., Nield, J., Novenko, E., Ryabogina, N., Solovieva, N., Willis, K., Zernitskaya, V., 2017. Vegetation of Eurasia from the last glacial maximum to present: Key biogeographic patterns. Quat. Sci. Rev. 157, 80–97. https://doi.org/10.1016/j.quascirev.2016.11.022

Bosmans, J.H.C., Drijfhout, S.S., Tuenter, E., Lourens, L.J., Hilgen, F.J., Weber, S.L., 2012. Monsoonal response to mid-holocene orbital forcing in a high resolution GCM. Clim. Past 8, 723–740. https://doi.org/10.5194/cp-8-723-2012

Braconnot, P., Harrison, S.P., Kageyama, M., Bartlein, P.J., Masson-Delmotte, V., Abe-Ouchi, A., Otto-Bliesner, B., Zhao, Y., 2012. Evaluation of climate models using palaeoclimatic data. Nat. Clim. Chang. 2, 417–424. https://doi.org/10.1038/nclimate1456

Brady, E., Stevenson, S., Bailey, D., Liu, Z., Noone, D., Nusbaumer, J., Otto-Bliesner, B.L., Tabor, C., Tomas, R., Wong, T., Zhang, J., Zhu, J., 2019. The Connected Isotopic Water Cycle in the Community Earth System Model Version 1. J. Adv. Model. Earth Syst. 11, 2547–2566. https://doi.org/10.1029/2019MS001663

Brierley, C.M., Zhao, A., Harrison, S.P., Braconnot, P., Williams, C.J.R., Thornalley, D.J.R., Shi, X., Peterschmitt, J., Ohgaito, R., Kaufman, D.S., Kageyama, M., Hargreaves, J.C., Erb, M.P., Emile-Geay, J., D'Agostino, R.D., Chandan, D., Carré, M., Bartlein, P.J., Zheng, W., Zhang, Z., Zhang, Q., Yang, H., Volodin, E.M., Tomas, R.A., Routson, C., Peltier, R., Otto-

Bliesner, B., Morozova, P.A., McKay, N.P., Lohmann, G., Legrande, A.N., Guo, C., Cao, J., Brady, E., Annan, J.D., Abe-Ouchi, A., 2020. Large-scale features and evaluation of the PMIP4-CMIP6 midHolocene simulations. Clim. Past Discuss. https://doi.org/10.5194/cp-2019-168

Brovkin, V., Lorenz, S., Raddatz, T., Ilyina, T., Stemmler, I., Toohey, M., Claussen, M., 2019. What was the source of the atmospheric CO2 increase during the Holocene? Biogeosciences 16, 2543–2555. https://doi.org/10.5194/bg-16-2543-2019

Cai, Y., Zhang, H., Cheng, H., An, Z., Lawrence Edwards, R., Wang, X., Tan, L., Liang, F., Wang, J., Kelly, M., 2012. The Holocene Indian monsoon variability over the southern Tibetan Plateau and its teleconnections. Earth Planet. Sci. Lett. 335–336, 135–144. https://doi.org/10.1016/j.epsl.2012.04.035

Charney, J., Stone, P.H., Quirk, W.J., 1975. Drought in the Sahara: A Biogeophysical Feedback Mechanism. Science (80-.). 187, 434–435. https://doi.org/10.1126/science.187.4175.434

Charney, J.G., 1975. Dynamics of deserts and drought in the Sahel. Q. J. R. Meteorol. Soc. 101, 193–202.

COHMAP Members, 1988. Climatic Changes of the Last 18,000 Years: Observations and Model Simulations. Science (80-.). 241, 1043–1052. https://doi.org/10.1126/science.241.4869.1043

Collins, J.A., Prange, M., Caley, T., Gimeno, L., Beckmann, B., Mulitza, S., Skonieczny, C., Roche, D., Schefuß, E., 2017. Rapid termination of the African Humid Period triggered by northern high-latitude cooling. Nat. Commun. 8, 1372. https://doi.org/10.1038/s41467-017-01454-y

Dansgaard, W., 1964. Stable isotopes in precipitation. Tellus 16, 436–468.

Dansgaard, W., Johnsen, S.J., Clausen, H.B., Dahl-Jensen, D., Gundestrup, N.S., Hammer, C.U., Hvidberg, C.S., Steffensen, J.P., Sveinbjörnsdottir, A.E., Jouzel, J., Bond, G., 1993. Evidence for general instability of past climate from a 250-kyr ice-core record. Nature 364, 218–220. https://doi.org/10.1038/364218a0

Dee, S., Emile-Geay, J., Evans, M.N., Allam, A., Steig, E.J., Thompson, D.M., 2015. PRYSM: An open-source framework for PRoxY System Modeling, with applications to oxygen-isotope systems. J. Adv. Model. Earth Syst. 7, 1220–1247. https://doi.org/10.1002/2015MS000447

deMenocal, P., Ortiz, J., Guilderson, T., Adkins, J., Sarnthein, M., Baker, L., Yarusinsky, M., 2000. Abrupt onset and termination of the African Humid Period: Quat. Sci. Rev. 19, 347–361. https://doi.org/10.1016/S0277-3791(99)00081-5

Dong, J., Yongjin Wang, Hai Cheng, Hardt, B., Edwards, R.L., Xinggong Kong, Jiangying Wu, Shitao Chen, Dianbing Liu, Xiuyang Jiang, Kan Zhao, 2010. A high-resolution stalagmite record of the Holocene East Asian monsoon from Mt Shennongjia, central China. The Holocene 20, 257–264. https://doi.org/10.1177/0959683609350393

Drijfhout, S., Bathiany, S., Beaulieu, C., Brovkin, V., Claussen, M., Huntingford, C., Scheffer, M., Sgubin, G., Swingedouw, D., 2015. Catalogue of abrupt shifts in Intergovernmental Panel on Climate Change climate models. Proc. Natl. Acad. Sci. U. S. A. 112, E5777–E5786. https://doi.org/10.1073/pnas.1511451112

Egerer, S., Claussen, M., Reick, C., Stanelle, T., 2016. The link between marine sediment records and changes in Holocene Saharan landscape: Simulating the dust cycle. Clim. Past 12, 1009–1027. https://doi.org/10.5194/cp-12-1009-2016

Eltahir, E.A.B., 1998. A soil moisture-rainfall feedback mechanism 1. Theory and observations. Water Resour. Res. 34, 765–776. https://doi.org/10.1029/97WR03499

Ghan, S.J., Liu, X., Easter, R.C., Zaveri, R., Rasch, P.J., Yoon, J., 2012. Toward a Minimal Representation of Aerosols in Climate Models: Comparative Decomposition of Aerosol Direct, Semidirect, and Indirect Radiative Forcing. J. Clim. 25, 6461–6476. https://doi.org/10.1175/JCLI-D-11-00650.1

Ghan, S.J., Smith, S.J., Wang, M., Zhang, K., Pringle, K., Carslaw, K., Pierce, J., Bauer, S., Adams, P., 2013. A simple model of global aerosol indirect effects. J. Geophys. Res. Atmos. 118, 6688–6707. https://doi.org/10.1002/jgrd.50567

Griffiths, M.L., Johnson, K.R., Pausata, F.S.R., White, J.C., Henderson, G.M., Wood, C.T., Yang, H., Ersek, V., Conrad, C., Sekhon, N., 2020. End of Green Sahara amplified mid- to late Holocene megadroughts in mainland Southeast Asia. Nat. Commun. 11, 4204. https://doi.org/10.1038/s41467-020-17927-6

Haywood, A.M., Valdes, P.J., Aze, T., Barlow, N., Burke, A., Dolan, A.M., von der Heydt, A.S., Hill, D.J., Jamieson, S.S.R., Otto-Bliesner, B.L., Salzmann, U., Saupe, E., Voss, J., 2019. What can Palaeoclimate Modelling do for you? Earth Syst. Environ. 3, 1–18. https://doi.org/10.1007/s41748-019-00093-1

He, F., Shakun, J.D., Clark, P.U., Carlson, A.E., Liu, Z., Otto-Bliesner, B.L., Kutzbach, J.E., 2013. Northern Hemisphere forcing of Southern Hemisphere climate during the last deglaciation. Nature 494, 81–85. https://doi.org/10.1038/nature11822

Hély, C., Lézine, A.-M., Contributors, A., 2014. Holocene changes in African vegetation: tradeoff between climate and water availability. Clim. Past 10, 681–686. https://doi.org/10.5194/cp-10-681-2014

Hermann, N.W., Oster, J.L., Ibarra, D.E., 2018. Spatial patterns and driving mechanisms of mid-Holocene hydroclimate in western North America. J. Quat. Sci. 33, 421–434. https://doi.org/10.1002/jqs.3023

Hernández, A., Martin-Puertas, C., Moffa-Sánchez, P., Moreno-Chamarro, E., Ortega, P., Blockley, S., Cobb, K.M., Comas-Bru, L., Giralt, S., Goosse, H., Luterbacher, J., Martrat, B., Muscheler, R., Parnell, A., Pla-Rabes, S., Sjolte, J., Scaife, A.A., Swingedouw, D., Wise, E., Xu, G., 2020. Modes of climate variability: Synthesis and review of proxy-based reconstructions through the Holocene. Earth-Science Rev. 209, 103286. https://doi.org/10.1016/j.earscirev.2020.103286

Hoelzmann, P., Jolly, D., Harrison, S.P., Laarif, F., Bonnefille, R., Pachur, H., 1998. Mid-Holocene land-surface conditions in northern Africa and the Arabian Peninsula: A data set for the analysis of biogeophysical feedbacks in the climate system. Global Biogeochem. Cycles 12, 35–51. https://doi.org/10.1029/97GB02733

Hopcroft, P.O., Valdes, P.J., Ingram, W., 2021. Using the Mid-Holocene "Greening" of the Sahara to Narrow Acceptable Ranges on Climate Model Parameters. Geophys. Res. Lett. 48, 1–20. https://doi.org/10.1029/2020GL092043

Hurrell, J.W., Holland, M.M., Gent, P.R., Ghan, S., Kay, J.E., Kushner, P.J., Lamarque, J.F., Large, W.G., Lawrence, D., Lindsay, K., Lipscomb, W.H., Long, M.C., Mahowald, N., Marsh, D.R., Neale, R.B., Rasch, P., Vavrus, S., Vertenstein, M., Bader, D., Collins, W.D., Hack, J.J., Kiehl, J., Marshall, S., 2013. The community earth system model: A framework for collaborative research. Bull. Am. Meteorol. Soc. 94, 1339–1360. https://doi.org/10.1175/BAMS-D-12-00121.1

Indermühle, A., Stocker, T.F., Joos, F., Fischer, H., Smith, H.J., Wahlen, M., Deck, B., Mastroianni, D., Tschumi, J., Blunier, T., Meyer, R., Stauffer, B., 1999. Holocene carbon-cycle dynamics based on CO2 trapped in ice at Taylor Dome, Antarctica. Nature 398, 121–

126. https://doi.org/10.1038/18158

Jolly, D., Prentice, I.C., Bonnefille, R., Ballouche, A., Bengo, M., Brenac, P., Buchet, G., Burney, D., Cazet, J., Cheddadi, R., Edorh, T., Elenga, H., Elmoutaki, S., Guiot, J., Laarif, F., Lamb, H., Lezine, A., Maley, J., Mbenza, M., Peyron, O., Reille, M., Reynaud-Farrera, I., Riollet, G., Ritchie, J.C., Roche, E., Scott, L., Ssemmanda, I., Straka, H., Umer, M., Van Campo, E., Vilimumbalo, S., Vincens, A., Waller, M., 1998. Biome reconstruction from pollen and plant macrofossil data for Africa and the Arabian peninsula at 0 and 6000 years. J. Biogeogr. 25, 1007–1027. https://doi.org/10.1046/j.1365-2699.1998.00238.x

Joussaume, S., Taylor, K.E., Braconnot, P., Mitchell, J.F.B., Kutzbach, J.E., Harrison, S.P., Prentice, I.C., Broccoli, A.J., Abe-Ouchi, A., Bartlein, P.J., Bonfils, C., Dong, B., Guiot, J., Herterich, K., Hewitt, C.D., Jolly, D., Kim, J.W., Kislov, A., Kitoh, A., Loutre, M.F., Masson, V., McAvaney, B., McFarlane, N., de Noblet, N., Peltier, W.R., Peterschmitt, J.Y., Pollard, D., Rind, D., Royer, J.F., Schlesinger, M.E., Syktus, J., Thompson, S., Valdes, P., Vettoretti, G., Webb, R.S., Wyputta, U., 1999. Monsoon changes for 6000 years ago: Results of 18 simulations from the Paleoclimate Modeling Intercomparison Project (PMIP). Geophys. Res. Lett. 26, 859–862. https://doi.org/10.1029/1999GL900126

Kageyama, M., Braconnot, P., Harrison, S.P., Haywood, A.M., Jungclaus, J., Otto-Bliesner, B.L., Peterschmitt, J.-Y., Abe-Ouchi, A., Albani, S., Bartlein, P.J., Brierley, C., Crucifix, M., Dolan, A., Fernandez-Donado, L., Fischer, H., Hopcroft, P.O., Ivanovic, R.F., Lambert, F., Lunt, D.J., Mahowald, N.M., Peltier, W.R., Phipps, S.J., Roche, D.M., Schmidt, G.A., Tarasov, L., Valdes, P.J., Zhang, Q., Zhou, T., 2016. PMIP4-CMIP6: the contribution of the Paleoclimate Modelling Intercomparison Project to CMIP6. Geosci. Model Dev. Discuss. 1–46. https://doi.org/10.5194/gmd-2016-106

Kattsov, V., Federation, R., Reason, C., Africa, S., Uk, A.A., Uk, T.A., Baehr, J., Uk, A.B., Catto, J., Canada, J.S., Uk, A.S., 2013. Evaluation of Climate Models, in: Intergovernmental Panel on Climate Change (Ed.), Climate Change 2013 - The Physical Science Basis. Cambridge University Press, Cambridge, pp. 741–866. https://doi.org/10.1017/CBO9781107415324.020

Kaufman, D.S., McKay, N.P., Routson, C.C., Erb, M., Davis, B.A.S., Heiri, O., Jaccard, S., Tierney, J.E., Dätwyler, C., Axford, Y., Brussel, T., Cartapanis, O., Chase, B.M., Dawson, A., de Vernal, A., Engels, S., Jonkers, L., Marsicek, J., Moffa-Sánchez, P., Morrill, C., Orsi,

A., Rehfeld, K., Saunders, K., Sommer, P.S., Thomas, E., Tonello, M., Tóth, M., Vachula, R., Andreev, A., Bertrand, S., Biskaborn, B., Bringué, M., Brooks, S., Caniupán, M., Chevalier, M., Cwynar, L., Emile-Geay, J., Fegyveresi, J., Feurdean, A., Finsinger, W., Fortin, M.-C., Foster, L., Fox, M., Gajewski, K., Grosjean, M., Hausmann, S., Heinrichs, M., Holmes, N., Ilyashuk, B., Ilyashuk, E., Juggins, S., Khider, D., Koinig, K., Langdon, P., Larocque-Tobler, I., Li, J., Lotter, A., Luoto, T., Mackay, A., Magyari, E., Malevich, S., Mark, B., Massaferro, J., Montade, V., Nazarova, L., Novenko, E., Pařil, P., Pearson, E., Peros, M., Pienitz, R., Płóciennik, M., Porinchu, D., Potito, A., Rees, A., Reinemann, S., Roberts, S., Rolland, N., Salonen, S., Self, A., Seppä, H., Shala, S., St-Jacques, J.-M., Stenni, B., Syrykh, L., Tarrats, P., Taylor, K., van den Bos, V., Velle, G., Wahl, E., Walker, I., Wilmshurst, J., Zhang, E., Zhilich, S., 2020. A global database of Holocene paleotemperature records. Sci. Data 7, 1–34. https://doi.org/10.1038/s41597-020-0445-3

Knutti, R., Masson, D., Gettelman, A., 2013. Climate model genealogy: Generation CMIP5 and how we got there. Geophys. Res. Lett. 40, 1194–1199. https://doi.org/10.1002/grl.50256

Konecky, B.L., Dee, S.G., Noone, D.C., 2019a. WaxPSM: A Forward Model of Leaf Wax Hydrogen Isotope Ratios to Bridge Proxy and Model Estimates of Past Climate. J. Geophys. Res. Biogeosciences 124, 2107–2125. https://doi.org/10.1029/2018JG004708

Konecky, B.L., Noone, D.C., Cobb, K.M., 2019b. The Influence of Competing Hydroclimate Processes on Stable Isotope Ratios in Tropical Rainfall. Geophys. Res. Lett. 46, 1622–1633. https://doi.org/10.1029/2018GL080188

Kutzbach, J., Bonan, G., Foley, J., Harrison, S.P., 1996. Vegetation and soil feedbacks on the response of the African monsoon to orbital forcing in the early to middle Holocene. Nature 384, 623–626. https://doi.org/10.1038/384623a0

Kutzbach, J.E., 1981. Monsoon Climate of the Early Holocene: Climate Experiment with the Earth's Orbital Parameters for 9000 Years Ago. Science (80-.). 214, 59–61. https://doi.org/10.1126/science.214.4516.59

Lejeune, Q., Davin, E.L., Gudmundsson, L., Winckler, J., Seneviratne, S.I., 2018. Historical deforestation locally increased the intensity of hot days in northern mid-latitudes. Nat. Clim. Chang. 8, 386–390. https://doi.org/10.1038/s41558-018-0131-z

Levis, S., Bonan, G.B., Bonfils, C., 2004. Soil feedback drives the mid-Holocene North African monsoon northward in fully coupled CCSM2 simulations with a dynamic vegetation model.

Clim. Dyn. 23, 791–802. https://doi.org/10.1007/s00382-004-0477-y

Liu, Z., Otto-Bliesner, B.L., He, F., Brady, E.C., Tomas, R., Clark, P.U., Carlson, A.E., Lynch-Stieglitz, J., Curry, W., Brook, E., Erickson, D., Jacob, R., Kutzbach, J., Cheng, J., 2009. Transient Simulation of Last Deglaciation with a New Mechanism for Bolling-Allerod Warming. Science (80-.). 325, 310–314. https://doi.org/10.1126/science.1171041

Liu, Z., Zhu, J., Rosenthal, Y., Zhang, X., Otto-Bliesner, B.L., Timmermann, A., Smith, R.S., Lohmann, G., Zheng, W., Timm, O.E., 2014. The Holocene temperature conundrum. Proc. Natl. Acad. Sci. 111, E3501--E3505. https://doi.org/10.1073/pnas.1407229111

McGee, D., DeMenocal, P.B., Winckler, G., Stuut, J.B.W., Bradtmiller, L.I., 2013. The magnitude, timing and abruptness of changes in North African dust deposition over the last 20,000 yr. Earth Planet. Sci. Lett. 371–372, 163–176. https://doi.org/10.1016/j.epsl.2013.03.054

Metcalfe, S.E., Barron, J.A., Davies, S.J., 2015. The Holocene history of the North American Monsoon: "known knowns" and "known unknowns" in understanding its spatial and temporal complexity. Quat. Sci. Rev. 120, 1–27. https://doi.org/10.1016/j.quascirev.2015.04.004

Pausata, F.S.R., Emanuel, K.A., Chiacchio, M., Diro, G.T., Zhang, Q., Sushama, L., Stager, J.C., Donnelly, J.P., 2017a. Tropical cyclone activity enhanced by Sahara greening and reduced dust emissions during the African Humid Period. Proc. Natl. Acad. Sci. U. S. A. https://doi.org/10.1073/pnas.1619111114

Pausata, F.S.R., Messori, G., Zhang, Q., 2016. Impacts of dust reduction on the northward expansion of the African monsoon during the Green Sahara period. Earth Planet. Sci. Lett. 434, 298–307. https://doi.org/10.1016/j.epsl.2015.11.049

Pausata, F.S.R., Qiong, Z., Muschitiello, F., Lu, Z., Chafik, L., Niedermeyer, E.M., Stager, J.C., Cobb, K.M., Liu, Z., 2017b. Greening of the Sahara suppressed ENSO activity during the Mid-Holocene. Nat. Geosci. under rev. https://doi.org/10.1038/ncomms16020

Peltier, W.R., Argus, D.F., Drummond, R., 2015. Space geodesy constrains ice age terminal deglaciation: The global ICE-6G_C (VM5a) model. J. Geophys. Res. Solid Earth 120, 450–487. https://doi.org/10.1002/2014JB011176

Perez-Sanz, A., Li, G., González-Sampériz, P., Harrison, S.P., 2014. Evaluation of modern and mid-Holocene seasonal precipitation of the Mediterranean and northern Africa in the

CMIP5 simulations. Clim. Past 10, 551–568. https://doi.org/10.5194/cp-10-551-2014

Prentice, I.C., Harrison, S.P., Jolly, D., Guiot, J., 1998. The climate and biomes of Europe at 6000 yr BP: Comparison of model simulations and pollen-based reconstructions. Quat. Sci. Rev. 17, 659–668. https://doi.org/10.1016/S0277-3791(98)00016-X

Rozanski, K., Araguás-Araguás, L., Gonfiantini, R., 1993. Isotopic Patterns in Modern Global Precipitation, in: Swart, P.K., Lohmann, K.C., Mckenzie, J., Savin, S. (Eds.), Climate Change in Continental Isotopic Records. American Geophysical Union, pp. 1–36. https://doi.org/10.1029/GM078p0001

Sha, L., Ait Brahim, Y., Wassenburg, J.A., Yin, J., Peros, M., Cruz, F.W., Cai, Y., Li, H., Du, W., Zhang, H., Edwards, R.L., Cheng, H., 2019. How Far North Did the African Monsoon Fringe Expand During the African Humid Period? Insights From Southwest Moroccan Speleothems. Geophys. Res. Lett. 46, 14093–14102. https://doi.org/10.1029/2019GL084879

Skinner, C.B., Poulsen, C.J., 2016. The role of fall season tropical plumes in enhancing Saharan rainfall during the African Humid Period. Geophys. Res. Lett. 43, 349–358. https://doi.org/10.1002/2015GL066318

Sowers, T., 2010. Atmospheric methane isotope records covering the Holocene period. Quat. Sci. Rev. 29, 213–221. https://doi.org/10.1016/j.quascirev.2009.05.023

Sun, W., Wang, B., Zhang, Q., Pausata, F.S.R., Chen, D., Lu, G., Yan, M., Ning, L., Liu, J., 2019. Northern Hemisphere land monsoon precipitation increased by the Green Sahara during mid-Holocene. Geophys. Res. Lett. 2019GL082116. https://doi.org/10.1029/2019GL082116

Swann, A.L.S., Fung, I.Y., Liu, Y., Chiang, J.C.H., 2014. Remote vegetation feedbacks and the mid-Holocene Green Sahara. J. Clim. 27, 4857–4870. https://doi.org/10.1175/JCLI-D-13-00690.1

Tabor, C., Otto-Bliesner, B., Liu, Z., 2020. Speleothems of South American and Asian Monsoons Influenced by a Green Sahara. Geophys. Res. Lett. 1–11. https://doi.org/10.1029/2020gl089695

Tarasov, P.E., Webb, T., Andreev, A.A., Afanas'eva, N.B., Berezina, N.A., Bezusko, L.G., Blyakharchuk, T.A., Bolikhovskaya, N.S., Cheddadi, R., Chernavskaya, M.M., Chernova, G.M., Dorofeyuk, N.I., Dirksen, V.G., Elina, G.A., Filimonova, L. V., Glebov, F.Z., Guiot,

J., Gunova, V.S., Harrison, S.P., Jolly, D., Khomutova, V.I., Kvavadze, E. V., Osipova, I.M., Panova, N.K., Prentice, I.C., Saarse, L., Sevastyanov, D. V., Volkova, V.S., Zernitskaya, V.P., 1998. Present-day and mid-Holocene biomes reconstructed from pollen and plant macrofossil data from the former Soviet Union and Mongolia. J. Biogeogr. 25, 1029–1053. https://doi.org/10.1046/j.1365-2699.1998.00236.x

Tierney, J.E., Pausata, F.S.R., DeMenocal, P.B., 2017. Rainfall regimes of the Green Sahara. Sci. Adv. 3, e1601503. https://doi.org/10.1126/sciadv.1601503

Vamborg, F.S.E., Brovkin, V., Claussen, M., 2011. The effect of a dynamic background albedo scheme on Sahel/Sahara precipitation during the mid-Holocene. Clim. Past 7, 117–131. https://doi.org/10.5194/cp-7-117-2011

Winkler, K., Fuchs, R., Rounsevell, M., Herold, M., 2021. Global land use changes are four times greater than previously estimated. Nat. Commun. 12, 2501. https://doi.org/10.1038/s41467-021-22702-2

Xie, X., Zhang, H., Liu, X., Peng, Y., Liu, Y., 2017. Sensitivity study of cloud parameterizations with relative dispersion in CAM5.1: Impacts on aerosol indirect effects. Atmos. Chem. Phys. 17, 5877–5892. https://doi.org/10.5194/acp-17-5877-2017

Chapter 2 Modulation of Mid-Holocene African Rainfall by Dust Aerosol Direct and Indirect Effects

Co-authors: Christopher B. Skinner, Christopher J. Poulsen, and Jiang Zhu

2.1 Abstract

Climate model simulations of the mid-Holocene (MH) consistently underestimate northern African rainfall for reasons not fully understood. While most models incorporate orbital forcing and vegetation feedbacks, they neglect dust reductions associated with greater vegetation cover. Here we simulate the MH climate response to reduced Saharan dust using CESM CAM5-chem, which resolves direct and indirect dust aerosol effects. Direct aerosol effects increase Saharan and Sahel convective rainfall by ~16% and 8%. In contrast, indirect aerosol effects decrease stratiform rainfall, damping the dust-induced total rainfall increase by ~13% in the Sahara and ~59% in the Sahel. Sensitivity experiments indicate the dust-induced precipitation anomaly in the Sahara and Sahel (0.27 and 0.18 mm/day) is smaller than the anomaly from MH vegetation cover (1.19 and 1.08 mm/day). Although sensitive to dust radiative properties, sea surface temperatures, and indirect aerosol effect parameterization, our results suggest that dust reductions had competing effects on MH African rainfall.

2.2 Plain Language Summary

Six thousand years ago, changes in Earth's orbit led to greater summer season solar radiation over northern Africa. The increase in energy resulted in higher rainfall amounts, widespread vegetation, and reduced dust aerosols over regions that today are desert. In this study we use a climate model, CESM CAM5-chem, that accounts for the ways dust aerosols interact with sunlight and cloud droplets to examine how the reduction in Saharan dust during this past humid time affected rainfall. When dust aerosols are reduced in the model, more sunlight reaches the surface, the Sahara warms, and convective rainfall from the West African Monsoon increases.

However, through dust-cloud droplet interactions, the same reduction in dust decreases nonconvective rainfall, which is less prevalent during the monsoon season but still important, and thus dampens the total rainfall increase. Overall, dust reduction leads to a rainfall response that is dependent on rainfall type. Lastly, we compare the rainfall response of reducing dust to that of increasing vegetation cover and find that while important, the response from dust is considerably weaker.

2.3 Introduction

Northern Africa has experienced wet and dry phases fluctuating on orbital time scales since at least the late Miocene (deMenocal, 1995; Zhang et al., 2014). At the end of the African Humid Period (AHP; ~14.8 to 5.5 ka BP), the most recent wet phase, portions of the Sahara transitioned from a largely vegetated landscape to desert within only a few centuries (deMenocal et al., 2000; Tierney et al., 2017). Proxy records and general circulation models provide evidence that Quaternary orbital-scale humid periods, including the early to mid-Holocene (MH) AHP, are linked to precession-driven enhancements of boreal summer insolation, which strengthen monsoonal flow and increase rainfall across northern Africa (deMenocal, 1995; Kutzbach, 1981; Tjallingii et al., 2008; Tuenter et al., 2007). Insolation changes alone, however, are insufficient to explain the climate and ecological changes inferred from AHP proxies (Joussaume et al., 1999). The latest MH (6 ka BP) climate model simulations from Paleoclimate Modelling Intercomparison Project Phase 3, which, by design, include orbital insolation changes but neglect biogeophysical changes in northern Africa, underestimate AHP precipitation by as much as 400 mm/year (Perez-Sanz et al., 2014).

The discrepancy between proxy-derived and climate model estimates of rainfall has spurred investigation of the land-atmosphere interactions that shaped northern African hydroclimate change (e.g., Braconnot et al., 1999; Charney, 1975; Claussen et al., 1999; Claussen & Gayler, 1997; Vamborg et al., 2014). Several lines of proxy evidence indicate that steppe, savanna, and shrub vegetation reached up to 31°N (Hoelzmann et al., 1998; Jolly et al., 1998; Shanahan et al., 2015; Tierney et al., 2017). By reducing Saharan surface reflectance and enhancing evapotranspiration, expanded vegetation cover modified the local surface energy balance and increased both moist static energy and rainfall (Charney, 1975; Charney et al., 1975; Eltahir, 1998). Climate modeling studies have confirmed vegetation as a positive feedback on

precessional forcing to enhance AHP precipitation (Boos & Korty, 2016; Brovkin et al., 1998; Knorr & Schnitzler, 2006; Levis et al., 2004; Patricola & Cook, 2007; Skinner & Poulsen, 2016). However, even after accounting for vegetation expansion, climate models do not adequately simulate the intensity and northward extent of rainfall inferred from Saharan proxy records (Brostrom et al., 1998; Hoelzmann et al., 1998; Tierney et al., 2017).

Vegetation also indirectly impacts northern African climate through its control on dust mobilization. During the AHP, vegetation in the Sahara resulted in dust aerosol emissions two to three times lower than today (deMenocal et al., 2000; Egerer et al., 2016; McGee et al., 2013). This decrease in dust is postulated to have impacted AHP precipitation through direct, indirect, and semidirect dust aerosol effects (Pausata et al., 2016; Perlwitz & Miller, 2010; Williams et al., 2016). Direct aerosol effects describe the scattering and absorption of radiation by aerosols (Ghan et al., 2012). Indirect aerosol effects account for alterations to cloud optical properties and precipitation efficiency, through changes in droplet number concentration and size, that occur when aerosols nucleate cloud droplets (Ghan et al., 2013; X. Xie et al., 2017). Semidirect aerosol effects include the response of clouds to radiative heating of atmospheric aerosols (Ghan et al., 2012; Grassl, 1975). Over present-day northern Africa, direct dust aerosol effects impact rainfall variability by influencing surface warming and, by extension, deep convection (J. Huang et al., 2009). The response of rainfall to dust indirect aerosol effects is less understood; studies have shown that Saharan dust aerosols nucleate ice clouds, and liquid clouds to a lesser extent, and suppress rainfall in northern Africa (DeMott et al., 2003; J. Huang et al., 2009; Rosenfeld et al., 2001; Sassen et al., 2003).

Vegetation-driven dust reductions on AHP precipitation have received relatively little attention. To date, most model simulations, including those from Paleoclimate Modelling Intercomparison Project Phase 3, specify preindustrial (PI) dust loading (Braconnot et al., 2011; Taylor et al., 2012). Using a model that only resolves direct aerosol effects, Pausata et al. (2016) accounted for changes in MH vegetation cover and the associated dust reduction and found that a reduced dust load enhanced local rainfall by as much as 2.5 mm/day over the Sahara and shifted the West African Monsoon (WAM) northward. With the same model, Messori et al. (2018) showed that increased moisture recycling was a key driver of the rainfall response to reduced atmospheric dust load. However, the potential role of indirect aerosol effects, which have at least equal global radiative forcing (Myhre et al., 2013), on AHP precipitation, have never been explored.

Here, we investigate the role of dust on MH African climate with the CESM CAM5-chem model, which includes both direct and indirect aerosol effects. For context, we also compare the role of dust in shaping MH African climate with that of orbital forcing and vegetation cover.

2.4 Model Experiments and Methods

We employed the Community Atmosphere Model version 5 with tropospheric chemistry (CAM5-chem) coupled to the Community Land Model version 4.0 (CLM4.0; Neale et al., 2012; Oleson et al., 2010). The atmosphere (CAM5-chem) and land (CLM4.0) models are run with a grid resolution of 0.9° latitude × 1.25° longitude. CAM5-chem contains 30 vertical levels; CLM4.0 contains 15 soil-column layers. CAM5-chem is suited for studies involving atmospheric aerosols because it explicitly predicts ice and mixed-phase immersion, deposition, and contact nucleation by dust aerosols for stratiform clouds; these explicit nucleation processes are absent for convective clouds (Neale et al., 2012; Tilmes et al., 2015). In general, the addition of microphysics parameterizations related to aerosol indirect effects lead to better simulation of regional rainfall (Lin et al., 2018). Sagoo and Storelvmo (2017) show that increased dust leads to enhanced ice nucleation and suppressed tropical rainfall in CAM5, consistent with observations (e.g., Rosenfeld et al., 2001). Over Africa, the model reasonably simulates modern precipitation, including the seasonal cycle and total rainfall amount (Skinner & Poulsen, 2016). A description of aerosol properties in CAM5-chem can be found in 2.10 Supplementary Information.

In CLM4.0, vegetation leaf area index (LAI) and stem area index (SAI) are prescribed for each plant functional type and vary monthly. Dust is mobilized diagnostically from the land surface by the Dust Entrainment and Deposition model from Zender et al. (2003). We follow Skinner and Poulsen (2016) and use prescribed monthly varying MH sea surface temperatures (SSTs) calculated by adding the SST anomalies from the fully coupled CCSM4 MH 6 ka simulation (Gent et al., 2011; Taylor et al., 2012) to average monthly SSTs from years 1870 to 1890 of the merged Hadley-OI observation data set (Hurrell et al., 2008). In order to equilibrate the atmosphere model with the land model, each simulation is run for 35 years, with the last 30 years used in analysis, following Skinner and Poulsen (2016).

Table 2.1. List of simulations and boundary conditions, northern WAM limits (°N), and JJAS dust aerosol optical depth and rainfall (mm/day).

Simulation	Orbital forcing[a]	Vegetation[a]	Soil albedo[a]	Mobilizes Saharan dust?	Northern limit of West African Monsoon	Dust aerosol optical depth[b]	Total rainfall[b]	Convective rainfall[b]	Stratiform rainfall[b]
PI Control	PI	PI	PI	Yes	19.3	**0.43** 0.30	**0.26** 4.41	**0.22** 3.73	**0.04** 0.68
MH Control	MH	MH	MH	No	28.7	**0.02** 0.01	**2.54** 7.62	**2.26** 5.90	**0.28** 1.72
MH HighDust	MH	MH	MH	Yes	27.8	**0.96** 0.24	**2.27** 7.44	**1.95** 5.47	**0.32** 1.97
MH DesertVeg	MH	PI	MH	No	25.9	**0.03** 0.02	**1.35** 6.54	**1.21** 5.36	**0.14** 1.18
MH DesertSoil	MH	MH	PI	No	28.7	**0.02** 0.01	**2.39** 7.51	**2.15** 5.82	**0.24** 1.69
MH Orbital	MH	PI	PI	Yes	22.1	**0.48** 0.24	**0.62** 5.50	**0.54** 4.48	**0.08** 1.02

[a]PI=Preindustrial, MH=Mid-Holocene. [b]Averages for Sahara (**bold text**) and Sahel (plain text).

We ran a total of six CAM5-chem simulations to isolate the individual and combined contributions of orbital forcing, vegetation cover, soil albedo, and dust emissions on MH African climate (Table 2.1). Our control simulations, *PI Control* and *MH Control*, have orbital parameters, greenhouse gas concentrations, SSTs, and land surface parameters, including soil albedo and vegetation cover, set to PI and MH values, respectively (Table S2.1). Our prescription of MH vegetation included changes to plant functional type percentage and values of LAI (Figure S2.1 and Table S2.2; Davies et al., 2015; Hoelzmann et al., 1998; Levis et al., 2004; Pausata et al., 2016). MH values for dry and saturated soil albedo are prescribed separately from vegetation (Table S2.2), and soil texture is not changed from PI values in any simulation. In CLM4.0, dust mobilization is prohibited when leaf and stem area values (LAI + SAI) exceed 0.3 (Oleson et al., 2010). In *MH Control*, northern African LAI + SAI exceeded this threshold year-round preventing dust mobilization over the prescribed land surface. A comparison between *MH Control* and *PI Control* provides an estimate of the total climate change between the MH and PI time periods (Figures S2.2 and S2.3).

Sensitivity experiments were conducted to isolate the individual impacts of dust loading (*MH HighDust*), orbital forcing (*MH Orbital*), MH vegetation (*MH DesertVeg*), and MH soil albedo (*MH DesertSoil*). The *MH HighDust* simulation is identical to *MH Control* except the

vegetational control on dust mobilization was removed. Thus, *MH HighDust* allowed dust emissions to occur in the presence of a vegetated Sahara (Table 2.1). *MH Orbital* is identical to *PI Control* except for its specified MH orbit. *MH DesertVeg* and *MH DesertSoil* are both identical to *MH Control* except *MH DesertVeg* includes PI Saharan vegetation (i.e., a desert Sahara) and *MH DesertSoil* contains PI soil albedo values underneath a vegetated MH Sahara (Table 2.1). We prohibited dust mobilization in *MH DesertVeg* despite the simulation's absence of MH vegetation. A description of the offline radiative transfer calculation method used to isolate the direct aerosol effect associated with Saharan dust can be found in 2.10 Supplementary Information. We assessed the statistical significance of changes between simulations at the 95% confidence level using the Student's t test with the assumption of different population variances. Given the considerably larger changes in dust loading over the Sahara (20–31°N, 20°W–30°E) in our experiments (Figure 2.1a), we focus primarily on climate changes in this region. We provide detailed analyses of the Sahel (10–20°N, 15°W–30°E) climate response in Table 2.1 and the Supporting Information.

2.5 Results

2.5.1 Saharan Dust Mobilization

Simulated dust aerosol optical depth (AOD) varies substantially between simulations due to the dependence of dust mobilization on vegetation and wind speed (Table 2.1 and Figure S2.4; Zender et al., 2003). For *MH HighDust*, the average monsoon season (JJAS = June, July, August, September) dust AOD over the Sahara is 123% higher than *PI Control* (Table 2.1). High dust AOD occurs because of the strong enhancement of monsoon flow associated with the combined influences of greater MH summer insolation and a lower surface albedo (Figures S2.3 and S2.4). In *MH Control* and *MH DesertSoil*, Saharan dust mobilization is prohibited because the prescribed vegetation LAI + SAI values exceed 0.3; however, the Sahara dust AOD in these simulations is not strictly zero with values of ~0.2–0.3, representing trace dust emissions originating from distant source regions (Table 2.1 and Figure S2.4). Differences between *MH Control* and *MH HighDust* isolate the simulated climate response to a 98% reduction in JJAS dust AOD over the Sahara (Figure 2.1a). In *MH Orbital*, dust AOD is 12% higher than *PI Control* due to slightly enhanced monsoon flow and greater convergence along the intertropical front from the MH increase in

summer insolation (Figures S2.3 and S2.4). Averages of single-scatter albedo over the Sahara, which illustrate the absorption properties of the dust layer, are in Table S2.3.

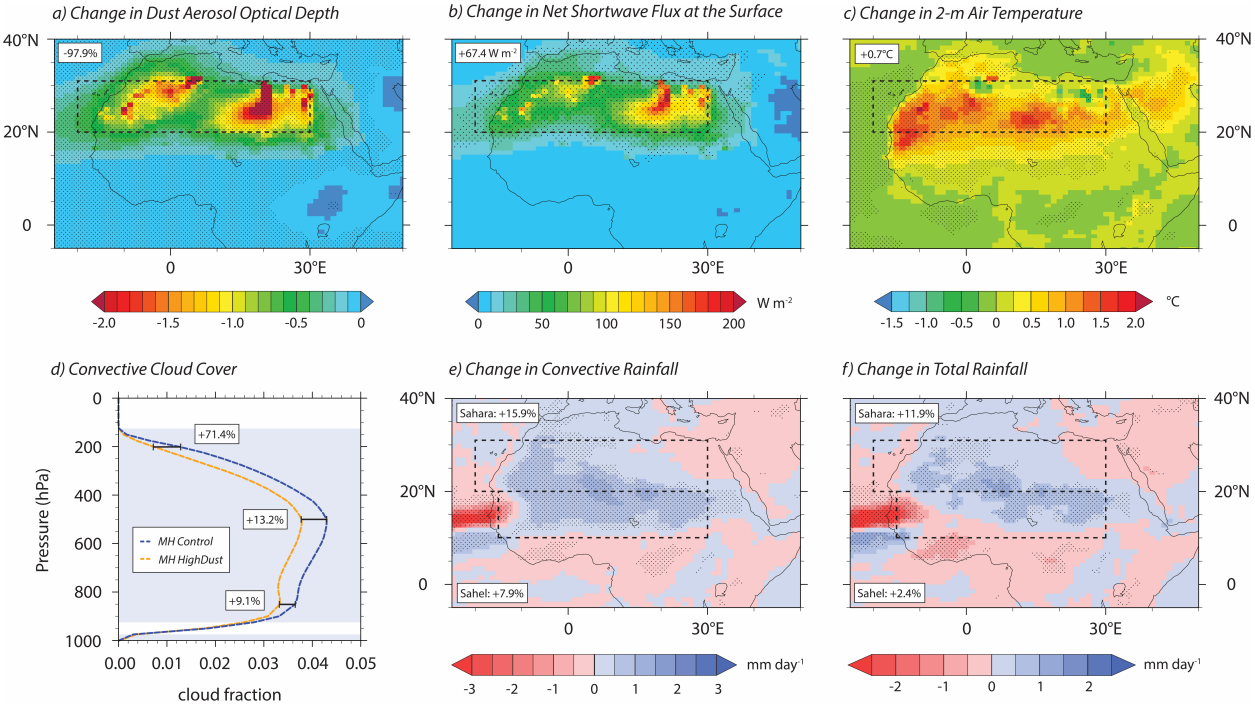

Figure 2.1. June, July, August, September differences between *MH Control* and *MH HighDust* in (a) dust aerosol optical depth, (b) net surface shortwave radiation flux diagnosed from offline radiation calculations, (c) 2-m air temperature, (d) profile of convective cloud cover averaged over the Sahara, (e) convective rainfall, and (f) total rainfall. In spatial maps, dashed boxes signify Saharan (upper) and Sahel (lower in (e)–(f)) extent used to calculate percent changes noted in left corner(s) of each panel. Numbers in atmospheric profile represent the percent change in cloud fraction at specific atmospheric levels (850, 500, and 200 hPa). Stippling in spatial maps and shading in the atmospheric profile indicate statistically significant differences at the 95% confidence level.

2.5.2 Direct Dust Aerosol Effects

The direct aerosol effects associated with a reduction in Saharan dust in CAM5-chem (*MH Control–MH HighDust*) act to increase net surface and top-of-the-atmosphere (TOA) shortwave radiation and surface temperature throughout the Sahara, which lead to increased convective rainfall. Our offline radiation calculation indicates that JJAS Saharan-average net downward shortwave radiation increases by 67.4 and 13.7 W/m^2 at the surface and TOA, respectively, due to reduction in backscattering from the removal of dust (Figure 2.1b, Table S2.4, and Figure S2.5). Direct aerosol effects warm the Sahara partly by enhanced TOA forcing, which couples upper tropospheric temperatures with the surface via convective mixing (Figure 2.1c; Miller et al., 2014).

The excess energy input at the surface is partitioned into positive sensible and latent heat fluxes (Figure S2.5), increasing convection and convective cloud cover throughout the atmospheric column (Figure 2.1d). The enhanced convective cloud cover contributes to the 15.9% increase in JJAS convective rainfall (from 1.95 to 2.26 mm/day) over the Sahara (Table 2.1 and Figure 2.1e), contributing substantially to the total precipitation increase of 11.9% (from 2.27 to 2.54 mm/day; Table 2.1 and Figure 2.1f). Likewise, JJAS convective rainfall increases by 7.9% in the Sahel (from 5.47 to 5.90 mm/day), contributing to a total rainfall increase of 2.4% (from 7.44 to 7.62 mm/day; Table 2.1). This result agrees qualitatively with previous modeling studies that find increased northern African precipitation in response to enhanced direct radiative forcing from a reduced dust load (J. Huang et al., 2009; Pausata et al., 2016). We note that the magnitude of rainfall response has been found to be sensitive to details of the radiative properties of dust with stronger absorbing dust leading to greater monsoonal rainfall (Hopcroft & Valdes, 2018; Miller, Tegen, et al., 2004; Strong et al., 2015).

2.5.3 Indirect Dust Aerosol Effects

Our dust sensitivity experiment further demonstrates that the indirect aerosol effects associated with reduced Saharan dust loading act to decrease stratiform rainfall over the Sahara and Sahel, and thus dampen the rainfall increase from direct dust aerosol effects. When JJAS dust is reduced, the average in-cloud droplet number concentration decreases and in-cloud droplet radius increases throughout much of the atmospheric column (Figure 2.2a-d and Figure S2.6c–f), consistent with expected indirect aerosol effects (Ghan et al., 2013; X. Xie et al., 2017) and previous research in northern Africa (DeMott et al., 2003; Rosenfeld et al., 2001). As a result of the altered stratiform cloud microphysics, Saharan- and Sahel-average JJAS stratus cloud fraction decreases through nearly the entire atmospheric column (Figure 2.2e, Figure S2.6b). These decreases in stratus cloud cover contribute to a 12.5% reduction (0.32 to 0.28 mm/day) in JJAS stratiform rainfall over the Sahara (Table 2.1 and Figure 2.2f). In the Sahel, a larger magnitude reduction in stratiform rainfall (from 1.97 to 1.72 mm/day) occurs due to the higher stratus cloud cover there (Table 2.1, Figure 2.2e–f, and Figure S2.6b). The stratiform rainfall difference due to dust in the Sahel is more than six times higher (0.25 vs 0.04 mm/day); however, the percent reduction is similar in both regions (−12.7% vs −12.5%; Table 2.1).

While the dominant type of precipitation over northern Africa is convective rainfall, which comprises over 70% of total rainfall in each simulation (Table 2.1), the decrease in stratiform rainfall, stemming from indirect aerosol effects, counteracts the increase in convective rainfall and thus dampens the total precipitation increase by 13.1% over the Sahara and 58.6% over the Sahel (Table 2.1). Overall, total JJAS precipitation increases by 11.9% (0.27 mm/day) and 2.4% (0.18 mm/day) over the Sahara and Sahel, respectively, resulting from 0.31 and 0.43 mm/day increases in convective rainfall and 0.04 and 0.25 mm/day decreases in stratiform rainfall (Table 2.1, Figure 2.1e-f, and Figure 2.2f).

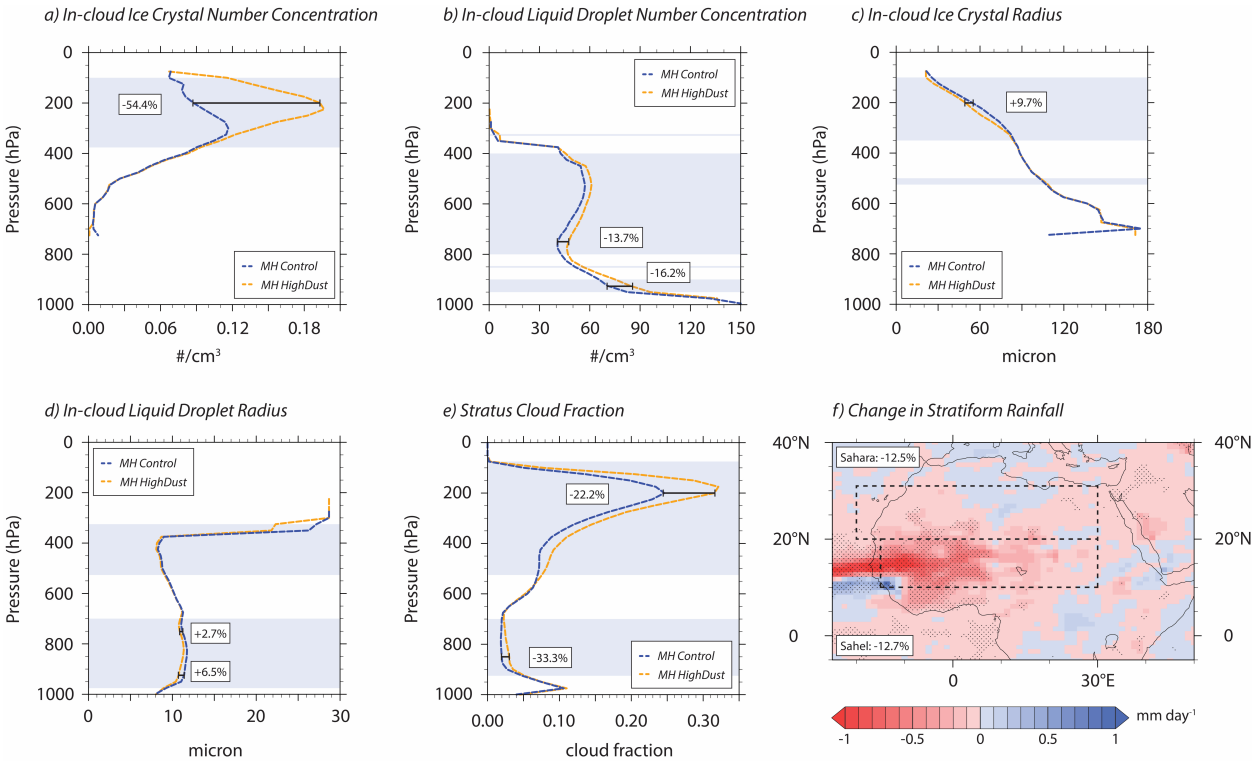

Figure 2.2. June, July, August, September Saharan-average atmospheric profiles for (a) in-cloud ice crystal number concentration, (b) in-cloud liquid droplet number concentration, (c) in-cloud ice crystal radius, (d) in-cloud liquid droplet radius, (e) stratus cloud fraction, and (f) spatial map of stratiform rainfall difference between *MH Control* and *MH HighDust*. Atmospheric profile and spatial map description same as Figure 2.1. "In-cloud" variables are calculated by dividing the specified cloud variable (e.g., ice crystal number concentration) by its fractional occurrence. Calculated differences for profile levels are shown as follows: (a) 200, (b) 750 and 925, (c) 200, (d) 750 and 925, and (e) 200 and 850 hPa.

2.5.4 Comparison of Dust, Orbital, and Vegetation Effects

To quantify the MH northern African rainfall response to orbital forcing and vegetation, we calculate the change in total JJAS precipitation for each simulation relative to *PI Control*. *MHControl* exhibits the largest Saharan rainfall increase and northward expansion with 2.28 mm/day higher rainfall and a northern WAM limit 9.4° further north than *PI Control* (2.10 Supplementary Information and Table 2.1). The three simulations with MH vegetation (*MH Control*, *MH HighDust*, and *MH DesertSoil*) exhibit rainfall and northern WAM limit increases more than double that from orbital forcing alone (Table 2.1). The increase in Saharan-average JJAS rainfall due to dust (direct and indirect aerosol effects combined) is 0.27 mm/day (0.18 mm/day in the Sahel), while the response due solely to vegetation is 1.19 mm/day (1.08 mm/day in the Sahel; Table 2.1; *MH Control–MH HighDust* compared with *MH Control–MH DesertVeg*). Though much less than the response to vegetation, the Saharan precipitation response to dust forcing alone is not insubstantial and is comparable to that from orbital forcing (0.36 mm/day; Table 2.1; *MH Orbital–PI Control*).

2.6 Discussion

Our results indicate that a reduced Saharan dust load during the humid MH had complex and competing influences on cloud properties and precipitation in northern Africa. We find that changes in direct dust aerosol effects increase MH African precipitation, in agreement with previous studies (e.g., Pausata et al., 2016; Williams et al., 2016), and that changes in indirect dust aerosol effects decrease stratiform rainfall, dampening the overall increase in MH African precipitation. Although our experiments cannot directly differentiate direct and indirect aerosol effects of dust in CAM5-chem, we show that direct dust aerosol effects lead to enhanced net radiation, which increases convective clouds and rainfall (Figure 2.1), whereas the reductions in stratus clouds and stratiform rainfall likely result from the cloud droplet changes associated with indirect dust aerosol effects (Figure 2.2) because indirect aerosol effects are predicted for stratiform clouds, but are absent for convective clouds.

While we cannot rule out that aerosol absorption or surface warming due to direct dust aerosol effects played a role in decreasing stratiform cloud cover (Figure 2.2e; Bretherton, 2015; Perlwitz & Miller, 2010), indirect aerosol effects likely play a larger role in driving the decrease. Aerosol absorption over the Sahara shows large decreases of up to 80% from the surface to ~500

hPa when dust is reduced (Figure S2.7), which is inconsistent with the stratiform cloud reduction profile at these levels. The changes in indirect aerosol effects (Figure 2.2a–d) are more consistent with the low- and high-level decreases in stratiform cloud cover and insignificant changes at ~600 hPa. Likewise, we tested the response to surface warming in our simulations by performing a sensitivity experiment with darker soil (*MH Control–MH DesertSoil*) to simulate the response of stratus clouds to land surface warming (Figure S2.8). The darkened soil produces surface warming of 0.2 °C over grasslands in the northeastern Sahara and a slight (nonsignificant) increase in stratus cloud cover in that region (Figure S2.8). Based on these results, we argue that, at the very least, aerosol absorption and surface warming are not driving the stratiform cloud reductions to a greater degree than indirect aerosol effects.

Modeling results on the response of African monsoonal rainfall to MH dust forcing differ quantitatively here from previous studies (e.g., Pausata et al., 2016). However, the exact reasons for the discrepancy are difficult to address, as previous studies employed different climate models with different physical parameterizations and used distinct experiment designs. We highlight that these differences, especially prescription of SST and the corresponding absence of ocean surface energy balance, require us to make a qualitative comparison between our results and those of Pausata et al. (2016). Coordinated climate model experiments using multiple models are needed to further assess these differences; however, there are several observations we can make.

In our study, the average dust-induced MH Saharan precipitation anomaly is 0.27 mm/day (with local maxima up to 1.5 mm/day; Table 2.1 and Figure 2.1f), while Pausata et al. (2016) simulates anomalies of 0.5 to 2.5 mm/day (an average Saharan value was not given). We attribute a portion of this discrepancy to the addition of indirect aerosol effects in our model, which are lacking in EC-Earth. The total dust-induced Saharan rainfall increase in our study (11.9% in the Sahara and 2.4% in the Sahel) includes changes to both dust direct (impacting convective rainfall) and indirect (impacting stratiform rainfall) aerosol effects. If we instead only consider changes in direct aerosol effects (i.e., convective rainfall), our simulations exhibit a 13.7% increase in Saharan rainfall (5.8% in the Sahel; Table 2.1). Thus, inclusion of indirect aerosol effects dampens the overall Saharan precipitation increase from reduced dust by 13.1% (58.6% in the Sahel; Table 2.1). If this damping from indirect aerosol effects holds in EC-Earth, its dust-induced rainfall anomaly would be smaller and produce better intermodel agreement.

Atmosphere-ocean coupling may also account for a portion of the dust-induced rainfall response discrepancy across climate models. Our dust-induced MH precipitation anomaly is likely sensitive to the uncertainties in ocean coupling and may differ with a dynamic ocean. EC-Earth from Pausata et al. (2016) includes dynamic SSTs that adjust to changes in atmospheric dust loading (Hazeleger et al., 2012; Madec & the NEMO Team, 2008). SSTs warm, in response to reduced dust, and increase WAM rainfall (Pausata et al., 2016). In the absence of indirect dust aerosol effects, however, the SST warming may be overestimated (Sagoo & Storelvmo, 2017). Our simulations have fixed SSTs, which, by nature, cannot respond to changes in dust loading. This potentially limits the magnitude of rainfall increase because the reduction in net surface radiation is not compensated by reduced evaporation (Miller, Perlwitz, et al., 2004; Yoshioka et al., 2007). However, SST prescription likely cannot explain the entire discrepancy. Williams et al. (2016) shows that the increase in African rainfall due to the SST response to reduced dust cannot account for the ~1–2 mm/ day difference between CAM5-chem and EC-Earth.

Physical parameterization of clouds and rainfall also likely contributes to the discrepancy. Generally, differences in convective and microphysics parameterization schemes have been shown to modify the rainfall response to dust aerosols (H. Huang et al., 2018; Solmon et al., 2012). More specifically, CAM5-chem differs from EC-Earth in that it utilizes a diagnostic microphysics scheme instead of a prognostic scheme (Forbes et al., 2011; Neale et al., 2012), which may account for a portion of its reduced rainfall anomaly. Analysis by S. Xie et al. (2012) suggests that CAM5 (with a diagnostic microphysics scheme) predicts ~2 mm/day less rainfall over equatorial Africa than CAM4 (with a prognostic microphysics scheme). A comparison of the rainfall response to vegetation in CAM5-chem and EC-Earth suggests a similar difference in rainfall sensitivity may exist between these models. EC-Earth ($MH_{GS2\text{-}PD}$–MH_{CNTL} in Pausata et al., 2016) exhibits a larger rainfall increase (>6 mm/day) than CAM5-chem (*MH HighDust–MH Orbital*; <5 mm/day), despite exhibiting a similar Saharan surface albedo change (within 0.05; Figure S2.9). However, this is not a clean comparison because our experiment changes dust AOD, while Pausata et al. (2016) does not. Yet, the larger response in EC-Earth may suggest larger rainfall sensitivity in the model.

While the total precipitation response to MH dust, and especially indirect aerosol effects, is fairly small in CAM5-chem, our results confirm that inclusion of MH dust changes improves AHP model-data comparisons (Figure S2.10). However, given the failure of our most realistic MH

simulation (*MH Control*) to fully enhance MH northern African rainfall to 31°N, we suggest that either (1) additional mechanisms are required beyond inclusion of the MH reduction in Saharan dust in AHP simulations, or (2) the hydroclimate responses to existing forcings and feedbacks in CAM5-chem are underestimated. With our analysis, we have identified for the first time a role of indirect dust aerosol effects in shaping MH northern African precipitation change. Our results suggest that models that do not incorporate indirect dust aerosol effects likely overestimate the dust contribution to enhanced precipitation, with the caveat that CAM5-chem neglects indirect aerosol effects in convective clouds, including ice nucleation, which may have potentially important impacts (Hoose et al., 2008; Vergara-Temprado et al., 2017). Future work should seek to calculate dust-induced MH precipitation anomalies with the full range of indirect aerosol effects.

2.7 Conclusion

We use CESM CAM5-chem, a climate model that resolves direct and indirect aerosol effects, to investigate the impact of dust on MH African climate. We find that when dust is reduced over the Sahara, the associated direct dust aerosol effects lead to a positive radiative forcing at the surface and TOA, warmer surface temperatures, increased convection, and increased convective rainfall. Due to the overwhelmingly convective nature of northern Africa during the MH monsoon season, the increase in convective rainfall ultimately supports a ~12% increase in total Saharan precipitation (2.4% in the Sahel). A concurrent decrease in indirect dust aerosol effects, which impact stratiform microphysics in CAM5-chem, counteracts the increase in convective rainfall. The reduction in Saharan dust loading leads to reduced number concentrations and increased size of cloud droplets. Consequently, stratiform rainfall decreases, which dampens the total Saharan precipitation response to dust by ~13% (58.6% in the Sahel). The results indicate that the inclusion of indirect dust aerosol effects has a secondary but important influence on MH African precipitation amount and characteristics (stratiform vs convective). This work also has implications for future climate in the Sahel, as it improves our understanding of the vegetation-dust-precipitation feedback, which may be key in shaping future precipitation as land use change and continued warming alter vegetation and dust mobilization in northern Africa (Evan et al., 2016; Yu et al., 2016; Zhu et al., 2016). Though the sign of the overall precipitation response to reduced dust in CAM5-chem matches that in previous work, the magnitude of precipitation change

is considerably smaller (regardless of the inclusion of indirect effects), highlighting the need for improved understanding and simulation of dust-rainfall responses in order to better understand the role of dust in shaping past and future climates.

2.8 Acknowledgments

This work was supported by National Science Foundation award 1602956. We thank Marco Gaetani, Francesco Pausata, Cheng Zhou, and Allison Steiner for helpful discussion. We also thank Ron Miller and one anonymous reviewer for their insightful and constructive comments. We acknowledge high-performance computing support from Cheyenne (doi:10.5065/ D6RX99HX) provided by NCAR's Computational and Information Systems Laboratory, sponsored by the National Science Foundation. This research was supported in part through computational resources and services provided by Advanced Research Computing at the University of Michigan, Ann Arbor. Data link available online (at https://github.com/ alexjt28).

2.9 References

Boos, W. R., & Korty, R. L. (2016). Regional energy budget control of the intertropical convergence zone and application to mid-Holocene rainfall. *Nature Geoscience*, *9*(12), 892–897. https://doi.org/10.1038/ngeo2833

Braconnot, P., Joussaume, S., Marti, O., & de Noblet, N. (1999). Synergistic feedbacks from ocean and vegetation on the African monsoon response to mid-Holocene insolation. *Geophysical Research Letters, 26,* 2481-2484. https://doi.org/10.1029/1999GL006047

Braconnot, P., Harrison, S. P., Otto-Bliesner, B., Abe-Ouchi, A., Jungclaus, J., & Peterschmitt, J.-Y. (2011). The Paleoclimate Modeling Intercomparison Project contribution to CMIP5. *CLIVAR Exchanges, 56*(16–2), 15-19. http://www.clivar.org/sites/default/files/ documents/Exchanges56.pdf

Bretherton, C. S. (2015). Insights into low-latitude cloud feedbacks from high-resolution models. *Philosophical Transactions of the Royal Society A, 373*(2054), 1-19. https://doi.org/10. 1098/rsta.2014.0415

Brostrom, A., Coe, M., Harrison, S. P., Gallimore, R., Kutzbach, J. E., Foley, J., et al. (1998). Land surface feedbacks and palaeomonsoons in northern Africa. *Geophysical Research*

Letters, 25(19), 3615–3618. https://doi.org/10.1029/98GL02804

Brovkin, V., Claussen, M., Petoukhov, V., & Ganopolski, A. (1998). On the stability of the atmosphere-vegetation system in the Sahara/Sahel region. *Journal of Geophysical Research, 103*(D24), 31,613-31,624. https://doi.org/10.1029/1998JD200006

Charney, J. G. (1975). Dynamics of deserts and drought in the Sahel. *Quarterly Journal of the Royal Meteorological Society, 101*(428), 193–202.

Charney, J., Stone, P. H., & Quirk, W. J. (1975). Drought in the Sahara: A Biogeophysical Feedback Mechanism. *Science*, *187*(4175), 434–435. https://doi.org/10.1126/science.187.4175.434

Claussen, M., & Gayler, V. (1997). The Greening of the Sahara during the Mid-Holocene: Results of an Interactive Atmosphere-Biome. *Global Ecology and Biogeography Letters*, *6*(5), 369–377. https://doi.org/10.2307/2997337

Claussen, M., Kubatzki, C., Brovkin, V., Ganopolski, A., Hoelzmann, P., & Pachur, H.-J. (1999). Simulation of an abrupt change in Saharan vegetation in the mid-Holocene. *Geophysical Research Letters*, *26*(14), 2037–2040. https://doi.org/10.1029/1999GL900494

Davies, F. J., Renssen, H., Blaschek, M., & Muschitiello, F. (2015). The impact of Sahara desertification on arctic cooling during the Holocene. *Climate of the Past, 11*(3), 571–586. https://doi.org/10.5194/cp-11-571-2015

deMenocal, P. (1995). Plio-Pleistocene African climate. *Science, 270*, 53-59.

deMenocal, P., Ortiz, J., Guilderson, T., Adkins, J., Sarnthein, M., Baker, L., & Yarusinsky, M. (2000). Abrupt onset and termination of the African Humid Period: Rapid climate responses to gradual insolation forcing. *Quaternary Science Reviews, 19*, 347–361. https://doi.org/10. 1016/S0277-3791(99)00081-5

DeMott, P. J., Sassen, K., Poellot, M. R., Baumgardner, D., Rogers, D. C., Brooks, S. D., et al. (2003). African dust aerosols as atmospheric ice nuclei. *Geophysical Research Letters*, *30*(14), 1732. https://doi.org/10.1029/2003GL017410

Egerer, S., Claussen, M., Reick, C., & Stanelle, T. (2016). The link between marine sediment records and changes in Holocene Saharan landscape: Simulating the dust cycle. *Climate of the Past, 12*, 1009–1027. https://doi.org/10.5194/cp-12-1009-2016

Eltahir, E. A. B. (1998). A soil moisture-rainfall feedback mechanism 1. Theory and

observations. *Water Resources Research*, *34*(4), 765–776. https://doi.org/10.1029/97WR03499

Evan, A. T., Flamant, C., Gaetani, M., & Guichard, F. (2016). The past, present and future of African dust. *Nature*, *531*(7595), 493–495. https://doi.org/10.1038/nature17149

Forbes, R., Tompkins, A. M., & Untch, A. (2011). A new prognostic bulk microphysics scheme for the IFS. *ECMWF Technical Memorandum*. (No. 649). Reading, UK: European Centre for Medium-Range Weather Forecasts.

Gent P. R., Danabasoglu, G., Donner, L. J., Holland, M. M., Hunke, E. C., Jayne, S. R., et al. (2011). The Community Climate System Model Version 4. *Journal of Climate*, *24*, 4973–4991. https://doi.org/10.1175/2011JCLI4083.1

Ghan, S. J., Liu, X., Easter, R. C., Zaveri, R., Rasch, P. J., & Yoon, J. (2012). Toward a minimal representation of aerosols in climate models: Comparative decomposition of aerosol direct, semidirect, and indirect radiative forcing. *Journal of Climate*, *25*, 6461–6476. https://doi.org/10.1175/JCLI-D-11-00650.1

Ghan, S. J., Smith, S. J., Wang, M., Zhang, K., Pringle, K., Carslaw, K., et al. (2013). A simple model of global aerosol indirect effects. *Journal of Geophysical Research: Atmospheres*, *118*, 6688–6707. https://doi.org/10.1002/jgrd.50567

Grassl, H. (1975). Albedo reduction and radiative heating of clouds by absorbing aerosol particles. *Beitr. Phys. Atmos., 48*, 199-209.

Hazeleger, W., Wang, X., Severijns, C., Ştefănescu, S., Bintanja, R., Sterl, A., et al. (2012). EC-Earth V2.2: description and validation of a new seamless earth system prediction model. *Climate Dynamics*, *39*(11), 2611–2629. https://doi.org/10.1007/s00382-011-1228-5

Hoelzmann, P., Jolly, D., Harrison, S. P., Laarif, F., Bonnefille, R., & Pachur, H.-J. (1998). Mid-Holocene land-surface conditions in northern Africa and the Arabian peninsula: A data set for the analysis of biogeophysical feedbacks in the climate system. *Global Biogeochemical Cycles, 12*(1), 35–51. https://doi.org/10.1029/97GB02733

Hoose, C., Lohmann, U., Erdin, R., & Tegen, I. (2008). The global influence of dust mineralogical composition on heterogeneous ice nucleation in mixed-phase clouds. *Environmental Research Letters*, *3*(025003), 1-14 https://doi.org/10.1088/1748-9326/3/2/025003

Hopcroft, P. O., & Valdes, P. J. (2018). On the role of dust-climate feedbacks during the mid-

Holocene. *Geophysical Research Letters*. https://doi.org/10.1029/2018GL080483

Huang, J., Zhang, C., & Prospero, J. M. (2009). African aerosol and large-scale precipitation variability over West Africa. *Environmental Research Letters, 4*, 1–8. https://doi.org/10.1088/1748-9326/4/1/015006

Huang, H., Gu, Y., Xue, Y., Jiang, J., & Zhao, B. (2018). Assessing aerosol indirect effect on clouds and regional climate of East/South Asia and West Africa using NCEP GFS. *Climate Dynamics*. https://doi.org/10.1007/s00382-018-4476-9

Hurrell, J. W., Hack, J. J., Shea, D., Caron, J. M., & Rosinski, J. (2008). A new sea surface temperature and sea ice boundary dataset for the community atmosphere model. *Journal of Climate, 21*(19), 5145-5153. https://doi.org/10.1175/2008JCLI2292.1

Jolly, D., Prentice, I. C., Bonnefille, R., Ballouche, A., Bengo, M., Brenac, P., et al. (1998). Biome reconstruction from pollen and plant macrofossil data for Africa and the Arabian peninsula at 0 and 6000 years. *Journal of Biogeography, 25*(6), 1007–1027. https://doi.org/10.1046/j.1365-2699.1998.00238.x

Joussaume, S., Taylor, K. E., Braconnot, P., Mitchell, J. F. B., Kutzbach, J. E., Harrison, S. P., et al. (1999). Monsoon changes for 6000 years ago: Results of 18 simulations from the Paleoclimate Modeling Intercomparison Project (PMIP). *Geophysical Research Letters*, *26*(7), 859–862. https://doi.org/10.1029/1999GL900126

Knorr, W., & Schnitzler, K. (2006). Enhanced albedo feedback in North Africa from possible combined vegetation and soil-formation processes. *Climate Dynamics*, *26*, 55–63. https://doi.org/10.1007/s00382-005-0073-9

Kutzbach, J. E. (1981). Monsoon climate of the early Holocene: Climate experiment with the earth's orbital parameters for 9000 years ago. *Science*, *214*(4516), 59–61.

Levis, S., Bonan, G. B., & Bonfils, C. (2004). Soil feedback drives the mid-Holocene North African monsoon northward in fully coupled CCSM2 simulations with a dynamic vegetation model. *Climate Dynamics, 23*, 791–802. https://doi.org/10.1007/s00382-004-0477-y

Lin, L., Xu, Y., Wang, Z., Diao, C., Dong, W., & Xie, S.-P. (2018). Changes in extreme rainfall over India and China attributed to regional aerosol-cloud interaction during the late 20th century rapid industrialization. *Geophysical Research Letters*, *45*, 1–9. https://doi.org/10.1029/2018GL078308

Madec, G., and the NEMO Team. (2008). NEMO ocean engine. *Note du Pôle de modélisation de Institut Pierre-Simon Laplace*. (No. 27). Paris, France: Institut Pierre-Simon Laplace. Retrieved from https://www.nemo-ocean.eu/wp-content/uploads/NEMO_book.pdf

McGee, D., DeMenocal, P. B., Winckler, G., Stuut, J. B. W., & Bradtmiller, L. I. (2013). The magnitude, timing and abruptness of changes in North African dust deposition over the last 20,000 yr. *Earth and Planetary Science Letters, 371–372*, 163–176. https://doi.org/10.1016/j.epsl.2013.03.054

Messori, G., Gaetani, M., Zhang, Q., Zhang, Q., & Pausata, F. S. R. (2018). The water cycle of the mid-Holocene West African Monsoon: The role of vegetation and dust emission changes. *International Journal of Climatology*, 1-13. https://doi.org/10.1002/joc.5924

Miller, R. L., Tegen, I., & Perlwitz, J. (2004a). Surface radiative forcing by soil dust aerosols and the hydrologic cycle. *Journal of Geophysical Research: Atmospheres*, *109*(D04203), 1-24. https://doi.org/10.1029/2003JD004085

Miller, R. L., Perlwitz, J., & Tegen, I. (2004b). Modeling Arabian dust mobilization during the Asian summer monsoon: The effect of prescribed versus calculated SST. *Geophysical Research Letters*, *31*(22), 1–4. https://doi.org/10.1029/2004GL020669

Miller, R. L., Knippertz, P., Pérez García-Pando, C., Perlwitz, J. P., & Tegen, I. (2014). Impact of Dust Radiative Forcing upon Climate. In P. Knippertz & J.-B. W. Stuut (Eds.), *Mineral Dust: A Key Player in the Earth System* (pp. 327–357). Dordrecht: Springer Netherlands. https://doi.org/10.1007/978-94-017-8978-3_13

Myhre, G., D. Shindell, F.-M., Bréon, W., Collins, J., Fuglestvedt, J., Huang, D., et al. (2013). Anthropogenic and Natural Radiative Forcing. In T.F. Stocker, D. Qin, G.-K. Plattner, M. Tignor, S. K. Allen, J.Boschung, et al. (Eds.), *Climate Change 2013: The Physical Science Basis. Contribution of Working Group I to the Fifth Assessment Report of the Intergovernmental Panel on Climate Change* (pp. 659-740). Cambridge, UK and New York: Cambridge University Press.

Neale, R. B., Chen, C.-C., Gettelman, A., Lauritzen, P. H., Park, S., Williamson, D. L., et al. (2012). *Description of the NCAR Community Atmosphere Model* (CAM5.0) (NCAR/TN-486+STR). Boulder, CO: National Center for Atmospheric Research.

Oleson, K. W., Lawrence, D. M., Bonan, G. B., Flanner, M. G., Kluzek, E., Lawrence, P. J. et al. (2010). *Technical description of version 4.0 of the Community Land Model* (CLM)

(NCAR/TN-478+STR). Boulder, CO: National Center for Atmospheric Research.

Patricola, C. M., & Cook, K. H. (2007). Dynamics of the West African monsoon under mid-Holocene precessional forcing: Regional climate model simulations. *Journal of Climate, 20,* 694-716. https://doi.org/10.1175/JCLI4013.1.

Pausata, F. S. R., Messori, G., & Zhang, Q. (2016). Impacts of dust reduction on the northward expansion of the African monsoon during the Green Sahara period. *Earth and Planetary Science Letters, 434*, 298–307. https://doi.org/10.1016/j.epsl.2015.11.049

Perez-Sanz, A., Li, G., González-Sampériz, P., & Harrison, S. P. (2014). Evaluation of modern and mid-Holocene seasonal precipitation of the Mediterranean and northern Africa in the CMIP5 simulations. *Climate of the Past*, *10*(2), 551–568. https://doi.org/10.5194/cp-10-551-2014

Perlwitz, J., & Miller, R. L. (2010). Cloud cover increase with increasing aerosol absorptivity: A counterexample to the conventional semidirect aerosol effect. *Journal of Geophysical Research Atmospheres*, *115*(8), 1–23. https://doi.org/10.1029/2009JD012637

Rosenfeld, D., Rudich, Y., & Lahav, R. (2001). Desert dust suppressing precipitation: A possible desertification feedback loop. *Proceedings of the National Academy of Sciences of the United States of America*, *98*(11), 5975–5980. https://doi.org/10.1073/pnas.101122798

Sagoo, N., & Storelvmo, T. (2017). Testing the sensitivity of past climates to the indirect effects of dust. *Geophysical Research Letters*, *44*, 5807–5817. https://doi.org/10.1002/2017GL072584

Sassen, K., DeMott, P. J., Prospero, J. M., & Poellot, M. R. (2003). Saharan dust storms and indirect aerosol effects on clouds: CRYSTAL-FACE results. *Geophysical Research Letters*, *30*(12), 1633. https://doi.org/10.1029/2003GL017371

Shanahan, T. M., Mckay, N. P., Hughen, K. A., Overpeck, J. T., Otto-Bliesner, B., Heil, C. W., et al. (2015). The time-transgressive termination of the African Humid Period. *Nature Geoscience, 8*, 140–144. https://doi.org/10.1038/NGEO2329

Skinner, C. B., & Poulsen, C. J. (2016). The role of fall season tropical plumes in enhancing Saharan rainfall during the African Humid Period. *Geophysical Research Letters, 43*, 349–358. https://doi.org/10.1002/2015GL066318

Solmon, F., Elguindi, N., & Mallet, M. (2012). Radiative and climatic effects of dust over West Africa, as simulated by a regional climate model. *Climate Research*, *52*(1), 97–113.

https://doi.org/10.3354/cr01039

Strong, J. D. O., Vecchi, G. A., & Ginoux, P. (2015). The response of the tropical Atlantic and West African climate to Saharan dust in a fully coupled GCM. *Journal of Climate*, *28*(18), 7071–7092. https://doi.org/10.1175/JCLI-D-14-00797.1

Taylor, K. E., Stouffer, R. J., & Meehl, G. A. (2012). An overview of CMIP5 and the experiment design. *Bulletin of the American Meteorological Society*, *93*(4), 485–498. https://doi.org/10.1175/BAMS-D-11-00094.1

Tierney, J. E., Pausata, F. S. R., & deMenocal, P. B. (2017). Rainfall regimes of the Green Sahara. *Science Advances, 3*, 1–9. https://doi.org/10.1126/sciadv.1601503

Tilmes, S., Lamarque, J. F., Emmons, L. K., Kinnison, D. E., Ma, P. L., Liu, X., et al. (2015). Description and evaluation of tropospheric chemistry and aerosols in the Community Earth System Model (CESM1.2). *Geoscientific Model Development, 8*, 1395–1426. https://doi.org/10.5194/gmd-8-1395-2015

Tjallingii, R., Claussen, M., Stuut, J. B. W., Fohlmeister, J., Jahn, A., Bickert, T., et al. (2008). Coherent high-and low-latitude control of the northwest African hydrological balance. *Nature Geoscience, 1*, 670–675. https://doi.org/10.1038/ngeo289

Tuenter, E., Weber, S. L., Hilgen, F. J., & Lourens, L. J. (2007). Simulating sub-Milankovitch climate variations associated with vegetation dynamics. *Climate of the Past, 3*, 169–180. https://doi.org/10.5194/cp-3-169-2007

Vamborg, F. S. E., Brovkin, V., & Claussen, M. (2014). Background albedo dynamics improve simulated precipitation variability in the Sahel region. *Earth System Dynamics*, *5*, 89–101. https://doi.org/10.5194/esd-5-89-2014

Vergara-Temprado, J., Murray, B. J., Wilson, T. W., O'Sullivan, D., Browse, J., Pringle, K. J., et al. (2017). Contribution of feldspar and marine organic aerosols to global ice nucleating particle concentrations. *Atmospheric Chemistry and Physics*, *17*(5), 3637–3658. https://doi.org/10.5194/acp-17-3637-2017

Williams, R. H., McGee, D., Kinsley, C. W., Ridley, D. A., Hu, S., Fedorov, A., et al. (2016). Glacial to Holocene changes in trans-Atlantic Saharan dust transport and dust-climate feedbacks. *Science Advances, 2*, 1–11. https://doi.org/10.1126/sciadv.1600445

Xie, S., Ma, H. Y., Boyle, J. S., Klein, S. A., & Zhang, Y. (2012). On the correspondence between short- and long-time-scale systematic errors in CAM4/CAM5 for the year of

tropical convection. *Journal of Climate*, *25*(22), 7937–7955. https://doi.org/10.1175/JCLI-D-12-00134.1

Xie, X., Zhang, H., Liu, X., Peng, Y., & Liu, Y. (2017). New cloud parameterization with relative dispersion in CAM5.1: model evaluation and impacts on aerosol indirect effects. *Atmospheric Chemistry and Physics, 17*, 5877-5892. https://doi.org/10.5194/acp-17-5877-2017

Yoshioka, M., Mahowald, N. M., Conley, A. J., Collins, W. D., Fillmore, D. W., Zender, C. S., & Coleman, D. B. (2007). Impact of desert dust radiative forcing on Sahel precipitation: Relative importance of dust compared to sea surface temperature variations, vegetation changes, and greenhouse gas warming. *Journal of Climate*, *20*(8), 1445–1467. https://doi.org/10.1175/JCLI4056.1

Yu, M., Wang, G., & Pal, J. S. (2016). Effects of vegetation feedback on future climate change over West Africa. *Climate Dynamics*, *46*(11–12), 3669–3688. https://doi.org/10.1007/s00382-015-2795-7

Zender, C. S. (2003). Mineral Dust Entrainment and Deposition (DEAD) model: Description and 1990s dust climatology. *Journal of Geophysical Research*, *108*(D14), 4416. https://doi.org/10.1029/2002JD002775

Zhang, Z., Ramstein, G., Schuster, M., Li, C., Contoux, C., & Yan, Q. (2014). Aridification of the Sahara desert caused by Tethys Sea shrinkage during the Late Miocene. *Nature*, *513*(7518), 401–404. https://doi.org/10.1038/nature13705

Zhu, Z., Piao, S., Myneni, R. B., Huang, M., Zeng, Z., Canadell, J. G., et al. (2016). Greening of the Earth and its drivers. *Nature Climate Change*, *6*(8), 791–795. https://doi.org/10.1038/nclimate3004

2.10 Supplementary information

Aerosols

In CAM5-chem, aerosols are predicted with the three-mode version of the Modal Aerosol Module. The size range for dust bins is 0.1-1.0 μm in accumulation mode and 1.0-10 μm in coarse mode. Aerosol radiative properties (e.g. single-scatter albedo) are a function of wet refractive index and wet surface radius (Neale et al., 2012).

Offline radiative transfer calculations

To isolate the direct aerosol effect associated with reduced Saharan dust, offline radiative transfer calculations were performed following the methodology of Colman (2003) with the parallel offline radiative transfer (PORT) tool (Conley et al., 2013). This method calculates radiative perturbations caused by a Saharan dust reduction, while keeping other radiation-related fields (e.g., temperature, water vapor, and clouds) unchanged. We conducted two control offline radiation calculations for *MH Control* and *MH HighDust*, respectively, with high frequency output of radiation-related fields. We then performed a sensitivity offline radiation calculation of the MH Control case with only the dust aerosol fields substituted by those from *MH HighDust*. The radiation perturbation was diagnosed as the difference between the sensitivity and MH Control offline radiation calculations. To ensure the offline radiation calculation reproduced the online version in CAM5-chem, 6-hourly radiation fields were used. To reduce potential interannual variation, the offline radiation calculation was conducted for five years for each case, with the last four used in analysis.

Northern limit of the West African monsoon

To define the northern limit of the West African Monsoon (WAM), we use a threshold of 2 mm/day, adapted from 60 mm/month, averaged over the zonal region 15°W–20°E (Pausata et al., 2016). With monthly model output, we calculate the northernmost latitude that exceeds 2 mm/day for each month over the zonal region. We find the northernmost latitude for each year, taken as the maximum of the year's monthly values, and create a distribution of northernmost latitudes for each of the 30 simulated years. The median value of each respective simulation's 30-year distribution is determined as the northernmost latitude the WAM reaches in that simulation.

Like Pausata et al. (2016), we use the median, as opposed to the mean, because it uses percentiles and is not affected by the shape of the distribution.

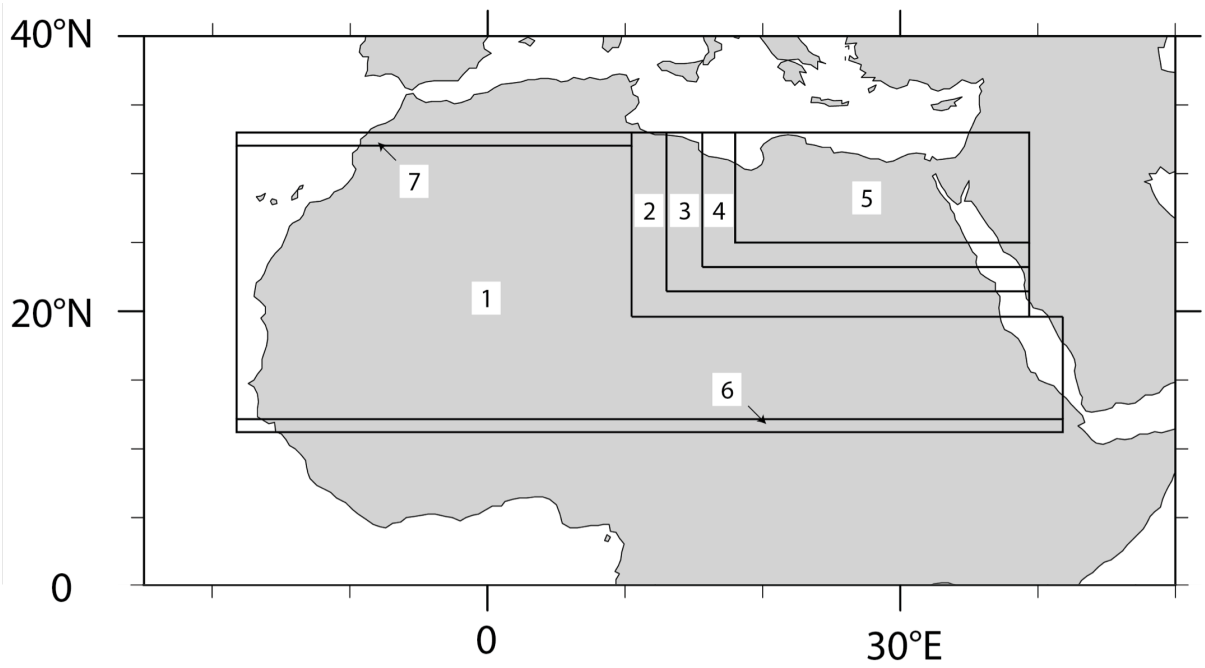

Figure S2.1. Mid-Holocene prescribed land surface zones. Details regarding plant functional type, leaf area index, and soil albedo specifications for each numbered zone are listed in Table S2.2.

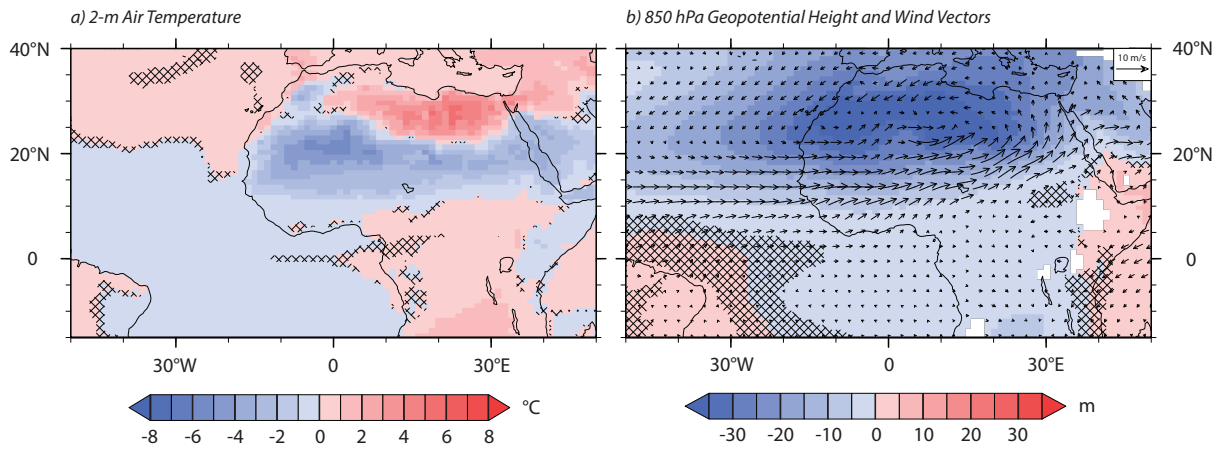

Figure S2.2. Difference (*MH Control–PI Control*) in monsoon season (JJAS) a) 2-m air temperature and b) 850 hPa geopotential height and winds. Differences that are not significant at the 95% confidence level are shown by cross-hatching.

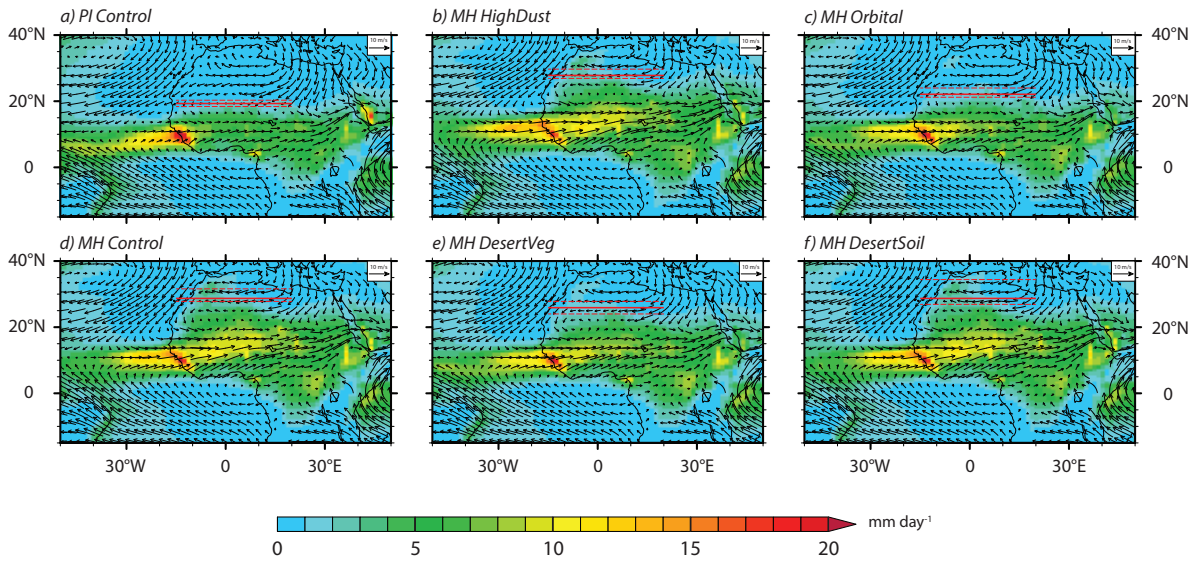

Figure S2.3. Monsoon season (JJAS) total precipitation and 850 hPa wind vectors for a) *PI Control*, b) *MH HighDust*, c) *MH Orbital*, d) *MH Control*, e) *MH DesertVeg*, and f) *MH DesertSoil* simulations. Solid red line represents the median northernmost latitude reached by the West African Monsoon (WAM) throughout the 30-year simulations. Dashed lines above and below the median latitude represent 75th and 25th percentile latitudes, respectively.

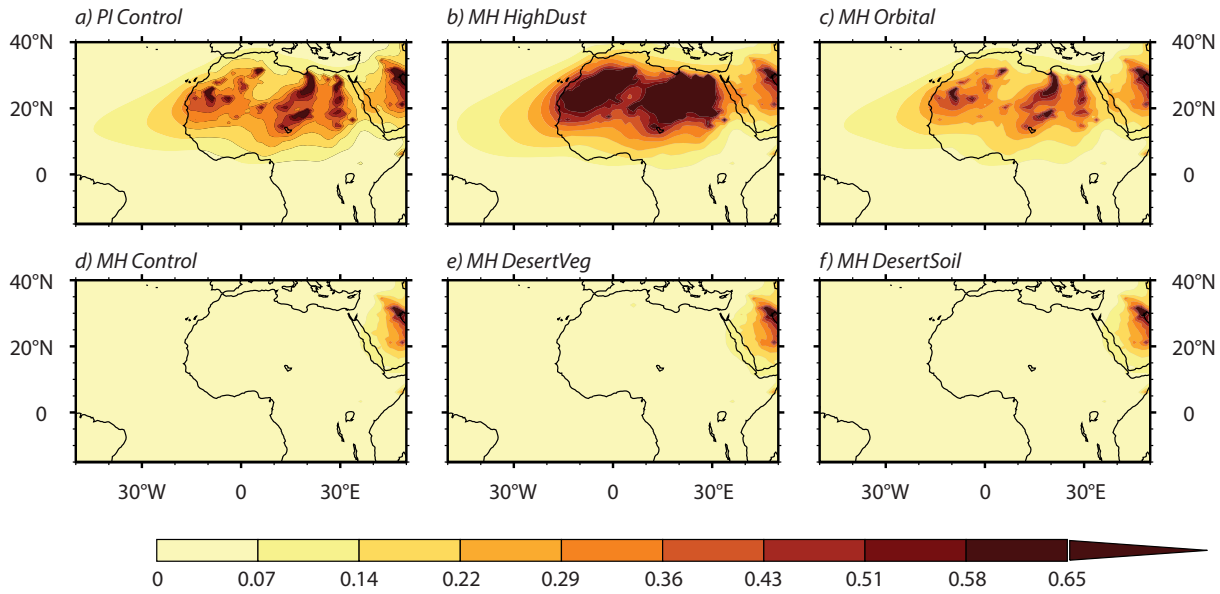

Figure S2.4. Annual dust aerosol optical depth (AOD) for a)–f) each CESM CAM5-chem simulation. Comparison of a) and b) with dust output from EC-Earth simulations in Pausata et al. (2016) and Gaetani et al. (2017) (see Gaetani et al. (2017), Figures S1a and S1b) demonstrates that CAM5-chem more closely captures the present-day dust distribution in the western Sahara. Note also that the increased dust AOD in b) compared with c) occurs due to stronger monsoon flow from expanded vegetation cover.

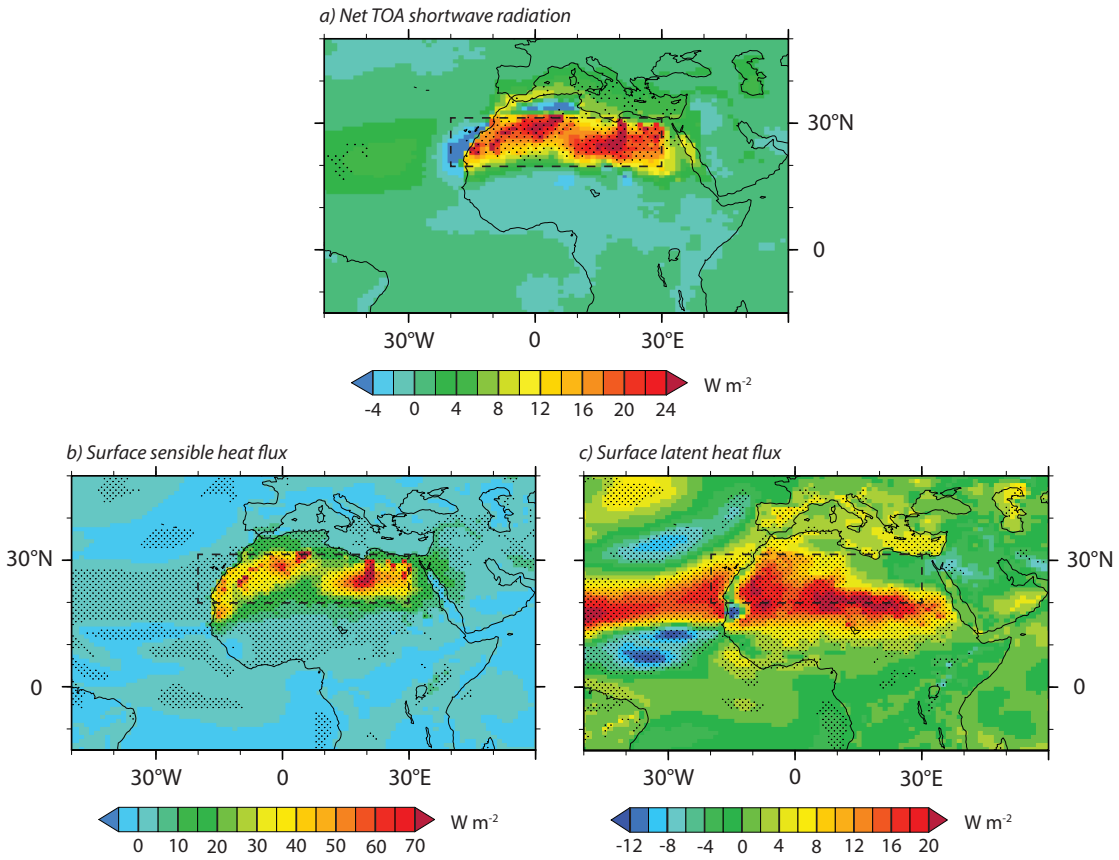

Figure S2.5. Monsoon season (JJAS) difference (*MH Control–MH HighDust*) for a) net shortwave radiative flux at TOA, b) surface sensible heat flux, and c) surface latent heat flux. a) represents radiative differences due to direct dust aerosol effects only from offline radiation calculations. b) and c) incorporate all radiative effects and feedbacks. Positive differences represent a net downward flux for a) and upward flux for b) and c). Stippling represents statistically significant differences at the 95% confidence level.

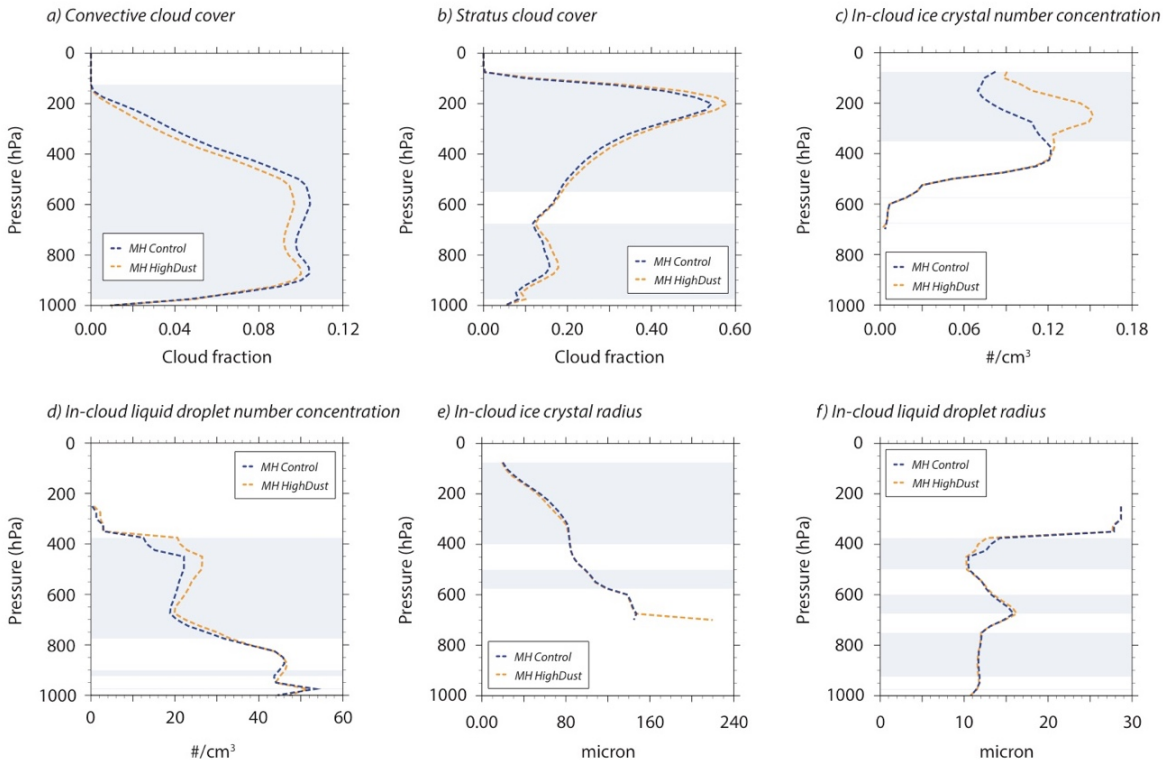

Figure S2.6. Monsoon season (JJAS) Sahel-averaged (10–20°N, 15°W–30°E) atmospheric profiles for *MH Control* and *MH HighDust* for a) convective cloud cover, b) stratus cloud cover, c) in-cloud ice crystal number concentration, d) in-cloud liquid droplet number concentration, e) in-cloud ice crystal radius, and f) in-cloud liquid droplet radius. Blue shading indicates statistically significant differences at the 95% confidence level. "In-cloud" variables are calculated by dividing the specified model output variable (i.e. ice crystal number concentration) by the fractional occurrence of ice or liquid.

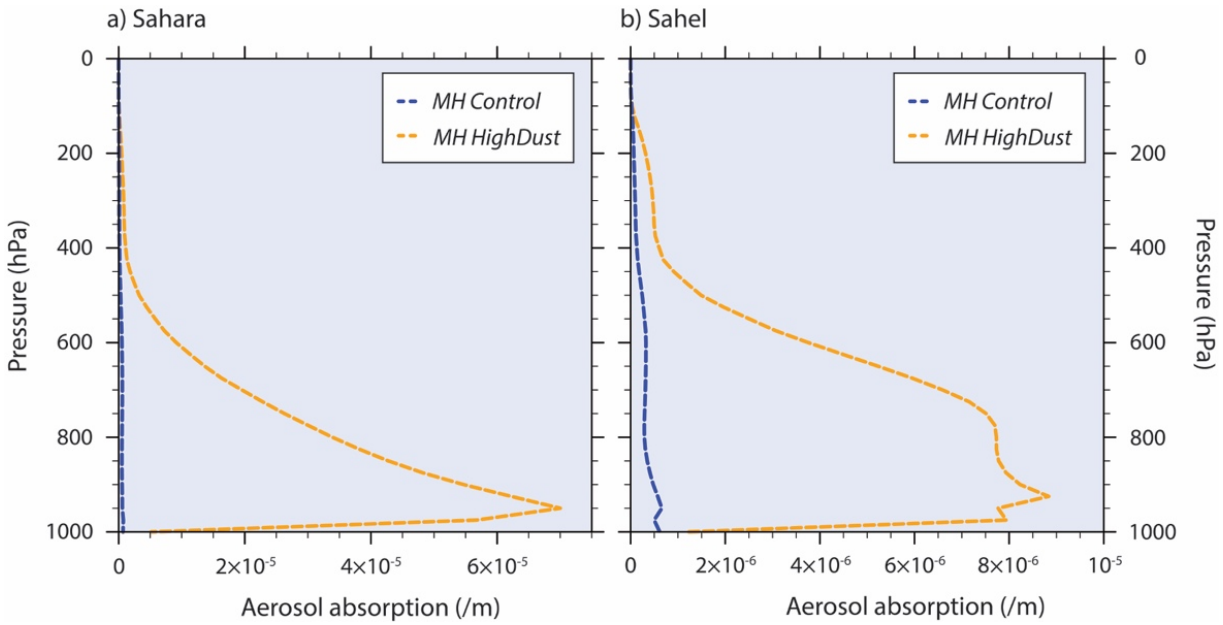

Figure S2.7. Monsoon season (JJAS) a) Saharan-averaged and b) Sahel-averaged atmospheric profile of aerosol absorption for *MH Control* and *MH HighDust*. Differences are statistically significant at the 95% confidence level at all levels.

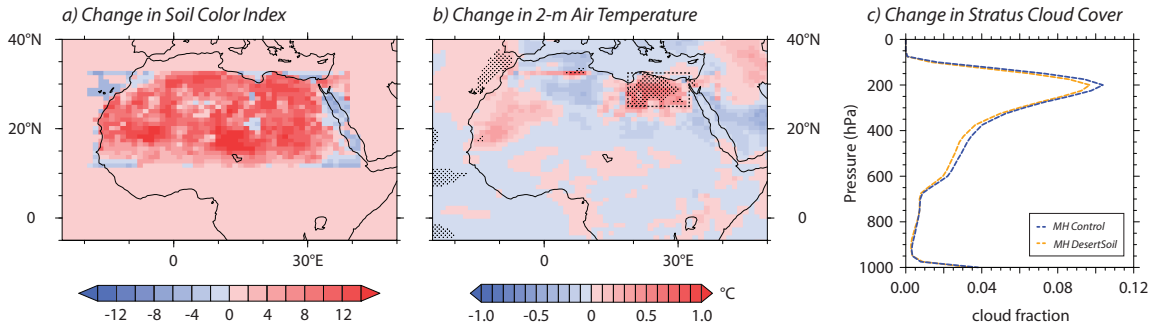

Figure S2.8. Sensitivity experiment with darker soil (*MH Control–MH DesertSoil*) showing a) change in soil color index (no units), b) the corresponding change in monsoon season (JJAS) 2-m air temperature, and c) the JJAS atmospheric profile of stratus cloud cover over the dashed region of surface warming in b) (25–32.5°N, 18.75°–32.5°E). For a), red values represent simultaneous decreases in albedo and increases in soil darkness. An increase in soil color index of 12, as exhibited across much of the Sahara, is representative of a decrease in dry and saturated albedo of ~0.14 and ~0.13, respectively. For example, this change could occur with a shift from Color Class 2 to Color Class 14 as shown in Table 3.3 of Oleson et al. (2010), which displays the dry and saturated albedo values associated with each index in CLM4.0. For b) and c), we highlight the region of warming in the northeastern Sahara because its prescribed vegetation (grassland) allows for greater interaction between the soil and solar radiation than the prescribed vegetation throughout the rest of the Sahara (mostly denser shrub). Thus, the change in soil albedo warms the surface here, while it has no significant effect on the remainder of the Sahara. Stippling in b) represents statistically significant differences at the 95% confidence level. The values in c) are not statistically significant at the 95% confidence level, but do illustrate a weak increase in stratus cloud cover throughout much of the atmospheric column.

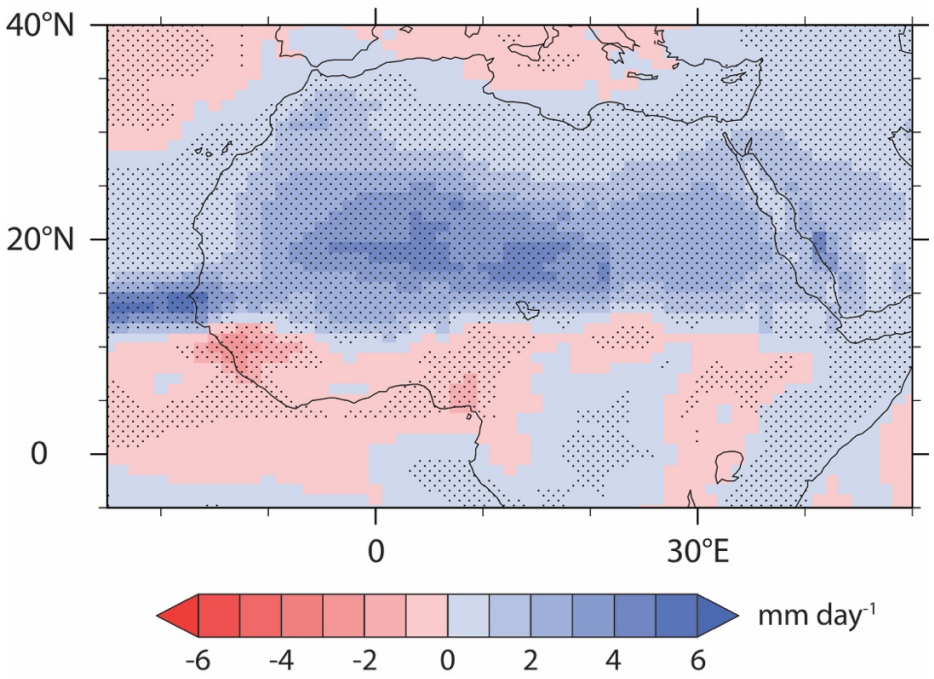

Figure S2.9. Monsoon season (JJAS) total precipitation from sensitivity experiment with expanded vegetation cover (darker surface albedo) and no reduction in dust (*MH HighDust–MH Orbital*). Stippling represents statistically significant differences at the 95% confidence level. To test difference in rainfall response to vegetation albedo changes without a reduction in dust, compare this figure to Figure 5b from Pausata et al. (2016).

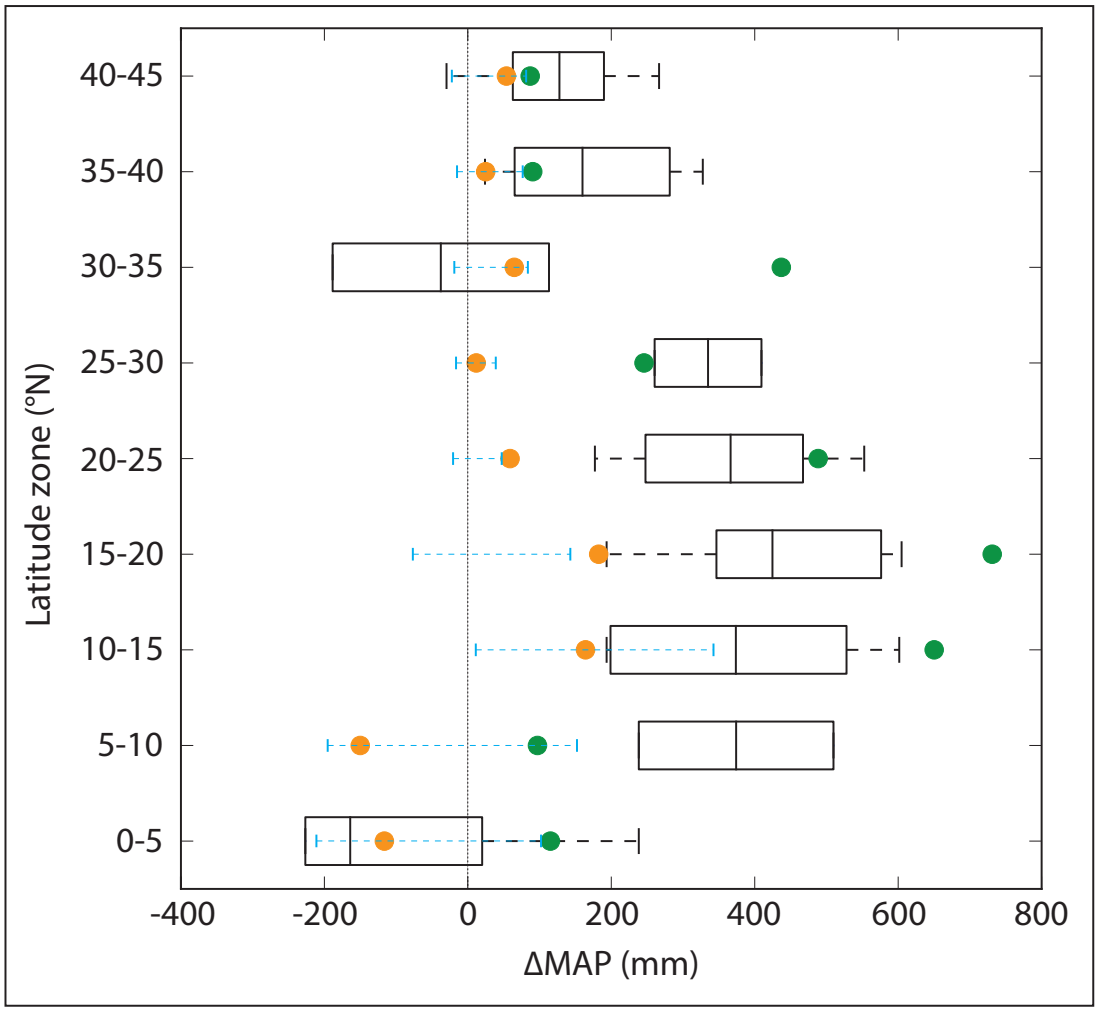

Figure S2.10. Changes in mean annual precipitation (MAP) from climate model simulations and reconstructions for 5° latitude bands between 20°W–30°E. Data for the reconstructions are from Bartlein et al. (2011) and are displayed as boxplots, which include the mean, 25% and 75% quartiles, and full range. Boxplots are calculated from available Bartlein et al. (2011) data points within each latitudinal band. CAM5-chem model results from this paper are shown by green dots (*MH Control–PI Control*) and orange dots (*MH Orbital–PI Control*). The full range of mid-Holocene PMIP3 model results (MH – PI) from Perez-Sanz et al. (2014) are shown as blue dashed lines. For both CAM5-chem and PMIP3, the results are calculated for the grid cells with available data in Bartlein et al. (2011). This figure is adapted from Fig. 6 in Perez-Sanz et al. (2014).

Table S2.1. Greenhouse gas concentrations, orbital parameters, and dust boundary conditions for simulations of Preindustrial (PI) and mid-Holocene (MH) time periods.

Time Period	CH_4	Eccentricity	Obliquity	Precession	Dust emissions
Preindustrial (PI)	791.6 ppb	0.016724	23.446°	102.04°	Mobilized over Sahara
Mid-Holocene (MH) with PI vegetation	650 ppb	0.018682	24.105°	0.87°	Mobilized over Sahara[a]
Mid-Holocene (MH) with MH vegetation	650 ppb	0.018682	24.105°	0.87°	Not mobilized over Sahara[a]

[a]Unless stated otherwise in Model Experiments and Methods.

Table S2.2. Mid-Holocene prescribed land surface characteristics for each zone. Numbered zones correspond with Figure S2.1.

Zone	Plant functional types	Leaf area index	Soil albedo
1	100% Broadleaf evergreen temperate shrub	Broadleaf evergreen temperate shrub = 2.6	0.18 (dry) - 0.09 (saturated)
2	75% Broadleaf evergreen temperate shrub, 25% Warm c4 grass	Broadleaf evergreen temperate shrub = 2.6; Warm c4 grass = 0.33 (Jan-Apr), 1.0 (May-Dec)	0.18 (dry) - 0.09 (saturated)
3	50% Broadleaf evergreen temperate shrub, 50% Warm c4 grass	Broadleaf evergreen temperate shrub = 2.6; Warm c4 grass = 0.33 (Jan-Apr), 1.0 (May-Dec)	0.20 (dry) - 0.10 (saturated)
4	25% Broadleaf evergreen temperate shrub, 75% Warm c4 grass	Broadleaf evergreen temperate shrub = 2.6; Warm c4 grass = 0.33 (Jan-Apr), 1.0 (May-Dec)	0.22 (dry) - 0.11 (saturated)
5	100% Warm c4 grass	Warm c4 grass = 0.33 (Jan-Apr), 1.0 (May-Dec)	0.22 (dry) - 0.11 (saturated)
6	20% Bare, 40% Warm c4 grass, 34% Broadleaf evergreen temperate shrub, 3% Broadleaf deciduous tropical tree, 3% Cool c3 grass	Bare = 0, Broadleaf deciduous tropical tree = 0.87 (Jan-Apr), 2.6 (May-Dec); Cool c3 grass = 0.33 (Jan-Apr), 1.0 (May-Dec); Warm c4 grass = 0.33 (Jan-Apr), 1.0 (May-Dec); Broadleaf evergreen temperate shrub = 2.6	0.22 (dry) - 0.11 (saturated)
7	57% Bare, 40% Broadleaf evergreen temperate shrub, 3% Broadleaf deciduous temperate shrub	Bare = 0; Broadleaf deciduous temperature shrub = 0.87 (Jan-Apr), 2.6 (May-Dec); Broadleaf evergreen temperate shrub = 2.6	0.23 (dry) - 0.12 (saturated)

Table S2.3. Monsoon season (JJAS) Saharan-averaged values for single-scatter albedo for each simulation. In CAM5-chem, aerosol single-scatter albedo is predicted as a function of wet refractive index and wet surface radius (Neale et al., 2012). Lower values represent aerosols with greater absorption and higher values represent aerosols with weaker absorption. Values differ between simulations due to the amount of aerosol over the Sahara.

Simulation	Single-scatter albedo
PI Control	0.887
MH Control	0.950
MH HighDust	0.884
MH DesertVeg	0.942
MH DesertSoil	0.949
MH Orbital	0.887

Table S2.4. Offline radiation calculations of changes in average monsoon season (JJAS) net radiative fluxes at the surface and the top-of-atmosphere (TOA) over the Sahara (20–31°N, 20°W–30°E) due to MH dust reductions. Here offline calculation was used to separate the direct aerosol effects from the total radiation changes after accounting for feedbacks in the system (e.g., clouds, temperature, and water vapor). For comparison, total changes in radiation, including both direct aerosol effects and feedbacks, are shown in the bottom row.

		Difference (*MH Control – MH HighDust*) (W m^{-2})
Surface (direct aerosol effects)[b]	SW	+67.4
	LW	+17.3
	Total[a]	+84.7
TOA (direct aerosol effects)[b]	SW	+13.7
	LW	-4.8
	Total[a]	+8.9
TOA (total = direct aerosol effects + feedbacks)[b]	SW	+16.5
	LW	-18.4
	Total[a]	-1.9

[a]Shortwave flux + Longwave flux = Total flux. [b]Positive values represent downward

References

Bartlein, P. J., Harrison, S. P., Brewer, S., Connor, S., Davis, B. A. S., Gajewski, K., et al. (2011). Pollen-based continental climate reconstructions at 6 and 21 ka: A global synthesis. *Climate Dynamics*, 37, 775–802. https://doi.org/10.1007/s00382-010-0904-1

Colman, R. (2003). A comparison of climate feedbacks in general circulation models. *Climate Dynamics*, 20(7–8), 865–873. https://doi.org/ 10.1007/s00382-003-0310-z

Conley, A. J., Lamarque, J. F., Vitt, F., Collins, W. D., & Kiehl, J. (2013). PORT, a CESM tool for the diagnosis of radiative forcing. *Geoscientific Model Development*, 6(2), 469–476. https://doi.org/10.5194/gmd-6-469-2013

Gaetani, M., Messori, G., Zhang, Q., Flamant, C., & Pausata, F. S. R. (2017). Understanding the mechanisms behind the northward extension of the West African Monsoon during the mid-Holocene. *Journal of Climate*, 30(19), 7621–7642. https://doi.org/10.1175/JCLI- D-16-0299.1

Neale, R. B., Chen, C.-C., Gettelman, A., Lauritzen, P. H., Park, S., Williamson, D. L., et al. (2012). *Description of the NCAR Community Atmosphere Model* (CAM5.0) (NCAR/TN-486+STR). Boulder, CO: National Center for Atmospheric Research.

Oleson, K. W., Lawrence, D. M., Bonan, G. B., Flanner, M. G., Kluzek, E., Lawrence, P. J. et al. (2010). *Technical description of version 4.0 of the Community Land Model* (CLM) (NCAR/TN-478+STR). Boulder, CO: National Center for Atmospheric Research.

Pausata, F. S. R., Messori, G., & Zhang, Q. (2016). Impacts of dust reduction on the northward expansion of the African monsoon during the Green Sahara period. *Earth and Planetary Science Letters, 434*, 298–307. https://doi.org/10.1016/j.epsl.2015.11.049

Perez-Sanz, A., Li, G., González-Sampériz, P., & Harrison, S. P. (2014). Evaluation of modern and mid-Holocene seasonal precipitation of the Mediterranean and northern Africa in the CMIP5 simulations. *Climate of the Past*, *10*(2), 551–568. https://doi.org/10.5194/cp-10-551-2014

Chapter 3 Water Isotopic Constraints on the Enhancement of the Mid-Holocene West African Monsoon

Co-authors: Clay R. Tabor, Christopher J. Poulsen, and Christopher B. Skinner

3.1 Abstract

During the early to mid-Holocene, changes in orbital precession led to considerable increases in West African monsoon (WAM) rainfall compared to today and shifted its reach further north. However, climate proxies and paleoclimate model simulations disagree over fundamental aspects of the mid-Holocene (MH; 6 ka BP) enhancement of the WAM. Here, we use a water isotope-enabled Earth system model (iCESM1) to, for the first time, directly compare simulated northern African hydroclimatic change between the mid- Holocene and pre-industrial era (PI) with the hydroclimate signal inferred from leaf wax *n*-alkanes in order to study the WAM's past spatial change. iCESM1 simulates a northernmost WAM extent of ~24°N, which broadly agrees with the extent inferred from pollen and dust records (23–28°N) but falls short of that from leaf wax *n*-alkanes (27–31°N). While the isotopic composition of rainfall (δD_P) inferred from leaf wax *n*-alkanes is lower during the MH than the PI, simulated MH δD_P is higher in northwestern Africa, especially in boreal fall. This discrepancy can be reconciled by interpreting the inferred signal of leaf wax *n*-alkanes as being reflective of the isotopic composition of soil water (δD_S) and its subsequent influence by soil evaporation. We postulate that leaf wax *n*-alkanes may overestimate inferred mean annual precipitation rates in the MH by not incorporating the enrichment of precipitation shown by iCESM1. Our results have broad implications for reconstruction of past hydrologic change in northern Africa and lend further support to the northernmost WAM extents inferred from pollen and dust records.

3.2 Introduction

On orbital time scales, northern Africa experiences wet phases of higher-than-present annual rainfall rates, with the most recent wet phase occurring in the early to mid-Holocene (~11 to 5 ka BP; deMenocal et al., 2000; Tierney et al., 2017a; Shi et al., 2020). During these pluvial periods, steppe, savanna, and shrub vegetation covered what is today a desert, transforming northern Africa into a so-called "Green Sahara" (Dallmeyer et al., 2020; Hoelzmann et al., 1998; Jolly et al., 1998). The increased annual rainfall rates during these wet phases were driven by an intensification of the West African monsoon (WAM), which largely occurs due to orbitally enhanced summer insolation and rainfall-vegetation feedbacks (Kutzbach, 1981; Kutzbach et al., 1996; Shi et al., 2020). Hydroclimate proxy records tie the early to mid-Holocene WAM enhancement to orbital precession and suggest a transition to drier conditions during the mid- to late Holocene (e.g., Collins et al., 2017; deMenocal et al., 2000; Palchan and Torfstein, 2019; Tierney et al., 2017a, 2017b). However, there is considerable disagreement regarding the spatial structure and northward penetration of the WAM near the peak of the mid-Holocene (MH; 6 ka BP) Green Sahara, particularly in northwestern Africa where the monsoon likely reached farthest north (e.g., Lézine et al., 2011; Pausata et al., 2016; Palchan and Torfstein, 2019; Sha et al., 2019; Tierney et al., 2017a). In light of the devastating 1970s and 1980s Sahel droughts, a comprehensive understanding of the past spatial constraints on the WAM is critical for improving projections of this highly variable hydrologic system on which the economy and livelihood of millions of people depend (Pausata et al., 2020).

Several proxies, including leaf wax *n*-alkanes, pollen, and dust, suggest that, during the MH, the WAM was wider and stronger than today and its extent was shifted further north. However, the proxies provide different estimates for the northernmost extent of the WAM, broadly defined as the northernmost latitude with annual precipitation rates in excess of 730 mm/year (Pausata et al., 2016), and each study specifies its extent in a distinct way. Recent leaf wax *n*-alkane records off the coast of northwestern Africa are interpreted as indicating MH annual rainfall rates greater than 700 mm/year as far north as 31°N, suggesting the MH WAM reached this latitude that is 15–20° north of its present-day extent (Sultan and Janicot, 2003; Tierney et al., 2017a). While 90% of the MH rainfall increase at 31°N occurred from June to September, it is possible that the large precipitation increase inferred at 31°N is also fueled by an increase in winter precipitation from the Mediterranean (Tierney et al., 2017a). However, modeling studies (e.g.,

Pausata et al., 2016) and a Moroccan speleothem record at 31°N, which records low carbonate $\delta^{18}O$ values during the MH that are interpreted to represent high rainfall rates (Sha et al., 2019), suggest that the inferred MH increase in rainfall is best interpreted as an enhancement of the WAM. Furthermore, a collection of pollen and dust flux records suggest a more modest northernmost WAM extent between 23°N and 28°N in northwestern Africa (Bartlein et al., 2011; Hély et al., 2014; Lézine et al., 2011; Palchan and Torfstein, 2019). These records indicate substantial increases in rainfall over the Sahara and Sahel, with annual rates between 200 and 700 mm/year, but limited northward movement of the WAM into northwestern Africa.

Given the various interpretations of MH hydroclimate from northern African proxies, climate models have been used to simulate MH northern African climate and reconcile the disagreement. Most climate models of MH northern Africa have simulated far less precipitation and a relatively limited northward extension of the WAM than inferred from several proxy records, precluding insights into previous WAM behavior (Braconnot et al., 2012; D'Agostino et al., 2019; Pausata et al., 2016; Thompson et al., 2019; Tierney et al., 2017a). For example, the simulations from the Paleoclimate Modeling Intercomparison Project Phase 3 (PMIP3) underestimate MH northern African annual rainfall by ~400 mm/year, when compared with estimates from pollen, and simulate a northernmost WAM extent south of 20°N (Perez-Sanz et al., 2014). The majority of these simulations do not include modification of northern African vegetation from the desert preindustrial era (PI) (Braconnot et al., 2011; Otto-Bliesner et al., 2017). Inclusion of vegetation over the Sahara, either through specifying the vegetation as a boundary condition or through the implementation of a dynamic vegetation model, allows for climate-vegetation feedbacks and results in a simulated northernmost WAM extent that can reach the lower latitude estimate inferred from pollen and dust records, but not the higher latitude estimate from leaf wax *n*-alkanes (Dallmeyer et al., 2020; Pausata et al., 2016; Thompson et al., 2019).

Thus, it remains unclear whether climate models with MH vegetation underestimate the true northern extent of the MH WAM or whether the isotopic signature of leaf wax *n*-alkanes overestimates the MH WAM extent. To date, climate model-proxy comparisons of MH northern African hydroclimate have mostly been indirect, comparing rainfall rates inferred from proxies with model-simulated rainfall (e.g., Braconnot et al., 2012; Perez-Sanz et al., 2014; Tierney et al., 2017a). The inclusion of water isotope tracers in Earth system models allows for direct comparison between proxy and modeled isotope values (Cauquoin et al., 2019). We use these capabilities to

help reduce the uncertainty in our reconstructions of MH WAM extension by directly comparing the δD (ratio of D to H) from leaf wax *n*-alkanes, referred to as δD_{WAX}, with model-simulated δD over northern Africa.

Leaf wax *n*-alkane δD_{WAX} is used as a biomarker for past rainfall rates due to its inferred ability to record the average isotopic composition of rainwater (δD_P) over a given watershed (Gat, 1996; Kahmen et al., 2013; Sachse et al., 2012). In connecting δD_{WAX} to past rainfall rate, two critical assumptions are made. First, rainfall rate is assumed to vary inversely with the isotopic composition of rainfall (known as the amount effect; Dansgaard, 1964; Kahmen et al., 2013; Sachse et al., 2012) as present-day tropical rainfall rate and δD_P have been shown to be inversely related on monthly to annual timescales (e.g., Risi et al., 2008a). Second, the isotopic composition of root-integrated soil water (δD_S), which is the source water for the plant, is assumed to reflect that of local precipitation (δD_P) (Kahmen et al., 2013; Rozanski et al., 1993; Sachse et al., 2012). With these assumptions in mind, Holocene δD_{WAX} records are used to infer changes in past rainfall rate (e.g., Collins et al., 2017; Tierney et al., 2017a). Consequently, a collection of ten δD_{WAX} records that span back to at least the early Holocene suggests that northern Africa experienced higher rainfall rates due to an enhanced WAM during the MH (Table 3.1).

Table 3.1. List of leaf wax *n*-alkane sites

#	Location	MH–PI δD_P	MH–PI δD_{WAX}	Lat	Lon	Data Source
1	Gulf of Aden	-14.5*	-13.0	12.0°N	44.3°E	Tierney & deMenocal (2013)
2	Gulf of Aden	N/A	-7.0	12.1°N	44.4°E	Tierney et al. (2017b)
3	Lake Tana	-14.0*	-10.0	12.0°N	37.3°E	Costa et al. (2014)
4	Gulf of Guinea	-13.0	-14.0	2.5°N	9.4°E	Collins et al. (2017)
5	Lake Bosumtwi	-9.5	-8.0	6.5°N	1.4°E	Shanahan et al. (2015)
6	West African Margin	-18.5*	-16.5	15.5°N	18.0°W	Niedermeyer et al. (2010)
7	West African Margin	-13.0	-7.0	19.4°N	17.3°W	Tierney et al. (2017a)
8	West African Margin	-15.5	-12.0	23.2°N	17.9°W	Tierney et al. (2017a)
9	West African Margin	-19.0	-11.0	26.8°N	15.1°W	Tierney et al. (2017a)
10	West African Margin	-11.0	-10.0	30.9°N	10.6°W	Tierney et al. (2017a)

*δD_P values are calculated from both δD_{WAX} and $\delta^{13}C_{WAX}$ data available in publication using methodology described by Tierney et al. (2017a).

However, these assumptions do not always hold true. Several tropical hydrological studies (e.g., Ampuero et al., 2020; Bedaso et al., 2019; Konecky et al., 2011, 2016, 2019a; Munksgaard et al., 2019; Wolf et al., 2020) suggest that δD_P is not always a reliable predictor of local rainfall

rate. Large-scale microphysical and dynamical processes (i.e., sub-cloud rain re-evaporation, convective intensity, moisture sourcing, etc.) can exert a stronger control on δD_P than does rainfall rate (Bony et al., 2008; Konecky et al., 2019a; Risi et al., 2008a, 2008b; Tabor et al., 2018). Additionally, the assumption that δD_S reflects δD_P may not always be true in highly evaporative arid environments (Kanner et al., 2014; Konecky et al., 2019b) and, when this is the case, inferred changes in rainfall rate may be overly inflated as high evaporation leads to exceedingly D-enriched rainfall. Furthermore, δD_{WAX} has a strong seasonal bias, especially in monsoon regions such as the present-day Sahel, because biosynthesis of leaf waxes peaks during the growing season (Niedermeyer et al., 2016; Tipple et al., 2013). Given the number of complicating factors surrounding δD_{WAX} and its recorded climate signal, including its relationship with rainfall rate, paleoclimate model simulations can help interpretation by providing a systematic view of the climate conditions present for past leaf wax growth in northern Africa and by filling in the seasonal gaps not recorded by δD_{WAX}.

Here, we use the water isotope-enabled Community Earth System Model version 1 (iCESM1) to evaluate hydroclimatic and isotopic (i.e., δD_P, δD_S, and δD_{WAX}) changes in northern Africa during the MH and PI. We then use our model output to interpret the hydroclimate signal from a dataset of ten δD_{WAX} records throughout northern Africa. Our results have broad implications for northern African paleoclimate reconstruction of the structure and northward extension of the WAM.

3.3 Methods

We employed the fully coupled Earth system model, iCESM1 (Brady et al., 2019), which is comprised of the Community Atmosphere Model version 5.3 (iCAM5), the Community Land Model version 4.0 (iCLM4), the River Transport Model, the Community Ice Code version 4.0, Parallel Ocean Program version 2, and a coupler connecting them (Hurrell et al., 2013). In iCESM1, water isotopes have been incorporated in each model component. iCESM1 reasonably simulates global δD for the present day; however, the model exhibits a depleted bias in the present-day tropics compared with satellite and ground-based observations (Nusbaumer et al., 2017). The iCESM1 simulations were run with a grid resolution of 1.9° × 2.5° for both the atmosphere and land surface and nominal 1° × 1° for the ocean. The water isotope-enabled atmosphere model,

iCAM5, consists of 30 vertical levels (Nusbaumer et al., 2017), and the water isotope-enabled land surface model, iCLM4, consists of 15 soil-column layers (Wong et al., 2017).

We ran three iCESM1 simulations to isolate the influence of a Green Sahara: a Pre-industrial simulation ($PI_{CONTROL}$), a mid-Holocene simulation (MH_{VEG}), and a mid-Holocene simulation with desert conditions over the present-day Sahara region (MH_{DESERT}) (Table 3.2). The $PI_{CONTROL}$ simulation consists of PI orbital settings and greenhouse gas (GHG) concentrations and a present-day desert Sahara, while the MH_{VEG} simulation consists of MH orbital settings and GHG concentrations, in accordance with Otto-Bliesner et al. (2017), and a vegetated "Green Sahara." The MH_{DESERT} simulation consists of MH orbital settings and GHG concentrations, but it contains present-day desert conditions in the Sahara as in $PI_{CONTROL}$. The sensitivity experiment $MH_{DESERT} - PI_{CONTROL}$ isolates the impact of a changed orbital and GHG configuration, while the sensitivity experiment $MH_{VEG} - MH_{DESERT}$ isolates the impact of an expansion in northern African vegetation cover. The combined impact of the altered orbital and GHG configuration and expanded northern African vegetation cover are demonstrated by the sensitivity experiment $MH_{VEG} - PI_{CONTROL}$. While still idealized, $MH_{VEG} - PI_{CONTROL}$ represents the most realistic change between the MH and PI in our study and, for this reason, we focus primarily on this experiment in 3.4 Results when we compare our model outputs to MH–PI values of northern African δD_{WAX}.

Table 3.2. iCESM1 simulations and their respective boundary conditions

Simulation	Orbital Configuration	CO_2 (ppm)	CH_4 (ppb)	N_2O (ppb)	CFC_{11} (ppt)	Saharan Land Surface
$PI_{CONTROL}$	PI	284.7	791.6	275.7	12.5	Desert
MH_{DESERT}	MH	264.4	597.0	262.0	0.0	Desert
MH_{VEG}	MH	264.4	597.0	262.0	0.0	Vegetated

In order to mimic a Green Sahara in MH_{VEG}, we modified the prescribed vegetation boundary conditions in iCLM4. We first calculated the zonal average land surface variables, which include leaf and stem area index, from the $PI_{CONTROL}$ simulation over the present-day Sahel region at 11°N. In MH_{VEG}, these average land surface variables replaced bare ground in grid cells where bare ground exceeded 10% in $PI_{CONTROL}$, which was the case for most of the Sahara and Arabian Peninsula. The resulting vegetated land surface is broadly consistent with pollen records of the Green Sahara (Hoelzmann et al., 1998; Jolly et al., 1998), with notable increases in C_3 grass, C_4

grass, and tropical tree cover and decreases in bare ground. The increase in leaf area index associated with the Green Sahara in MH_{VEG} prohibited dust aerosol mobilization from the northern African land surface (Oleson et al., 2010). Thus, MH_{VEG}–$PI_{CONTROL}$ exhibits the climate change resulting from increased vegetation cover and reduced dust aerosol emissions, which has been shown to improve agreement between models and proxy records of MH northern African hydroclimate (Pausata et al., 2016; Thompson et al., 2019).

MH_{VEG} and MH_{DESERT} were run for 350 years, and $PI_{CONTROL}$ was run for 250 years. The last 50 years of each run were used to calculate a climatology. The top-of-atmosphere energy imbalance over each of these 50-year averages was less than 0.15 Wm^{-2}, confirming that the runs were in energetic equilibrium. We assessed the statistical significance of changes in model simulated values at the 95% confidence level using the Student's *t* test and assumed different population variances. We weighted simulated values of δD_P by rainfall amount, the isotopic composition of water vapor (δD_{VAPOR}) by specific humidity, and, in order to capture the simulated isotopic signal of the water that enters the model plant roots, we weighted simulated values of δD_S by both soil water amount and rooting depth fraction.

In order to calculate the northernmost extent of the WAM for each simulation (Pausata et al., 2016; Thompson et al., 2019), we first found the northernmost latitude with rainfall in exceedance of 2 mm/day (or 730 mm/year) averaged over the zonal region 15°W– 20°E for each month of the last 50 simulated years. We took the maximum latitude for each year and created a 50-year distribution of northernmost latitudes. The simulation's determined northernmost WAM extent was the median value of this 50-year distribution, since the median is not impacted by the shape of the distribution (Pausata et al., 2016).

We compiled ten published leaf wax *n*-alkane records that extend at least to the early Holocene and span across northern Africa (Table 3.1). For comparison with iCESM1, we compiled the MH–PI (6 ka–0 ka) δD_{WAX} value, and δD_{WAX}-inferred δD_P value if published, for each record (Table 3.1). We calculated MH and PI δD_P values for proxies in the Gulf of Aden, Lake Tana, and the West African Margin using published δD_{WAX} and $\delta^{13}C_{WAX}$ records and the methodology described in Tierney et al. (2017a), but did not calculate δD_P for proxy #2 in the Gulf of Aden since $\delta^{13}C_{WAX}$ values were not published in that study (Tierney et al., 2017b). We calculated model-inferred δD_{WAX} values with model δD_P and δD_S as inputs and weighted the values according to vegetation type using the methodology described by Konecky et al. (2019b) (see 3.9

Supplementary Information). We then compared the model-inferred δD_{WAX} values directly with proxy record δD_{WAX}.

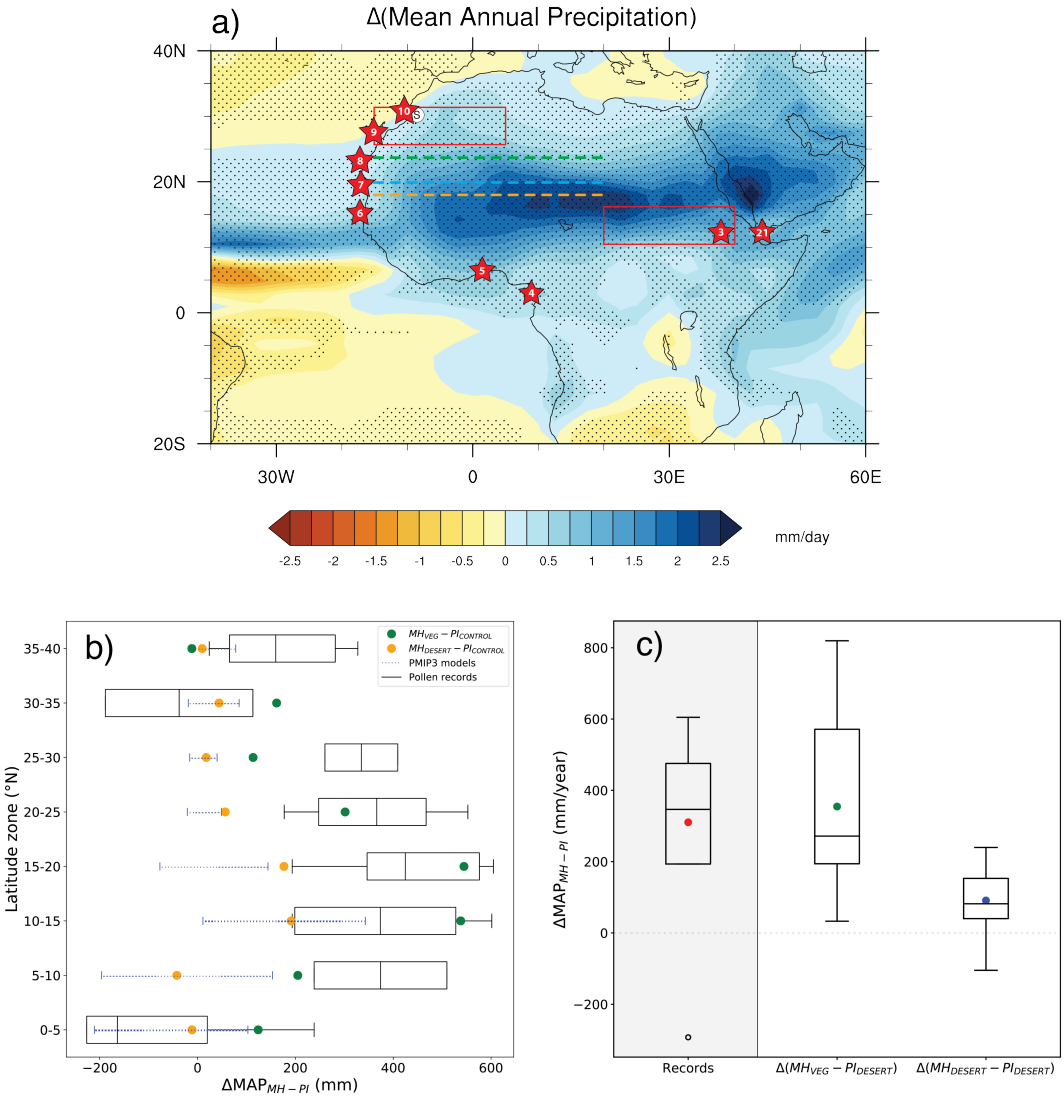

Figure 3.1. Model-proxy comparisons in rainfall. a) Simulated MH_{VEG}–$PI_{CONTROL}$ difference in mean annual precipitation (MAP). Numbered stars represent leaf wax *n*-alkane record locations listed in Table 3.1. White circle represents speleothem record from Sha et al. (2019). Red boxes indicate the spatial extent of the northwestern Sahara and eastern Sahel. Stippling represents statistically significant differences at the 95% confidence level. Dashed lines indicate northernmost extent of the West African monsoon; $PI_{CONTROL}$ (orange), MH_{DESERT} (blue), and MH_{VEG} (green). b) MH–PI differences in MAP at 5° latitude bands between pollen data (boxes; Bartlein et al., 2011), PMIP3 models (dotted line; Perez-Sanz et al., 2014), and this study's iCESM1 results (dots; green for MH_{VEG}–$PI_{CONTROL}$ and yellow for MH_{DESERT}–$PI_{CONTROL}$). Each latitude band is averaged over the zonal region 20°W–30°E. b) is adapted from Figure 6 in Perez-Sanz et al. (2014). c) MH–PI MAP difference between pollen records (Bartlein et al., 2011) and this study's iCESM1 results for MH–PI, shown by $\Delta(MH_{VEG}–PI_{CONTROL})$, and orbital forcing only, shown by $\Delta(MH_{DESERT}–PI_{CONTROL})$, averaged over the region 0–35°N, 20°W–50°E. Colored dots represent mean values. For both b) and c), boxplot lines represent median values and modeled results are derived from the grid cells corresponding to available data in Bartlein et al. (2011).

3.4 Results

3.4.1 Mean annual precipitation

Simulated mean annual precipitation (MAP) increases throughout the Sahara and Sahel during the MH relative to the PI (MH_{VEG}–$PI_{CONTROL}$) (Figure 3.1a), which agrees with many modeling and proxy studies (e.g., Bartlein et al., 2011; Braconnot et al., 2012; D'Agostino et al., 2019; Collins et al., 2017; Hély et al., 2014; Lézine et al., 2011; Palchan and Torfstein, 2019; Tierney et al., 2017a). This increase is largely due to enhancement of the boreal summer monsoonal circulation (Figure S3.1; e.g., Kutzbach, 1981; Gaetani et al., 2017). The northernmost WAM extent (see 3.3 Methods) for $PI_{CONTROL}$, MH_{DESERT}, and MH_{VEG} is 18.0°N, 19.9°N, and 23.7°N, respectively (Figure 3.1a). Comparison with Global Precipitation Climatology Centre (GPCC) historical precipitation data (Schneider et al., 2018) shows that iCESM1 provides a good match with observations in Africa, although it does slightly overestimate the northernmost WAM extent ($PI_{CONTROL}$: 18.0°N vs. GPCC: 16.25°N; Figure S3.2). For MH_{VEG}, the extent of ~24°N falls within the lower estimate from pollen and dust records (e.g., Bartlein et al., 2011; Hély et al., 2014; Lézine et al., 2011; Palchan and Torfstein, 2019). Though our iCESM1 MH simulations match regional precipitation estimates from pollen more closely than simulations from the PMIP3 and PMIP4 ensemble of models (Braconnot et al., 2012; Brierley et al., 2020), iCESM1 still underestimates the overall enhancement of rainfall inferred from pollen proxies, especially in the northern Sahara (25–30°N; Figure 3.1b). In comparison to the increase in rainfall due to orbital forcing alone (MH_{DESERT}–$PI_{CONTROL}$), the simulated increase in MH_{VEG}–$PI_{CONTROL}$ reduces the model-proxy discrepancy with pollen-inferred MAP by 72% (Figure 3.1c).

The simulated MH_{VEG}–$PI_{CONTROL}$ increase in MAP is consistent with the lower MH δD_{WAX} values, relative to the PI, at each proxy site across northern Africa under the assumption that δD_{WAX} varies inversely with rainfall rate (Figure 3.1a, Table 3.1). However, the simulated MH_{VEG}–$PI_{CONTROL}$ δD_P response varies spatially (Figure 3.2a). Precipitation over the eastern Sahel (10.4–16.1°N, 20–40°E) is relatively depleted, in line with a MH_{VEG} MAP increase of 1.38 mm/day (67% increase; Table 3.3). However, precipitation over the northwestern Sahara (25.6–31.3°N, 15°W–5°E) is relatively enriched despite a MH_{VEG} MAP increase of 0.35 mm/day (219% increase; Table 3.3). Given the presence of leaf wax *n*-alkane records near these two regions and their contrasting MH_{VEG}–$PI_{CONTROL}$ δD_P responses in iCESM1, we focus the remainder of our analysis on the changes in these two regions.

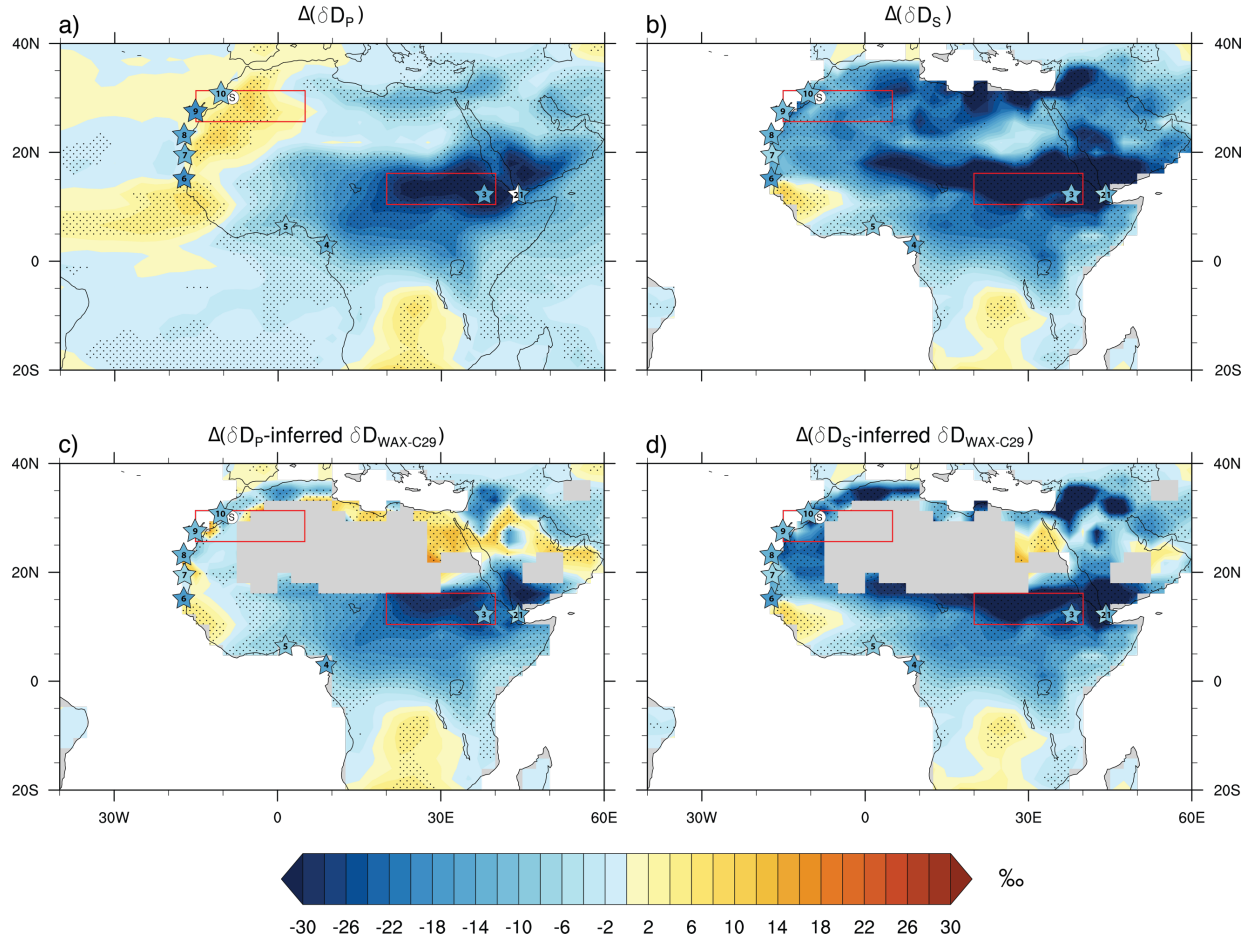

Figure 3.2. Simulated MH_{VEG}–$PI_{CONTROL}$ difference in annually-averaged a) rainfall amount-weighted δD_P, b) soil water- and root depth fraction-weighted δD_S, c) δD_P-inferred $\delta D_{WAX\text{-}C29}$, and d) δD_S-inferred $\delta D_{WAX\text{-}C29}$. Colored stars indicate each leaf wax *n*-alkane record's MH–PI change in a) δD_{WAX}-inferred δD_P and b-d) δD_{WAX}. White circle represents speleothem record from Sha et al. (2019). iCESM1-inferred $\delta D_{WAX\text{-}C29}$ is vegetation-corrected with the methodology of Konecky et al. (2019b) with inputs from iCESM-simulated c) δD_P and d) δD_S. Grey outline in c-d) represents model grid cells with 0% vegetation in $PI_{CONTROL}$. Explanation of the treatment of western margin grid cells in c-d) can be found in 3.9 Supplementary Information. For all panels, red boxes indicate the spatial extent of the northwestern Sahara and eastern Sahel. Stippling represents statistically significant differences at the 95% confidence level.

Table 3.3. Annual mean hydroclimate variables for $PI_{CONTROL}$, MH_{DESERT}, and MH_{VEG} averaged over the northwestern Sahara and eastern Sahel regions

Hydroclimate Variable (units)	*Northwestern Sahara*			*Eastern Sahel*		
	$PI_{CONTROL}$	MH_{DESERT}	MH_{VEG}	$PI_{CONTROL}$	MH_{DESERT}	MH_{VEG}
MAP (mm/day)	0.16	0.23	0.51	2.06	2.50	3.44
δD_P (‰)	–43.4	–44.7	–39.9	–24.6	–49.9	–53.7
δD_S (‰)	–31.1	–38.8	–49.4	–22.6	–45.7	–57.0
δD_P-inferred $\delta D_{WAX\text{-}C29}$ (‰)	–166.9	–167.3	–167.2	–152.5	–174.4	–178.3
δD_S-inferred $\delta D_{WAX\text{-}C29}$ (‰)	–157.3	–162.8	–173.8	–150.7	–170.8	–181.1
Evaporation[a]	0.15 (98.1%)	0.22 (98.1%)	0.37 (70.4%)	1.18 (68.2%)	1.39 (71.0%)	1.36 (51.1%)
Transpiration[a]	0.00 (1.9%)	0.00 (1.9%)	0.16 (29.6%)	0.55 (31.8%)	0.57 (29.0%)	1.30 (48.9%)

[a]Values represented as "mm/day (% of total evapotranspiration flux)"

3.4.2 Northwestern Sahara

3.4.2.1 Water isotopic signal

In the northwestern Sahara, the assumptions for connecting δD_{WAX} to past rainfall rate are violated (both ΔMAP and $\Delta\delta D_P$ increase, $\Delta\delta D_S$ does not match $\Delta\delta D_P$ in sign), suggesting the amount effect is not suited for interpreting paleohydrology from leaf wax *n*-alkanes in this region. Despite simulated MH_{VEG} increases in MAP in the northwestern Sahara, simulated MH_{VEG} δD_P is higher than $PI_{CONTROL}$ by 3.5‰ (Figures 3.2a and S3.3, Table 3.3). In contrast, MH_{VEG} values of δD_S are lower than $PI_{CONTROL}$ by 18.3‰. We observe a similar pattern in iCESM1-inferred leaf wax C29 values (see 3.9 Supplementary Information) as MH_{VEG} δD_P-inferred $\delta D_{WAX\text{-}C29}$ exhibits little to no change from $PI_{CONTROL}$, but δD_S-inferred $\delta D_{WAX\text{-}C29}$ is lower by 16.5‰ (Figure 3.2c-d).

In MH_{VEG}, the monsoon season, roughly from May to October, is lengthened relative to $PI_{CONTROL}$ and the bulk of precipitation enhancement occurs during this time (Figure 3.3). This result provides further evidence for the interpretation of the 31°N leaf wax *n*-alkane record (Tierney et al., 2017a) as an increase in WAM rainfall and not as being partially due to an increase in boreal winter rain. The strongest enrichment of rainfall and water vapor occurs during July–October, whereas soil water in MH_{VEG} is more depleted than $PI_{CONTROL}$ year-round (Figure 3.3). In

addition to the discrepancy between simulated ΔMAP and $\Delta\delta D_P$ in iCESM1, there is also a mismatch in sign between the MH–PI δD_{WAX}-inferred $\Delta\delta D_P$ from leaf wax *n*-alkane records and simulated $\Delta\delta D_P$ along the coast of northwestern Africa. This mismatch disappears when comparing δD_{WAX}-inferred $\Delta\delta D_P$ from leaf wax *n*-alkane records with simulated $\Delta\delta D_S$ in iCESM1 (Figure 3.2). Given these isotopic mismatches in the northwestern Sahara, it is clear that rainfall rate is not the primary control on the isotopic signal in this region.

3.4.2.2 Mechanisms for water isotopic change

In the northwestern Sahara, higher simulated MH_{VEG} δD_P values are primarily driven by a strengthening of the Saharan Heat Low (SHL) and an increase in vegetation cover. The SHL develops over the northwestern Sahara during the monsoon season as a dynamical response to seasonal surface heating (Lavaysse et al., 2009). In agreement with previous studies, our simulations exhibit a stronger and northward shifted SHL in the MH (MH_{VEG} and MH_{DESERT}) in response to orbital, GHG, and vegetation forcing (Figure S3.4; e.g., Gaetani et al., 2017; Skinner and Poulsen, 2016). The strengthened SHL in MH_{VEG} enriches northwestern Saharan precipitation by enhancing the contribution of heavy water vapor originating from the Mediterranean that eventually advects to the northwestern Sahara. A stronger SHL enhances anticyclonic circulation aloft, strengthening the mid-tropospheric easterly winds associated with the African Easterly Jet and increasing moisture advection from the northeastern portion of the continent (Figures 3.4, S3.4, and S3.5; Thorncroft and Blackburn, 1999). This moisture is sourced from the Mediterranean Sea and contains higher isotopic values of δD_{VAPOR} compared with moisture from the North Atlantic, which is the main source of moisture to the northwestern Sahara during the remainder of the year (Lacour et al., 2017). This seasonal signal in δD_{VAPOR}, which is skillfully simulated by iCESM1 (Figure S3.6), is enhanced over the northwestern Sahara in MH_{VEG} as both anomalous easterly flow and moisture transport at mid- and low-levels (500 hPa and below) develop over the northwestern Sahara (Figures 3.4, S3.4, and S3.7). This mechanism appears most prominently during the late monsoon season and into boreal fall, which contributes to the timing of strongest MH_{VEG} precipitation enrichment (Figure 3.4 and S3.6).

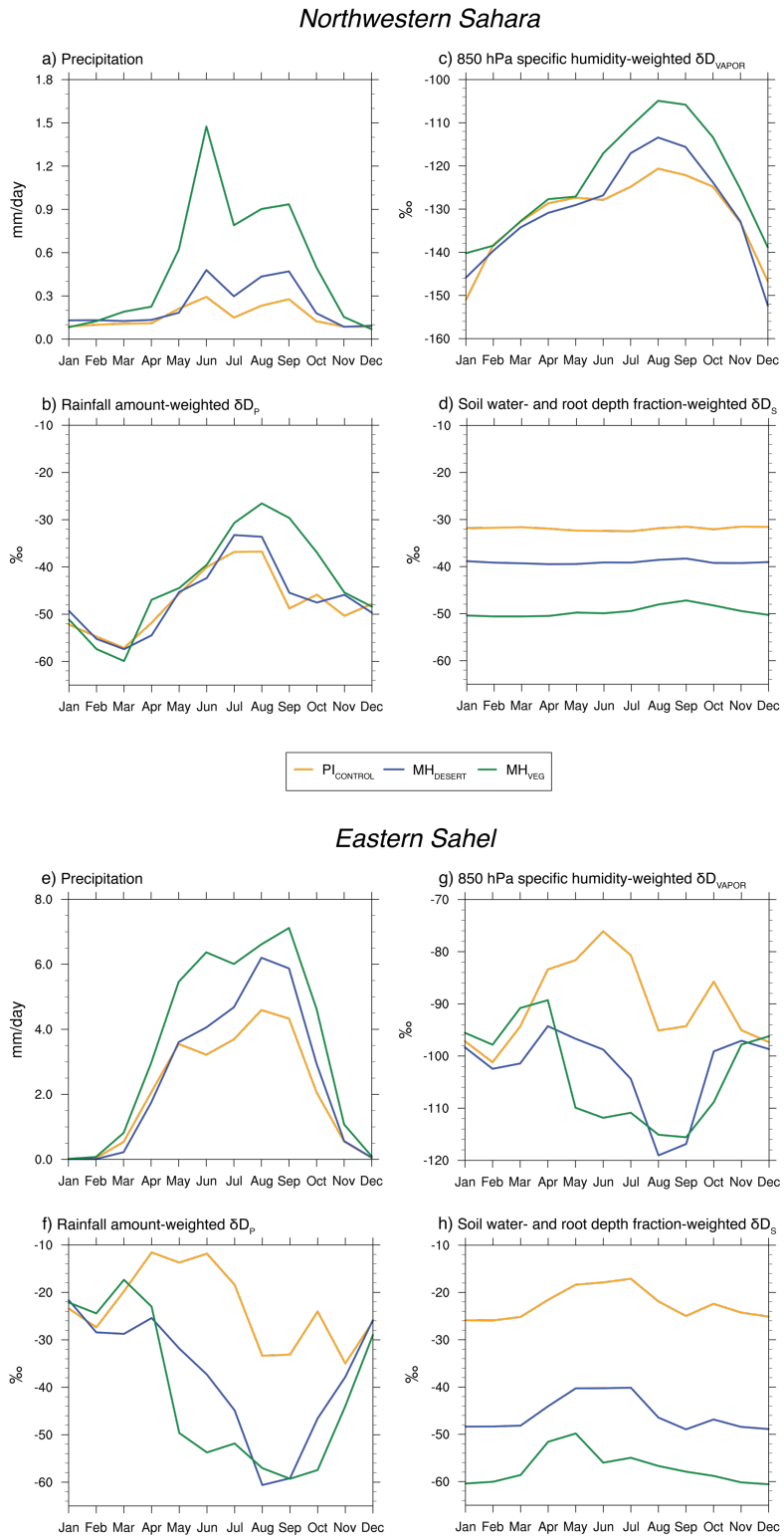

Figure 3.3. Simulated seasonal cycle averaged over the a-d) northwestern Sahara and e-h) eastern Sahel of (a,e) precipitation, (b,f) rainfall amount-weighted δD_P, (c,g) specific humidity-weighted δD_{VAPOR} at 850 hPa, and (d,h) soil water- and root depth fraction-weighted δD_S for $PI_{CONTROL}$ (orange), MH_{DESERT} (blue), and MH_{VEG} (green).

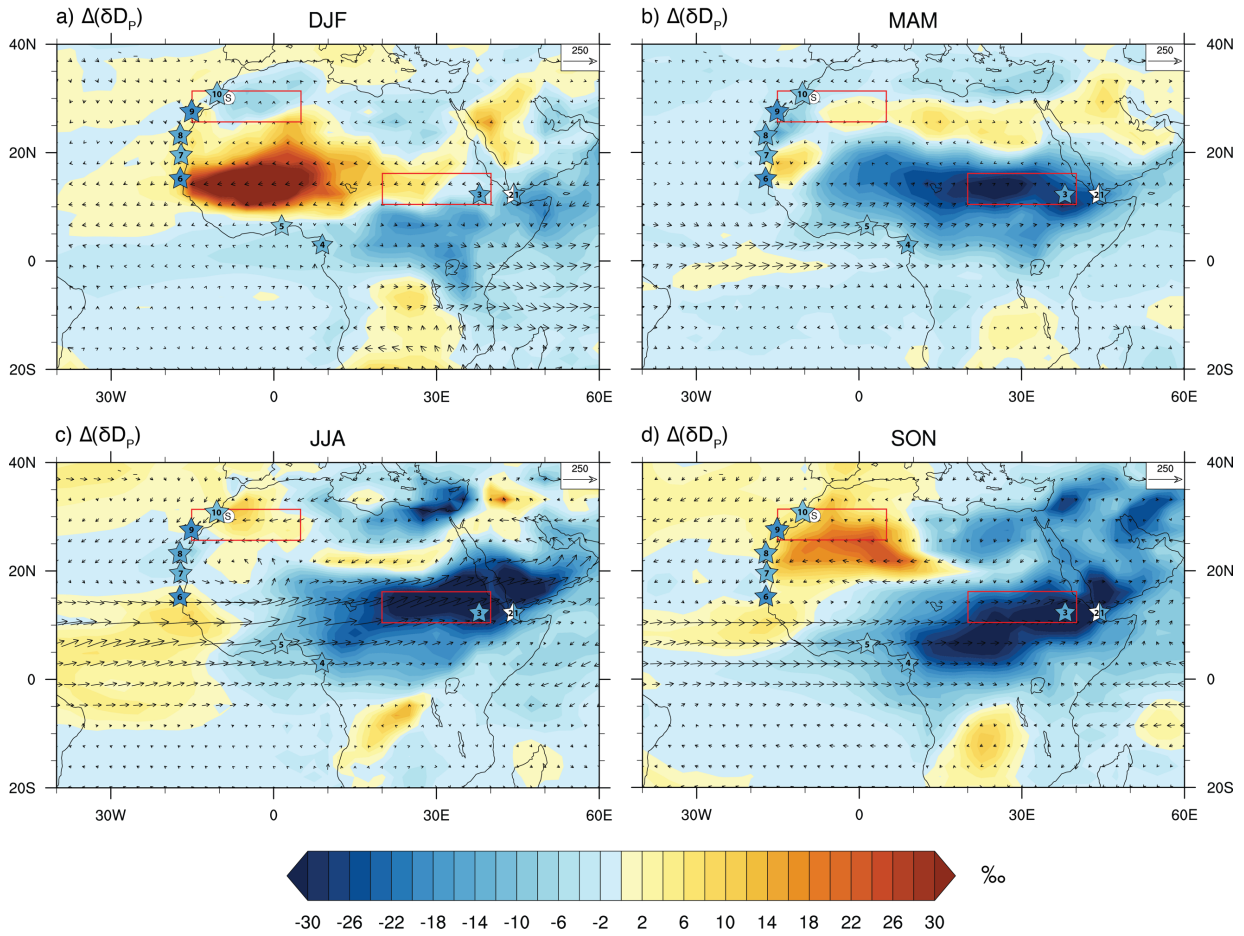

Figure 3.4. Seasonally-averaged MH_{VEG}–$PI_{CONTROL}$ difference in rainfall amount-weighted δD_P (shadings, ‰) and vertically-integrated moisture flux (vectors, 250 kg $m^{-1}s^{-1}$). Color of numbered leaf wax *n*-alkane sites, shown by numbered stars, indicates each record's MH–PI δD_{WAX}-inferred δD_P change (Table 3.1). White circle represents speleothem record from Sha et al. (2019). Red boxes indicate the spatial extent of the northwestern Sahara and eastern Sahel.

Changes in insolation and GHGs alone are enough to produce higher δD_P in the northwestern Sahara by strengthening the SHL (Figure S3.4), as has been seen in previous water isotope-enabled climate modeling studies that change orbital configuration albeit with stronger orbital forcing (Battisti et al., 2014). Increasing vegetation cover throughout the Sahara (Figure 3.5a), however, considerably amplifies this pattern of enriched precipitation by modifying the contributions of evaporation and transpiration to the total evapotranspiration (ET) flux in MH_{VEG}. In $PI_{CONTROL}$, the total ET flux over bare ground is dominated (~98%) by evaporation (Table 3.3), leading to enrichment of the soil water pool and depletion of the vapor pool, as light isotopologues are transferred out of the soil water pool and into the atmosphere (Figure 3.5). In MH_{VEG}, the land

surface is covered by grasses and trees, which, relative to the desert Sahara, lead to a decrease in the ratio of evaporation-to-total evapotranspiration (E:ET) by 28% (Table 3.3). As a result, the vegetated Sahara experiences reduced evaporative enrichment of the soil water, which occurs because more of the heavy isotopologues are transpired out of the soil pool and into the atmosphere when the Sahara is vegetated, as in MH_{VEG}, than when it is deserted, as in $PI_{CONTROL}$ (Figures 3.2b and 3.5).

Transpiration comprises ~30% of the total ET flux in the vegetated Sahara, compared with just 2% in the desert Sahara (Table 3.3). Unlike evaporation, transpiration does not fractionate δD in iCESM1 (Wong et al., 2017) because the associated timescales of simulation are much longer than the turnover time of water within a plant (Gat, 1996). Transfer of enriched water vapor via transpiration has been shown to enrich δD_P in present day East Africa (Levin et al., 2009). In MH_{VEG} relative to $PI_{CONTROL}$, enhanced transpiration leads to relatively enriched water vapor and a depleted soil water pool over the area of increased vegetation, especially in the Central Sahara, because the heavy isotopologues are more readily transpired to the atmosphere (Figures 3.2b, 3.5, and 3.6). Enriched water vapor in MH_{VEG} relative to MH_{DESERT} confirms that this signal is the result of increased vegetation cover. The relatively enriched water vapor in MH_{VEG} is advected westward and rained out over the northwestern Sahara (Figure 3.4).

Taken together, the changes in northern African moisture sourcing and ET flux that occur from changes in both orbital and GHG configuration and vegetation cover lead to a mismatch between MH_{VEG}–$PI_{CONTROL}$ $\Delta\delta D_P$ and $\Delta\delta D_S$ in the northwestern Sahara. Due to the ET flux, δD_P and δD_S closely resemble each other in a vegetated Sahara; however, evaporative enrichment in a desert Sahara contributes to an offset between the two (Figure S3.3). These differences between a desert and vegetated Sahara explain the simultaneous MH_{VEG}–$PI_{CONTROL}$ enrichment in δD_P and depletion in δD_S that occurs in the northwestern Sahara.

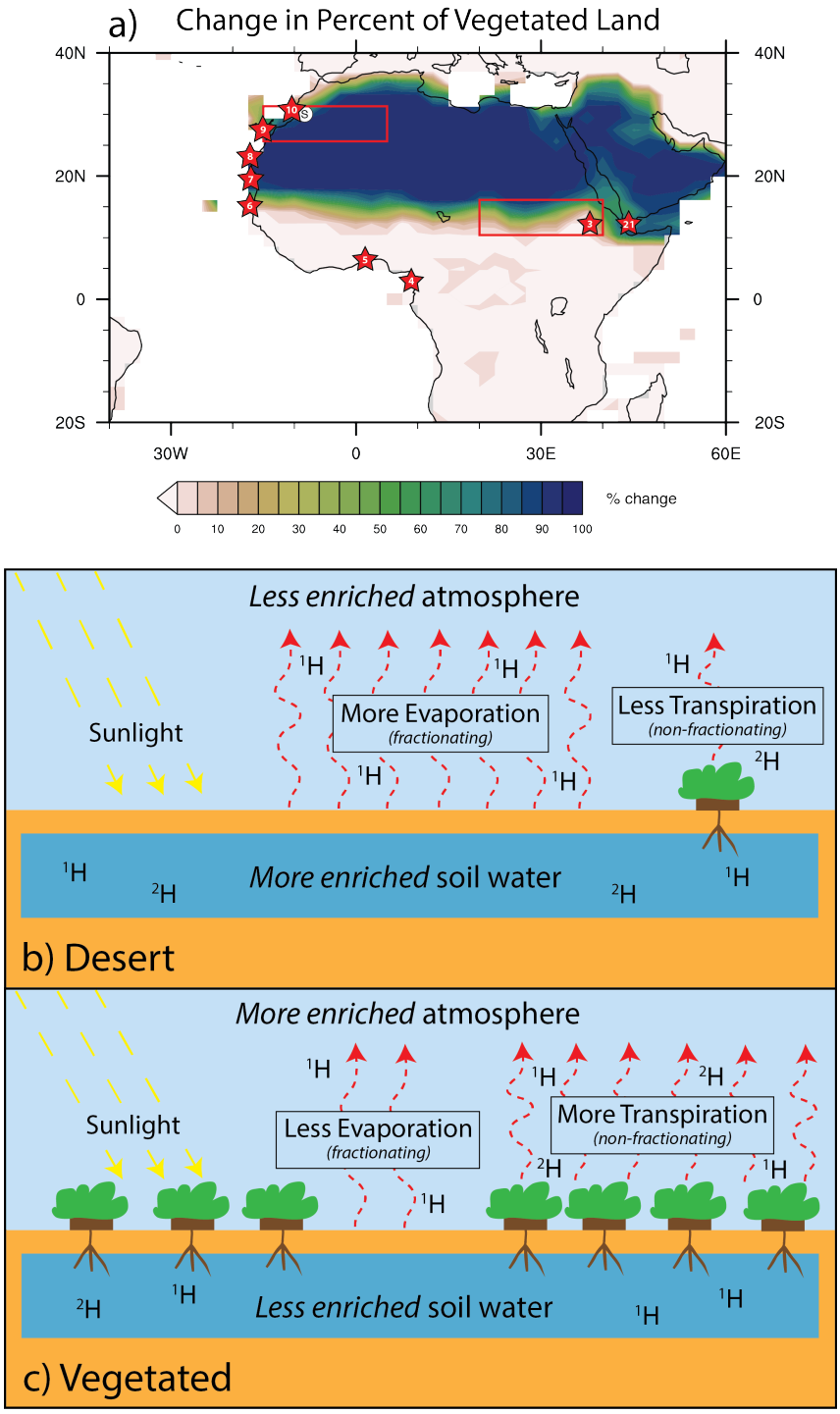

Figure 3.5. Isotopic and evapotranspiration (ET) flux differences between a desert and green Sahara. a) MH_{VEG}–$PI_{CONTROL}$ increase in percentage of land covered by vegetation. Numbered stars in a) represent leaf wax *n*-alkane record locations (Table 3.1). White circle represents speleothem record from Sha et al. (2019). Red boxes indicate the spatial extent of the northwestern Sahara and eastern Sahel. b-c) Schematic illustrating differences in the ET flux between the b) deserted and c) vegetated Sahara and the resulting impacts on the δD of the atmosphere and soil water pool. In a b) desert Sahara, evaporative enrichment of the soil water pool leads to relatively higher δD_S and lower δD_{VAPOR}. In a c) vegetated Sahara, increased transpiration leads to relatively lower δD_S and higher δD_{VAPOR}. ET flux values can be found in Table 3.3.

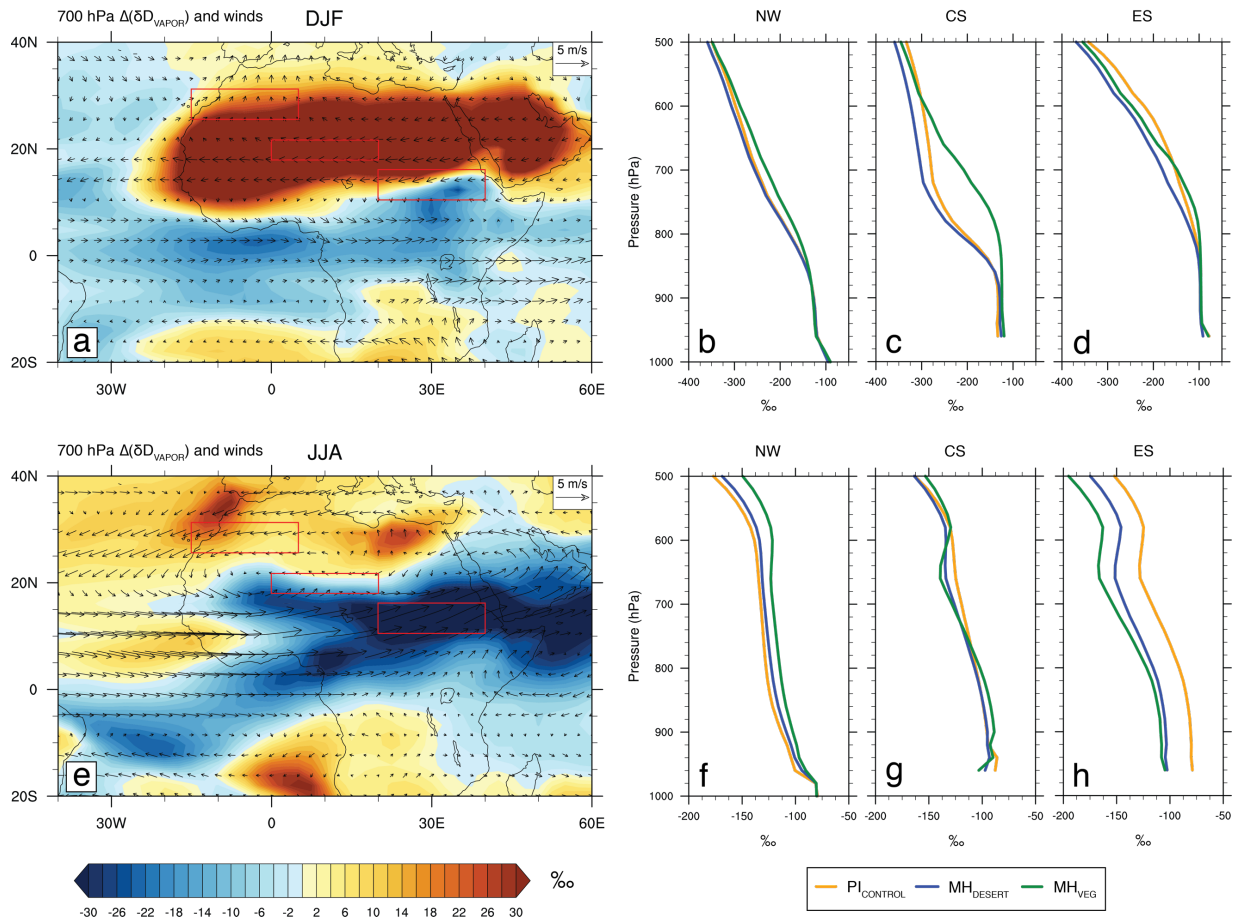

Figure 3.6. Seasonally-averaged MH_{VEG}–$PI_{CONTROL}$ difference in 700 hPa specific humidity-weighted δD_{VAPOR} and wind vectors for a) boreal winter (DJF) and e) boreal summer (JJA). Red boxes indicate the spatial extent of the northwestern Sahara (NW), central Sahara (CS; 18.0– 21.7°N, 0–20°E), and eastern Sahel (ES). b-d) DJF mid-tropospheric atmospheric profiles of specific humidity-weighted δD_{VAPOR} averaged over the b) NW, c) CS, and d) ES. f-h) same as b-d) but for JJA. The DJF plots (a-d) show a strong pattern of water vapor enrichment over the area of vegetation increase in MH_{VEG} because transpiration dominates the δD_{VAPOR} signal during this season. However, this pattern is weaker during JJA (e-h) when isotopic processes related to the monsoon dominate the δD_{VAPOR} signal.

3.4.3 Eastern Sahel

In the eastern Sahel, the assumptions for connecting δD_{WAX} to past rainfall rate are supported (ΔMAP and $\Delta\delta D_P$ vary inversely, $\Delta\delta D_S$ matches $\Delta\delta D_P$ in sign), suggesting the amount effect may be suitable for interpreting leaf wax *n*-alkanes in this region. Specifically, MH_{VEG} MAP increases relative to $PI_{CONTROL}$ in the eastern Sahel, and simulated MH_{VEG} values of δD_P, δD_S, δD_P-inferred $\delta D_{WAX\text{-}C29}$, and δD_S-inferred $\delta D_{WAX\text{-}C29}$ are all lower than in $PI_{CONTROL}$ (Figures 3.1 and 3.2, Table 3.3). Similar to the northwestern Sahara, the largest changes (MH_{VEG}–$PI_{CONTROL}$) in precipitation and isotopic composition in the eastern Sahel occur during the monsoon season,

which, like the northwestern Sahara, is lengthened in MH_{VEG}. However, in the eastern Sahel, the magnitude of precipitation and isotopic differences is far greater (Figure 3.3). Furthermore, simulated ΔδDP agrees in sign with the δD_{WAX}-inferred $\Delta\delta D_P$ from leaf wax *n*-alkane records in the eastern Sahel (Figure 3.2). This isotopic pattern of depleted eastern Sahel rainfall agrees well with previous water isotope-enabled climate model simulations that change orbital configuration (Battisti et al., 2014).

Boreal summer monsoon circulation produces lower MH_{VEG} δD_P values compared to $PI_{CONTROL}$ in the eastern Sahel. The eastern Sahel lies directly in the path of enhanced monsoonal low-level westerlies and moisture transport in MH_{VEG} (Figures 3.4 and 3.6). Through Rayleigh distillation, heavy isotopologues are preferentially rained out as air parcels move inland from the equatorial Atlantic to the eastern Sahel, decreasing δD_P (Figure 3.4) (Dansgaard, 1964; Gat, 1996; Rozanski et al., 1993). In addition, a small portion of depleted water vapor derived from the Indian Ocean to the east further lowers δD_P in the eastern Sahel (Figures 3.4 and S3.5). Overall, the regional monsoon dynamics in the eastern Sahel lead to its far different $\Delta\delta D_P$ response than that of the northwestern Sahara.

3.5 Discussion

3.5.1 δD_{WAX} isotopic signal and implications for the West African monsoon

The results of our model-proxy comparison show mixed agreement between iCESM1 and northern African leaf wax *n*-alkane records. iCESM1 simulates increased MH annual rainfall throughout the Sahara and Sahel, in agreement with interpretations from several proxy records (Figure 3.1a; e.g., Bartlein et al., 2011; Collins et al., 2017; Hély et al., 2014; Palchan and Torfstein, 2019; Tierney et al., 2017a, 2017b). However, its simulated MH northernmost WAM extent is ~24°N, which falls short of the 27–31°N estimate from leaf wax *n*-alkanes and the Moroccan speleothem record. Furthermore, iCESM1 and leaf wax *n*-alkane records disagree over the sign of MH–PI $\Delta\delta D_P$ over northwestern Africa with leaf wax *n*-alkane records indicating lower MH values and iCESM1 simulating the opposite (Figures 3.2a, Table 3.1). Further analysis into the interpretation of the leaf wax *n*-alkane hydroclimate signal is required to explain the model-proxy discrepancy.

One explanation for the model-proxy mismatch is that the water isotopic signal from leaf wax *n*-alkanes is biased to the early boreal summer growing season associated with the onset of the monsoon (Tipple et al., 2013). Since the simulated MH enrichment of rainfall occurs during the boreal summer and fall (Figure 3.3), the early summer bias may minimize the late summer and fall contribution of δD_P to δD_{WAX}. However, our results suggest that the seasonal bias accounts for no more than a small contribution to the model-proxy discrepancy, since there is little to no simulated difference in northwestern African δD_P between the MH and PI in the early summer months (Figure 3.3b).

The more likely reason for model-proxy mismatch is that the northwestern African leaf wax *n*-alkanes are reflecting the signal of δD_S, and its subsequent influence by soil evaporation, rather than δD_P. Better agreement between the MH–PI difference in northwestern African leaf wax *n*-alkanes and simulated $\Delta\delta D_S$, rather than $\Delta\delta D_P$ (Figure 3.2), provides support for this explanation. We also note that simulated MH δD_S is systematically lower than the PI throughout the year, reducing any impact from potential seasonal bias (Figure 3.3). In the PI, soil water (δD_S) taken up by the roots of plants to synthesize leaf wax *n*-alkanes experiences strong evaporation and therefore has a relatively enriched isotopic composition in comparison to precipitation (δD_P). During the MH, increases in vegetation lead to a reduction in soil evaporation, which results in a relatively less enriched isotopic signature of soil water compared to the PI (Figures 3.5 and S3.3). Therefore, when analyzing the difference between the vegetated MH and desert PI, as in MH_{VEG}–PI_{DESERT}, MH δD_{WAX} values are lower than the PI despite MH δD_P values being higher. This process can also explain the low MH carbonate $\delta^{18}O$ values in the Moroccan speleothem record as the soil water infiltrating the cave system would have contained the same isotopic signature as the soil water reflected by leaf wax *n*-alkanes. This finding lends support to studies based on pollen and dust records that have inferred a more southern limit of 23–28°N for the WAM (Bartlein et al., 2011; Hély et al., 2014; Palchan and Torfstein, 2019), since it is likely that the leaf wax *n*-alkanes near 27–31°N do not reflect changes in δD_P.

Furthermore, while we find that the lower MH δD_{WAX} in northwestern Africa is likely the result of leaf wax *n*-alkanes being reflective of the isotopic signature of δD_S, and its subsequent influence by soil evaporation, our findings are relevant for the MH WAM even in the case that this interpretation of the isotopic systematics is overly simplified. In arid environments, leaf wax *n*-alkanes have been shown to rapidly take up water into their roots during precipitation events

(Feakins and Sessions, 2010), which does not allow time for the soil water to become evaporated. This runs counter to the idea that leaf wax *n*-alkanes would reflect evaporatively enriched soil water in an arid environment. Therefore, decoupling of δD_P and δD_S, as we show in Figure 3.2, would be irrelevant in northwestern Africa as the plant waxes would reflect the isotopic signature of precipitation (δD_P). In this case, lower MH δD_{WAX} at 27–31°N would not be the result of evaporated soil water and instead would either be due to increased rainfall amount in this region, as suggested by Tierney et al. (2017a), or non-amount effect processes that could isotopically deplete rainfall without increasing it. As these northernmost leaf wax *n*-alkane records would be on the fringe of the MH WAM, it is likely that non-amount effect processes, such as upstream fractionation where rainout or moisture sourcing changes upstream from northwestern Africa could deplete advected vapor (Konecky et al., 2019a), would be prevalent and could cause the lower δD_{WAX} seen in the MH.

3.5.2 Uncertainties in the δD_{WAX} isotopic signal

While representing one of the most complex reconstructions of the hydroclimate and isotopic dynamics in MH and PI northern Africa, our simulations do not capture the full complexity concerning the leaf wax *n*-alkane isotopic system. Our use of iCESM1 and WaxPSM allows for prediction of the likely isotopic dynamics present in leaf wax *n*-alkanes, but these models do not explicitly simulate the synthesis of plant waxes and their subsequent dispersal into the environment. Thus, many assumptions must be made in order to represent this complex process. With this in mind, the following section provides a more nuanced discussion of the uncertainties involved in interpreting northern African isotopic change from leaf wax *n*-alkanes.

Additional complicating factors regarding the uncertainties of comparing our simulations with leaf wax *n*-alkane records must be considered. First, since the type of vegetation determines its interactions with the leaf wax *n*-alkane isotopic system (Kahmen et al., 2013; Sachse et al., 2012), differences between the actual and simulated vegetation in the MH and PI may contribute to differences in rooting depth or plant strategies for dealing with water scarcity. Therefore, differences in plant type could impact the resulting MH–PI isotopic change. Second, although it aligns with previous isotope modeling results (Battisti et al., 2014), our simulated MH enriched precipitation and depleted soil water in northwestern Africa could be an artifact of iCESM1 since climate models are known to have difficulty simulating MH African climate (i.e., Braconnot et al.,

2012; Tierney et al., 2017a). If this were true, one alternative explanation for the MH reduction in δD_{WAX} could be that the wax-shed, the area from which the leaf wax *n*-alkanes originate, for the proxy sites off the northwestern African coast is not well-understood or defined. The lower MH δD_{WAX} at proxy sites between 27–31°N could in theory be due to wind-blown processes transporting these plant waxes from lower latitudes where the monsoon was enhanced. Our simulated wind patterns over the northwestern Sahara give credibility to this possible mechanism (Figure S3.4). Although these complicating factors underscore the uncertainty in MH leaf wax *n*-alkanes and our simulation of their isotopic signal, the mechanisms simulated in iCESM1 that invoke hydroclimatic and isotopic change in northern Africa, namely the changes in moisture sourcing and soil evaporation, represent notable advancements in our understanding of the processes that impacted the MH WAM.

Due to the large uncertainties present within the leaf wax *n*-alkane isotope system and our comparison with iCESM1, further in-depth consideration of these various complicating factors is beyond the scope of this study. Likewise, we demonstrate that the interpretation of leaf wax *n*-alkane records overestimating the MH WAM extent is a result that holds merit despite the uncertainties present in leaf wax *n*-alkane isotope systematics. Future work can further disentangle these complicating factors by investigating the isotope systematics at play in MH northern Africa in greater detail and connecting this change to the reconstruction of climate from various proxy records.

3.5.3 Regional implications for model-proxy comparisons

Our study's process of identifying MAP–δD_P and δD_P–δD_S relationships for model-proxy comparison provides a framework for evaluation of these relationships in other regions throughout the tropics and subtropics. Although it is beyond the scope of this study to provide in-depth analysis of the region-specific atmospheric and land surface dynamics contributing to MH–PI hydroclimate changes in other regions around the world, we present a brief overview of MH–PI differences in MAP, δD_P, and δD_S throughout the tropics and subtropics. Using our iCESM1 results, we find that other regions with mismatch between ΔMAP and $\Delta\delta D_P$ include the Yucatán Peninsula, Northeastern Brazil, China, and Indonesia (Figure 3.7). These are all regions where large-scale microphysical and dynamical processes may play a larger role than rainfall rate in

determining δD_P. However, unlike northwestern Africa, none of these regions have statistically significant differences between $\Delta\delta D_P$ and $\Delta\delta D_S$.

3.6 Conclusion

In this study, we evaluate the hydrologic and isotopic changes that occur in mid-Holocene (MH) and Pre-industrial (PI) northern Africa and compare the interpreted hydroclimate signal from leaf wax *n*-alkanes to results from a fully coupled water isotope-enabled Earth system model (iCESM1). Our modeling results agree with the northernmost extent of the West African monsoon indicated by pollen and dust records (23–28°N) but suggest that the northernmost extent inferred from leaf wax *n*-alkane records (27–31°N) is likely an overestimate.

While iCESM1 simulates increased annual rainfall across the Sahara and Sahel in the MH relative to the PI, in agreement with several proxy records, its isotopic response varies regionally. In the northwestern Sahara, simulated MH isotopic composition of precipitation (δD_P) is higher than the PI due to changes in the evapotranspiration flux and moisture sourcing that arise from a stronger Saharan Heat Low and increased vegetation cover. This contrasts with lower inferred δD_P from northwestern African leaf wax *n*-alkanes. However, simulated MH isotopic composition of soil water (δD_S) in this region is lower than in the PI due to reduced soil evaporation associated with increased vegetation cover and matches more closely with leaf wax *n*-alkane records than δD_P. This suggests that northwestern African leaf wax *n*-alkanes may reflect the isotopic signature of δD_S and its influence by soil evaporation. In the eastern Sahel, both simulated MH δD_P and δD_S are lower than the PI due to enhanced continental rainout associated with stronger monsoon circulation, and both agree with the inferred hydroclimate signal from leaf wax *n*-alkane records from this region. This work has broad implications for understanding the isotopic dynamics that impacted the West African monsoon in the mid-Holocene and better constrains the monsoon's extent during that time.

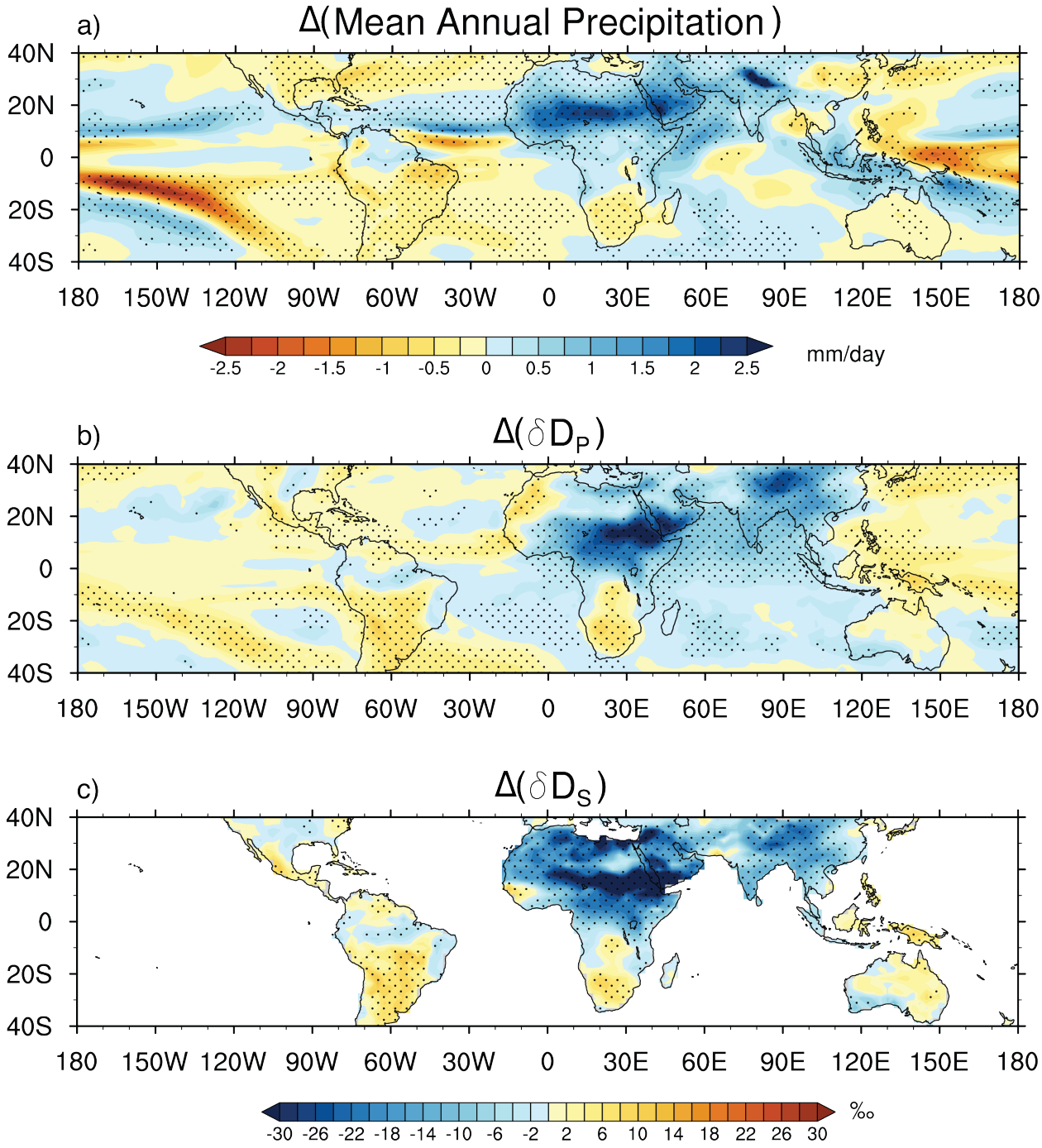

Figure 3.7. Simulated MH_{VEG}–$PI_{CONTROL}$ difference in annually-averaged a) precipitation, b) rainfall amount-weighted δD_P, and c) soil water- and root depth fraction-weighted δD_S throughout the tropics. Stippling represents statistically significant differences at the 95% confidence level.

3.7 Acknowledgments

This work was supported by National Science Foundation award 1602956. We thank Sylvia Dee, Naomi Levin, and Phoebe Aron for helpful discussion. We thank two anonymous reviewers for their constructive feedback that improved the quality of this manuscript and Bronwen Konecky for insightful discussion on leaf wax *n*-alkanes. We acknowledge high-performance computing support from Cheyenne (doi:10.5065/D6RX99HX) provided by NCAR's Computational and Information Systems Laboratory, sponsored by the National Science Foundation. Data is available online (at https://github.com/alexjt28).

3.8 References

Ampuero, A., Stríkis, N. M., Apaéstegui, J., Vuille, M., Novello, V. F., Espinoza, J. C., Cruz, F. W., Vonhof, H., Mayta, V. C., Martins, V. T. S., Cordeiro, R. C., Azevedo, V., Sifeddine, A., 2020. The Forest Effects on the Isotopic Composition of Rainfall in the Northwestern Amazon Basin. J. Geophys. Res. Atmos. 125. https://doi.org/10.1029/2019JD031445.

Bartlein, P.J., Harrison, S.P., Brewer, S., Connor, S., Davis, B.A.S., Gajewski, K., Guiot, J., Harrison-Prentice, T.I., Henderson, A., Peyron, O., Prentice, I.C., Scholze, M., Seppä, H., Shuman, B., Sugita, S., Thompson, R.S., Viau, A.E., Williams, J., Wu, H., 2011. Pollen-based continental climate reconstructions at 6 and 21 ka: a global synthesis. Clim. Dyn. 37, 775–802. https://doi.org/10.1007/s00382-010-0904-1

Battisti, D.S., Ding, Q., Roe, G.H., 2014. Coherent pan-Asian climatic and isotopic response to orbital forcing of tropical insolation. *J. Geophys. Res. Atmos.* 119, 11,997-12,020. https://doi.org/10.1002/2014JD021960

Bedaso, Z.K., DeLuca, N.M., Levin, N.E., Zaitchik, B.F., Waugh, D.W., Wu, S.-Y., Harman, C.J., Shanko, D., 2019. Spatial and temporal variation in the isotopic composition of Ethiopian precipitation. *J. Hydrol.* 124364. https://doi.org/10.1016/j.jhydrol.2019.124364

Bony, S., Risi, C., Vimeux, F., 2008. Influence of convective processes on the isotopic composition (δ 18 O and δ D) of precipitation and water vapor in the tropics: 1. Radiative-convective equilibrium and Tropical Ocean–Global Atmosphere–Coupled Ocean-Atmosphere Response Experiment (TOGA-CO. *J. Geophys. Res.* 113, D19305. https://doi.org/10.1029/2008JD009942

Braconnot, P., Harrison, S.P., Otto-Bliesner, B., Abe-Ouchi, A., Jungclaus, J., Peterschmitt, J.-Y., 2011. The paleoclimate modeling intercomparison project contribution to CMIP5, *CLIVAR Exchanges*.

Braconnot, P., Harrison, S.P., Kageyama, M., Bartlein, P.J., Masson-Delmotte, V., Abe-Ouchi, A., Otto-Bliesner, B., Zhao, Y., 2012. Evaluation of climate models using palaeoclimatic data. *Nat. Clim. Chang.* 2, 417–424. https://doi.org/10.1038/nclimate1456

Brady, E., Stevenson, S., Bailey, D., Liu, Z., Noone, D., Nusbaumer, J., Otto-Bliesner, B.L., Tabor, C., Tomas, R., Wong, T., Zhang, J., Zhu, J., 2019. The Connected Isotopic Water Cycle in the Community Earth System Model Version 1. *J. Adv. Model. Earth Syst.* 11, 2547–2566. https://doi.org/10.1029/2019MS001663

Brierley, C.M., Zhao, A., Harrison, S.P., Braconnot, P., Williams, C.J.R., Thornalley, D.J.R., Shi, X., Peterschmitt, J., Ohgaito, R., Kaufman, D.S., Kageyama, M., Hargreaves, J.C., Erb, M.P., Emile-Geay, J., D'Agostino, R.D., Chandan, D., Carré, M., Bartlein, P.J., Zheng, W., Zhang, Z., Zhang, Q., Yang, H., Volodin, E.M., Tomas, R.A., Routson, C., Peltier, R., Otto-Bliesner, B., Morozova, P.A., McKay, N.P., Lohmann, G., Legrande, A.N., Guo, C., Cao, J., Brady, E., Annan, J.D., Abe-Ouchi, A., 2020. Large-scale features and evaluation of the PMIP4-CMIP6 midHolocene simulations. *Clim. Past Discuss.* https://doi.org/10.5194/cp-2019-168

Cauquoin, A., Werner, M., Lohmann, G., 2019. Water isotopes - climate relationships for the mid-Holocene and pre-industrial period simulated with an isotope-enabled version of MPI-ESM. *Clim. Past Discuss.* 1–38. https://doi.org/10.5194/cp-2019-72

Collins, J.A., Prange, M., Caley, T., Gimeno, L., Beckmann, B., Mulitza, S., Skonieczny, C., Roche, D., Schefuß, E., 2017. Rapid termination of the African Humid Period triggered by northern high-latitude cooling. *Nat. Commun.* 8, 1372. https://doi.org/10.1038/s41467-017-01454-y

Costa, K., Russell, J., Konecky, B., Lamb, H., 2014. Isotopic reconstruction of the African Humid Period and Congo Air Boundary migration at Lake Tana, Ethiopia. *Quat. Sci. Rev.* 83, 58–67. https://doi.org/10.1016/j.quascirev.2013.10.031

Dallmeyer, A., Claussen, M., Lorenz, S.J., Shanahan, T., 2020. The end of the African humid period as seen by a transient comprehensive Earth system model simulation of the last 8000 years. *Clim. Past* 16, 117–140. https://doi.org/10.5194/cp-16-117-2020

D'Agostino, R., Bader, J., Bordoni, S., Ferreira, D., Jungclaus, J., 2019. Northern Hemisphere Monsoon Response to Mid-Holocene Orbital Forcing and Greenhouse Gas-Induced Global Warming. *Geophys. Res. Lett.* 46, 1591–1601. https://doi.org/10.1029/2018GL081589

Dansgaard, W., 1964. Stable isotopes in precipitation. *Tellus* 16, 436–468.

deMenocal, P., Ortiz, J., Guilderson, T., Adkins, J., Sarnthein, M., Baker, L., Yarusinsky, M., 2000. Abrupt onset and termination of the African Humid Period: *Quat. Sci. Rev.* 19, 347–361. https://doi.org/10.1016/S0277-3791(99)00081-5

Feakins, S.J., Sessions, A.L., 2010. Controls on the D/H ratios of plant leaf waxes in an arid ecosystem. *Geochim. Cosmochim. Acta* 74, 2128–2141. https://doi.org/10.1016/j.gca.2010.01.016

Gaetani, M., Messori, G., Zhang, Q., Flamant, C., Pausata, F.S.R., 2017. Understanding the Mechanisms behind the Northward Extension of the West African Monsoon during the Mid-Holocene. *J. Clim.* 30, 7621–7642. https://doi.org/10.1175/JCLI-D-16-0299.1

Gat, J.R., 1996. OXYGEN AND HYDROGEN ISOTOPES IN THE HYDROLOGIC CYCLE. *Annu. Rev. Earth Planet. Sci.* 24, 225–262. https://doi.org/10.1146/annurev.earth.24.1.225

Hély, C., Lézine, A.-M., Contributors, A., 2014. Holocene changes in African vegetation: tradeoff between climate and water availability. *Clim. Past* 10, 681–686. https://doi.org/10.5194/cp-10-681-2014

Hoelzmann, P., Jolly, D., Harrison, S.P., Laarif, F., Bonnefille, R., Pachur, H., 1998. Mid-Holocene land-surface conditions in northern Africa and the Arabian Peninsula: A data set for the analysis of biogeophysical feedbacks in the climate system. *Global Biogeochem. Cycles* 12, 35–51. https://doi.org/10.1029/97GB02733

Hurrell, J.W., Holland, M.M., Gent, P.R., Ghan, S., Kay, J.E., Kushner, P.J., Lamarque, J.F., Large, W.G., Lawrence, D., Lindsay, K., Lipscomb, W.H., Long, M.C., Mahowald, N., Marsh, D.R., Neale, R.B., Rasch, P., Vavrus, S., Vertenstein, M., Bader, D., Collins, W.D., Hack, J.J., Kiehl, J., Marshall, S., 2013. The community earth system model: A framework for collaborative research. *Bull. Am. Meteorol. Soc.* 94, 1339–1360. https://doi.org/10.1175/BAMS-D-12-00121.1

Jolly, D., Prentice, I.C., Bonnefille, R., Ballouche, A., Bengo, M., Brenac, P., Buchet, G., Burney, D., Cazet, J., Cheddadi, R., Edorh, T., Elenga, H., Elmoutaki, S., Guiot, J., Laarif, F., Lamb, H., Lezine, A., Maley, J., Mbenza, M., Peyron, O., Reille, M., Reynaud-Farrera,

I., Riollet, G., Ritchie, J.C., Roche, E., Scott, L., Ssemmanda, I., Straka, H., Umer, M., Van Campo, E., Vilimumbalo, S., Vincens, A., Waller, M., 1998. Biome reconstruction from pollen and plant macrofossil data for Africa and the Arabian peninsula at 0 and 6000 years. *J. Biogeogr.* 25, 1007–1027. https://doi.org/10.1046/j.1365-2699.1998.00238.x

Kahmen, A., Schefuß, E., Sachse, D., 2013. Leaf water deuterium enrichment shapes leaf wax n-alkane δD values of angiosperm plants I: Experimental evidence and mechanistic insights. *Geochim. Cosmochim.* Acta 111, 39–49. https://doi.org/10.1016/j.gca.2012.09.003

Kanner, L.C., Buenning, N.H., Stott, L.D., Timmermann, A., Noone, D., 2014. The role of soil processes in δ 18 O terrestrial climate proxies. *Global Biogeochem. Cycles* 28, 239–252. https://doi.org/10.1002/2013GB004742

Konecky, B. L., Russell, J. M., Johnson, T. C., Brown, E. T., Berke, M. A., Werne, J. P, Huang, Y., 2011. Atmospheric circulation patterns during late Pleistocene climate changes at Lake Malawi, Africa. *Earth Planet. Sci. Lett.* 312, 318-326. https://doi.org/10.1016/j.epsl.2011.10.020

Konecky, B., Russell, J., Bijaksana, S., 2016. Glacial aridity in central Indonesia coeval with intensified monsoon circulation. *Earth Planet. Sci. Lett.* 437, 15–24. https://doi.org/10.1016/j.epsl.2015.12.037

Konecky, B.L., Noone, D.C., Cobb, K.M., 2019a. The Influence of Competing Hydroclimate Processes on Stable Isotope Ratios in Tropical Rainfall. *Geophys. Res. Lett.* 46, 1622–1633. https://doi.org/10.1029/2018GL080188

Konecky, B., Dee, S.G., Noone, D.C., 2019b. WaxPSM: A Forward Model of Leaf Wax Hydrogen Isotope Ratios to Bridge Proxy and Model Estimates of Past Climate. *J. Geophys. Res. Biogeosciences* 124, 2107–2125. https://doi.org/10.1029/2018JG004708

Kutzbach, J.E., 1981. Monsoon Climate of the Early Holocene: Climate Experiment with the Earth's Orbital Parameters for 9000 Years Ago. *Science* (80-.). 214, 59–61. https://doi.org/10.1126/science.214.4516.59

Kutzbach, J., Bonan, G., Foley, J., Harrison, S.P., 1996. Vegetation and soil feedbacks on the response of the African monsoon to orbital forcing in the early to middle Holocene. *Nature* 384, 623–626. https://doi.org/10.1038/384623a0

Lacour, J., Flamant, C., Risi, C., Clerbaux, C., Coheur, P., 2017. Importance of the Saharan heat low in controlling the North Atlantic free tropospheric humidity budget deduced from IASI

δ D observations. *Atmos. Chem. Phys.* 17, 9645–9663. https://doi.org/10.5194/acp-17-9645-2017

Lavaysse, C., Flamant, C., Janicot, S., Parker, D.J., Lafore, J.-P., Sultan, B., Pelon, J., 2009. Seasonal evolution of the West African heat low: a climatological perspective. *Clim. Dyn.* 33, 313–330. https://doi.org/10.1007/s00382-009-0553-4

Levin, N.E., Zipser, E.J., Cerling, T.E., 2009. Isotopic composition of waters from Ethiopia and Kenya: Insights into moisture sources for eastern Africa. *J. Geophys. Res.* 114, D23306. https://doi.org/10.1029/2009JD012166

Lézine, A.-M., Hély, C., Grenier, C., Braconnot, P., Krinner, G., 2011. Sahara and Sahel vulnerability to climate changes, lessons from Holocene hydrological data. *Quat. Sci. Rev.* 30, 3001–3012. https://doi.org/10.1016/j.quascirev.2011.07.006

Munksgaard, N.C., Kurita, N., Sánchez-Murillo, R., Ahmed, N., Araguas, L., Balachew, D.L., Bird, M.I., Chakraborty, S., Kien Chinh, N., Cobb, K.M., Ellis, S.A., Esquivel-Hernández, G., Ganyaglo, S.Y., Gao, J., Gastmans, D., Kaseke, K.F., Kebede, S., Morales, M.R., Mueller, M., Poh, S.C., Santos, V. dos, Shaoneng, H., Wang, L., Yacobaccio, H., Zwart, C., 2019. Data Descriptor: Daily observations of stable isotope ratios of rainfall in the tropics. *Sci. Rep.* 9, 14419. https://doi.org/10.1038/s41598-019-50973-9

Niedermeyer, E.M., Schefuß, E., Sessions, A.L., Mulitza, S., Mollenhauer, G., Schulz, M., Wefer, G., 2010. Orbital- and millennial-scale changes in the hydrologic cycle and vegetation in the western African Sahel: insights from individual plant wax δD and δ13C. *Quat. Sci. Rev.* 29, 2996–3005. https://doi.org/10.1016/j.quascirev.2010.06.039

Niedermeyer, E.M., Forrest, M., Beckmann, B., Sessions, A.L., Mulch, A., Schefuß, E., 2016. The stable hydrogen isotopic composition of sedimentary plant waxes as quantitative proxy for rainfall in the West African Sahel. *Geochim. Cosmochim. Acta* 184, 55–70. https://doi.org/10.1016/j.gca.2016.03.034

Nusbaumer, J., Wong, T.E., Bardeen, C., Noone, D., 2017. Evaluating hydrological processes in the Community Atmosphere Model Version 5 (CAM5) using stable isotope ratios of water. *J. Adv. Model. Earth Syst.* 9, 949–977. https://doi.org/10.1002/2016MS000839

Oleson, K.W., Lawrence, D.M., Gordon, B., Flanner, M.G., Kluzek, E., Peter, J., Levis, S., Swenson, S.C., Thornton, E., Dai, A., Decker, M., Dickinson, R., Feddema, J., Heald, C.L., Lamarque, J., Niu, G., Qian, T., Running, S., Sakaguchi, K., Slater, A., Stöckli, R., Wang,

A., Yang, L., Zeng, Xiaodong, Zeng, Xubin, 2010. Technical description of version 4.0 of the Community Land Model (CLM), NCAR Tech. Note NCAR/TN-478+STR. https://doi.org/10.5065/D6FB50WZ

Otto-Bliesner, B.L., Braconnot, P., Harrison, S.P., Lunt, D.J., Abe-Ouchi, A., Albani, S., Bartlein, P.J., Capron, E., Carlson, A.E., Dutton, A., Fischer, H., Goelzer, H., Govin, A., Haywood, A., Joos, F., LeGrande, A.N., Lipscomb, W.H., Lohmann, G., Mahowald, N., Nehrbass-Ahles, C., Pausata, F.S.R., Peterschmitt, J.-Y., Phipps, S.J., Renssen, H., Zhang, Q., 2017. The PMIP4 contribution to CMIP6 – Part 2: Two interglacials, scientific objective and experimental design for Holocene and Last Interglacial simulations. *Geosci. Model Dev.* 10, 3979–4003. https://doi.org/10.5194/gmd-10-3979-2017

Palchan, D., Torfstein, A., 2019. A drop in Sahara dust fluxes records the northern limits of the African Humid Period. *Nat. Commun.* 10, 3803. https://doi.org/10.1038/s41467-019-11701-z

Pausata, F.S.R., Messori, G., Zhang, Q., 2016. Impacts of dust reduction on the northward expansion of the African monsoon during the Green Sahara period. *Earth Planet. Sci. Lett.* 434, 298–307. https://doi.org/10.1016/j.epsl.2015.11.049

Pausata, F.S.R., Gaetani, M., Messori, G., Berg, A., Maia de Souza, D., Sage, R.F., DeMenocal, P.B., 2020. The Greening of the Sahara: Past Changes and Future Implications. *One Earth* 2, 235–250. https://doi.org/10.1016/j.oneear.2020.03.002

Perez-Sanz, A., Li, G., González-Sampériz, P., Harrison, S.P., 2014. Evaluation of modern and mid-Holocene seasonal precipitation of the Mediterranean and northern Africa in the CMIP5 simulations. *Clim. Past* 10, 551–568. https://doi.org/10.5194/cp-10-551-2014

Risi, C., Bony, S., Vimeux, F., Descroix, L., Ibrahim, B., Lebreton, E., Mamadou, I., Sultan, B., 2008a. What controls the isotopic composition of the African monsoon precipitation? Insights from event-based precipitation collected during the 2006 AMMA field campaign. *Geophys. Res. Lett.* 35, L24808. https://doi.org/10.1029/2008GL035920

Risi, C., Bony, S., Vimeux, F., 2008b. Influence of convective processes on the isotopic composition (δ 18 O and δ D) of precipitation and water vapor in the tropics: 2. Physical interpretation of the amount effect. *J. Geophys. Res.* 113, D19306. https://doi.org/10.1029/2008JD009943

Rozanski, K., Araguás-Araguás, L., Gonfiantini, R., 1993. Isotopic Patterns in Modern Global Precipitation, in: Swart, P.K., Lohmann, K.C., Mckenzie, J., Savin, S. (Eds.), *Climate Change in Continental Isotopic Records*. American Geophysical Union, pp. 1–36. https://doi.org/10.1029/GM078p0001

Sachse, D., Billault, I., Bowen, G.J., Chikaraishi, Y., Dawson, T.E., Feakins, S.J., Freeman, K.H., Magill, C.R., McInerney, F.A., van der Meer, M.T.J., Polissar, P., Robins, R.J., Sachs, J.P., Schmidt, H.-L., Sessions, A.L., White, J.W.C., West, J.B., Kahmen, A., 2012. Molecular Paleohydrology: Interpreting the Hydrogen-Isotopic Composition of Lipid Biomarkers from Photosynthesizing Organisms. *Annu. Rev. Earth Planet. Sci.* 40, 221–249. https://doi.org/10.1146/annurev-earth-042711-105535

Schneider, Udo; Becker, Andreas; Finger, Peter; Meyer-Christoffer, Anja; Ziese, Markus, 2018. GPCC Full Data Monthly Product Version 2018 at 2.5°: Monthly Land-Surface Precipitation from Rain-Gauges built on GTS-based and Historical Data. https://doi.org/10.5676/DWD_GPCC/FD_M_V2018_250

Sha, L., Ait Brahim, Y., Wassenburg, J.A., Yin, J., Peros, M., Cruz, F.W., Cai, Y., Li, H., Du, W., Zhang, H., Edwards, R.L., Cheng, H., 2019. How Far North Did the African Monsoon Fringe Expand During the African Humid Period? Insights From Southwest Moroccan Speleothems. *Geophys. Res. Lett.* 46, 14093–14102. https://doi.org/10.1029/2019GL084879

Shanahan, T.M., McKay, N.P., Hughen, K.A., Overpeck, J.T., Otto-Bliesner, B., Heil, C.W., King, J., Scholz, C.A., Peck, J., 2015. The time-transgressive termination of the African Humid Period. *Nat. Geosci.* 8, 140–144. https://doi.org/10.1038/ngeo2329

Shi, X., Lohmann, G., Sidorenko, D., Yang, H., 2020. Early-Holocene simulations using different forcings and resolutions in AWI-ESM. *The Holocene* 30, 996–1015. https://doi.org/10.1177/0959683620908634

Skinner, C.B., Poulsen, C.J., 2016. The role of fall season tropical plumes in enhancing Saharan rainfall during the African Humid Period. *Geophys. Res. Lett.* 43, 349–358. https://doi.org/10.1002/2015GL066318

Sultan, B., Janicot, S., 2003. The West African Monsoon Dynamics. Part II: The "Preonset" and "Onset" of the Summer Monsoon. *J. Clim.* 16, 3407–3427. https://doi.org/10.1175/1520-0442(2003)016<3407:TWAMDP>2.0.CO;2

Tabor, C.R., Otto-Bliesner, B.L., Brady, E.C., Nusbaumer, J., Zhu, J., Erb, M.P., Wong, T.E., Liu, Z., Noone, D., 2018. Interpreting Precession-Driven δ 18 O Variability in the South Asian Monsoon Region. *J. Geophys. Res. Atmos.* 123, 5927–5946. https://doi.org/10.1029/2018JD028424

Thompson, A.J., Skinner, C.B., Poulsen, C.J., Zhu, J., 2019. Modulation of Mid-Holocene African Rainfall by Dust Aerosol Direct and Indirect Effects. *Geophys. Res. Lett.* 46, 3917–3926. https://doi.org/10.1029/2018GL081225

Thorncroft, C., Blackburn, M., 1999. Maintenance of the African easterly jet. *Q. J. R. Meteorol. Soc.* 125, 763–786. https://doi.org/10.1256/smsqj.55501

Tierney, J.E., DeMenocal, P.B., 2013. Abrupt Shifts in Horn of Africa Hydroclimate Since the Last Glacial Maximum. *Science* (80-.). 342, 843–846. https://doi.org/10.1126/science.1240411

Tierney, J.E., Pausata, F.S.R., DeMenocal, P.B., 2017a. Rainfall regimes of the Green Sahara. *Sci. Adv.* 3, e1601503. https://doi.org/10.1126/sciadv.1601503

Tierney, J.E., DeMenocal, P.B., Zander, P.D., 2017b. A climatic context for the out-of-Africa migration. *Geology* 45, 1023–1026. https://doi.org/10.1130/G39457.1

Tipple, B.J., Berke, M.A., Doman, C.E., Khachaturyan, S., Ehleringer, J.R., 2013. Leaf-wax n-alkanes record the plant-water environment at leaf flush. *Proc. Natl. Acad. Sci.* 110, 2659–2664. https://doi.org/10.1073/pnas.1213875110

Wong, T.E., Nusbaumer, J., Noone, D.C., 2017. Evaluation of modeled land-atmosphere exchanges with a comprehensive water isotope fractionation scheme in version 4 of the Community Land Model. *J. Adv. Model. Earth Syst.* 9, 978–1001. https://doi.org/10.1002/2016MS000842

Wolf, A., Roberts, W.H.G., Ersek, V., Johnson, K.R., Griffiths, M.L., 2020. Rainwater isotopes in central Vietnam controlled by two oceanic moisture sources and rainout effects. *Sci. Rep.* 10, 16482. https://doi.org/10.1038/s41598-020-73508-z

3.9 Supplementary Information

Leaf wax proxy system model

We calculate iCESM1-inferred δD_{WAX} using the methodology of leaf wax forward model WaxPSM (Konecky et al., 2019b). The initial input is either simulated δD_P (Figure 3.2a) or δD_S (Figure 3.2b), which is then "vegetation-corrected" by weighting the apparent fractionation (ε) factor by the vegetation fraction, and corresponding vegetation type-specific ε value, in each model grid cell (Konecky et al., 2019b; Sachse et al., 2012). Since WaxPSM uses ε values for C_{29} *n*-alkanes, we report our simulated results as δD_P-inferred $\delta D_{WAX\text{-}C29}$ (Figure 3.2c) and δD_S-inferred $\delta D_{WAX\text{-}C29}$ (Figure 3.2d).

In $PI_{CONTROL}$, the western margin of northern Africa, which is adjacent to proxy sites #6-10, consists of 100% bare ground. For leaf wax *n*-alkane proxies to record values during the PI, vegetation must have been present in this region. Thus, in order to compare proxy-based leaf wax *n*-alkane values with our iCESM1-inferred $\delta D_{WAX\text{-}C29}$ results, we convert the vegetation fraction west of 2.5°W in $PI_{CONTROL}$ from 100% bare ground to 50% C_4 grass, 25% shrub, and 25% tree, which has an average weighted ε of –121.0‰. This is likely a reasonable, and conservative, estimate because both leaf wax *n*-alkane and pollen evidence suggests that present-day C_4 grass percentage ranges from ~10–80% (Huang et al., 2000; Niedermeyer et al., 2010; Schefuβ et al., 2005) and $\delta^{13}C_{WAX}$ data from proxy sites #8-10 indicates an increase in C_3 shrubs and trees in the present-day compared to the MH (Tierney et al., 2017a). Furthermore, the transition between the Mediterranean and Sahara Desert has been categorized as being comprised of mixed C_3/C_4 vegetation, while the Sahara Desert is dominated by C_4 grasses (Schefuβ et al., 2005). Overall, our result that values from the western (#6-10) proxies match simulated δD_S more closely than δD_P is largely insensitive to the choice of converted vegetation fraction. This holds true unless PI vegetation is converted to 100% shrub; however, that is not a reasonable vegetation estimate for the western margin of northern Africa during the PI.

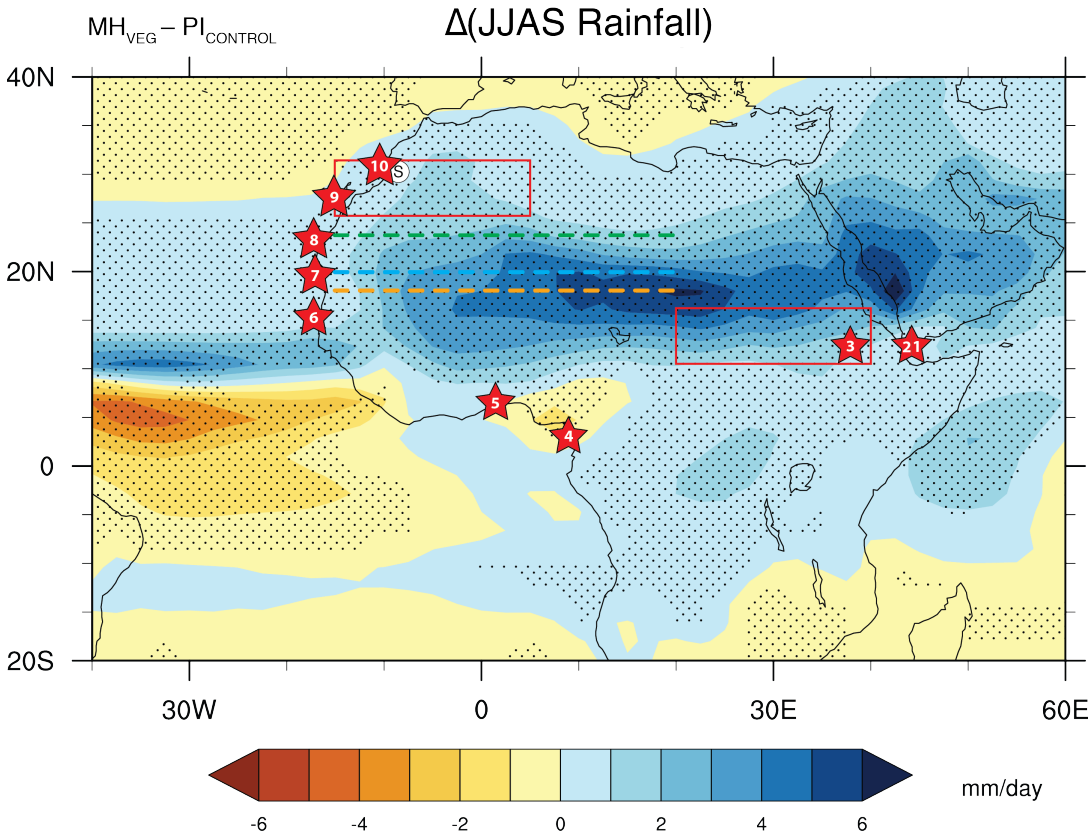

Figure S3.1. Simulated MH_{VEG}–$PI_{CONTROL}$ difference in monsoon season (JJAS) rainfall. Numbered stars represent leaf wax *n*-alkane record locations listed in Table 3.1. White circle represents speleothem record from Sha et al. (2019). Red boxes indicate the spatial extent of the northwestern Sahara and eastern Sahel. Stippling represents statistically significant differences at the 95% confidence level. Dashed lines indicate northernmost WAM extents as shown in Figure 3.1: $PI_{CONTROL}$ (orange), MH_{DESERT} (blue), and MH_{VEG} (green).

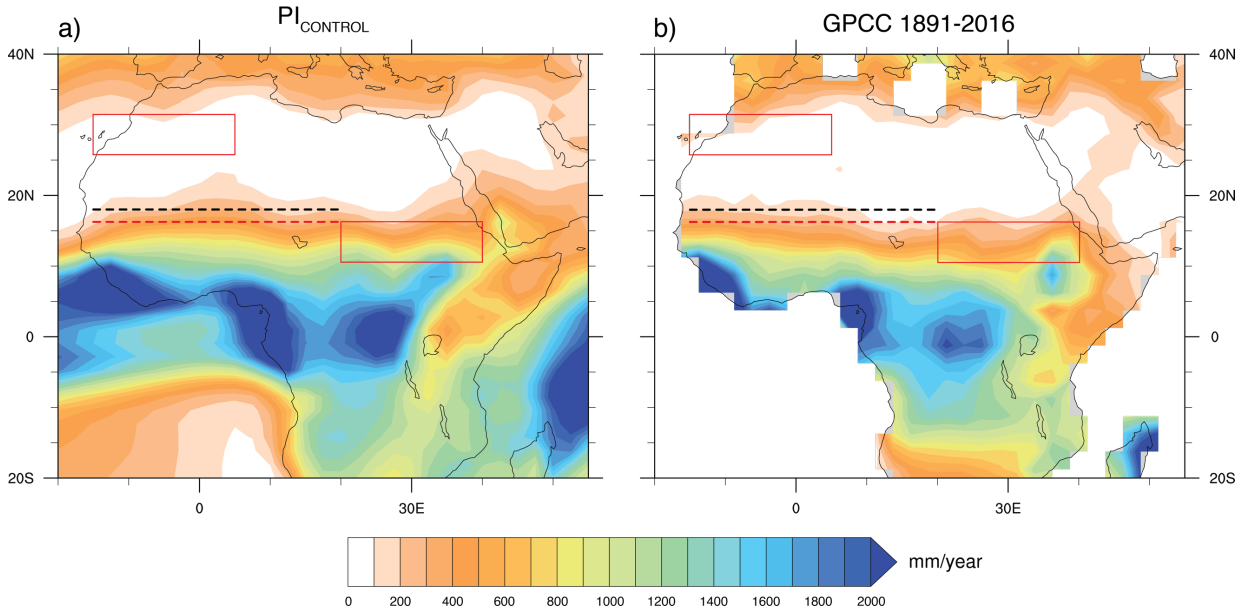

Figure S3.2. Mean annual precipitation for a) $PI_{CONTROL}$ and b) observational data from Global Precipitation Climatology Centre (GPCC; Schneider et al., 2016) from 1891–2016. Red boxes indicate the spatial extent of the northwestern Sahara and eastern Sahel. The dashed lines represent the northernmost WAM extent (see 3.3 Methods) calculated for $PI_{CONTROL}$ (black) and GPCC (red). Some of the discrepancies between $PI_{CONTROL}$ and GPCC may be related to the differences in greenhouse gas concentrations and aerosol forcing between the two time periods.

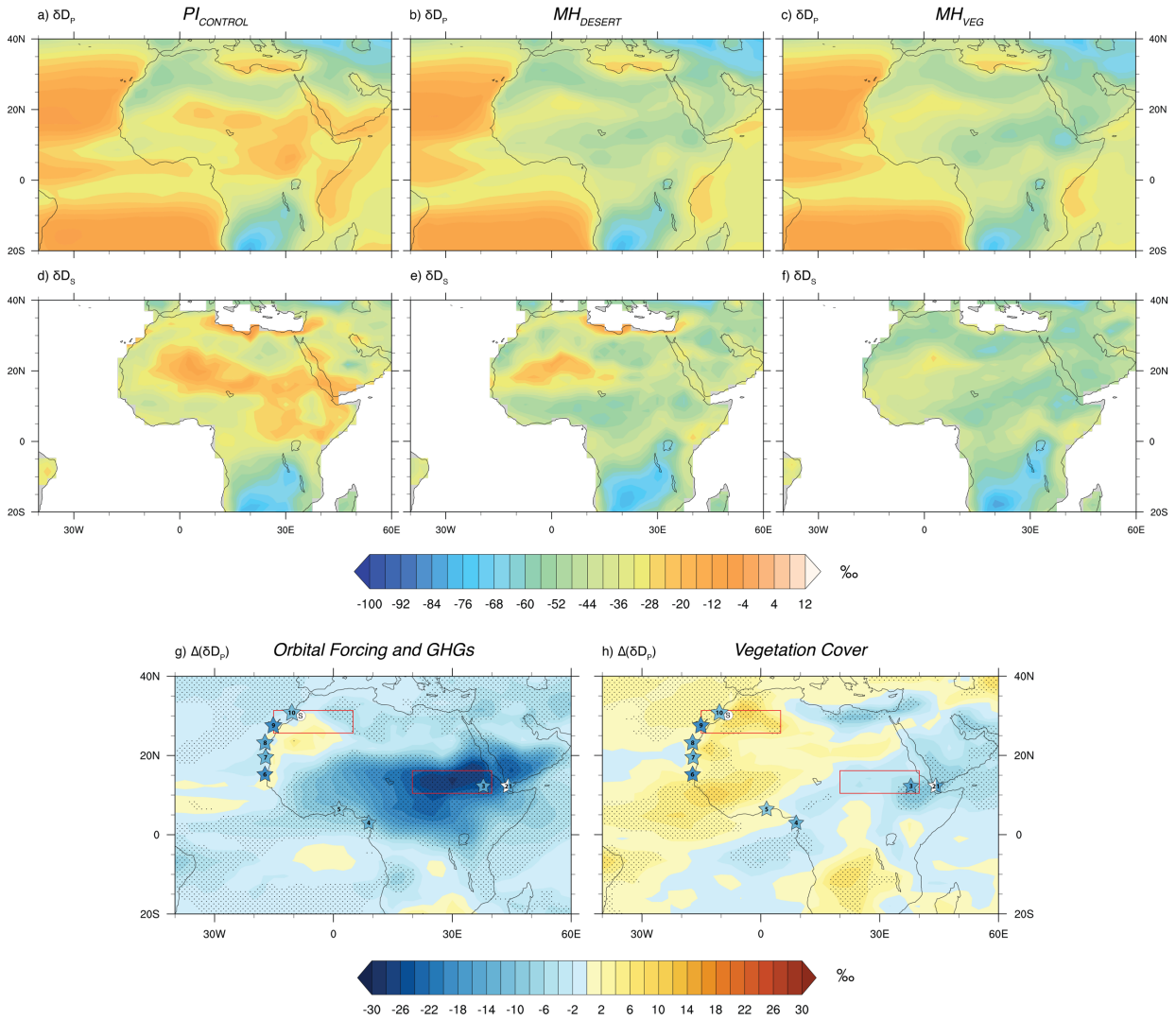

Figure S3.3. Simulated annually-averaged rainfall amount-weighted δD_P and soil water- and root depth fraction-weighted δD_S for a,d) $PI_{CONTROL}$, b,e) MH_{DESERT}, and c,f) MH_{VEG} and difference plots of δD_P isolating changes in g) orbital forcing and GHGs (MH_{DESERT}–$PI_{CONTROL}$) and h) an increase in vegetation cover (MH_{VEG}–MH_{DESERT}). Figure 3.2a isolates the difference in δD_P between MH_{VEG} and $PI_{CONTROL}$. Colored stars indicate leaf wax *n*-alkane record locations and each record's MH–PI δD change in δD_{WAX}-inferred δD_P. White circle represents speleothem record from Sha et al. (2019). Red boxes indicate the spatial extent of the northwestern Sahara and eastern Sahel. Stippling represents statistically significant differences at the 95% confidence level.

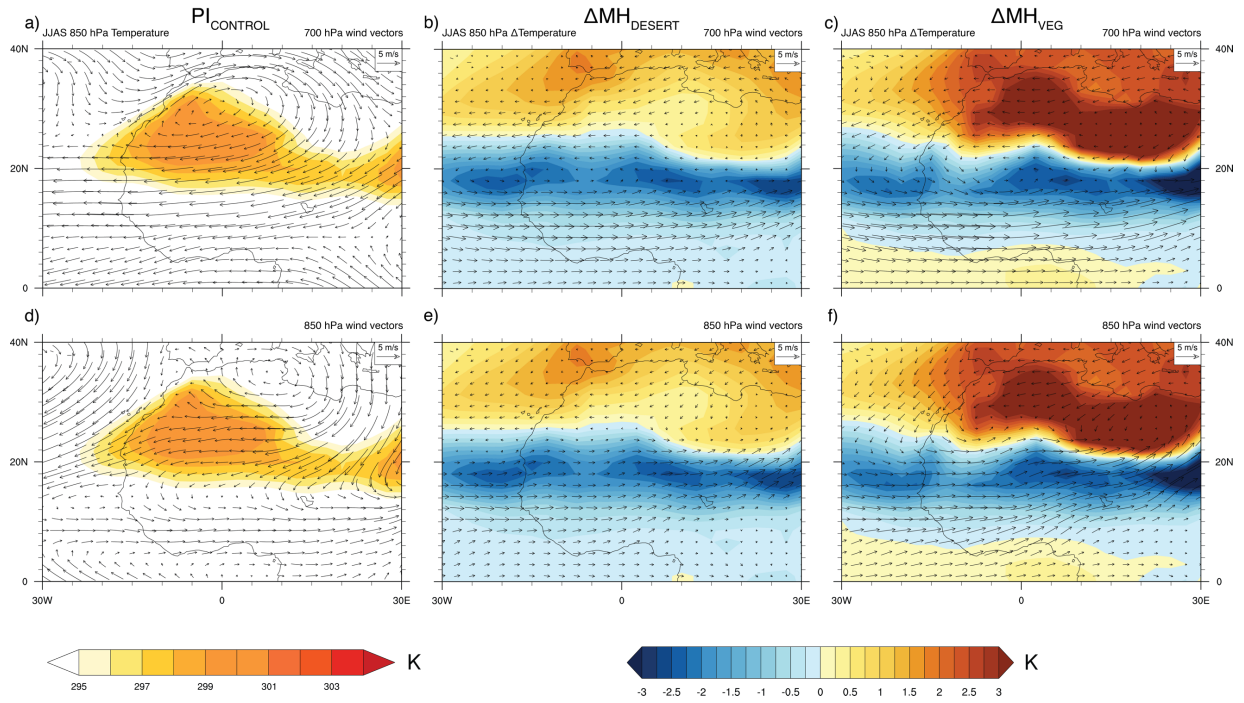

Figure S3.4. Strengthening of the Saharan Heat Low (SHL). Simulated June, July, August, September (JJAS) 850 hPa temperature for $PI_{CONTROL}$ with a) 700 and d) 850 hPa wind vectors. Change with respect to $PI_{CONTROL}$ is shown for b,e) MH_{DESERT} and c,f) MH_{VEG}. Warmer temperature and enhanced easterlies between 15°N and 25°N in MH_{VEG} and MH_{DESERT} indicate a stronger SHL in these simulations compared with $PI_{CONTROL}$.

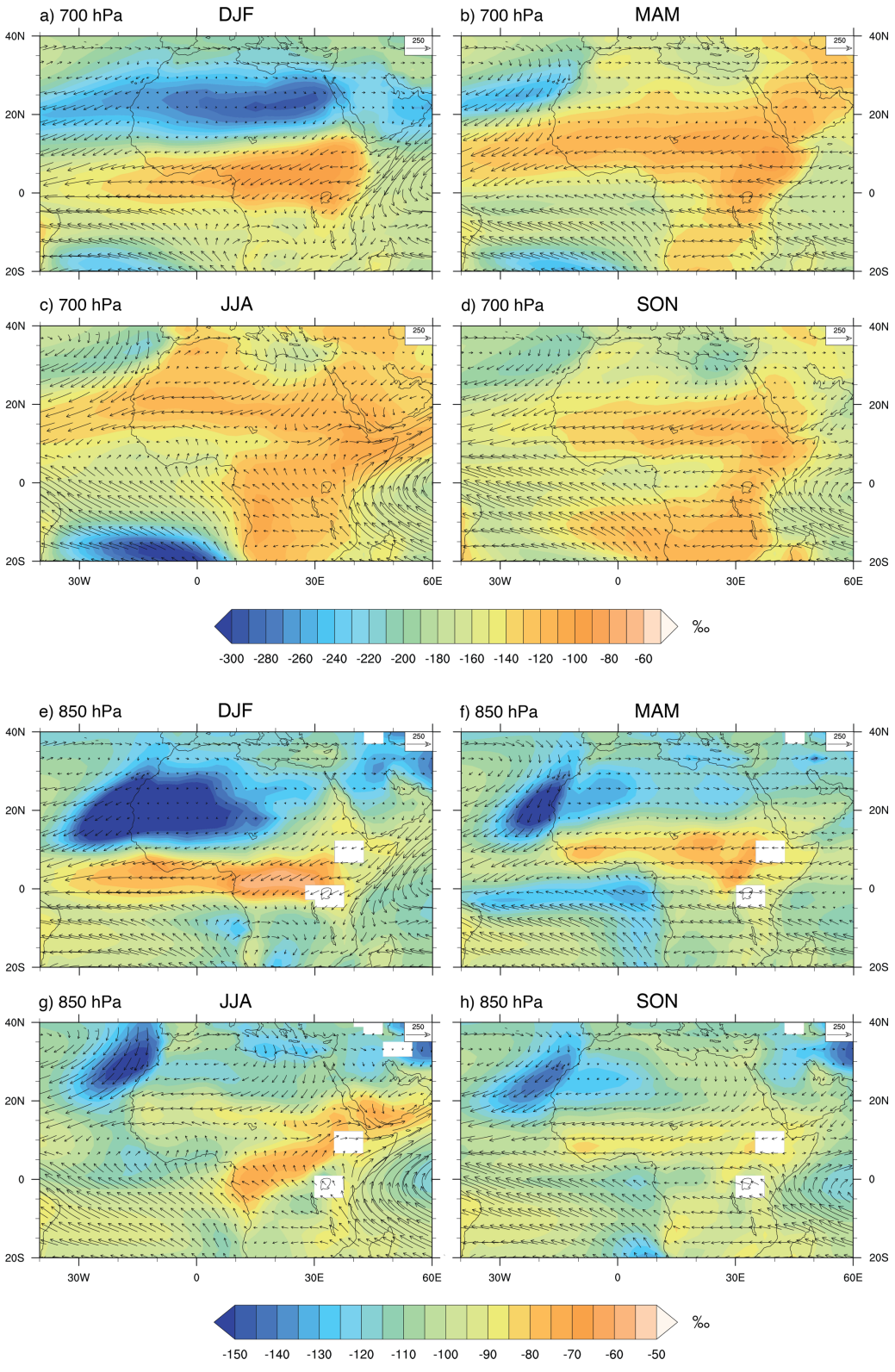

Figure S3.5. Simulated seasonally-averaged $PI_{CONTROL}$ specific humidity-weighted δD_{VAPOR} (shadings) at a-d) 700 hPa and e-h) 850 hPa and vertically-integrated moisture flux (vectors, 250 kg m^{-1} s^{-1}).

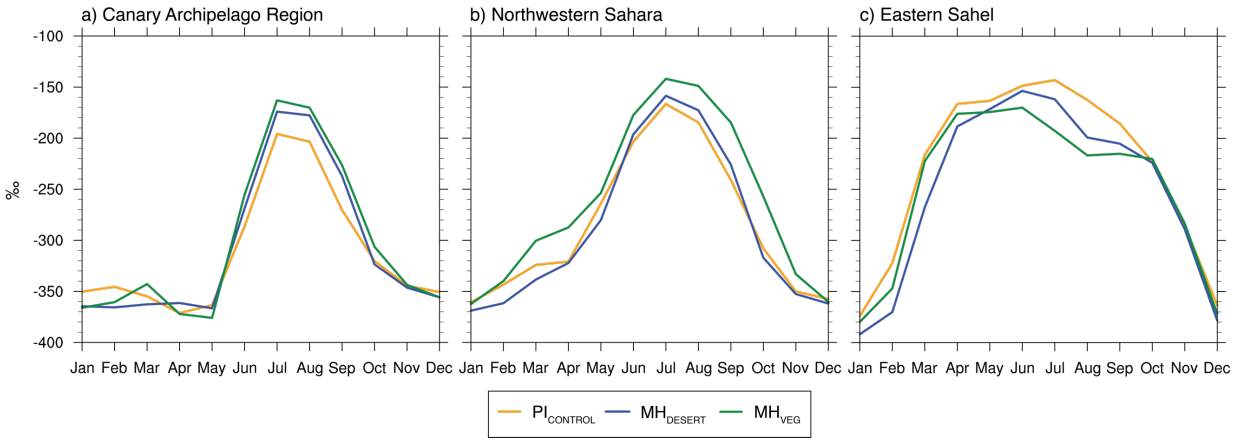

Figure S3.6. Simulated seasonal cycle of 500 hPa specific humidity-weighted δD_{VAPOR} averaged over the a) Canary Archipelago Region (27.5–29.4°N, 17.5–12.5°W), b) northwestern Sahara, and c) eastern Sahel for $PI_{CONTROL}$ (orange), MH_{DESERT} (blue), and MH_{VEG} (green). The spatial extent for the Canary Archipelago Region is derived from Lacour et al. (2017) and comparison of a) with Figure 2a in Lacour et al. (2017) demonstrates that iCESM skillfully simulates the seasonal cycle of water vapor isotopes over the eastern Atlantic Ocean.

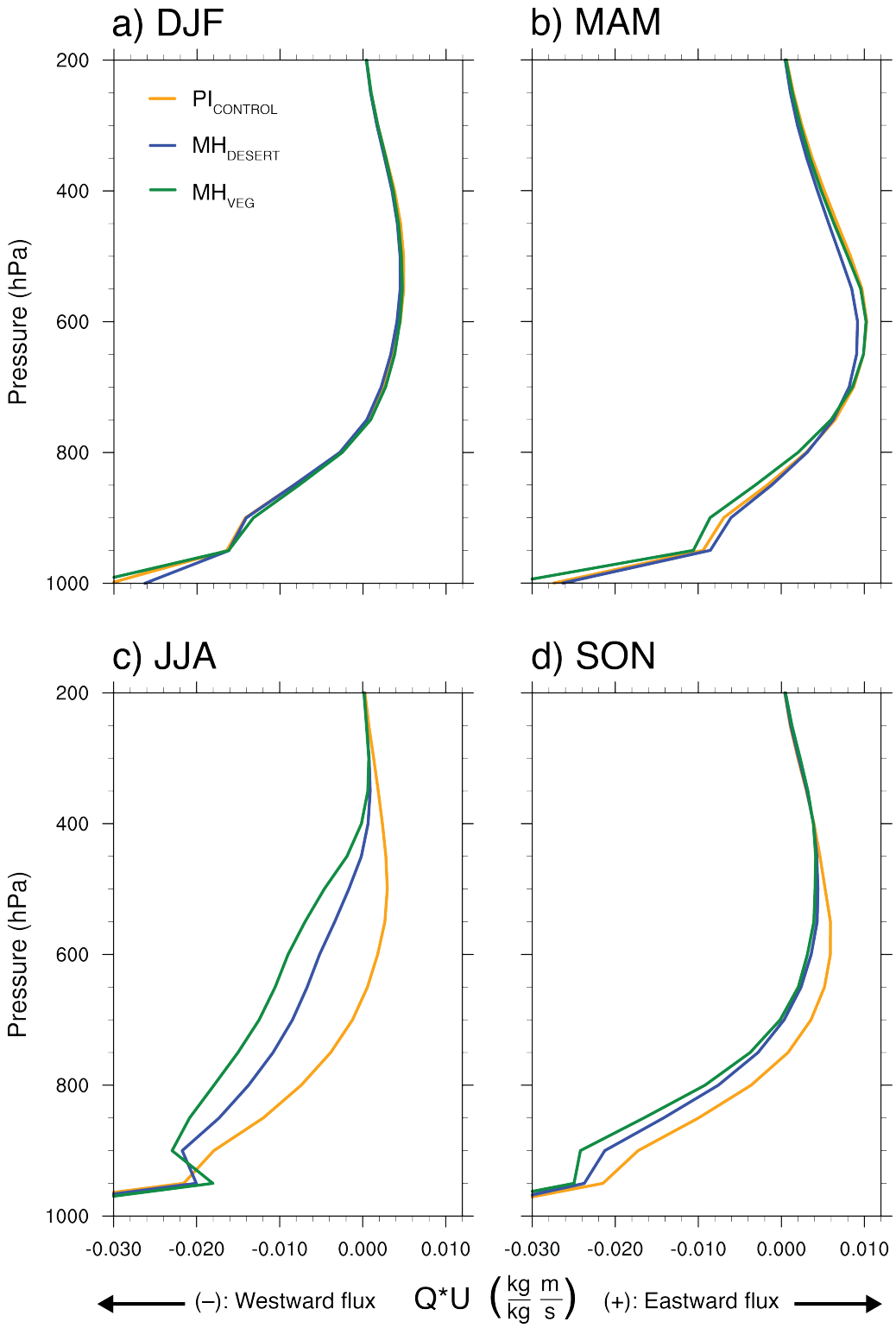

Figure S3.7. Seasonally-averaged simulated atmospheric profile of the a-d) zonal moisture flux (Q*U, kg kg^{-1} m s^{-1}) averaged over the northwestern Sahara. Negative values (leftward) indicate anomalous westward moisture flux and positive values (rightward) indicate anomalous eastward moisture flux.

References

Huang, Y., Dupont, L., Sarnthein, M., Hayes, J.M., Eglinton, G., 2000. Mapping of C4 plant input from North West Africa into North East Atlantic sediments. *Geochim. Cosmochim. Acta* 64, 3505–3513. https://doi.org/10.1016/S0016-7037(00)00445-2

Konecky, B., Dee, S.G., Noone, D.C., 2019b. WaxPSM: A Forward Model of Leaf Wax Hydrogen Isotope Ratios to Bridge Proxy and Model Estimates of Past Climate. *J. Geophys. Res. Biogeosciences* 124, 2107–2125. https://doi.org/10.1029/2018JG004708

Lacour, J., Flamant, C., Risi, C., Clerbaux, C., Coheur, P., 2017. Importance of the Saharan heat low in controlling the North Atlantic free tropospheric humidity budget deduced from IASI δ D observations. *Atmos. Chem. Phys.* 17, 9645–9663. https://doi.org/10.5194/acp-17-9645-2017

Niedermeyer, E.M., Schefuß, E., Sessions, A.L., Mulitza, S., Mollenhauer, G., Schulz, M., Wefer, G., 2010. Orbital- and millennial-scale changes in the hydrologic cycle and vegetation in the western African Sahel: insights from individual plant wax δD and δ13C. *Quat. Sci. Rev.* 29, 2996–3005. https://doi.org/10.1016/j.quascirev.2010.06.039

Sachse, D., Billault, I., Bowen, G.J., Chikaraishi, Y., Dawson, T.E., Feakins, S.J., Freeman, K.H., Magill, C.R., McInerney, F.A., van der Meer, M.T.J., Polissar, P., Robins, R.J., Sachs, J.P., Schmidt, H.-L., Sessions, A.L., White, J.W.C., West, J.B., Kahmen, A., 2012. Molecular Paleohydrology: Interpreting the Hydrogen-Isotopic Composition of Lipid Biomarkers from Photosynthesizing Organisms. *Annu. Rev. Earth Planet. Sci.* 40, 221–249. https://doi.org/10.1146/annurev-earth-042711-105535

Schefuß, E., Schouten, S., Schneider, R.R., 2005. Climatic controls on central African hydrology during the past 20,000 years. *Nature* 437, 1003–1006. https://doi.org/10.1038/nature03945

Schneider, Udo; Becker, Andreas; Finger, Peter; Meyer-Christoffer, Anja; Ziese, Markus, 2018. GPCC Full Data Monthly Product Version 2018 at 2.5°: Monthly Land-Surface Precipitation from Rain-Gauges built on GTS-based and Historical Data. https://doi.org/10.5676/DWD_GPCC/FD_M_V2018_250

Sha, L., Ait Brahim, Y., Wassenburg, J.A., Yin, J., Peros, M., Cruz, F.W., Cai, Y., Li, H., Du, W., Zhang, H., Edwards, R.L., Cheng, H., 2019. How Far North Did the African Monsoon Fringe Expand During the African Humid Period? Insights From Southwest Moroccan Speleothems. *Geophys. Res. Lett.* 46, 14093–14102. https://doi.org/10.1029/2019GL084879

Tierney, J.E., Pausata, F.S.R., DeMenocal, P.B., 2017a. Rainfall regimes of the Green Sahara. *Sci. Adv.* 3, e1601503. https://doi.org/10.1126/sciadv.1601503

Chapter 4 Constraining Hydroclimate Interpretations of the North American Monsoon Since the Last Glacial Maximum

Co-authors: Christopher J. Poulsen and Jiang Zhu

4.1 Abstract

Despite its importance for sustaining human populations and ecosystems in southwestern North America, little is understood regarding the response of the North American monsoon (NAM) to orbital-scale climate forcings since the Last Glacial Maximum (LGM). While southwestern North American proxy reconstructions of late Pleistocene and Holocene $\delta^{18}O$ of speleothem calcite ($\delta^{18}O_C$) and δD of leaf wax *n*-alkanes (δD_{WAX}) differ from reconstructions from other Northern Hemisphere monsoonal regions, their signal has been difficult to interpret due to the complex influence of seasonality and moisture source location on stable water isotope values reconstructed from a small number of continuous isotopic records from this region. Here, we investigate the orbital-scale changes in both summer and winter hydroclimate in southwestern North America from the LGM to the Preindustrial era (PI) to better understand the evolution of the NAM and its isotopic signature. We show that the North American monsoon generally increases in strength from the LGM to the PI and introduce the hypothesis that the greening of the African Sahara in the early to mid-Holocene may suppress NAM rainfall, especially at the northern fringe of the monsoon, via modifications to the local Walker circulation. This chapter provides a first-ever comparison between water isotope-enabled Earth system models and proxy reconstructions in southwestern North America to investigate NAM hydroclimate in the late Pleistocene and Holocene. Thus, this work contributes to disentangling the influences of summer and winter hydroclimate on reconstructions of $\delta^{18}O_C$ and δD_{WAX} in order to better understand the NAM evolution since the LGM.

4.2 Introduction

The North American monsoon (NAM) system provides water resources that help to sustain large populations and diverse ecosystems in the region of southwestern North America that encompasses northwestern Mexico and the southwestern United States (Adams and Comrie, 1997; Ray et al., 2007). Projections of the NAM rainfall response to future greenhouse gas (GHG) warming range widely, from little to no projected change in rainfall to large reductions by as much as 50% (Cook and Seager, 2013; Pascale et al., 2017, 2018). Thus, an improved understanding of the NAM response to climate forcings in Earth's past will help us better predict how this highly variable hydrologic system may respond to climate forcings in the future. Yet, uncertainties in our understanding of NAM evolution and its response to orbital-scale climate change since the Last Glacial Maximum (LGM, 21 ka BP; thousand years before present) preclude insight into how it may respond to future climate forcings.

The North American monsoon is used to refer to many different hydrological phenomena throughout North and Central America. Here we refer to it as the rainfall that occurs largely between June and September in northwestern Mexico and the U.S. states of Arizona and New Mexico as the development of a thermal low draws moisture from the Gulfs of California and Mexico northward along the Sierra Madre Occidental mountain range (Adams and Comrie, 1997; Barlow et al., 1998; Dominguez et al., 2016; Hu and Dominguez, 2015; Jana et al., 2018). The NAM, along with monsoon systems in Africa and Asia, comprises the Northern Hemisphere land monsoon system (Sun et al., 2019; Wang and Ding, 2008). Much of the isotopic evidence for past changes in NAM rainfall intensity comes from speleothem and leaf wax *n*-alkane proxy records.

Large uncertainties in the interpretations of these records remain an obstacle for reconstructing the NAM rainfall response to orbital-scale climate forcings. Few records from southwestern North America provide a continuous quantitative reconstruction of isotopic change (i.e., $\delta^{18}O_C$ or δD_{WAX}) since the LGM (Bhattacharya et al., 2018; Metcalfe et al., 2015). Furthermore, complexities associated with the isotopic records and relating them to changes in NAM rainfall intensity have prompted contradictory interpretations of the broadly consistent isotopic changes reconstructed by five speleothem and leaf wax *n*-alkane records (Asmerom et al., 2010, 2007; Bhattacharya et al., 2018; Truebe, 2016; Wagner et al., 2010). These challenges have been further compounded by the fact that no previous studies have compared water isotope-

enabled climate model results with those from proxy records, precluding insight into the physical mechanisms responsible for the observed isotopic change.

In comparison to the other Northern Hemisphere monsoons in Africa and Asia, reconstructions of NAM intensity since the LGM show that it may not have always varied in concert with the monsoons from these other regions. In the early and mid-Holocene (~10–5 ka), the African and Asian monsoons are thought to have been stronger than in the Preindustrial (PI) era, evidenced by negative excursions in isotopic proxy reconstructions of speleothem calcite ($\delta^{18}O_C$) and leaf wax *n*-alkanes (δD_{WAX}) (Cai et al., 2012; Collins et al., 2017; Dong et al., 2010; Tierney et al., 2017; Yuan et al., 2004). These monsoons were initially strengthened by orbitally-enhanced insolation and subsequent land surface-climate feedbacks, such as the greening of the African Sahara (Cai et al., 2012; Dong et al., 2010; Joussaume et al., 1999; Pausata et al., 2016; Thompson et al., 2021, 2019). However, speleothem and leaf wax *n*-alkane reconstructions of the NAM instead exhibit an opposite (positive) isotopic excursion during the early and mid-Holocene (Asmerom et al., 2010, 2007; Bhattacharya et al., 2018; Truebe, 2016; Wagner et al., 2010). If these isotopic reconstructions are related directly to NAM rainfall intensity through the amount effect interpretation (Dansgaard, 1964), the positive isotopic excursion suggests a weakened NAM during the early and mid-Holocene. However, interpretations of the positive isotopic excursion vary widely (Asmerom et al., 2010, 2007; Truebe, 2016; Wagner et al., 2010), representing large uncertainties in our understanding of southwestern North American hydrology from the LGM to the PI. Given that Northern Hemisphere monsoons, including the NAM, are predicted to become more intense in the early and mid-Holocene in response to orbitally-enhanced insolation, the opposing isotopic response of the NAM warrants further attention.

What could contribute to such a differing isotopic, and potentially hydrologic, response of the NAM to orbital-scale climate forcings? One possible explanation is that changes in the local and regional Walker circulation suppressed the NAM, outweighing the predicted strengthening from orbital insolation (Asmerom et al., 2007). In the modern, southwestern North America resides underneath a narrow ascending branch of the subtropical Walker circulation; however, it is directly eastward of a larger descending branch (Schwendike et al., 2014). If the Walker circulation were modified, enhanced subsidence associated with the descending branch could have potentially overwhelmed the narrow ascending branch and weakened the NAM. The greening of the African Sahara in the early and mid-Holocene, referred to as the Green Sahara, has been shown to modify

the interhemispheric Walker circulation, inducing changes in atmospheric circulation worldwide (Griffiths et al., 2020; Pausata et al., 2017a, 2017b; Tabor et al., 2020). Therefore, the Green Sahara likely had an effect on local Walker circulation and could have potentially strengthened the descending branch or weakened ascent over southwestern North America and suppressed NAM rainfall in the early and mid-Holocene. However, this mechanism has not yet been investigated for its impact on the NAM.

In addition, the link between NAM rainfall intensity and the southwestern North American isotopic proxy reconstructions may be poorly understood due to the complexity of the region's annual cycle in precipitation $\delta^{18}O$ ($\delta^{18}O_P$). In the boreal winter, rainfall is driven primarily by westerly storm tracks from the eastern Pacific and contains relatively low $\delta^{18}O_P$ values (~–11‰), whereas boreal summer rainfall comes largely from the NAM and contains relatively higher $\delta^{18}O_P$ values (~–3‰) (Asmerom et al., 2010; Eastoe and Dettman, 2016; Oster et al., 2019). Thus, greater contributions of winter rainfall theoretically contribute to more negative $\delta^{18}O_P$ values in proxy reconstructions, while greater contributions of NAM rainfall contribute to more positive values. However, on orbital time scales, increases in NAM rainfall intensity are also associated with lower $\delta^{18}O_P$ values (Oster et al., 2019), meaning that, in reconstructions, lower $\delta^{18}O_P$ may be related to either higher winter rainfall amounts or increased NAM rainfall intensity. Therefore, when analyzing isotopic proxy reconstructions from southwestern North America, isotopic evidence of changes in winter rainfall intensity may obscure that of summer rainfall, complicating the hydroclimatic interpretations from these reconstructions.

To overcome these challenges in interpreting the NAM rainfall response to orbital-scale climate forcings, we use simulations of the water isotope-enabled Community Earth System Model (iCESM1.2) at time slices between the LGM and PI to reconstruct hydroclimate in southwestern North America. We analyze how the combined changes in $\delta^{18}O$ and δD of precipitation and soil (i.e., $\delta^{18}O_P$, $\delta^{18}O_S$, δD_P, δD_S), rainfall, and temperature during both the summer and winter contribute to isotopic reconstructions from five continuous speleothem and leaf wax *n*-alkane proxy records in this region. In addition, we investigate how the greening of the African Sahara may weaken the early and mid-Holocene NAM and improve agreement between our model simulations and proxy reconstructions.

Table 4.1. Full list of the simulations run in this study and their respective specifications and boundary conditions.

Simulation	*Years Run*	*Orbit Year*	*CO_2 (ppm)*	*CH_4 (ppb)*	*N_2O (ppb)*	*Global ice cover (%)*	*Saharan vegetation*	*Global dust optical depth*
$PI_{CONTROL}$	900	1850 CE	284.7	791.6	275.7	9.15	Desert	0.023
3ka	900	3 ka BP	275.0	580.0	270.0	8.73	Desert	0.021
$6ka_{ORB}$	400	6 ka BP	264.4	597.0	262.0	8.86	Desert	0.020
$6ka_{GS}$	200	6 ka BP	264.4	597.0	262.0	8.86	Vegetated	0.004
$9ka_{ORB}$	300	9 ka BP	260.2	658.5	255.0	9.29	Desert	0.053
$9ka_{GS}$	900	9 ka BP	260.2	658.5	255.0	9.29	Vegetated	0.004
12ka	900	12 ka BP	252.6	477.9	235.6	11.26	Desert	0.020
14ka	900	14 ka BP	238.2	636.8	255.4	15.89	Desert	0.023
16ka	900	16 ka BP	223.8	451.6	199.1	17.65	Desert	0.024
18ka	900	18 ka BP	190.0	370.0	245.0	18.93	Desert	0.025
21ka	900	21 ka BP	190.0	375.0	200.0	19.23	Desert	0.026

4.3 Methods

4.3.1 Climate model simulations

We ran simulations of the fully coupled water isotope-enabled Community Earth System Model version 1.2 (iCESM1.2; Brady et al., 2019) at nine different time slices at ~2–3 ka intervals between the LGM and the PI. A full list of the simulations and their respective greenhouse gas configurations can be found in Table 4.1. iCESM1.2 is comprised of the Community Atmosphere Model version 5 (iCAM5; Nusbaumer et al., 2017), Community Land Model version 4 (iCLM4; Wong et al., 2017), Community Ice Code version 4.0 (iCICE4), Parallel Ocean Program version 2 (iPOP2), River Transport Model, and a coupler connecting them (Hurrell et al., 2013). iCAM5 has 30 vertical levels and iCLM4 has 15 soil-column layers; both were run with a grid resolution of 1.9°×2.5°. iPOP2 was run with nominal 1° resolution. Each simulation consists of GHG concentrations and ice sheet reconstruction from the ICE-6G (Peltier et al., 2015) in conjunction with its respective orbit year (Figure 4.1). The length, in model years, of each simulation is shown in Table 4.1 and climatologies were calculated from the last 100 years of each simulation. The 6 ka simulations were branched from an original 900-year simulation with 6 ka boundary conditions (see Chapter 5 Thompson et al., submitted to *Science Advances*), and the simulation referred to as $9ka_{ORB}$ was branched from $9ka_{GS}$. The top-of-atmosphere energy imbalance for each simulation over this averaging period was <0.1 W/m^2. Climate variables calculated from these model simulations have been weighted by the change in fraction of each month to account for the paleo calendar effect (Bartlein and Shafer, 2019).

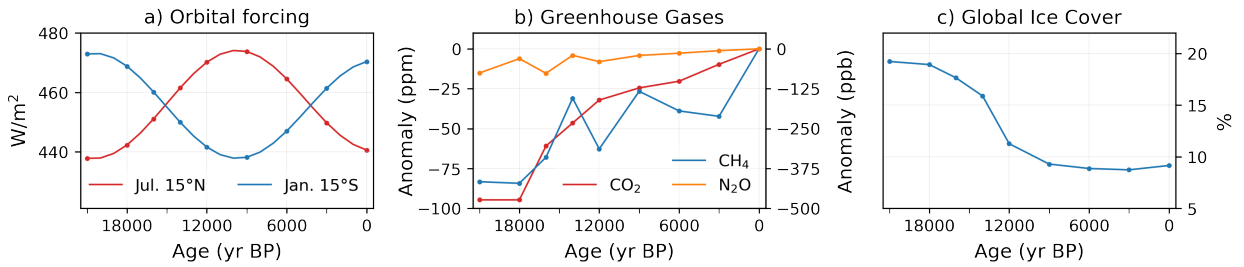

Figure 4.1. Specifications for a) orbital forcing, b) greenhouse gases (CO_2: ppm; CH_4 and N_2O: ppb), and c) global percentage of ice cover used in the iCESM1.2 time slice simulations. Small dots indicate values at each time slice. Values in a) are derived from Berger & Loutre (1991).

From ~11.7 to 5 ka, a host of geochemical proxy evidence suggests an expansion in shrub and grassland vegetation (i.e., greening) throughout the African Sahara (Bartlein et al., 2011; deMenocal et al., 2000; Hoelzmann et al., 1998; Jolly et al., 1998; McGee et al., 2013; Tierney et al., 2017). To account for these changes in our time slice simulations at 9 and 6 ka, we incorporated PMIP4 Tier 2 protocol (Otto-Bliesner et al., 2017) in two experiments entitled "*9ka*$_{GS}$" and "*6ka*$_{GS}$" (GS = "Green Sahara") where we replaced bare ground desert with 100% shrub at ~10–25°N and 100% C_4 grass at 25–35°N (see Chapter 5 Thompson et al., submitted to *Science Advances*, for detailed information on these simulations). We darkened soil color to account for changes suggested in Levis et al. (2004) by decreasing average surface albedo in northern Africa by ~0.13 (Oleson et al., 2010). We prescribed seasonally varying values of leaf area index over the Sahara with summer values reaching as high as 3.0 for shrub and 1.5 for grass. All other simulations used in this study (*PI*$_{CONTROL}$, *3ka*, *6ka*$_{ORB}$, *9ka*$_{ORB}$, *12ka*, *14ka*, *16ka*, *18ka*, *21ka*) contained the appropriate orbital, GHG, and ice cover changes for their respective time periods (Table 4.1), but had vegetation (i.e., plant functional type, soil color, and leaf area index) that was roughly consistent with the PI extent. Increased vegetation cover in the Sahara also reduced dust aerosol loading in *9ka*$_{GS}$ and *6ka*$_{GS}$ (Table 4.1). In these simulations, prescribed leaf area index exceeded values of 0.3 throughout the Sahara and prohibited dust from mobilizing from its land surface.

In our calculation of simulated isotopic values, we weighted simulated values of $\delta^{18}O_P$ and δD_P by precipitation amount. Values of $\delta^{18}O_S$ were weighted by soil water amount at 10 cm depth for comparison with speleothem records. Values of δD_S were weighted by both soil water amount and the plant rooting depth fraction for comparison with leaf wax *n*-alkane records. Because iCESM1.2 simulates high rainfall amounts at the onset and decline of the NAM in comparison

with present-day reanalysis data from Global Precipitation Climatology Centre (GPCC) (Figure 4.2a), we investigate the seasonality in NAM hydroclimate by displaying the average winter (DJFMAM) and summer (JJASON) climate in 4.4 Results. Previous studies have generally shown that climate models can reproduce changes in climate exhibited by proxy records in southwestern North America, but the overall magnitude of these changes is often too small (Harrison et al., 2015). For example, Paleoclimate Model Intercomparison Project (PMIP3) models underestimate the magnitude of North American rainfall inferred from proxies (Braconnot et al., 2012; Hermann et al., 2018). Therefore, we focus our comparison between iCESM1.2 and proxy reconstructions on the sign of the anomaly with respect to the PI and the direction of trends, which are informative regardless of whether the total magnitude of these model changes agrees with proxy data or not.

Table 4.2. List of proxy records used in this study.

Record Name	Type	Temporal coverage	Latitude	Longitude	Reference
Fort Stanton Cave	Speleothem	11.3–21 ka BP	33.50°N	105.20°W	Asmerom et al. (2010)
Pink Panther Cave	Speleothem	0–12.1 ka BP	32.08°N	105.17°W	Asmerom et al. (2007)
Cave of the Bells	Speleothem	11.5–21 ka BP	31.43°N	110.47°W	Wagner et al. (2010)
Cave of the Bells	Speleothem	0–7.1 ka BP	31.43°N	110.47°W	Truebe et al. (2016)
Guaymas Basin	Leaf wax	1.6–21 ka BP	27.48°N	112.10°W	Bhattacharya et al. (2018)
Mexican Margin	Leaf wax	1.5–21 ka BP	22.23°N	107.05°W	Bhattacharya et al. (2018)

4.3.2 Speleothem and leaf wax *n*-alkane proxy records

We compared our iCESM1.2 simulations with five speleothem and leaf wax *n*-alkane records from southwestern North America (Table 4.2). The speleothem records came from three separate caves (Cave of the Bells, Pink Panther Cave, and Fort Stanton Cave) that spanned discontinuously from 21 ka to the present (Figure 4.3a) (Asmerom et al., 2010, 2007; Truebe, 2016; Wagner et al., 2010). Interpretations of the sign of orbital-scale isotopic changes and their relation to summer monsoon rainfall intensity have been contradictory, with previous studies suggesting that more positive values of $\delta^{18}O_C$ either indicated higher (Truebe, 2016) or lower NAM rainfall amounts (Asmerom et al., 2010, 2007; Wagner et al., 2010). The leaf wax *n*-alkane records came from two locations in the Gulf of California and spanned continuously from 21 to ~1.5 ka (Figure 4.3c) (Bhattacharya et al., 2018). These records have been interpreted as showing the contribution of June–September (JAS) rainfall to the annual total, with more positive values of

δD_{WAX} interpreted as higher JAS rainfall percentage (Berke et al., 2015; Bhattacharya et al., 2018). As such, these records have broadly been interpreted as showing that NAM rainfall gradually increased in intensity since the LGM.

To capture the spatial region that encompasses these five records, we calculated model averages over the region 20–35°N and 115–100°W, hereafter referred to as the NAM region (red box in Figure 4.4). To account for spatial uncertainties, we compare averages of terrestrial grid cells within this domain with the speleothem reconstructions and averages of coastal grid cells within this domain with the leaf wax *n*-alkane reconstructions (Figure 4.5).

4.3.3 Proxy system modeling

For direct comparison with speleothem and leaf wax *n*-alkane records, we simulated values of $\delta^{18}O_C$ and δD_{WAX} at each time slice using the proxy system models PRYSM (Dee et al., 2015) and WaxPSM (Konecky et al., 2019), respectively, along with inputs from iCESM1.2. To simulate $\delta^{18}O_C$ (thick lines in Figure 4.3b), we used seasonal mean $\delta^{18}O_P$, $\delta^{18}O_S$, and annual mean surface temperature as inputs for the PRYSM speleothem sensor model. We specified the well-mixed aquifer recharge model with a mean transit time of 0.5 years for our PRYSM simulations (Dee et al., 2015). In order to test the dependence of simulated $\delta^{18}O_C$ values on changes in temperature, we also performed calculations that reduced the change in annual mean surface temperature between each time slice and the PI by 50% (thin lines in Figure 4.3b), in accordance with inferences that only as much as half of the variability in southwestern North American speleothem $\delta^{18}O_C$ values can be explained by changes in temperature (Asmerom et al., 2010; Wagner et al., 2010). To simulate δD_{WAX}, we used seasonal mean δD_P and δD_S as inputs and corrected for vegetation type by weighting the apparent fractionation factor by the vegetation fraction and its corresponding apparent fractionation value (Konecky et al., 2019). The simulated results from WaxPSM reflect those of C_{29} *n*-alkanes. This follows the method used in Thompson et al. (2021).

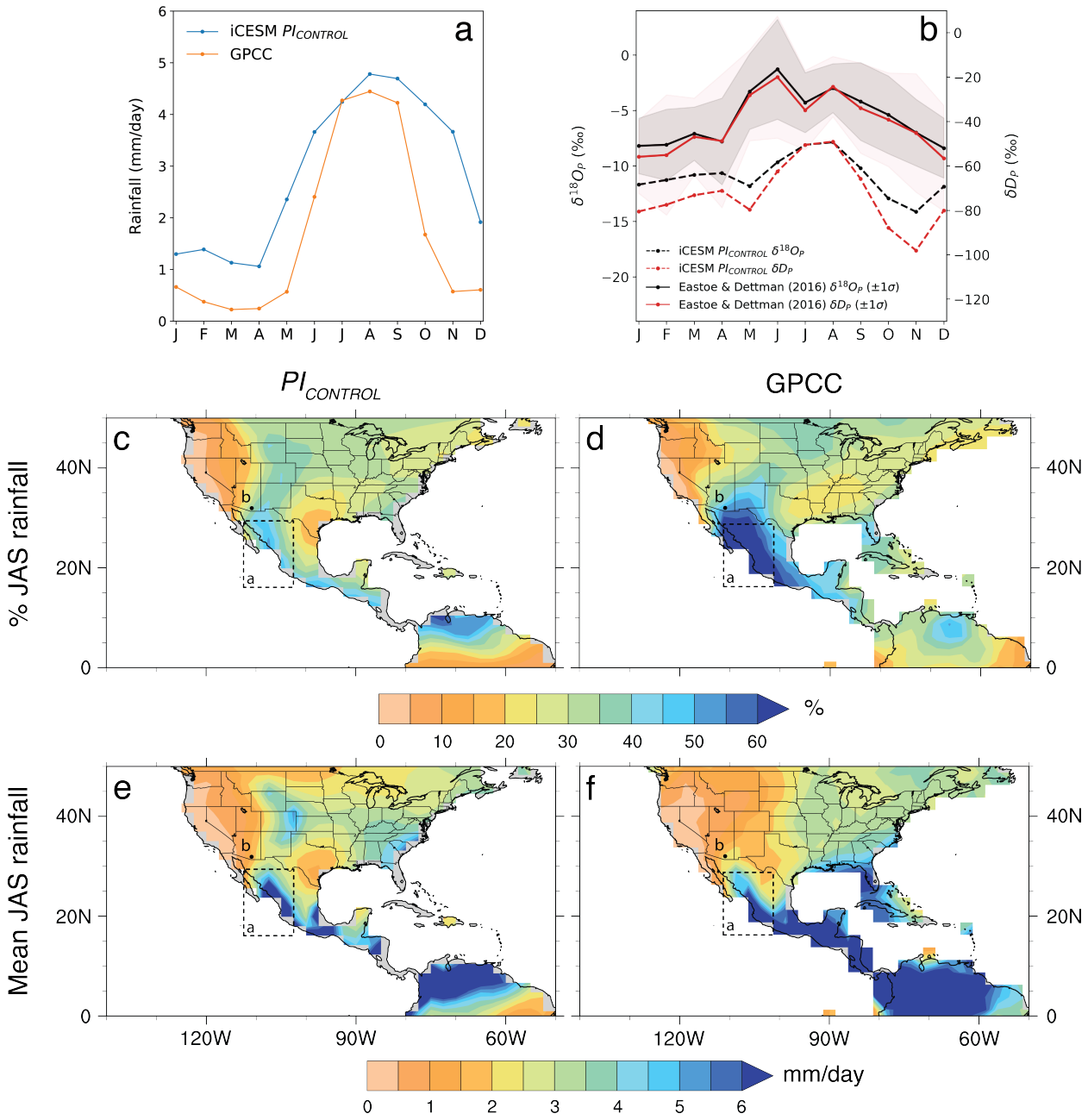

Figure 4.2. Comparison between iCESM simulation of the North American monsoon and modern rainfall and isotopic data. Seasonal cycles are shown for a) rainfall from iCESM $PI_{CONTROL}$ (blue) and Global Precipitation Climatology Centre (GPCC) reanalysis data (orange) averaged over ~16–29°N, 102–113°W, the core of the NAM in GPCC, and b) $\delta^{18}O_P$ (black) and δD_P (red) from iCESM $PI_{CONTROL}$ at ~31.3°N, 110°W (dashed lines) and average rainfall isotopic data for 1986–2012 (solid lines; Eastoe and Dettman, 2016) from Tucson, AZ. The percentage of annual rainfall that occurs during the months June–September and mean annual rainfall are shown for c) and e) $PI_{CONTROL}$ and d) and f) GPCC reanalysis data. Dashed boxes in c)–f) illustrate averaging regions used in a) for $PI_{CONTROL}$ and GPCC reanalysis data and dots in c)–f) illustrate location of b). GPCC reanalysis data is averaged over the time period 1960–2010. **Main takeaway:** iCESM1.2 is an appropriate tool for exploring the large-scale hydrologic and isotopic changes in southwestern North America on orbital time scales.

4.4 Results

4.4.1 Model evaluation of the North American monsoon

Based on comparison with GPCC reanalysis data, we find that iCESM1.2 reasonably simulates the large scale seasonal and spatial features of hydroclimate in southwestern North America (Figure 4.2). Simulated rainfall in $PI_{CONTROL}$ exhibits a NAM rainfall peak in August in excess of 4 mm/day, closely matching GPCC data. However, our simulated seasonal cycle shows that iCESM1.2 produces mean rainfall amounts higher than GPCC at the onset and decline of the monsoon (May–June and October–November). As a result, the contribution of JAS rainfall, which is often used as an indicator of NAM strength (Adams and Comrie, 1997; Metcalfe et al., 2015), is lower in iCESM1.2 than GPCC (Figure 4.2c-d); yet, our simulated mean rainfall amount in iCESM1.2 closely matches GPCC (Figure 4.2e-f). This is why we use JJASON and DJFMAM to represent the summer and winter seasons throughout the remainder of our results.

Simulated precipitation isotopic values ($\delta^{18}O_P$ and δD_P) also reasonably match modern values (Figure 4.2b). The magnitude of seasonal changes in $\delta^{18}O_P$ and δD_P in $PI_{CONTROL}$, where summer values are ~6–7 and ~30–50‰ higher than winter values, broadly matches the seasonal cycle of modern precipitation isotopes centered over Tucson, Arizona. There is a depleted bias year-round in iCESM1.2, but we largely minimize its impact by analyzing seasonal averages (JJASON and DJFMAM) and differences between time slice simulations.

Due to the relatively coarse resolution of our simulations (1.9°×2.5°), we do not capture finer scale processes associated with the NAM (Meyer and Jin, 2017); however, we determine from our comparison with GPCC that iCESM1.2 is an appropriate tool for exploring the large scale hydrologic and isotopic changes in southwestern North America on orbital time scales. This determination is also made in a previous study using a similar version of CESM1.2 that does not include water isotope tracers (Bhattacharya et al., 2018).

Through comparison of our simulated $\delta^{18}O_C$ and δD_{WAX} values with speleothem and leaf wax *n*-alkane records, we demonstrate that the modeled results utilizing precipitation and soil water isotopes as inputs broadly match the trend from the LGM to the PI in reconstructed $\delta^{18}O_C$ and δD_{WAX}. However, biases related to the temperature assumptions used in proxy system models contribute to large uncertainties and poor agreement between some model and proxy reconstructions (Figure 4.3). We provide further discussion on the potential uncertainties

contributing to these simulated results and their agreement, or disagreement, with proxy reconstructions of $\delta^{18}O_C$ and δD_{WAX} in 4.5 Discussion.

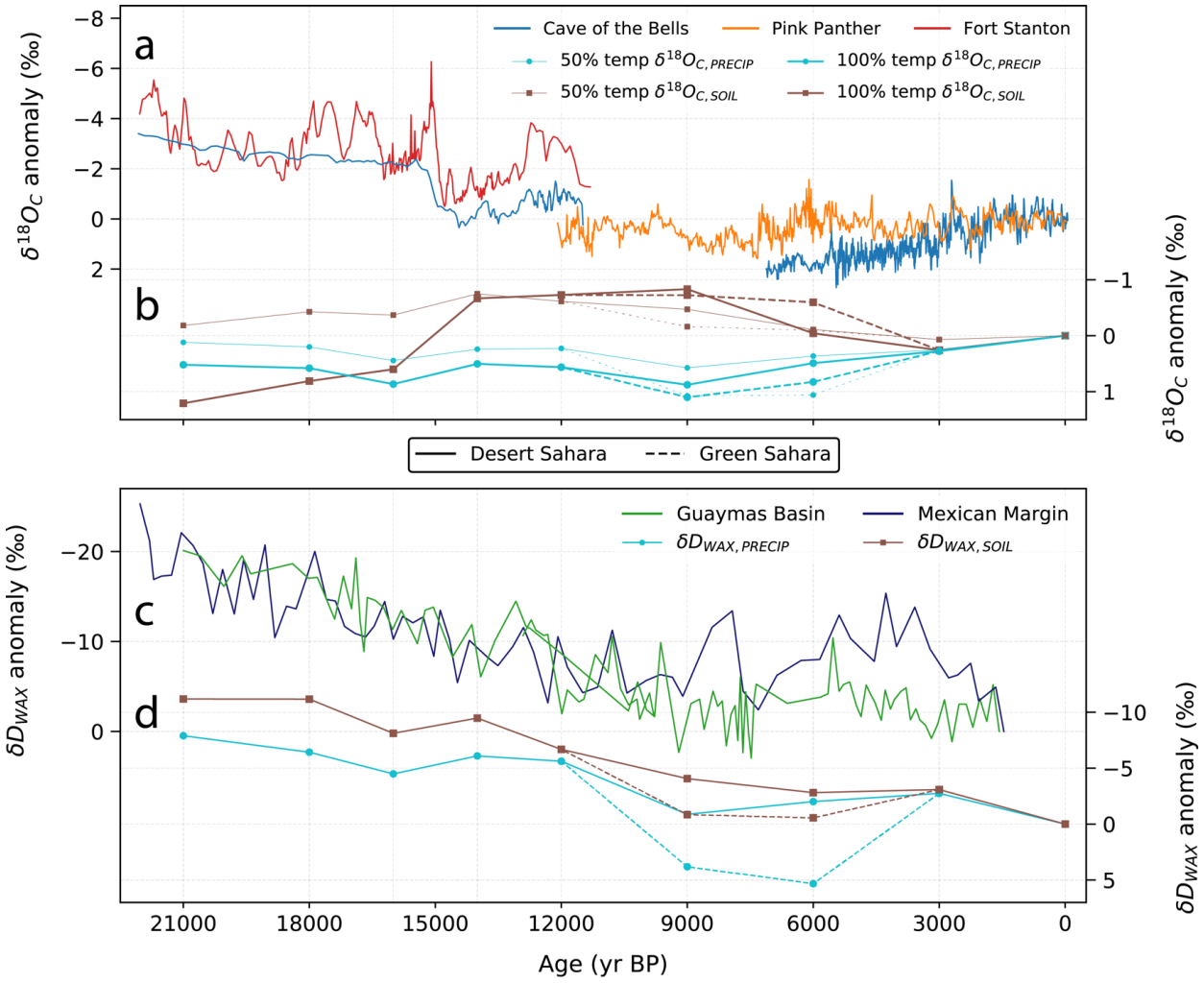

Figure 4.3. Comparison of anomalies, relative to the PI (1850 CE), from a) speleothem reconstructions of $\delta^{18}O_C$, b) model-simulated $\delta^{18}O_C$, c) leaf wax *n*-alkane reconstructions of δD_{WAX}, and d) model-simulated δD_{WAX}. Values of $\delta^{18}O_C$ in b) are simulated with the proxy system model PRYSM (Dee et al., 2015) using iCESM1.2 inputs of mean annual surface temperature and JJASON mean $\delta^{18}O_P$ (thick blue) and $\delta^{18}O_S$ (thick brown). Annual mean surface temperature anomaly relative to $PI_{CONTROL}$ is reduced in magnitude by 50% to provide a theoretical cave temperature input in line with Asmerom et al. (2010) for values shown by thin lines in b). Values of δD_{WAX} in d) are simulated with the proxy system model WaxPSM (Konecky et al., 2019) using iCESM1.2 inputs of JJASON mean δD_P (blue) and δD_S (brown). Simulated values are averages of b) terrestrial grid cells and d) coastal grid cells within our defined NAM region. The solid lines in b) and d) represent simulations that use the PI extent of vegetation (i.e., desert Sahara), whereas the dashed lines represent simulations that include a Green Sahara. **Main takeaway**: Simulated values of $\delta^{18}O_C$ and δD_{WAX} generally align with the proxy reconstructions, depending on the treatment of temperature in the speleothem proxy system model.

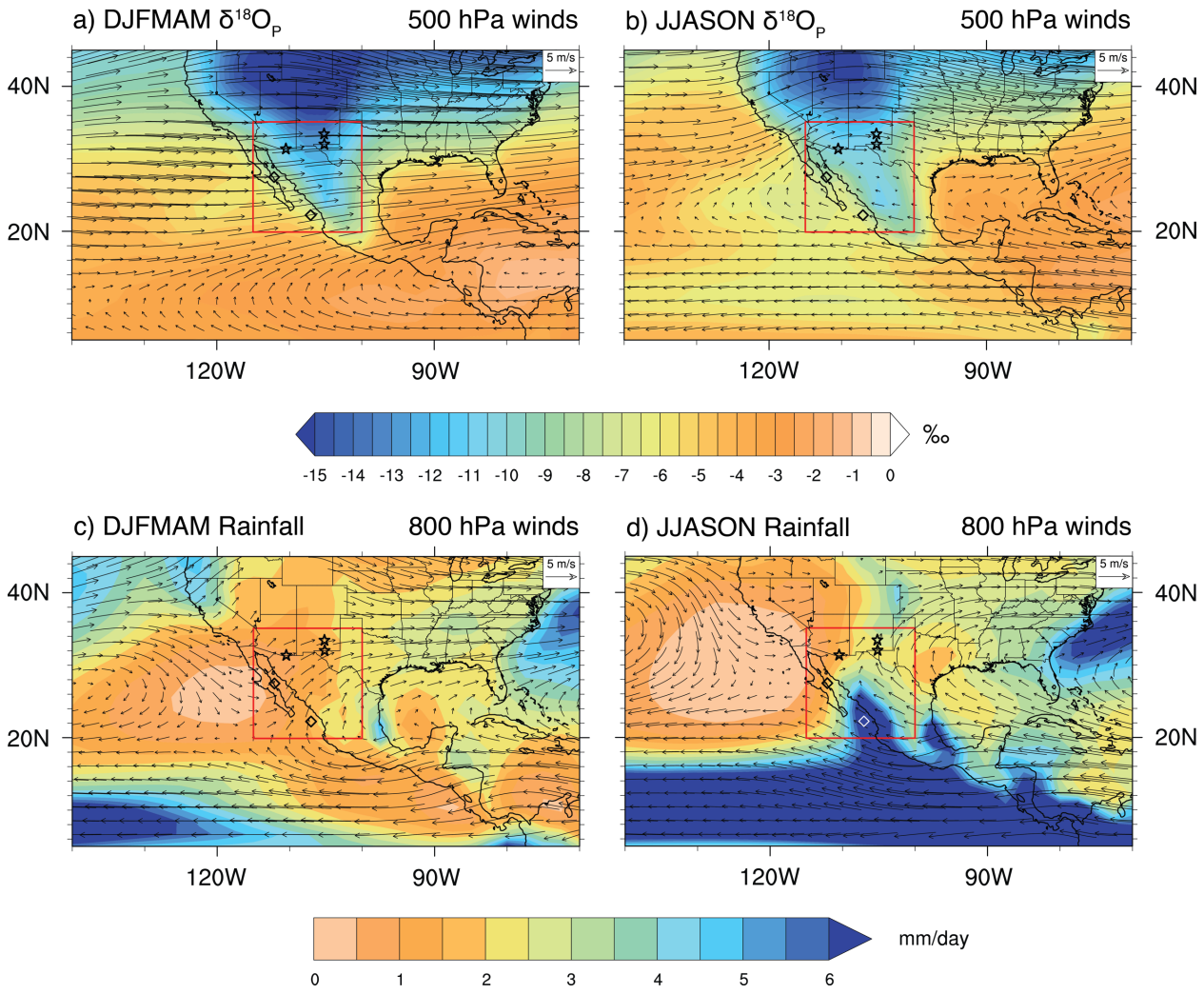

Figure 4.4. Simulated a) and c) winter (DJFMAM) and b) and d) summer (JJASON) rainfall amount weighted $\delta^{18}O_P$, with 500 hPa wind vectors, and mean rainfall, with 800 hPa wind vectors, for $PI_{CONTROL}$. Box indicates NAM region extent and stars (speleothem) and diamonds (leaf waxes) show proxy record locations. **Main takeaway:** This figure shows winter and summer atmospheric dynamics in the PI, providing a reference for subsequent figures.

4.4.2 Preindustrial atmospheric dynamics in southwestern North America

For comparison with the results in the following sections, we highlight the relevant winter (DJFMAM) and summer (JJASON) atmospheric dynamics in our PI simulation ($PI_{CONTROL}$). In the winter, low- and mid-level westerly wind flow associated with the North Pacific High advects moisture from the eastern Pacific to southwestern North America, resulting in a simulated NAM region mean of ~1.4 mm/day (Figure 4.4). This advected moisture contains relatively low precipitation isotopic values (NAM region winter $\delta^{18}O_P$ low of ~–11.2‰ in December) that extend south along the continental interior to 20°N (note low values in Figure 4.4a indicated by blue

shading). In the summer, southeasterly flow, as an extension of the Bermuda High to the east and intertropical convergence zone to the south, advects moisture from the Gulfs of Mexico and California into the NAM region, producing simulated NAM region mean rainfall of ~2.9 mm/day (Figure 4.4d). Anticyclonic flow at 500 hPa, centered on our defined NAM region, draws this moisture northward and is bordered on the west by drier air associated with the North Pacific High (Figure 4.4b,d). The southerly moisture flux contains continental precipitation isotopic values that are slightly higher than during the winter (NAM region summer $\delta^{18}O_P$ high of ~–6.7‰ in July); however, over the ocean in the southernmost area of our defined NAM region and south of 20°N, precipitation isotopic values are lower than during the winter (orange values in 4.4a versus yellow values in 4.4b) due to high rainfall amounts associated with the NAM and intertropical convergence zone (Figure 4.4d). The higher versus lower precipitation isotopic values over southwestern North America in $PI_{CONTROL}$ highlights the competing effects of seasonality and rainfall intensity on precipitation isotopic values that has thus far complicated interpretations from proxy reconstructions of $\delta^{18}O_C$ and δD_{WAX} (Asmerom et al., 2010; Oster et al., 2019).

4.4.3 Late Pleistocene evolution of the North American monsoon

Compared to $PI_{CONTROL}$, our late Pleistocene (*21ka* to *12ka*) simulations showcase a weaker NAM and slightly higher winter rainfall amounts (Figure 4.5). In accordance with previous studies (Asmerom et al., 2010; Bhattacharya et al., 2018, 2017; Wagner et al., 2010), we attribute these results to changes in Laurentide Ice Sheet cover and its effect on westerly moisture fluxes. From 21 to 12 ka, the Laurentide Ice Sheet gradually receded northward (Peltier et al., 2015), resulting in simulated warming of ~5°C in our defined NAM region (Figure 4.5d,h). The northward recession of ice impacts the westerly storm track, which is in a more southerly position during the LGM, by shifting it northward throughout the late Pleistocene (Figures 4.6 and 4.7). Over the defined NAM region in our *21ka* simulation, anomalous westerlies can be seen at low-levels (800 hPa) in the winter (Figure 4.6i) and mid-levels (500 hPa) in both the winter and summer (Figure 4.7i,j). In the subsequent simulations from *18ka* to *12ka*, these westerlies gradually weaken over the NAM region and shift northward (note disappearance of westerly wind anomalies from *21ka* to *12ka* simulations in DJFMAM plots in Figures 4.6 and 4.7), resulting in a weaker westerly moisture flux (Figure 4.8). By our *12ka* simulation, westerlies largely disappear and give way to mid-level southeasterly anomalies during the summer (Figures 4.7b and 4.8b).

As a result of the strong westerly moisture flux, summer rainfall in our *21ka* simulation is lower than in $PI_{CONTROL}$, most prominently by ~0.7 mm/day along the coastal region (Figure 4.5g). This corresponds with decreases relative to $PI_{CONTROL}$ in the percentage of summer relative to annual rainfall (i.e., JJASON/ANNUAL) of ~4% and 9% in the terrestrial and coastal areas of the NAM region, respectively (Figure 4.9). Summer rainfall totals gradually increase by ~1.1 mm/day along the coast of the NAM region from *21ka* to *12ka* (Figure 4.5 and JJASON plots in Figure 4.6) in conjunction with the increase in summer rainfall percentage (Figure 4.9) and enhanced southeasterly flow (JJASON plots in Figure 4.7). Conversely, winter rainfall in *21ka* is ~0.2 to 0.3 mm/day higher than $PI_{CONTROL}$ (Figure 4.5c,g) and remains relatively stable through the late Pleistocene simulations.

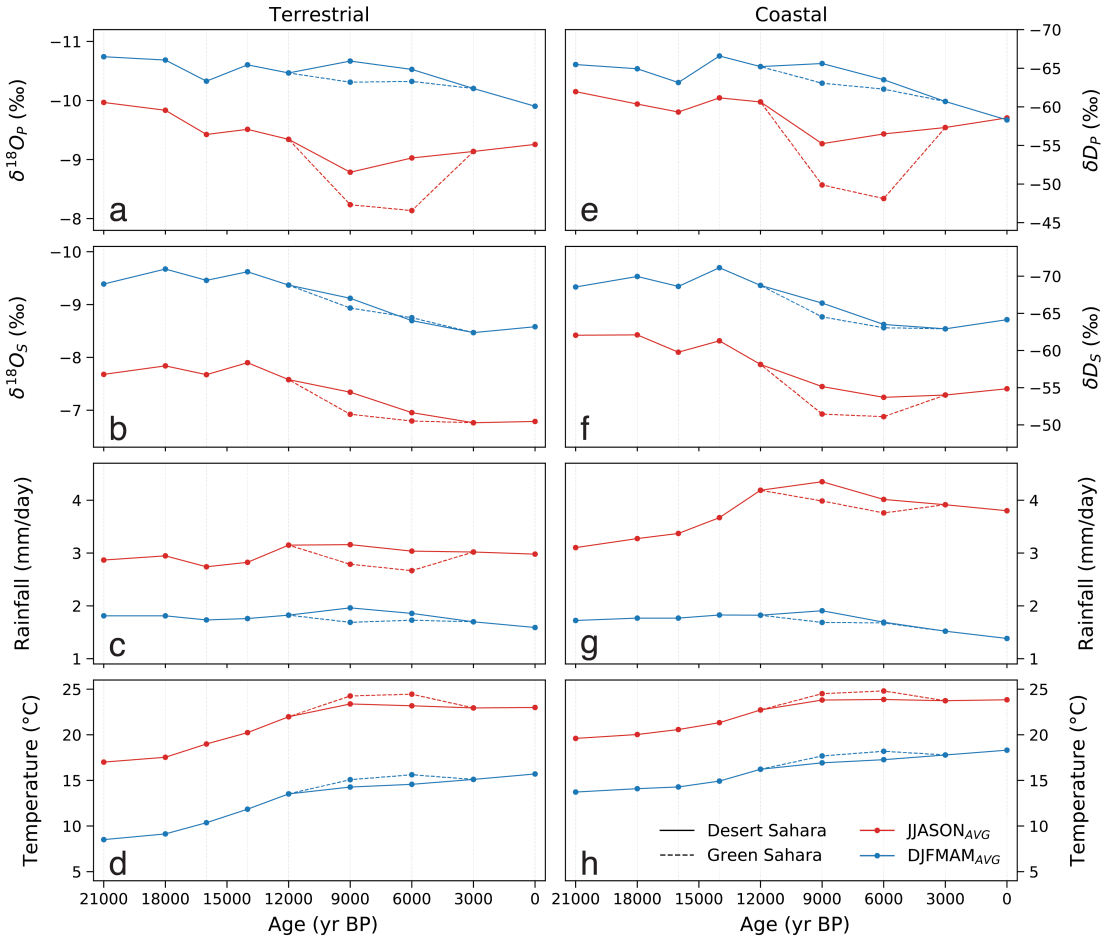

Figure 4.5. Simulated precipitation and soil water $\delta^{18}O/\delta D$, rainfall, and surface temperature for a)–d) terrestrial grid cells and e)–h) coastal grid cells in our defined NAM region during the summer (JJASON; red) and winter (DJFMAM; blue). The solid lines represent simulations that use the PI extent of vegetation (i.e., desert Sahara), whereas the dashed lines represent simulations that include a Green Sahara. **Main takeaway:** This figure shows the evolution of summer and winter climate from the LGM to the PI, indicating the contribution of summer and winter climate to the corresponding isotopic signals.

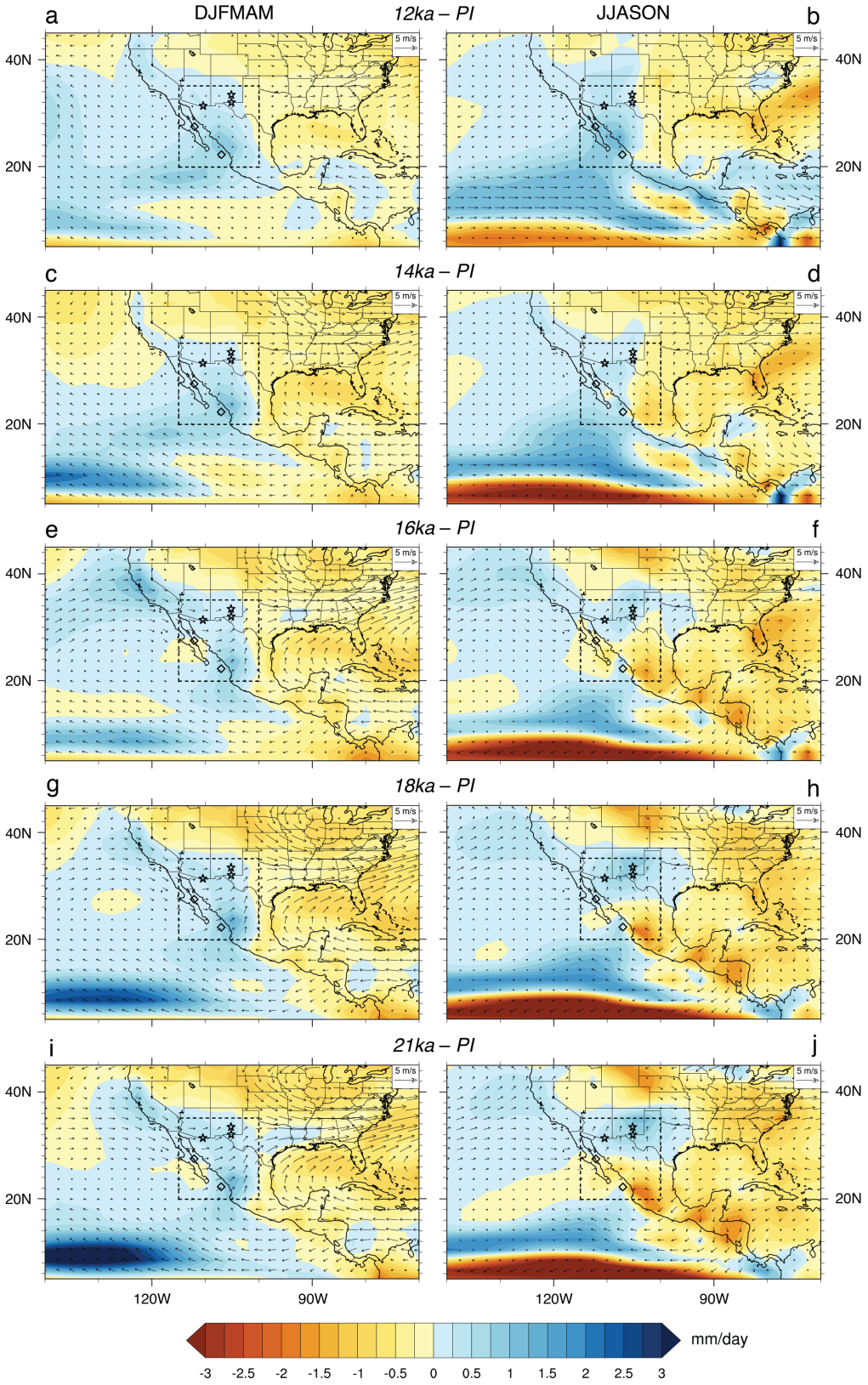

Figure 4.6. Simulated late Pleistocene winter (DJFMAM) and summer (JJASON) anomalies of rainfall (mm/day) and 800 hPa wind vectors (m/s) relative to *PI*$_{CONTROL}$. Description of dashed line, stars, and diamonds can be found in Figure 4.4. **Main takeaway:** Coastal summer rainfall gradually increases while winter rainfall remains stable.

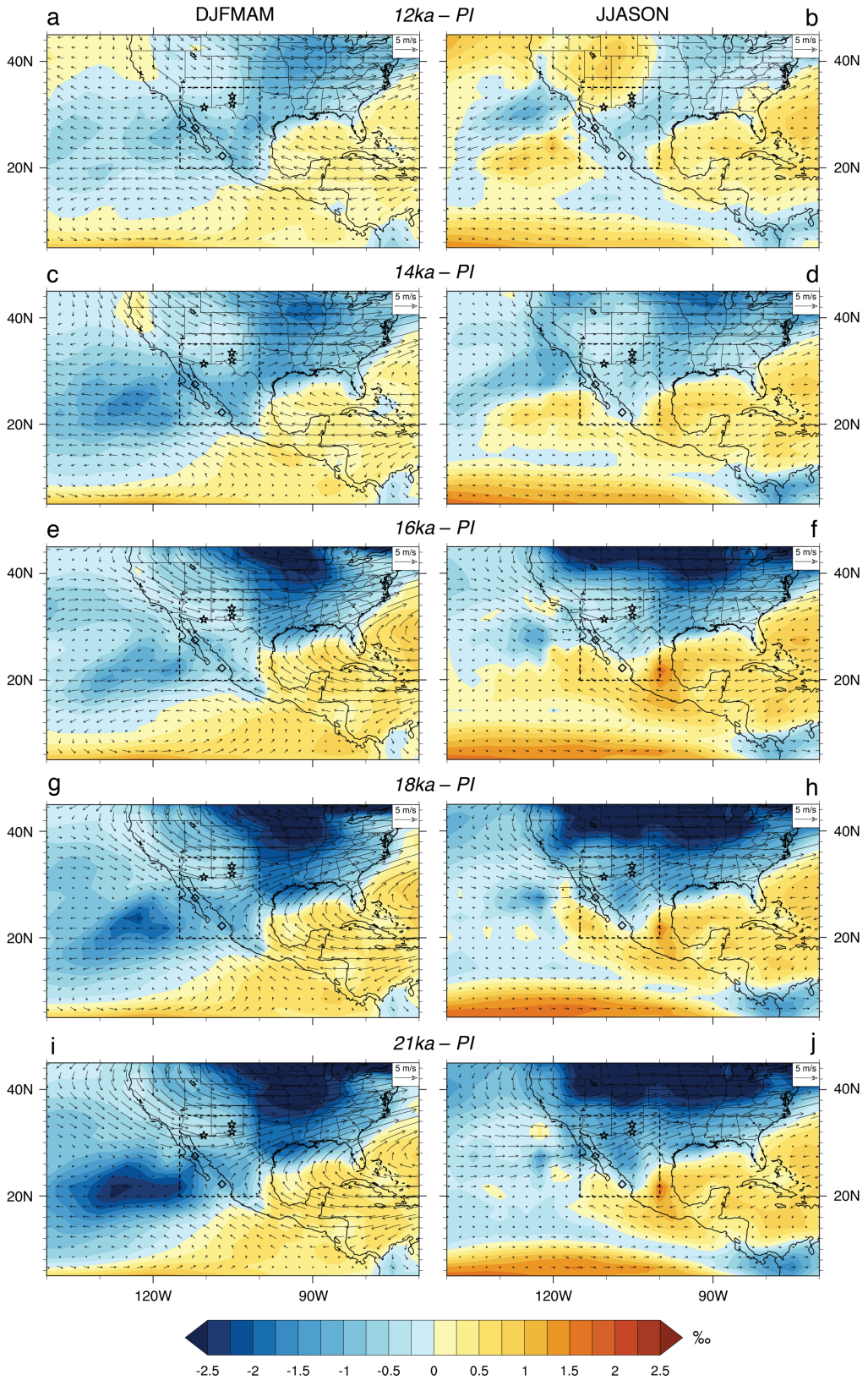

Figure 4.7. Same as Figure 4.6 but for $\delta^{18}O_P$ (‰) and 500 hPa wind vectors (m/s). **Main takeaway:** $\delta^{18}O_P$ anomalies are negative and exhibit a positive trend throughout the late Pleistocene.

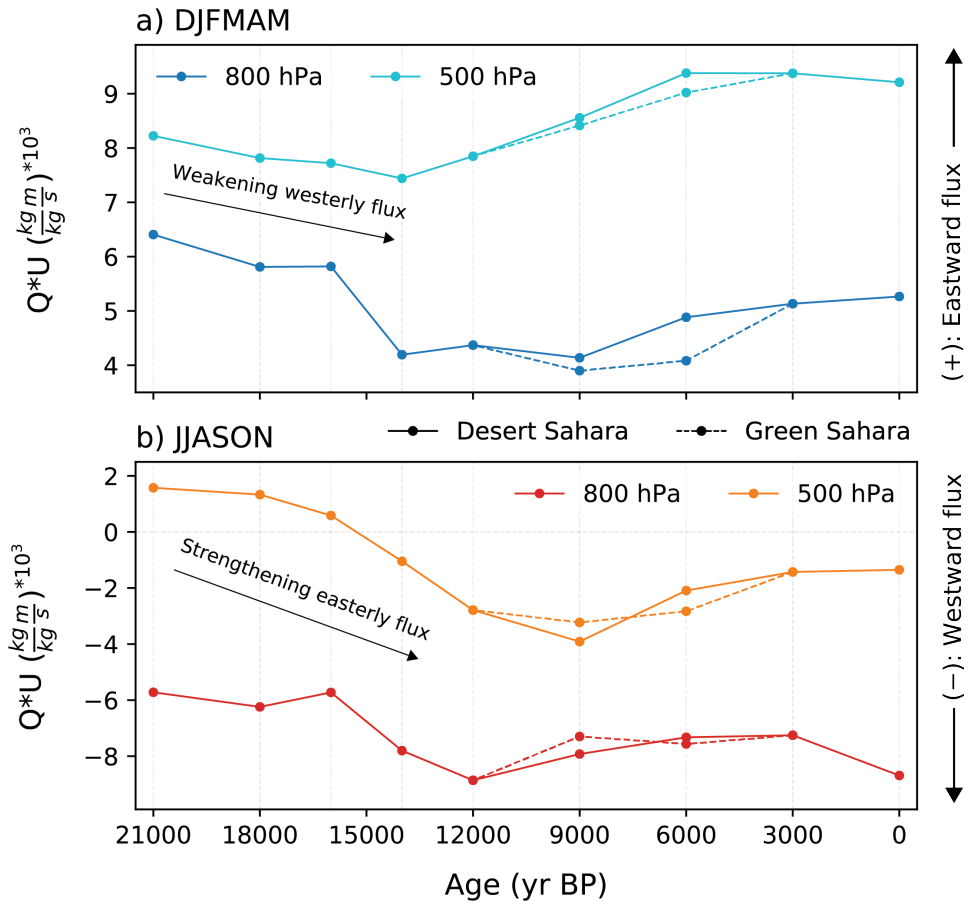

Figure 4.8. Evolution of simulated zonal moisture flux (Q*U) averaged over our defined NAM region and shown at 500 and 800 hPa for a) winter and b) summer. Units are multiplied by 10^3 to simplify y-axes labels. Positive values indicate an eastward (westerly) flux and negative values indicate a westward (easterly) flux. The solid lines represent simulations that use the PI extent of vegetation (i.e., desert Sahara), whereas the dashed lines represent simulations that include a Green Sahara. **Main takeaway:** The trend towards more negative values from *21ka* to *12ka* indicates a weakening of the anomalous westerly moisture flux or strengthening of the anomalous easterly flux and, in one case, a shift from anomalous westerlies to easterlies.

In concert with these changes in atmospheric dynamics and rainfall, simulated values of the isotopic composition of precipitation and soil water ($\delta^{18}O_P$, $\delta^{18}O_S$, δD_P, δD_S) are lower in all late Pleistocene simulations (*21ka* to *12ka*) relative to $PI_{CONTROL}$ (Figure 4.5). These simulated negative isotopic anomalies exist primarily due to the strengthened westerly moisture flux and lower percentage of summer rainfall. Increases in the westerly moisture flux in our *21ka* simulation advect moisture with an anomalously negative isotopic signature, relative to $PI_{CONTROL}$, reducing simulated $\delta^{18}O$ and δD anomalies by as much as –0.9‰ and –7.2‰, respectively, in the NAM region in both winter and summer (Figure 4.5a,b,e,f). Additionally, the rising percentage of simulated summer rainfall, most notably a coastal increase from ~64% in *21ka* to ~73% in *12ka*

(Figure 4.9), corresponds to the general increasing trend in $\delta^{18}O/\delta D$ exhibited by our late Pleistocene simulations. Taken together, the simulated negative isotopic anomalies are largely driven by a stronger westerly moisture flux, while the generally increasing trend in $\delta^{18}O/\delta D$ is tied to the weakening of these westerlies and gradual increase in the percentage of summer rainfall.

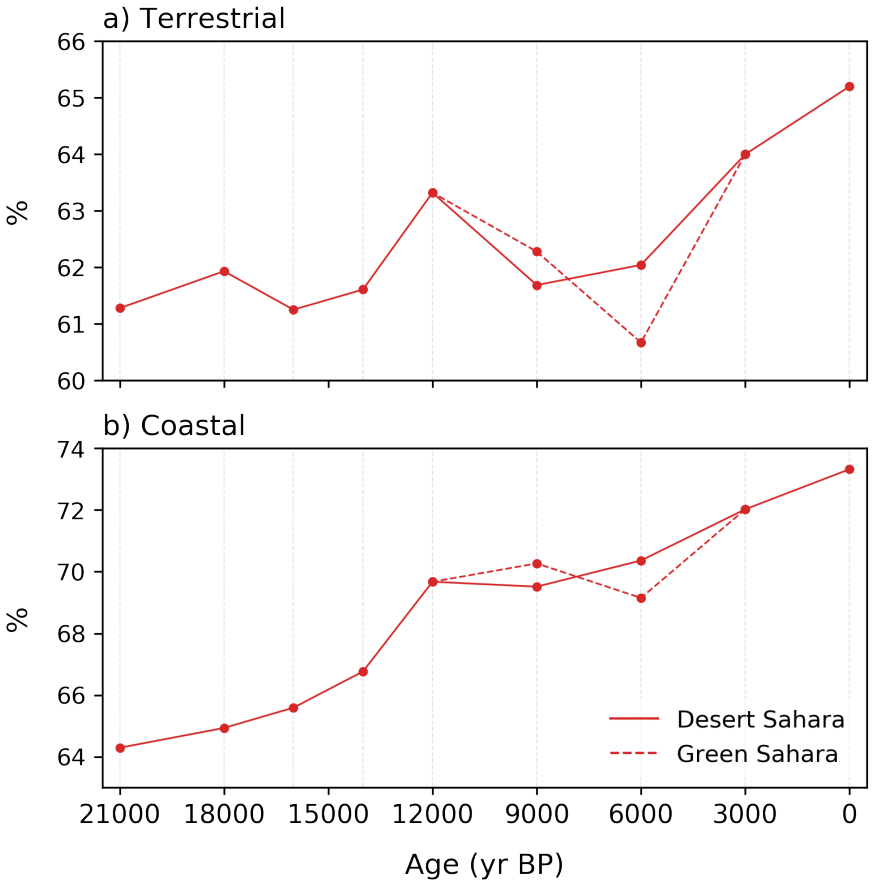

Figure 4.9. Percentage of summer rainfall versus the annual total (JJASON/ANNUAL) for a) terrestrial and b) coastal grid cells in the defined NAM region. The solid lines represent simulations that use the PI extent of vegetation (i.e., desert Sahara), whereas the dashed lines represent simulations that include a Green Sahara. **Main takeaway:** The percentage of summer rainfall gradually increases at both averaging sites from *21ka* to $PI_{CONTROL}$, but the coastal sites show less variability in the trend.

4.4.4 Holocene evolution of the North American monsoon

Our 9, 6, and 3 ka simulations produce NAM summer rainfall amounts that are slightly higher than $PI_{CONTROL}$, an increase that is largely driven by orbitally-enhanced summer insolation (Figure 4.5c,g). Winter rainfall amounts are also higher than in $PI_{CONTROL}$ (Figure 4.10). In tandem with the increases in rainfall, values of the isotopic composition of precipitation and soil water

during both the summer and winter are similar to or lower than $PI_{CONTROL}$ in $9ka_{ORB}$ and $6ka_{ORB}$, which account for changes in orbital insolation, GHGs, and ice cover, but not changes in African Sahara vegetation (Figures 4.5 and 4.11). While these results indicate a similar NAM response to orbital forcing as occurs in other Northern Hemisphere monsoons, the simulated $\delta^{18}O/\delta D$ anomalies do not agree with the more positive values exhibited by proxy reconstructions of $\delta^{18}O_C$ and δD_{WAX} from southwestern North America (Figure 4.3).

When we instead include African Sahara vegetation expansion with the changes in orbital insolation, GHGs, and ice cover (e.g., $9ka_{GS}$ and $6ka_{GS}$), simulated NAM summer rainfall anomalies decrease and $\delta^{18}O/\delta D$ anomalies increase relative to $PI_{CONTROL}$ (Figures 4.5, 4.10, and 4.11), in better agreement with proxy reconstructions (Figure 4.3). Winter rainfall also decreases as a result of the Green Sahara, yet is still slightly higher than in $PI_{CONTROL}$ (Figure 4.5c,g). Simulated mean summer rainfall decreases by ~0.4 mm/day in the NAM region as a direct result of Saharan greening, producing early and mid-Holocene NAM rainfall anomalies that are as much as ~0.3 mm/day lower than $PI_{CONTROL}$. These simulated anomalies fall below late Pleistocene values in terrestrial areas of the NAM region while remaining higher than all but *12ka* along the coast. Simulated winter rainfall in the NAM region decreases by as much as ~0.3 mm/day but is still slightly higher than $PI_{CONTROL}$ in the early and mid-Holocene. Therefore, the direct impact of African Sahara vegetation expansion in our model simulations is to reduce both summer and winter rainfall in our defined NAM region.

In concert with the simulated decreases in summer and winter rainfall that occur when accounting for all climate forcings (e.g., $9ka_{GS}$ and $6ka_{GS}$), simulated summer $\delta^{18}O_P$ and δD_P anomalies are as much as ~1.1 and 10.4‰ higher, respectively, than $PI_{CONTROL}$, while winter $\delta^{18}O_P$ and δD_P anomalies are as much as ~0.5 and ~5.3‰ higher, respectively (Figure 4.5a,e). Simulated values of $\delta^{18}O_S$ and δD_S, as integrators of the signal from precipitation, exhibit a similar, but muted, response (Figure 4.5b,f). However, unlike in our late Pleistocene simulations, these anomalously positive shifts in $\delta^{18}O/\delta D$ are not as easily explained by the strength of the westerly moisture flux (Figure 4.8) or the percentage of summer rainfall (Figure 4.9).

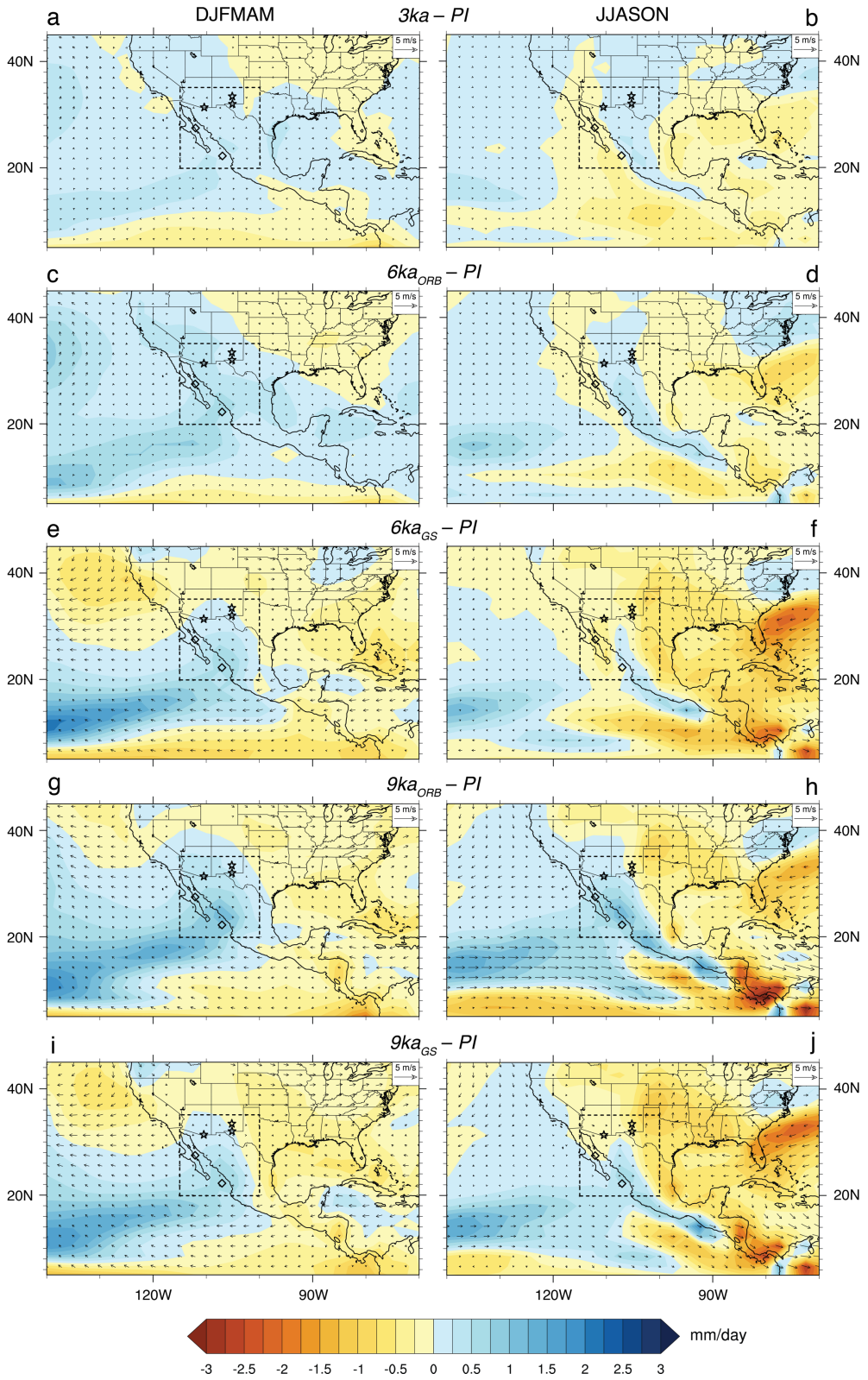

Figure 4.10. Simulated Holocene winter (DJFMAM) and summer (JJASON) anomalies of rainfall (mm/day) and 800 hPa wind vectors (m/s) relative to $PI_{CONTROL}$. Description of dashed line, stars, and diamonds can be found in Figure 4.4. **Main takeaway:** The direct impact of the Green Sahara (e.g., $6ka_{GS}$ – $6ka_{ORB}$) is to strongly reduce summer rainfall, while it also reduces winter rainfall to a smaller extent.

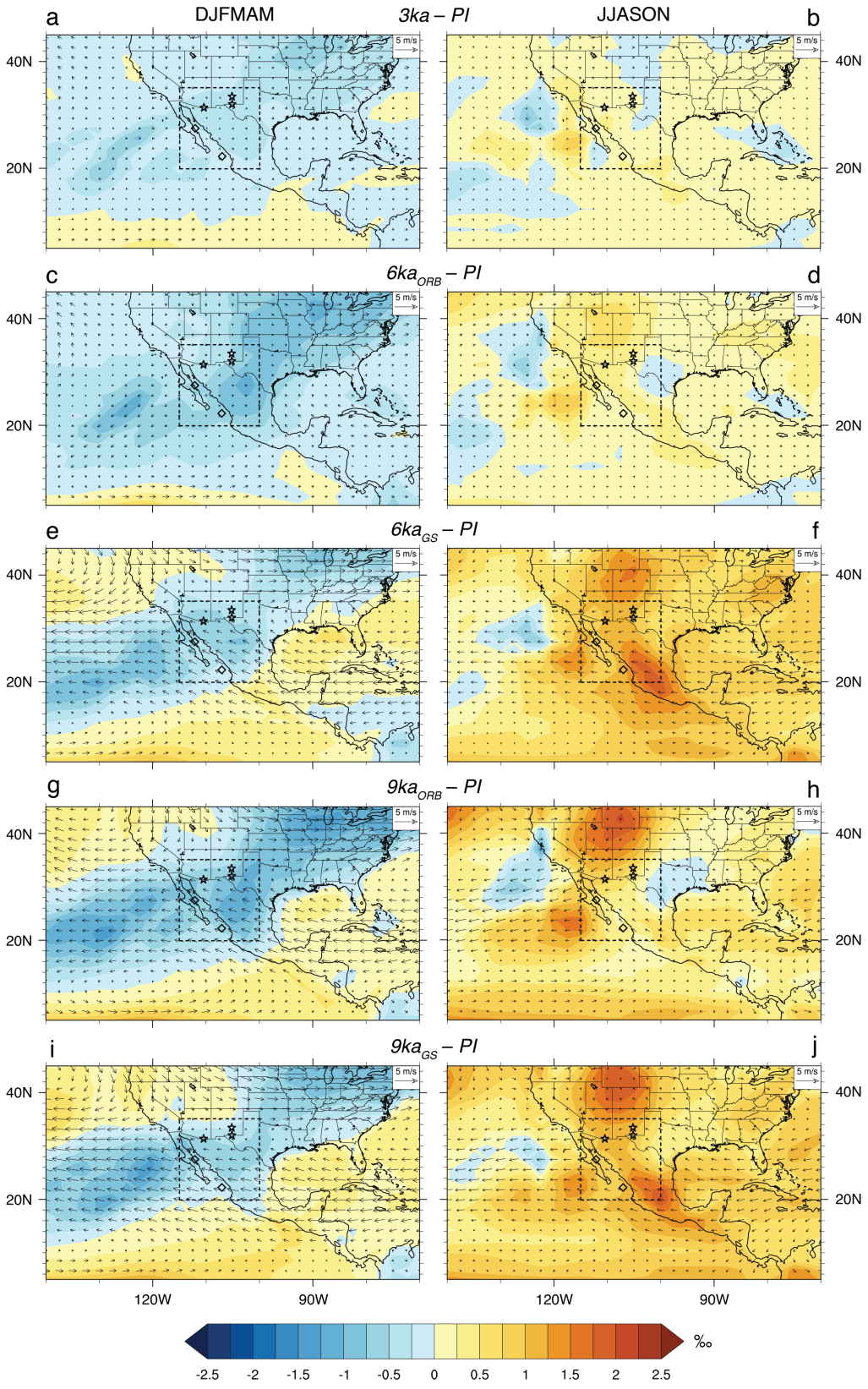

Figure 4.11. Same as Figure 4.10 but for $\delta^{18}O_P$ (‰) and 500 hPa wind vectors (m/s). **Main takeaway:** Summer $\delta^{18}O_P$ increases as a direct result of the Green Sahara. Winter values exhibit a smaller magnitude increase.

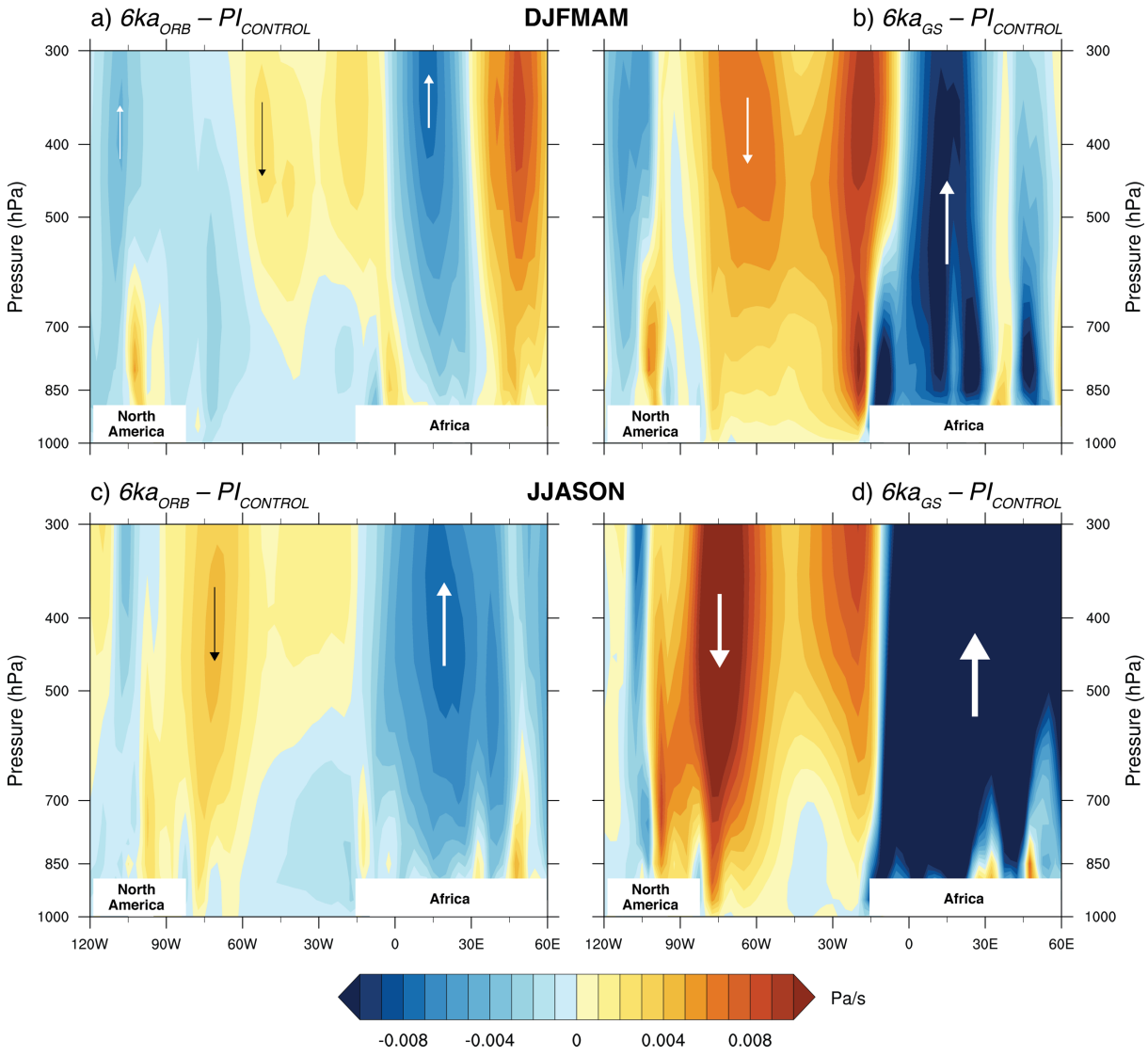

Figure 4.12. Simulated anomalies of vertical velocity (omega, ω) averaged over the zonal region 15–40°N for a) winter *6ka*$_{ORB}$, b) winter *6ka*$_{GS}$, c) summer *6ka*$_{ORB}$, and d) summer *6ka*$_{GS}$ relative to *PI*$_{CONTROL}$. Negative anomalies (blue) indicate upward vertical motion (i.e., ascent), while positive anomalies (red) indicate downward vertical motion (i.e., subsidence). The locations of North America and Africa are shown in white. **Main takeaway:** The greening of the African Sahara likely strengthens the ascending branch of local Walker circulation over Africa and descending branch over North America, leading to enhanced subsidence/weakened ascent over the NAM region.

4.4.5 Influence of the Green Sahara on subtropical Walker circulation

To understand why the Green Sahara leads to reductions in rainfall and increases in $\delta^{18}O/\delta D$ in our 9 and 6 ka simulations, we investigate the influence of greening on local Walker circulation in North America, which in turn impacts the NAM. In the modern, Walker circulation along the equator exhibits ascending motion over the African and South American continents,

associated with their summer monsoons, while corresponding descending branches occur directly to the west of these regions (Lau and Yang, 2002). The northern limits of the regional Walker circulation cell, which encompass the southern portions of the NAM region in the subtropical Northern Hemisphere, experience a similar pattern in the local Walker circulation with a narrow band of ascent located in northwestern Mexico during the summer and a large descending branch directly to its west (Schwendike et al., 2014; see JJA in their Figure 2).

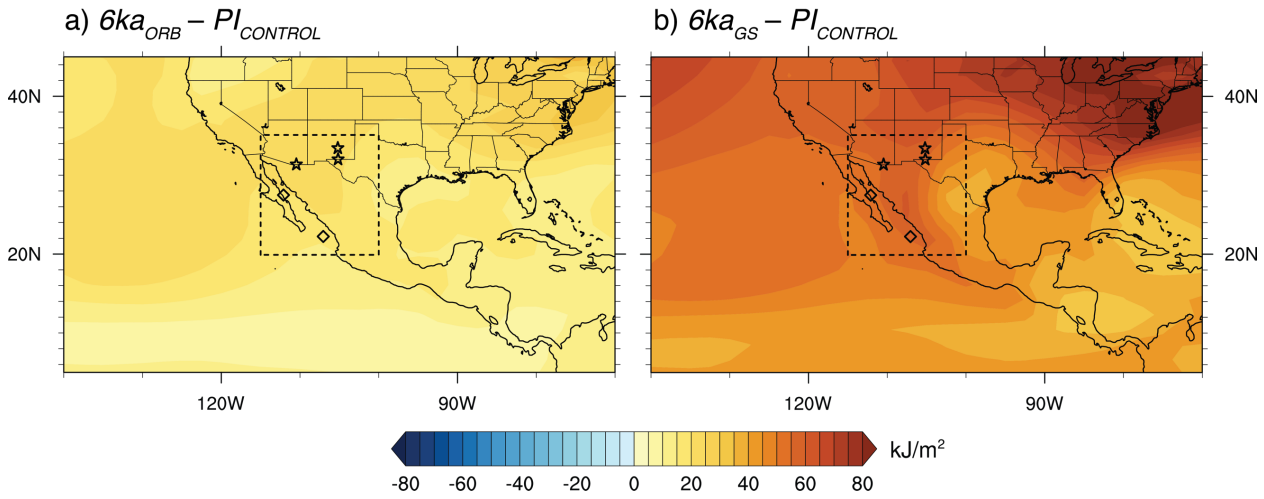

Figure 4.13. Simulated summer (JJASON) anomalies of vertically integrated moist static energy for a) $6ka_{ORB}$ and b) $6ka_{GS}$ relative to $PI_{CONTROL}$. Description of dashed line, stars, and diamonds can be found in Figure 4.4. **Main takeaway:** Without the accompanying changes in subtropical Walker circulation, the impact of the Green Sahara would be to strengthen the NAM through increased moist static energy.

In agreement with previous studies (Pausata et al., 2017a, 2017b), our simulations show that the Green Sahara vegetational forcing induces changes in the local Walker circulations in both Africa and North America. The prescription of Green Saharan vegetation change strengthens the ascending branch of local Walker circulation over the African continent and the descending branch over North America, which appears to overwhelm the narrow branch of ascent in North America and suppress simulated NAM summer and winter rainfall (Figure 4.12). With only the combined effect of changes in orbital insolation, GHGs, and ice cover (e.g., $6ka_{ORB}$), small shifts in the local Walker circulations in Africa and North America occur due to the orbitally-enhanced African monsoon (Kutzbach et al., 1996; Kutzbach, 1981; Shi et al., 2020). However, these changes have only a minor impact on simulated NAM summer rainfall and winter rainfall (see $9ka_{ORB}$ and $6ka_{ORB}$ in Figure 4.10). Despite a clear impact of the Green Sahara on local Walker circulation in both

Africa and North America, additional work is required to connect these effects spatially. Further discussion on this is provided in 4.5.3 Future Directions.

Without these potential changes in the local Walker circulation of North America, the simulated NAM at 9 and 6 ka instead increases in intensity. Monsoonal energy, depicted as changes in vertically integrated moist static energy in our simulations and often thought of as a theoretical indicator of monsoon strength (Geen et al., 2020), increases at 6 ka as a response to the Green Sahara, with large increases occurring in the region of narrow ascent in the local Walker circulation in North America (Figure 4.13). Yet, despite the increase in simulated moist static energy, our simulations show that the impact of the Green Sahara is to weaken NAM rainfall (Figure 4.10f,j).

In tandem with suppressed NAM summer rainfall in our $9ka_{GS}$ and $6ka_{GS}$ simulations, the presence of the Green Sahara increases simulated summer values of $\delta^{18}O/\delta D$ (Figures 4.5a,b,e,f and 4.11 *GS* vs. *ORB* simulations). In our 6 ka simulations, where this effect is seen most strongly ($6ka_{GS}$ and $6ka_{ORB}$), the greening of the African Sahara forces higher simulated summer $\delta^{18}O$ and δD values by as much as ~0.9 and 8.2‰, respectively (Figure 4.5a,b,e,f). As previous studies have shown regarding the amount effect and convection (Bony et al., 2008; Risi et al., 2008), the simulated isotopic increases are likely the result of enhanced sub-cloud evaporation, evidenced by a continually enriched pattern throughout the atmospheric column in water vapor isotopes directly above our defined NAM region (Figure 4.14). At 6 ka, simulated temperatures are warmer throughout the atmospheric column as a result of Saharan greening (Figure 4.15), thus providing a favorable environment for enhanced sub-cloud evaporation. Overall, these results illustrate that the Green Sahara can increase isotopic values of precipitation in southwestern North America and provides a potential explanation for the positive isotopic excursion at 9 and 6 ka in proxy records.

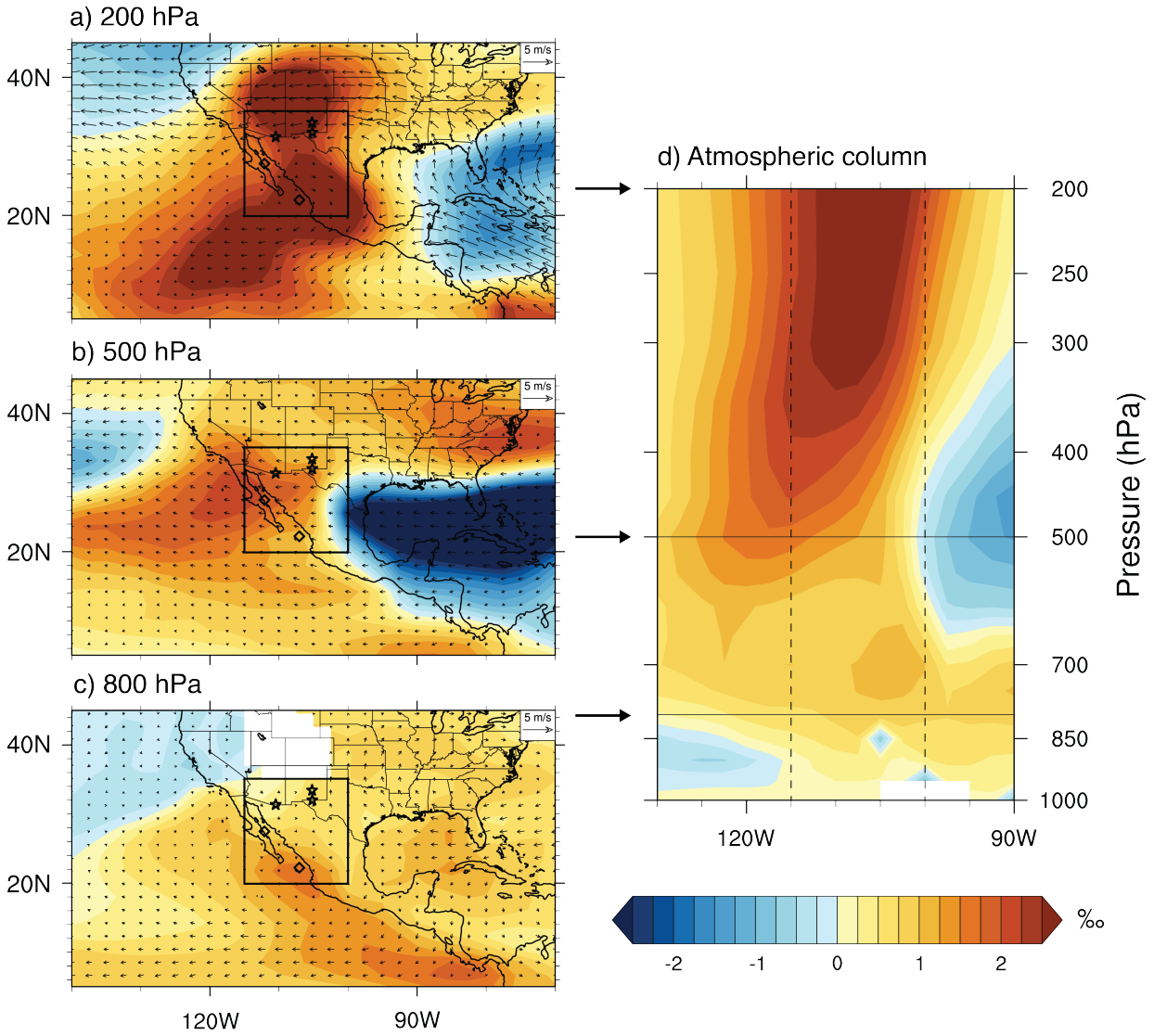

Figure 4.14. Simulated difference due to the 6 ka greening of the African Sahara ($6ka_{GS}$ – $6ka_{ORB}$) in summer (JJASON) $\delta^{18}O$ of water vapor at a) 200 hPa, b) 500 hPa, c) 800 hPa, and d) zonal average over 15–40°N for the atmospheric column. Description of dashed line, stars, and diamonds in a)–c) can be found in Figure 4.4. Vertical dashed line in d) indicates western and eastern boundaries of our defined NAM region and horizontal solid lines indicate atmospheric levels corresponding to a)–c). White space indicates topography or missing values. **Main takeaway:** Due to the mid-Holocene greening of the African Sahara, $\delta^{18}O_{VAPOR}$ values increase throughout the atmospheric column directly above the NAM region.

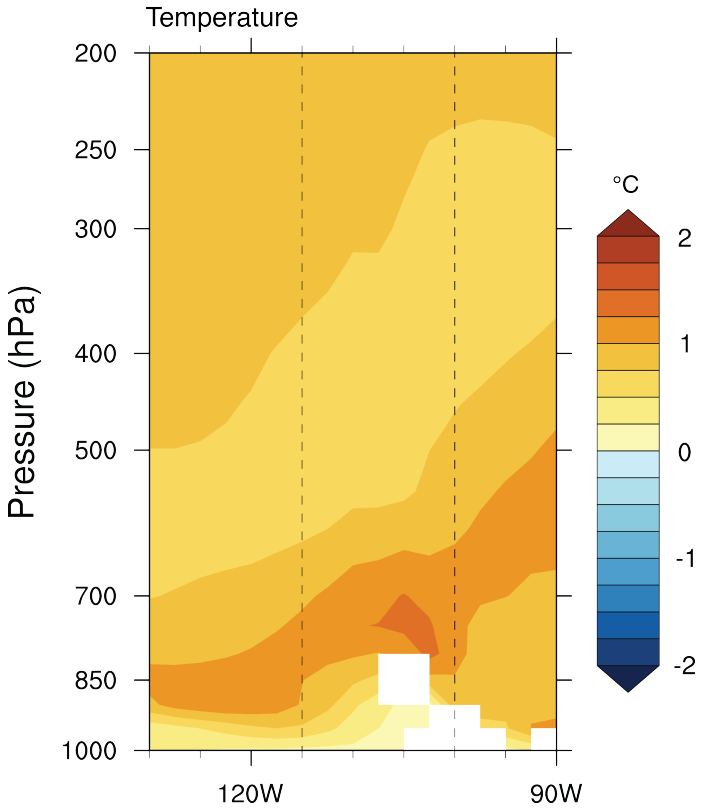

Figure 4.15. Simulated zonally averaged temperature difference for the atmospheric column due to the 6 ka greening of the African Sahara ($6ka_{GS} - 6ka_{ORB}$) in the summer (JJASON). Average is taken over zonal region 15–40°N. Vertical dashed line indicates western and eastern boundaries of our defined NAM region. White boxes indicate either topography or missing values. **Main takeaway:** The mid-Holocene greening of the African Sahara increases temperatures throughout the atmospheric column, producing favorable conditions for enhanced sub-cloud evaporation.

4.5 Discussion

4.5.1 Uncertainties in modeling changes in the North American monsoon

4.5.1.1 Proxy system modeling of speleothems

The degree of temperature dependence assumed in the speleothem proxy system model plays a large role in the agreement between PRYSM-simulated and speleothem reconstructed $\delta^{18}O_C$. On orbital time scales, the temperature within the cave is assumed to reflect the mean annual temperature at the surface above the cave (Hendy and Wilson, 1968; Wackerbarth et al., 2010). In our calculation of simulated $\delta^{18}O_C$ shown by the thick lines in Figure 4.3b, we follow the PRYSM guidelines regarding this temperature assumption and input iCESM1.2 values of mean annual surface temperature, which vary in a similar manner to summer and winter temperature (Figure

4.5). We also vary the dependence of temperature in our calculation of $\delta^{18}O_C$ based on inferences by Asmerom et al. (2010) and Wagner et al. (2010) that temperature changes had a negligible effect on values of southwestern North American speleothem $\delta^{18}O_C$. In our calculation of simulated $\delta^{18}O_C$ shown by the thin lines in Figure 4.3b, we modified the temperature input by lowering the magnitude of change between each time slice and the PI by 50%, based on the hypothesis by Asmerom et al. (2010) that only half of their observed $\delta^{18}O_C$ variability could be attributed to changes in temperature. This method represents a hypothetical case with a relatively lower impact of temperature on $\delta^{18}O_C$ values.

In comparison between speleothem $\delta^{18}O_C$ and our two methods for PRYSM-simulated $\delta^{18}O_C$, agreement in the sign of anomalies and trends largely depends on the temperature assumption. Using the traditional assumption relating cave temperature to mean annual surface temperature (thick lines in Figure 4.3b) (Dee et al., 2015; Wackerbarth et al., 2010), simulated $\delta^{18}O_C$, when $\delta^{18}O_P$ is used as the input (thick blue line), agrees with the positive anomalies in the early and mid-Holocene from speleothem $\delta^{18}O_C$ but not with the negative anomalies during the late Pleistocene. When $\delta^{18}O_S$ is used as the input (thick brown line), agreement is poor throughout the record. However, under the modified assumption of temperature dependence (thin lines in Figure 4.3b) (Asmerom et al., 2010; Wagner et al., 2010), PRYSM-simulated $\delta^{18}O_C$ values exhibit improved agreement with the speleothem reconstructions. The late Pleistocene anomalies are either negative ($\delta^{18}O_S$: thin brown line) or more negative ($\delta^{18}O_P$: thin blue line) than its traditional temperature assumption counterpart and Holocene anomalies are either positive ($\delta^{18}O_P$) or more positive ($\delta^{18}O_S$) than its traditional temperature assumption counterpart.

The large differences in model-data agreement between the two methods highlight the importance of temperature dependence on the calculation of $\delta^{18}O_C$ by proxy system models. PRYSM assumes an inverse relationship between temperature and $\delta^{18}O_C$ on the order of approximately –0.2‰/°C (Dee et al., 2015; Wackerbarth et al., 2010). This relationship is clearly seen in our simulated $\delta^{18}O_C$ with $\delta^{18}O_S$ as the input (thick brown line in Figure 4.3b) by its trend towards more negative values in the late Pleistocene simulations corresponding to large simulated warming over the same period. However, this trend does not match with the speleothem reconstructions. With the assumed temperature-$\delta^{18}O_C$ relationship, the warming of ~7°C that we simulate between our *21ka* and *12*ka simulations suggests a negative $\delta^{18}O_C$ trend of ~1.4‰, but

the proxy reconstructions from Cave of the Bells and Fort Stanton instead show a positive trend of ~2–4‰ (Figure 4.3a). On the basis of the temperature-$\delta^{18}O_C$ relationship, this positive trend in speleothem $\delta^{18}O_C$ indicates cooling of ~10–20°C or requires an increase in $\delta^{18}O_P$ by at least ~3.5–5.5‰ to outweigh the ~7°C warming, both of which are unreasonable results not supported by our simulations. Therefore, it may be more likely that temperature changes in southwestern North America had a negligible influence on $\delta^{18}O_C$ values in this region. This determination is bolstered by the fact that our simulated $\delta^{18}O_C$ with modified temperature dependence exhibits better agreement with speleothem reconstructions than the simulated values with the traditional temperature assumption.

4.5.1.2 Proxy system modeling of leaf wax *n*-alkanes

WaxPSM-simulated values of δD_{WAX} align closely with the proxy reconstructed δD_{WAX} when either δD_P or δD_S are used as inputs (Figure 4.3). While the magnitudes of change are different, we investigate the sign of anomalies and trends to capture the large-scale isotopic changes in our simulations and the proxy reconstructions. Our simulated values capture the proxy-reconstructed trend of increasing δD_{WAX} from the LGM to the late Holocene, including the positive peak in values at 9 to 6 ka. In accordance with previous studies suggesting that leaf wax *n*-alkanes likely represent the isotopic signal of δD_S (Konecky et al., 2019; Thompson et al., 2021), our results show that δD_S-inferred δD_{WAX} values match slightly more closely with the reconstructed δD_{WAX}, especially regarding the magnitude of impact by the Green Sahara. δD_S-inferred δD_{WAX} values show a moderate increase as a result of the Green Sahara, whereas δD_P-inferred δD_{WAX} exhibit larger fluctuations that do not align as well with reconstructed δD_{WAX}.

4.5.2 Implications for the evolution of the North American monsoon

Our results highlight the spatial and temporal evolution of the NAM and its isotopic signature from the LGM to the PI. In the core of the monsoon along the western coast of Mexico, summer rainfall is characterized by a weak monsoon in the LGM and gradually increases in strength towards the PI. This signal is captured by leaf wax *n*-alkane proxy records and our model simulations. This coastal region exhibits a strong influence by orbitally enhanced insolation

seasonality, which may generally outweigh the weakened ascent of local Walker circulation in North America that is induced by Saharan greening, and produces a stronger monsoon in *9ka* and *6ka* than in the late Pleistocene simulations (*21ka* to *12ka*). The isotopic signature generally reflects the pattern of a positive trend during the late Pleistocene and highlights the impacts of the Green Sahara in increasing $\delta^{18}O/\delta D$ mainly through enhanced sub-cloud evaporation at 9 and 6 ka. At the northern fringe of the NAM, the trend in summer rainfall is not as straightforward from the LGM to the PI, with increases throughout the late Pleistocene but decreases in the early Holocene. This signal is captured in our model simulations and generally matches speleothem proxy reconstructions. In *9ka* and *6ka*, simulated NAM summer rainfall is weaker than during the late Pleistocene simulations, showcasing this region's potential susceptibility to external vegetational forcing.

Due to the few continuous isotopic records present in southwestern North America, investigation of proxy records from nearby locations, especially those that may be partly impacted by NAM dynamics, can provide further insight into our inferred changes in the evolution of the NAM since the LGM. To this point, five speleothem and leaf wax *n*-alkane records from central Mexico and the western United States show an evolution of hydroclimate that is broadly consistent with our results (Figure 4.16). Two speleothem reconstructions of $\delta^{18}O_C$ from central Mexico (Juxtlahuaca cave: 17.4°N, 99.2°W; Diablo cave: 18.2°N, 99.9°W; Lachniet et al., 2013) show negative anomalies in the LGM followed by a positive trend towards ~12 ka. In addition, two speleothem reconstructions of $\delta^{18}O_C$ from the state of Nevada (Leviathan cave: 37.9°N, 115.6°W; Pinnacle cave: 36.0°N, 115.5°W) and one leaf wax *n*-alkane reconstruction of δD_{WAX} from Lake Elsinore in the state of California (33.7°N, 117.4°W) together exhibit a similar negative anomaly in the LGM and positive trend until ~10 ka (Kirby et al., 2013; Lachniet et al., 2014).

The records in each of these regions, however, demonstrate differing anomalies from 9 to 6 ka. The central Mexican speleothems show negative isotopic anomalies and a positive trend from 9 ka to the PI, whereas the western United States records showcase a positive isotopic anomaly from 9 to 6 ka and a negative trend towards the PI. Overall, these proxy records adjacent to our defined NAM region highlight the regional differences in strength and influence of NAM hydrology. The matching positive anomalies in records from the western United States, to the north of our defined NAM region suggests that increased isotopic values being possibly induced by local Walker circulation may be a feature indicative of the northern fringe of the NAM.

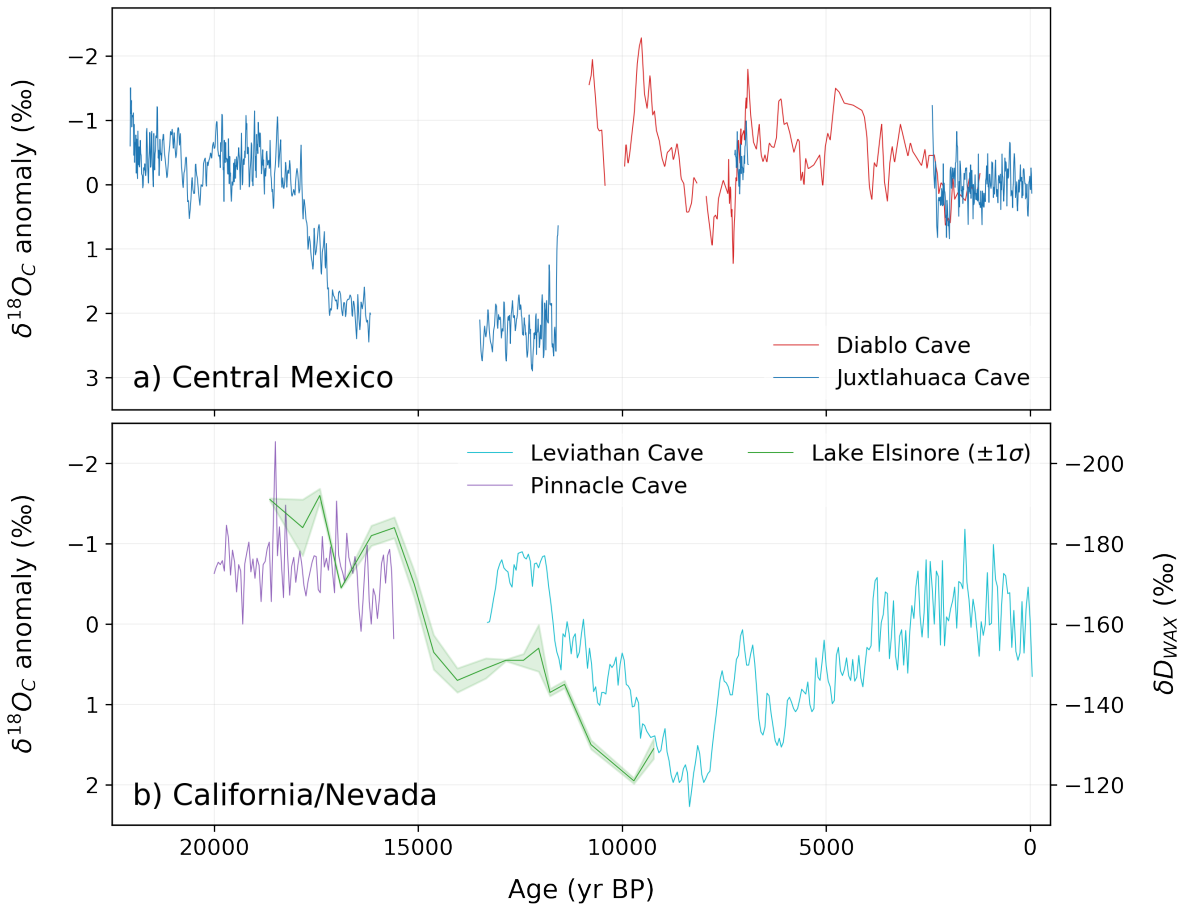

Figure 4.16. Isotopic proxy records from locations near our defined NAM region. Records are grouped by a) central Mexican speleothem reconstructions of $\delta^{18}O_C$ (Lachniet et al., 2013) and b) reconstructions of $\delta^{18}O_C$ and δD_{WAX} from the western United States (Kirby et al., 2013; Lachniet et al., 2014). **Main takeaway:** Nearby isotopic records illustrate many similarities with our model-proxy reconstruction of NAM region $\delta^{18}O_C$ and δD_{WAX} values.

4.5.3 Future directions

In this chapter, we showcase novel findings on orbital-scale NAM evolution and the region's modified seasonal hydrology through model-proxy comparison of $\delta^{18}O_C$ and δD_{WAX} reconstructions. We also propose the hypothesis that the greening of the African Sahara is likely responsible for positive isotopic anomalies in 9 and 6 ka through African vegetation's impact on local Walker circulation. However, several uncertainties remain that must be addressed in future work. The primary uncertainties are discussed in further detail in this section.

1. Why do anomalies of proxy system model simulated-$\delta^{18}O_C$ differ in sign when using inputs of $\delta^{18}O_P$ versus $\delta^{18}O_S$? At certain time slices in our Pleistocene/Holocene analysis of simulated $\delta^{18}O_C$, its agreement with speleothem reconstructions is heavily dependent on the choice

of input ($\delta^{18}O_P$ or $\delta^{18}O_S$) for the proxy system model (Figure 4.2). While we demonstrate that the assumption of temperature dependence also greatly influences the values of simulated $\delta^{18}O_C$, the atmospheric and land surface dynamics governing differences between simulated $\delta^{18}O_C$ with inputs of $\delta^{18}O_P$ or $\delta^{18}O_S$, as well as the inherent uncertainties present within the speleothem sensor model (Dee et al., 2015; Midhun et al., 2018), are yet to be fully analyzed. Further examination of these uncertainties will help to elucidate the factors contributing to agreement, or disagreement, between proxy system model results and speleothem reconstructions.

2. Did local vegetation changes in southwestern North America impact hydroclimate in the NAM region to a greater degree than remote Saharan vegetation effects? Our model design explicitly simulates the hydrologic and isotopic responses in southwestern North America to the greening of the African Sahara; however, we neglect land surface changes in North America by design. Like in the African Sahara, increased vegetation cover likely occurred during the early and mid-Holocene in southwestern North America (Bartlein et al., 2011), representing an additional factor in potentially modulating NAM region hydroclimate. Further attention should be paid to this potential mechanism and its impact on the NAM through either additional discussion of the possible ways in which this land surface change could impact isotopic reconstruction or additional experiments that incorporate these land surface changes.

3. How are the Green Sahara-induced changes in local Walker circulation in southwestern North America and Africa connected? Our results showcase both the anomalous ascent over the Sahara and descent over North America induced by the greening of the African Sahara. However, large uncertainties exist in connecting these two local circulations through a larger zonal pathway. Future work must disentangle the local Walker circulation responses in North American and Africa as a result of the Green Sahara and further establish a causal connection between the two regions in order to establish a robust impact of the Green Sahara on NAM hydroclimate.

4.6 Conclusion

In this chapter, we investigate orbital-scale changes in hydroclimate in southwestern North America to better understand the evolution of the North American monsoon since the Last Glacial Maximum. In doing so, we find that we can reasonably simulate the isotopic change indicated by speleothem and leaf wax *n*-alkane reconstructions of $\delta^{18}O_C$ and δD_{WAX} and thus improve our

understanding of the potential factors contributing to their isotopic changes. Between 21 and 12 ka, we find that $\delta^{18}O_C$ and δD_{WAX} are largely controlled by the westerly moisture flux associated with the waning Laurentide Ice Sheet and the contribution of summer rainfall to the annual total. In 9 and 6 ka, we put forth the hypothesis that the greening of the African Sahara likely contributes to a positive isotopic excursion that indicates a weaker monsoon than is predicted due to orbital, GHG, and ice cover changes alone. Without the impact of these remote vegetational changes, the positive excursion in $\delta^{18}O_C$ and δD_{WAX} likely does not exist and the monsoon is considerably stronger. Overall, our results provide for the first time a depiction of hydroclimatic change in southwestern North America showing a gradually increasing monsoon along the western Mexican coast from the LGM to the PI and a weakening of the monsoon inland potentially due to local Walker circulation impacts associated with the greening of the African Sahara in the early and mid-Holocene. Implications of our study include a better understanding of how the North American monsoon responds to large scale climate forcings and how this response can be detected in records of past climate change. Future work will address the uncertainties surrounding our experiment design, markedly those associated with proxy system modeling, and our proposed mechanism for connecting the greening of the African Sahara with the positive isotopic excursion in proxy reconstructions.

4.7 References

Adams, D.K., Comrie, A.C., 1997. The North American Monsoon. Bull. Am. Meteorol. Soc. 78, 2197–2213. https://doi.org/10.1175/1520-0477(1997)078<2197:TNAM>2.0.CO;2

Asmerom, Y., Polyak, V., Burns, S., Rassmssen, J., 2007. Solar forcing of Holocene climate: New insights from a speleothem record, southwestern United States. Geology 35, 1–4. https://doi.org/10.1130/G22865A.1

Asmerom, Y., Polyak, V.J., Burns, S.J., 2010. Variable winter moisture in the southwestern United States linked to rapid glacial climate shifts. Nat. Geosci. 3, 114–117. https://doi.org/10.1038/ngeo754

Barlow, M., Nigam, S., Berbery, E.H., 1998. Evolution of the North American monsoon system. J. Clim. 11, 2238–2257. https://doi.org/10.1175/1520-0442(1998)011<2238:EOTNAM>2.0.CO;2

Bartlein, P.J., Harrison, S.P., Brewer, S., Connor, S., Davis, B.A.S., Gajewski, K., Guiot, J., Harrison-Prentice, T.I., Henderson, A., Peyron, O., Prentice, I.C., Scholze, M., Seppä, H., Shuman, B., Sugita, S., Thompson, R.S., Viau, A.E., Williams, J., Wu, H., 2011. Pollen-based continental climate reconstructions at 6 and 21 ka: a global synthesis. Clim. Dyn. 37, 775–802. https://doi.org/10.1007/s00382-010-0904-1

Bartlein, P.J., Shafer, S.L., 2019. Paleo calendar-effect adjustments in time-slice and transient climate-model simulations (PaleoCalAdjust v1.0): impact and strategies for data analysis. Geosci. Model Dev. 12, 3889–3913. https://doi.org/10.5194/gmd-12-3889-2019

Berke, M.A., Tipple, B.J., Hambach, B., Ehleringer, J.R., 2015. Life form-specific gradients in compound-specific hydrogen isotope ratios of modern leaf waxes along a North American Monsoonal transect. Oecologia 179, 981–997. https://doi.org/10.1007/s00442-015-3432-1

Bhattacharya, T., Tierney, J.E., Addison, J.A., Murray, J.W., 2018. Ice-sheet modulation of deglacial North American monsoon intensification. Nat. Geosci. 11, 848–852. https://doi.org/10.1038/s41561-018-0220-7

Bhattacharya, T., Tierney, J.E., DiNezio, P., 2017. Glacial reduction of the North American Monsoon via surface cooling and atmospheric ventilation. Geophys. Res. Lett. 44, 5113–5122. https://doi.org/10.1002/2017GL073632

Bony, S., Risi, C., Vimeux, F., 2008. Influence of convective processes on the isotopic composition (δ 18 O and δ D) of precipitation and water vapor in the tropics: 1. Radiative-convective equilibrium and Tropical Ocean–Global Atmosphere–Coupled Ocean-Atmosphere Response Experiment (TOGA-CO. J. Geophys. Res. 113, D19305. https://doi.org/10.1029/2008JD009942

Braconnot, P., Harrison, S.P., Kageyama, M., Bartlein, P.J., Masson-Delmotte, V., Abe-Ouchi, A., Otto-Bliesner, B., Zhao, Y., 2012. Evaluation of climate models using palaeoclimatic data. Nat. Clim. Chang. 2, 417–424. https://doi.org/10.1038/nclimate1456

Brady, E., Stevenson, S., Bailey, D., Liu, Z., Noone, D., Nusbaumer, J., Otto-Bliesner, B.L., Tabor, C., Tomas, R., Wong, T., Zhang, J., Zhu, J., 2019. The Connected Isotopic Water Cycle in the Community Earth System Model Version 1. J. Adv. Model. Earth Syst. 11, 2547–2566. https://doi.org/10.1029/2019MS001663

Cai, Y., Zhang, H., Cheng, H., An, Z., Lawrence Edwards, R., Wang, X., Tan, L., Liang, F., Wang, J., Kelly, M., 2012. The Holocene Indian monsoon variability over the southern

Tibetan Plateau and its teleconnections. Earth Planet. Sci. Lett. 335–336, 135–144. https://doi.org/10.1016/j.epsl.2012.04.035

Collins, J.A., Prange, M., Caley, T., Gimeno, L., Beckmann, B., Mulitza, S., Skonieczny, C., Roche, D., Schefuß, E., 2017. Rapid termination of the African Humid Period triggered by northern high-latitude cooling. Nat. Commun. 8, 1372. https://doi.org/10.1038/s41467-017-01454-y

Cook, B.I., Seager, R., 2013. The response of the North American Monsoon to increased greenhouse gas forcing. J. Geophys. Res. Atmos. 118, 1690–1699. https://doi.org/10.1002/jgrd.50111

Dansgaard, W., 1964. Stable isotopes in precipitation. Tellus 16, 436–468.

Dee, S., Emile-Geay, J., Evans, M.N., Allam, A., Steig, E.J., Thompson, D.M., 2015. PRYSM: An open-source framework for PRoxY System Modeling, with applications to oxygen-isotope systems. J. Adv. Model. Earth Syst. 7, 1220–1247. https://doi.org/10.1002/2015MS000447

deMenocal, P., Ortiz, J., Guilderson, T., Adkins, J., Sarnthein, M., Baker, L., Yarusinsky, M., 2000. Abrupt onset and termination of the African Humid Period: Quat. Sci. Rev. 19, 347–361. https://doi.org/10.1016/S0277-3791(99)00081-5

Dominguez, F., Miguez-Macho, G., Hu, H., 2016. WRF with water vapor tracers: A study of moisture sources for the North American Monsoon. J. Hydrometeorol. 17, 1915–1927. https://doi.org/10.1175/JHM-D-15-0221.1

Dong, J., Yongjin Wang, Hai Cheng, Hardt, B., Edwards, R.L., Xinggong Kong, Jiangying Wu, Shitao Chen, Dianbing Liu, Xiuyang Jiang, Kan Zhao, 2010. A high-resolution stalagmite record of the Holocene East Asian monsoon from Mt Shennongjia, central China. The Holocene 20, 257–264. https://doi.org/10.1177/0959683609350393

Eastoe, C.J., Dettman, D.L., 2016. Isotope amount effects in hydrologic and climate reconstructions of monsoon climates: Implications of some long-term data sets for precipitation. Chem. Geol. 430, 78–89. https://doi.org/10.1016/j.chemgeo.2016.03.022

Geen, R., Bordoni, S., Battisti, D.S., Hui, K., 2020. Monsoons, ITCZs, and the Concept of the Global Monsoon. Rev. Geophys. 58, 1–45. https://doi.org/10.1029/2020RG000700

Griffiths, M.L., Johnson, K.R., Pausata, F.S.R., White, J.C., Henderson, G.M., Wood, C.T., Yang, H., Ersek, V., Conrad, C., Sekhon, N., 2020. End of Green Sahara amplified mid- to

late Holocene megadroughts in mainland Southeast Asia. Nat. Commun. 11, 4204. https://doi.org/10.1038/s41467-020-17927-6

Harrison, S.P., Bartlein, P.J., Izumi, K., Li, G., Annan, J., Hargreaves, J., Braconnot, P., Kageyama, M., 2015. Evaluation of CMIP5 palaeo-simulations to improve climate projections. Nat. Clim. Chang. 5, 735–743. https://doi.org/10.1038/nclimate2649

Hendy, C.H., Wilson, A.T., 1968. Palaeoclimatic Data from Speleothems. Nature 219, 48–51. https://doi.org/10.1038/219048a0

Hermann, N.W., Oster, J.L., Ibarra, D.E., 2018. Spatial patterns and driving mechanisms of mid-Holocene hydroclimate in western North America. J. Quat. Sci. 33, 421–434. https://doi.org/10.1002/jqs.3023

Hoelzmann, P., Jolly, D., Harrison, S.P., Laarif, F., Bonnefille, R., Pachur, H., 1998. Mid-Holocene land-surface conditions in northern Africa and the Arabian Peninsula: A data set for the analysis of biogeophysical feedbacks in the climate system. Global Biogeochem. Cycles 12, 35–51. https://doi.org/10.1029/97GB02733

Hu, H., Dominguez, F., 2015. Evaluation of oceanic and terrestrial sources of moisture for the North American monsoon using numerical models and precipitation stable isotopes. J. Hydrometeorol. 16, 19–35. https://doi.org/10.1175/JHM-D-14-0073.1

Hurrell, J.W., Holland, M.M., Gent, P.R., Ghan, S., Kay, J.E., Kushner, P.J., Lamarque, J.F., Large, W.G., Lawrence, D., Lindsay, K., Lipscomb, W.H., Long, M.C., Mahowald, N., Marsh, D.R., Neale, R.B., Rasch, P., Vavrus, S., Vertenstein, M., Bader, D., Collins, W.D., Hack, J.J., Kiehl, J., Marshall, S., 2013. The community earth system model: A framework for collaborative research. Bull. Am. Meteorol. Soc. 94, 1339–1360. https://doi.org/10.1175/BAMS-D-12-00121.1

Jana, S., Rajagopalan, B., Alexander, M.A., Ray, A.J., 2018. Understanding the Dominant Sources and Tracks of Moisture for Summer Rainfall in the Southwest United States. J. Geophys. Res. Atmos. 123, 4850–4870. https://doi.org/10.1029/2017JD027652

Jolly, D., Prentice, I.C., Bonnefille, R., Ballouche, A., Bengo, M., Brenac, P., Buchet, G., Burney, D., Cazet, J., Cheddadi, R., Edorh, T., Elenga, H., Elmoutaki, S., Guiot, J., Laarif, F., Lamb, H., Lezine, A., Maley, J., Mbenza, M., Peyron, O., Reille, M., Reynaud-Farrera, I., Riollet, G., Ritchie, J.C., Roche, E., Scott, L., Ssemmanda, I., Straka, H., Umer, M., Van Campo, E., Vilimumbalo, S., Vincens, A., Waller, M., 1998. Biome reconstruction from

pollen and plant macrofossil data for Africa and the Arabian peninsula at 0 and 6000 years. J. Biogeogr. 25, 1007–1027. https://doi.org/10.1046/j.1365-2699.1998.00238.x

Joussaume, S., Taylor, K.E., Braconnot, P., Mitchell, J.F.B., Kutzbach, J.E., Harrison, S.P., Prentice, I.C., Broccoli, A.J., Abe-Ouchi, A., Bartlein, P.J., Bonfils, C., Dong, B., Guiot, J., Herterich, K., Hewitt, C.D., Jolly, D., Kim, J.W., Kislov, A., Kitoh, A., Loutre, M.F., Masson, V., McAvaney, B., McFarlane, N., de Noblet, N., Peltier, W.R., Peterschmitt, J.Y., Pollard, D., Rind, D., Royer, J.F., Schlesinger, M.E., Syktus, J., Thompson, S., Valdes, P., Vettoretti, G., Webb, R.S., Wyputta, U., 1999. Monsoon changes for 6000 years ago: Results of 18 simulations from the Paleoclimate Modeling Intercomparison Project (PMIP). Geophys. Res. Lett. 26, 859–862. https://doi.org/10.1029/1999GL900126

Kirby, M.E., Feakins, S.J., Bonuso, N., Fantozzi, J.M., Hiner, C.A., 2013. Latest Pleistocene to Holocene hydroclimates from Lake Elsinore, California. Quat. Sci. Rev. 76, 1–15. https://doi.org/10.1016/j.quascirev.2013.05.023

Konecky, B.L., Dee, S.G., Noone, D.C., 2019. WaxPSM: A Forward Model of Leaf Wax Hydrogen Isotope Ratios to Bridge Proxy and Model Estimates of Past Climate. J. Geophys. Res. Biogeosciences 124, 2107–2125. https://doi.org/10.1029/2018JG004708

Kutzbach, J., Bonan, G., Foley, J., Harrison, S.P., 1996. Vegetation and soil feedbacks on the response of the African monsoon to orbital forcing in the early to middle Holocene. Nature 384, 623–626. https://doi.org/10.1038/384623a0

Kutzbach, J.E., 1981. Monsoon Climate of the Early Holocene: Climate Experiment with the Earth's Orbital Parameters for 9000 Years Ago. Science (80-.). 214, 59–61. https://doi.org/10.1126/science.214.4516.59

Lachniet, M.S., Asmerom, Y., Bernal, J.P., Polyak, V.J., Vazquez-Selem, L., 2013. Orbital pacing and ocean circulation-induced collapses of the Mesoamerican monsoon over the past 22,000 y. Proc. Natl. Acad. Sci. U. S. A. 110, 9255–9260. https://doi.org/10.1073/pnas.1222804110

Lachniet, M.S., Denniston, R.F., Asmerom, Y., Polyak, V.J., 2014. Orbital control of western North America atmospheric circulation and climate over two glacial cycles. Nat. Commun. 5. https://doi.org/10.1038/ncomms4805

Lau, K.-M., Yang, S., 2002. Walker circulation. Encycl. Atmos. Sci.

Levis, S., Bonan, G.B., Bonfils, C., 2004. Soil feedback drives the mid-Holocene North African

monsoon northward in fully coupled CCSM2 simulations with a dynamic vegetation model. Clim. Dyn. 23, 791–802. https://doi.org/10.1007/s00382-004-0477-y

McGee, D., DeMenocal, P.B., Winckler, G., Stuut, J.B.W., Bradtmiller, L.I., 2013. The magnitude, timing and abruptness of changes in North African dust deposition over the last 20,000 yr. Earth Planet. Sci. Lett. 371–372, 163–176. https://doi.org/10.1016/j.epsl.2013.03.054

Metcalfe, S.E., Barron, J.A., Davies, S.J., 2015. The Holocene history of the North American Monsoon: "known knowns" and "known unknowns" in understanding its spatial and temporal complexity. Quat. Sci. Rev. 120, 1–27. https://doi.org/10.1016/j.quascirev.2015.04.004

Meyer, J.D.D., Jin, J., 2017. The response of future projections of the North American monsoon when combining dynamical downscaling and bias correction of CCSM4 output. Clim. Dyn. 49, 433–447. https://doi.org/10.1007/s00382-016-3352-8

Midhun, M., Lekshmy, P.R., Ramesh, R., Yoshimura, K., Sandeep, K.K., Kumar, S., Sinha, R., Singh, A., Srivastava, S., 2018. The Effect of Monsoon Circulation on the Stable Isotopic Composition of Rainfall. J. Geophys. Res. Atmos. https://doi.org/10.1029/2017JD027427

Nusbaumer, J., Wong, T.E., Bardeen, C., Noone, D., 2017. Evaluating hydrological processes in the Community Atmosphere Model Version 5 (CAM5) using stable isotope ratios of water. J. Adv. Model. Earth Syst. 9, 949–977. https://doi.org/10.1002/2016MS000839

Oleson, K.W., Lawrence, D.M., Gordon, B., Flanner, M.G., Kluzek, E., Peter, J., Levis, S., Swenson, S.C., Thornton, E., Dai, A., Decker, M., Dickinson, R., Feddema, J., Heald, C.L., Lamarque, J., Niu, G., Qian, T., Running, S., Sakaguchi, K., Slater, A., Stöckli, R., Wang, A., Yang, L., Zeng, Xiaodong, Zeng, Xubin, 2010. Technical description of version 4.0 of the Community Land Model (CLM), NCAR Tech. Note NCAR/TN-478+STR. https://doi.org/10.5065/D6FB50WZ

Oster, J., Warken, S., Sekhon, N., Arienzo, M., Lachniet, M., 2019. Speleothem Paleoclimatology for the Caribbean, Central America, and North America. Quaternary 2, 5. https://doi.org/10.3390/quat2010005

Otto-Bliesner, B.L., Braconnot, P., Harrison, S.P., Lunt, D.J., Abe-Ouchi, A., Albani, S., Bartlein, P.J., Capron, E., Carlson, A.E., Dutton, A., Fischer, H., Goelzer, H., Govin, A., Haywood, A., Joos, F., LeGrande, A.N., Lipscomb, W.H., Lohmann, G., Mahowald, N.,

Nehrbass-Ahles, C., Pausata, F.S.R., Peterschmitt, J.-Y., Phipps, S.J., Renssen, H., Zhang, Q., 2017. The PMIP4 contribution to CMIP6 – Part 2: Two interglacials, scientific objective and experimental design for Holocene and Last Interglacial simulations. Geosci. Model Dev. 10, 3979–4003. https://doi.org/10.5194/gmd-10-3979-2017

Pascale, S., Boos, W.R., Bordoni, S., Delworth, T.L., Kapnick, S.B., Murakami, H., Vecchi, G.A., Zhang, W., 2017. Weakening of the North American monsoon with global warming. Nat. Clim. Chang. 7, 806–812. https://doi.org/10.1038/nclimate3412

Pascale, S., Kapnick, S.B., Bordoni, S., Delworth, T.L., 2018. The influence of CO2 forcing on North American monsoon moisture surges. J. Clim. 31, 7949–7968. https://doi.org/10.1175/JCLI-D-18-0007.1

Pausata, F.S.R., Emanuel, K.A., Chiacchio, M., Diro, G.T., Zhang, Q., Sushama, L., Stager, J.C., Donnelly, J.P., 2017a. Tropical cyclone activity enhanced by Sahara greening and reduced dust emissions during the African Humid Period. Proc. Natl. Acad. Sci. U. S. A. https://doi.org/10.1073/pnas.1619111114

Pausata, F.S.R., Messori, G., Zhang, Q., 2016. Impacts of dust reduction on the northward expansion of the African monsoon during the Green Sahara period. Earth Planet. Sci. Lett. 434, 298–307. https://doi.org/10.1016/j.epsl.2015.11.049

Pausata, F.S.R., Qiong, Z., Muschitiello, F., Lu, Z., Chafik, L., Niedermeyer, E.M., Stager, J.C., Cobb, K.M., Liu, Z., 2017b. Greening of the Sahara suppressed ENSO activity during the Mid-Holocene. Nat. Geosci. under rev. https://doi.org/10.1038/ncomms16020

Peltier, W.R., Argus, D.F., Drummond, R., 2015. Space geodesy constrains ice age terminal deglaciation: The global ICE-6G_C (VM5a) model. J. Geophys. Res. Solid Earth 120, 450–487. https://doi.org/10.1002/2014JB011176

Ray, A.J., Garfin, G.M., Wilder, M., Vásquez-León, M., Lenart, M., Comrie, A.C., 2007. Applications of Monsoon Research: Opportunities to Inform Decision Making and Reduce Regional Vulnerability. J. Clim. 20, 1608–1627. https://doi.org/10.1175/JCLI4098.1

Risi, C., Bony, S., Vimeux, F., 2008. Influence of convective processes on the isotopic composition (δ 18 O and δ D) of precipitation and water vapor in the tropics: 2. Physical interpretation of the amount effect. J. Geophys. Res. 113, D19306. https://doi.org/10.1029/2008JD009943

Schwendike, J., Govekar, P., Reeder, M.J., Wardle, R., Berry, G.J., Jakob, C., 2014. Local

partitioning of the overturning circulation in the tropics and the connection to the Hadley and Walker circulations. J. Geophys. Res. Atmos. 119, 1322–1339. https://doi.org/10.1002/2013JD020742

Shi, X., Lohmann, G., Sidorenko, D., Yang, H., 2020. Early-Holocene simulations using different forcings and resolutions in AWI-ESM. The Holocene 30, 996–1015. https://doi.org/10.1177/0959683620908634

Sun, W., Wang, B., Zhang, Q., Pausata, F.S.R., Chen, D., Lu, G., Yan, M., Ning, L., Liu, J., 2019. Northern Hemisphere land monsoon precipitation increased by the Green Sahara during mid-Holocene. Geophys. Res. Lett. 2019GL082116. https://doi.org/10.1029/2019GL082116

Tabor, C., Otto-Bliesner, B., Liu, Z., 2020. Speleothems of South American and Asian Monsoons Influenced by a Green Sahara. Geophys. Res. Lett. 1–11. https://doi.org/10.1029/2020gl089695

Thompson, A.J., Skinner, C.B., Poulsen, C.J., Zhu, J., 2019. Modulation of Mid-Holocene African Rainfall by Dust Aerosol Direct and Indirect Effects. Geophys. Res. Lett. 46, 3917–3926. https://doi.org/10.1029/2018GL081225

Thompson, A.J., Tabor, C.R., Poulsen, C.J., Skinner, C.B., 2021. Water isotopic constraints on the enhancement of the mid-Holocene West African monsoon. Earth Planet. Sci. Lett. 554, 116677. https://doi.org/10.1016/j.epsl.2020.116677

Tierney, J.E., Pausata, F.S.R., DeMenocal, P.B., 2017. Rainfall regimes of the Green Sahara. Sci. Adv. 3, e1601503. https://doi.org/10.1126/sciadv.1601503

Truebe, S.A., 2016. PAST CLIMATE , MODERN CAVES , AND FUTURE RESOURCE MANAGEMENT IN SPELEOTHEM PALEOCLIMATOLOGY: A Dissertation Submitted to the Faculty of the DEPARTMENT OF GEOSCIENCES In Partial Fulfillment of the Requirements For the Degree of DOCTOR OF PHILOSOPHY In the .

Wackerbarth, A., Scholz, D., Fohlmeister, J., Mangini, A., 2010. Modelling the δ18O value of cave drip water and speleothem calcite. Earth Planet. Sci. Lett. 299, 387–397. https://doi.org/10.1016/j.epsl.2010.09.019

Wagner, J.D.M., Cole, J.E., Beck, J.W., Patchett, P.J., Henderson, G.M., Barnett, H.R., 2010. Moisture variability in the southwestern United States linked to abrupt glacial climate change. Nat. Geosci. 3, 110–113. https://doi.org/10.1038/ngeo707

Wang, B., Ding, Q., 2008. Global monsoon: Dominant mode of annual variation in the tropics. Dyn. Atmos. Ocean. 44, 165–183. https://doi.org/10.1016/j.dynatmoce.2007.05.002

Wong, T.E., Nusbaumer, J., Noone, D.C., 2017. Evaluation of modeled land-atmosphere exchanges with a comprehensive water isotope fractionation scheme in version 4 of the Community Land Model. J. Adv. Model. Earth Syst. 9, 978–1001. https://doi.org/10.1002/2016MS000842

Yuan, D., Cheng, H., Edwards, R.L., Dykoski, C.A., Kelly, M.J., Zhang, M., Qing, J., Lin, Y., Wang, Y., Wu, J., Dorale, J., Zhisheng, A., Cai, Y., 2004. Timing, Duration, and Transitions of the Last Interglacial Asian Monsoon. Science (80-.). 304, 575–578. https://doi.org/10.1126/science.1091220

Chapter 5 Holocene Thermal Maximum Driven by Northern Hemisphere Vegetation Change

Co-authors: Jiang Zhu, Christopher J. Poulsen, Jessica E. Tierney, and Christopher B. Skinner

5.1 Abstract

The Holocene thermal maximum, a period of global warmth in early to mid-Holocene proxy reconstructions, is highly controversial. Model simulations of the Holocene have not reproduced this warming, leading to a model-data disagreement known as the Holocene Temperature Conundrum. Pollen records document an expansion of vegetation in the early and mid-Holocene African Sahara and Northern Hemisphere mid- and high latitudes, which has been overlooked in previous modeling studies. Here, we use time slice simulations of the Community Earth System Model to assess the impact of Northern Hemisphere vegetation change on Holocene annual mean temperatures. Our simulations indicate that expansion of Northern Hemisphere vegetation 9,000 and 6,000 years ago warms the Earth's surface by ~0.8 and 0.7°C, respectively, and largely resolves the conundrum in global and regional temperatures. Our results suggest that vegetation change is critical for reconstructing Holocene temperature evolution and highlight its role in driving a mid-Holocene temperature maximum.

5.2 Introduction

Paleoclimate reconstructions from the Temperature12k database, a global compilation of temperature proxies from 679 sites (hereafter referred to as T12K), suggest a gradual cooling of ~0.5°C from the Holocene thermal maximum (HTM) in the early to mid-Holocene (~8–6 ka BP; thousand years before present) to the preindustrial era (PI) (*1*, *2*). In contrast, climate models simulate global warming of ~0.5°C through the Holocene (*3*). This model-data mismatch, termed the "Holocene Temperature Conundrum", exposes uncertainty in our understanding of the ways in which the climate system responded to changes in insolation, greenhouse gases, ice cover, and

vegetation during the Holocene (*4*, *5*). Although some studies have raised the possibility that the HTM could reflect seasonal biases in the proxies (*6*), it appears to be robust in records that are interpreted as annual (*7*, *8*).

The warming trend shown in transient model experiments (*3*, *9*, *10*) is a predictable response to declining ice cover, modestly increasing greenhouse gas concentrations, and orbital-induced variations in insolation. Thus, assuming the T12K proxy trend is correct, the Holocene Temperature Conundrum may be attributable to the exclusion of additional relevant climate forcings. Some previous studies have examined the possible role of dust (*11*) and Arctic amplification (*12*) in increasing early and mid-Holocene annual temperatures. However, these studies either fail to show an HTM and cooling thereafter in annual temperatures or exclude other important forcings that are known to impact Holocene temperatures, such as changes in greenhouse gases.

One possible forcing mechanism that has not been thoroughly explored in modeling studies is the expansion of Holocene vegetation. Pollen records from the early and mid-Holocene show that grass and shrub vegetation expanded in the African Sahara (*13*, *14*), temperate deciduous forest cover increased in the Northern Hemisphere (NH) mid-latitudes (*15–17*), and boreal forest replaced tundra in the Arctic (*18–20*). Increases in vegetation cover warm the land surface by enhancing surface absorption of shortwave radiation directly through lowered albedo (*21*, *22*) and indirectly through limiting dust mobilization (*23*). While the impacts of NH vegetation change on regional Holocene climate, especially the African Sahara (*22–26*), have been widely studied, their effect on global annual temperatures is poorly understood. Furthermore, while some previous modeling studies have attempted to include the role of vegetation change with dynamic simulation of vegetation, they have failed to reproduce the vegetation extent inferred from pollen and, as a result, have likely underestimated vegetation-forced warming (*3*, *24*, *27*).

In this study, we use the Community Earth System Model (CESM1.2) to investigate the impact that NH vegetation change in the Holocene has on increasing annual temperatures and reducing model-proxy disagreement. We perform simulations for 9, 6, 3 ka BP and the PI with varying prescriptions of vegetation in the African Sahara, NH mid-latitudes, and Arctic (Table S5.1). In each Holocene experiment, we systematically increase vegetation cover from the PI extent to show the effect of regional vegetation change on regional and global surface temperatures (Figure S5.1). We then compare the results from our simulations with existing proxy

reconstructions from T12K. Our results highlight the role of vegetation in driving past climate change.

5.3 Results

5.3.1 Global temperature response to vegetation

The incorporation of Holocene vegetation change in our simulations drives a mid-Holocene thermal maximum and largely resolves the Holocene Temperature Conundrum by producing a closer match to the global mean temperature anomalies in proxy composite curves (Figure 5.1). Relative to simulations with PI vegetation (orange circles), simulated global temperatures increase by ~0.8 and 0.7°C at 9 and 6 ka BP (darkest green circles; *9ka* and *6ka*), respectively, with vegetation change over the African Sahara, NH mid-latitudes, and Arctic, and by ~0.2°C at 3 ka BP (tan circle; *3ka*) with partial vegetation change over the Sahara and NH mid-latitudes. These increases in NH vegetation place our simulated temperature anomalies within the 1σ range of the median of T12K individual reconstructions (black line, see 5.5 Materials and Methods). Our simulated annual temperature anomalies are somewhat colder than the Marcott et al. (*28*) reconstruction, which is based on a more limited proxy collection than T12K and may be biased by strong cooling trends in some North Atlantic sea surface temperature (SST) records (*3*, *7*).

Our Holocene simulations demonstrate that increased vegetation cover is a plausible mechanism for resolving the model-data discrepancy in Holocene temperatures. Without regional vegetation change (orange circles; $9ka_{PI\_VEG}$, etc.), our simulated temperature anomalies are colder than the T12K curve by as much as ~1.1°C (Figure 5.1), following the previous warming trends in CCSM3 and Paleoclimate Model Intercomparison simulations (*29*). Furthermore, the timing and magnitude of the HTM in our annual temperature anomalies correspond well with the T12K curve, suggesting that the ~8–6 ka BP peak is likely a result of both a waning ice sheet and vegetation change. In comparing proxy reconstructions with our boreal summer (JJA: June, July, August) global mean temperature anomalies, we find that our simulations no longer match T12K and instead shift the timing of the HTM to 9 ka BP (Figure S5.2), in line with NH JJA insolation (*4*). JJA temperature anomalies in CCSM3 simulations, where dynamical simulation of vegetation did not adequately produce changes inferred from pollen records, remain colder than T12K, especially

at 6 ka BP (Figure S5.2, blue line). This further suggests that vegetation, and not boreal summer bias, produces the observed warming.

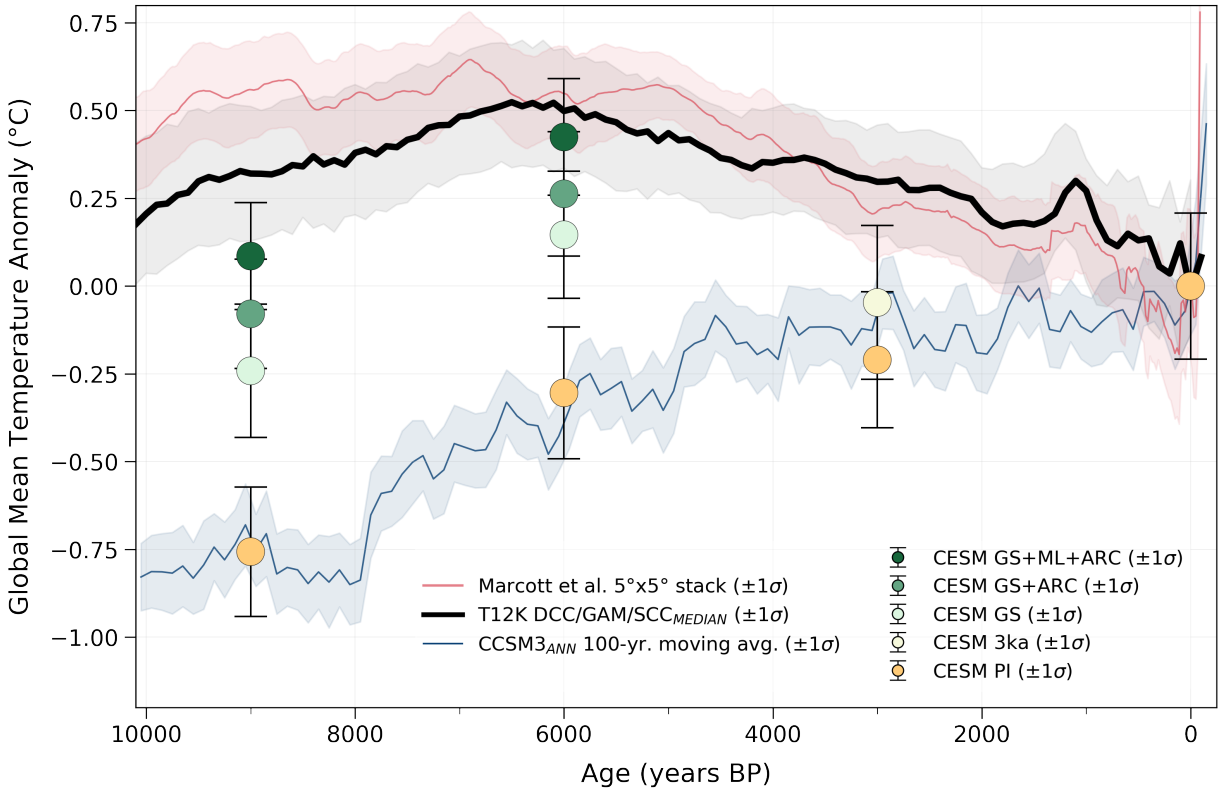

Figure 5.1. Model-proxy comparison of global mean surface temperature anomalies relative to 1850 CE. Colored circles show CESM1.2 annual global mean surface temperature anomalies (± one standard deviation) for all simulations with various degrees of increased NH vegetation (GS = Green Sahara; ML = mid-latitude greening, ARC = Arctic greening; 3 ka = partial vegetation changes in the Sahara and NH mid-latitudes; PI = PI vegetational extent; see 5.5 Materials and Methods and Table S5.1). Our simulated temperature anomalies are compared with the Marcott et al. (*28*) global standard 5°×5° temperature stack (red line ± one standard deviation, n=73), median of T12K individual reconstructions (DCC: Dynamic Calibrated Composite; GAM: General Additive Model; SCC: Standard Calibrated Composite; black line ± one standard deviation; n=679) (*1*), and the simulated global mean temperature anomalies from a transient CCSM3 simulation from the TraCE-21ka experiment (*30*, *31*) shown as the 100-year moving average ± one standard deviation from each 100-year interval.

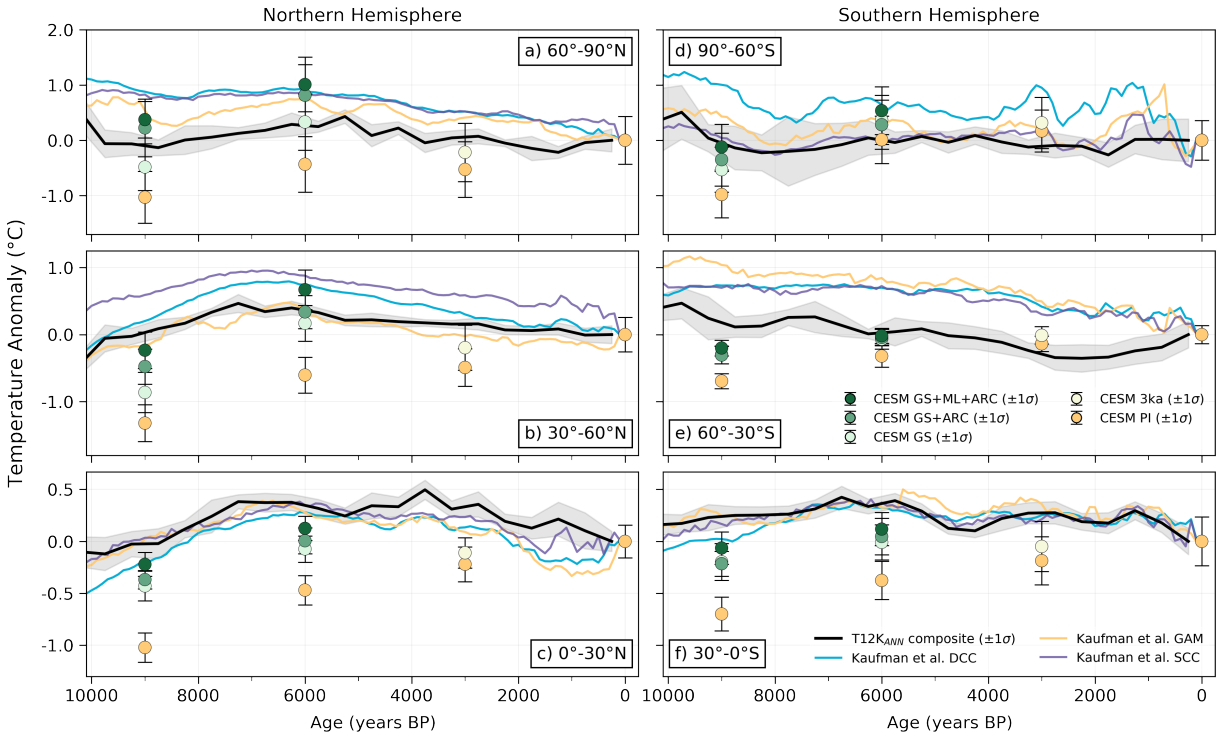

Figure 5.2. Model-proxy comparison of zonally averaged surface temperature anomalies relative to 1850 CE. Colored circles show zonally averaged annual CESM1.2 surface temperature anomalies (± one standard deviation) calculated only from model grid cells corresponding to the T12K$_{ANN}$ composite. Simulated temperature anomalies are compared at each 30° latitude band with the T12K$_{ANN}$ composite (black line ± one standard deviation) (*2*) and individual statistical reconstructions of mean surface temperature anomalies from T12K (DCC, blue line: Dynamic Calibrated Composite; GAM, orange line: General Additive Model; SCC, purple line: Standard Calibrated Composite) (*1*). Note the differences in y-axis values between latitude bands. Number of proxy records from T12K$_{ANN}$ in each latitude band are a) 71, b) 295, c) 89, d) 11, e) 31, and f) 83.

5.3.2 Regional warming by vegetation

The incorporation of vegetation change in our Holocene simulations also largely resolves the model-data discrepancy in zonally distributed temperature (Figure 5.2). Since Holocene temperature anomalies vary regionally in proxy reconstructions, with the largest warming taking place in the high latitudes and lessening towards the equator (*1–3*), any mechanism (i.e., vegetation cover) used to explain the Holocene Temperature Conundrum must also account for this heterogeneity in temperature anomalies. As such, we compare our model results with T12K proxies, from both annual composites (hereafter referred to as T12K$_{ANN}$) and individual reconstructions of mean surface temperature (see 5.5 Materials and Methods), across six zonal bands (Figure 5.2). Our simulations with PI vegetation (orange circles) fail to capture the reconstructed anomalies at all latitude bands and are, on average, colder than the T12K$_{ANN}$

composite anomalies at 9, 6, and 3 ka BP by 1.0°C, 0.6°C, and 0.3°C, respectively. The simulations with specified vegetation change simulate warmer temperatures north of 30°S and more closely match the proxies (*1*, *2*). North of 30°N, some of our vegetated simulations exceed the temperature anomalies from $T12K_{ANN}$, but still align with the T12K individual reconstructions of mean surface temperature (Figure 5.2a-b). South of 30°S, low data density (31 or fewer records in 30–60°S and 11 records in 60–90°S) likely increases the uncertainty in model-data comparison and precludes a robust assessment for these regions, although the simulations with vegetation change appear to match the data better at 9 ka BP (Figure 5.2d-e).

Since 9 and 6 ka BP experience large vegetation-induced warming in our simulations, we evaluate the spatial agreement in annual temperature between our simulations and the $T12K_{ANN}$ composite at these two time slices for six regions: North America, Greenland, Europe, South America, Africa, and Asia-Pacific (Table 5.1). These regions include all annual composite records north of 60°S in a compilation encompassing both terrestrial and marine records (Figure S5.3). The few open ocean records are grouped with the closest geographical terrestrial and ocean margin records. Antarctica is excluded from this analysis as low data density below 60°S inhibits robust conclusions for this region.

For our spatial analysis, we compare the temperature difference (ΔT) between 9 or 6 ka BP and the PI between $T12K_{ANN}$ and our simulations. To illustrate the improvement in model-data agreement due to NH vegetation change, we quantify the difference in model-data agreement between simulations with NH vegetation change (e.g., $9ka–PI_{CONTROL}$) and PI vegetation (e.g., $9ka_{PI\_VEG}–PI_{CONTROL}$) (see 5.5 Materials and Methods). To quantitatively assess the improvements in model-data agreement, we calculate the differences in weighted Cohen's κ statistic, the percentage of nearest-neighbor model grid cells that agree in sign of ΔT, and root-mean-square error (RMSE) normalized by the number of proxy records present in each region (see 5.5 Materials and Methods).

We find better model-data agreement in ~81% of categories across the six regions due to NH vegetation change in our simulations (Table 5.1). The strongest improvements occur in Asia-Pacific, Africa, and Europe, regions directly impacted by the prescribed vegetation expansion, and in South America, a region with known teleconnections to the African land surface (*32*). In these regions, on average, the weighted Cohen's κ statistic increases by 0.17, the nearest-neighbor grid cells that agree in sign increases by 38.6%, and RMSE decreases by 0.17°C. In North America,

where prescribed vegetation change also occurs, modest improvements in these categories may result from uncertainties relating to the Laurentide Ice Sheet at 9 ka BP and enhanced warming north of 70°N where few proxy records exist. Mixed improvement in model-data agreement due to vegetation change occurs in Greenland, likely as a result of low proxy data density and Greenland's distance from prescribed vegetation change (*33*).

Table 5.1. Regional improvement in model-data agreement by Northern Hemisphere vegetation change. Comparison between CESM1.2 and T12K$_{ANN}$ composite shown as increased agreement (green) and decreased agreement (brown), shaded by degree of change. Detailed description of each method can be found in 5.5 Materials and Methods and 5.8 Supplementary Information.

	Impact of 9 ka BP vegetation (9ka – 9ka$_{PI_VEG}$)				***Impact of 6 ka BP vegetation (6ka – 6ka$_{PI_VEG}$)***			
Region	***Number of records***	***Δ(Cohen's κ)***	***Δ(% Cells agree in sign with nearest-neighbor)***	***Δ(RMSE/ record) (°C)***	***Number of records***	***Δ(Cohen's κ)***	***Δ(% Cells agree in sign with nearest-neighbor)***	***Δ(RMSE/ record) (°C)***
North America	103	+0.05	+5.7%	−0.25	137	−0.01	+7.6%	+0.08
Greenland	17	+0.01	+16.7%	−0.16	18	−0.32	−33.3%	+0.45
Europe	103	+0.26	+37.1%	−0.13	120	+0.13	+38.9%	−0.28
South America	20	−0.04	+20.0%	−0.06	24	+0.13	+66.7%	−0.11
Africa	46	+0.15	+25.9%	−0.27	47	+0.25	+46.4%	−0.10
Asia-Pacific	54	+0.19	+36.4%	−0.23	56	+0.29	+37.1%	−0.17

5.3.3 Global temperature response to dust

Increased NH vegetation cover also resulted in reduced dust aerosol loading in 9 and 6 ka BP (*34*, *35*), which itself has been suggested as a potential solution to the Holocene Temperature Conundrum (*11*). To investigate vegetation-induced dust forcing at 6 ka BP, where we see the largest simulated anomalous warming, we run two additional sensitivity experiments that highlight the global temperature response to dust reduction with and without NH vegetation change (see 5.5 Materials and Methods). To test the response without NH vegetation change, we first run a simulation referred to as "*6ka$_{PI_VEG_LOWDUST}$*" that is identical to *6ka$_{PI_VEG}$* but has 72% lower dust aerosol optical depth (AOD) (Table S5.1). In this sensitivity experiment, reduced dust does not lead to an increase in the global temperature anomaly (Figure 5.3). Furthermore, to test the global

temperature response to a hypothetical dust reduction with NH vegetation change, we run an additional simulation referred to as "*6ka*$_{HIGHDUST}$" that is identical to *6ka* (with NH vegetation expansion) but has extremely high dust AOD (~400% higher than *6ka*$_{PI\_VEG}$; dust AOD of ~0.1 versus ~0.005 in *6ka*; Table S5.1). The hypothetical high dust loading in *6ka*$_{HIGHDUST}$ decreases the global temperature anomaly by ~0.25°C (Figure 5.3), compared to *6ka*. This result demonstrates that the total warming due to the combined effect of increased vegetation and reduced dust at 6 ka BP (*6ka*–*6ka*$_{PI\_VEG}$), which is approximately 0.73°C, is primarily the result of direct vegetation change because an extreme reduction in dust can at most explain ~35% of this warming.

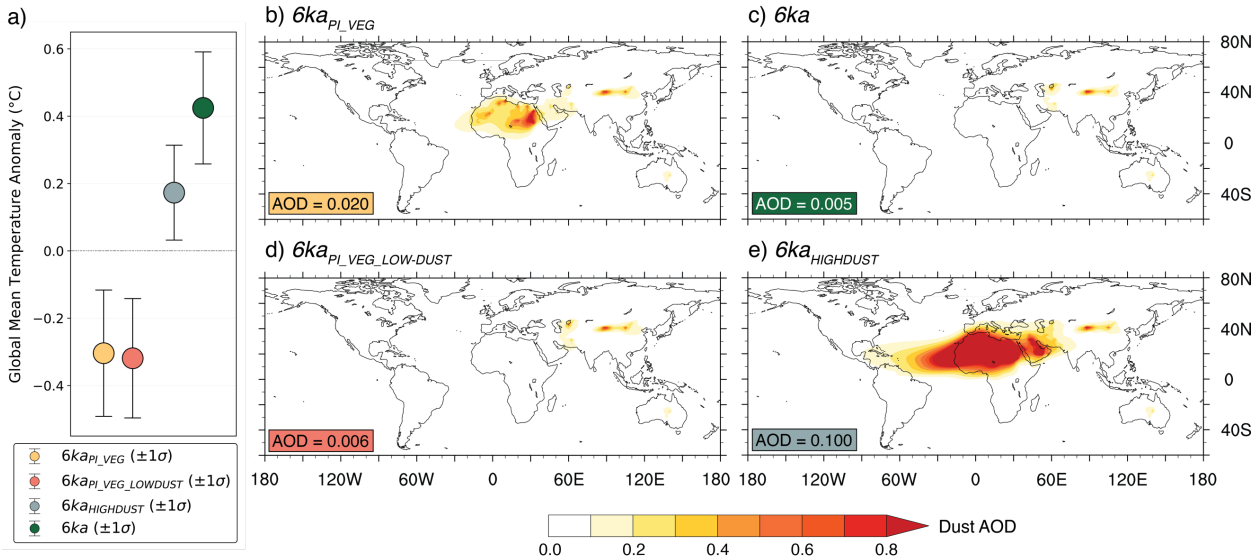

Figure 5.3. Global temperature change as a result of dust during 6 ka BP. a) Annual global mean surface temperature anomalies (relative to *PI*$_{CONTROL}$) for *6ka*$_{PI\_VEG}$ (far left), *6ka*$_{PI\_VEG\_LOWDUST}$ (middle left), *6ka*$_{HIGHDUST}$ (middle right), and *6ka* (far right). Annual dust aerosol optical depth (AOD) shown in b)–e). Global mean dust AOD for each simulation is reported with its corresponding color to a) in the bottom left of each panel.

5.3.4 Mechanism for warming

In accordance with previous studies (*21*, *36*, *37*), we find that vegetation-induced changes in surface albedo largely drive the increase in regional surface temperatures. We diagnose the shortwave (SW) radiative effect of NH vegetation change in 6 ka BP sensitivity experiments using approximate partial radiative perturbation (APRP) analysis (*38*) (see 5.5 Materials and Methods). We find that the SW radiative forcing associated with changes in vegetation albedo is +2.41 W/m^2

(Table S5.2), of which +1.91 W/m^2 comes from greening of the African Sahara where the shift from bare ground (desert) in the PI to shrub and grassland in 6 ka BP decreases albedo in our model by as much as 0.29 (*39*). The change in SW forcing by albedo outweighs modest decreases in global radiative feedbacks from clouds and non-cloud constituents (i.e., aerosols). Greening of the African Sahara leads to an increase in the net surface radiative flux of +15 W/m^2 and contributes to surface warming at all latitudes (Figure 5.4). Warming is particularly large in the Arctic, where NH vegetation amplifies warming initially driven primarily by sea ice loss (*12*).

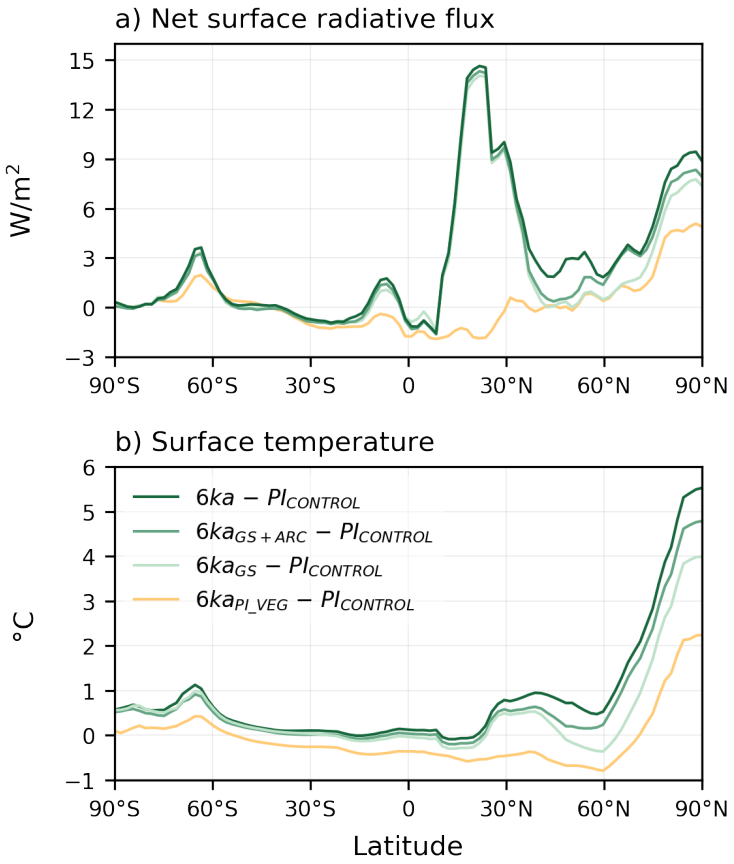

Figure 5.4. Contributions of radiative fluxes to surface warming. Annual zonal mean anomalies (relative to $PI_{CONTROL}$) of a) net surface radiative flux (shortwave–longwave) and b) surface temperature for 6 ka BP sensitivity experiments: $6ka_{PI\_VEG}$ (orange), $6ka_{GS}$ (light green), $6ka_{GS+ARC}$ (green), and *6ka* (darkest green).

5.4 Discussion

5.4.1 Potential biases in model-proxy comparison

Although T12K represents the best global proxy compilation to date, it still may exhibit spatial bias since the majority of available temperature proxies in T12K come from terrestrial sites in the NH mid-latitudes (*1*, *2*). In fact, only ~16% of T12K records are from the Southern Hemisphere and ~6% are from the high (>70°N) northern latitudes. The lack of high-latitude records may partly explain why our simulated Arctic temperatures are warmer than T12K composites (Figures 5.2 and S5.3). This is also supported by a recent study of early Holocene ice, lake, and marine records from Greenland that indicate better agreement with our simulated temperatures than with the few records from T12K (*40*). We also find that our simulated global mean temperature anomalies at 6 ka BP are ~0.2°C higher than when the global temperature is calculated using only model grid cells at the $T12K_{ANN}$ sites (comparison between Figures 5.1 and S5.4). This suggests that the uneven spatial distribution of $T12K_{ANN}$ sites likely leads to an underestimation of the HTM if a simple area-weighted mean is used (see 5.5 Materials and Methods).

Other potential biases may exist in the sensitivity of our model, CESM1.2, to the degree of our prescribed changes in NH vegetation. Our prescribed NH vegetation change is larger than previous studies (*3*, *30*, *31*), and so may partially contribute to the simulated large warming. For instance, we follow PMIP4 Tier 2 protocol that calls for 100% vegetation cover in the African Sahara (*41*) as opposed to a mixed environment with shrubs, grasses, and bare ground (*13*, *14*). As previous work has shown, differences in plant type and diversity when simulating the Green Sahara can affect the resulting climate (*42*). However, our choices of prescribed vegetation are rooted in evidence from several pollen studies (*5*, *13*, *14*, *19*, *20*) and highlight the significant ways in which changes in vegetation impacted Holocene climate. Future work can use climate models with updated dynamic vegetation schemes to further refine Holocene estimates of NH vegetation change and its subsequent impact on global temperature.

5.4.2 Reconstruction of the Holocene thermal maximum

Our results show that vegetation-induced warming gives rise to a Holocene thermal maximum at 6 ka BP, followed by a cooling trend towards the PI. In contrast, our simulations that

do not include the NH vegetation expansion, but only account for changes in orbital insolation, greenhouse gases, and ice cover, predict long-term warming through the Holocene.

Our findings differ from those of recent studies that suggest that seasonal biasing in proxy records was the source of the HTM (*6*, *43*). We attribute this disparity to the location of their records and their SST-only approach. These recent studies interpret their reconstructions as being indicative of global temperature, despite the fact that they represent tropical and sub-tropical SSTs, which have been shown to exhibit a muted HTM signal when compared to air temperatures from higher latitudes (*44*). To test the assumption that their records represent global temperatures, we estimate the average 6 ka BP SST using only model grid cells corresponding to the tropical and subtropical locations from (*6*). We find that this average SST is ~0.25°C colder than the global mean air temperature at 6 ka BP (Figure S5.5), implying that the SST-only proxy reconstructions are not representative of global mean air temperatures. Whether or not the other records from T12K, the majority of which are terrestrial pollen records, exhibit a seasonal bias that is not accounted for in the reconstruction technique remains an open question (*3*, *6*), yet one recent study of European pollen records suggests that they do represent annual temperature (*8*).

In summary, we show that the HTM is a robust feature in simulated annual global mean air temperatures, driven largely by NH vegetation change in our model simulations, and matches closely with the anomalies from T12K. Our results demonstrate that vegetation is the primary driver of the observed HTM and that other mechanisms, such as dust, ice cover, orbital forcing, or greenhouse gases, cannot directly account for the proxy-inferred early- and mid-Holocene warming without the changes in NH vegetation. Our findings further highlight the substantial influence of vegetation expansion and contraction on global climate. These results demonstrate that IPCC-class models (e.g., CESM1.2) can simulate a realistic temperature response to external climate forcings, but only when all relevant forcings are included. Our findings imply that future climate projections that include changes in vegetation are likely to produce more trustworthy predictions of future climate change.

5.5 Materials and Methods

5.5.1 Climate model simulations

We ran the fully coupled Community Earth System Model version 1.2 (CESM1.2) at 3,000-year intervals between 9 ka BP and the PI. The full list of simulations and respective parameters, boundary conditions, and variables of interest can be found in Table S5.1. CESM1.2 is composed of the Community Atmosphere Model version 5.3 (CAM5), Community Land Model 4.0 (CLM4), Community Ice Code version 4.0 (CICE4), Parallel Ocean Program version 2 (POP2), River Transport Model, and a coupler connecting them (*45*). The atmosphere model, with 30 vertical levels, and the land model, with 15 soil-column layers (*39*), were run with a grid resolution of 1.9°×2.5° while the ocean model was run with nominal 1° resolution. Each simulation contained orbital forcing, greenhouse gas concentrations (CO_2, CH_4, and N_2O), and ice sheet reconstruction from the ICE-6G (*46*) consistent with its respective time period. All simulations were run until top-of-atmosphere energy imbalance was less than 0.1 W/m^2. When calculating annual mean temperature, we adjusted values and weighted by the change in fraction of each month to account for the paleo calendar-effect (*47*). Climatologies were calculated from the last 50 years of each simulation.

To isolate the impact of NH regional vegetation change, we performed sensitivity experiments for 9, 6, and 3 ka BP (Table S5.1). Each of these simulations contained climate parameters (orbit year, GHGs, ice cover) for their respective time period and were compared to both a preindustrial control simulation entitled "$PI_{CONTROL}$" and a simulation for each time period containing prescribed vegetation consistent with the PI, entitled "$9ka_{PI\_VEG}$," "$6ka_{PI\_VEG}$," and "$3ka_{PI\_VEG}$" (orange boxes in Figure S5.1 and orange circles in Figure 5.1). Details of the $PI_{CONTROL}$ and $3ka_{PI\_VEG}$ simulations can be found in Tierney et al. (*48*) and Zhu & Poulsen (*49*). Vegetation phenology was prescribed in accordance with satellite observations, demonstrating a best estimate for PI vegetation. Subsequent variations in vegetation change were performed for 9, 6, and 3 ka BP in the African Sahara, NH mid-latitudes, and Arctic (Figure S5.6).

5.5.2 Prescribed vegetation

For both 9 and 6 ka BP, vegetation was incrementally increased in the African Sahara, NH mid-latitudes, and Arctic in accordance with PMIP4 Tier 2 guidelines (*41*) and evidence from

pollen records (*5*, *13*, *14*, *19*, *20*). We accounted for the Green Sahara, which expanded grass and shrub vegetation and enhanced the African hydrologic cycle (*13*, *14*, *23–25*), in a sensitivity experiment entitled "*9ka*$_{GS}$" and "*6ka*$_{GS}$" for 9 and 6 ka BP. This experiment greened the African Sahara by replacing bare ground desert with 100% shrub at ~10–25°N and 100% C_4 grass at 25–35°N (Figure S5.6a; light green boxes in Figure S5.1 and light green circles in Figure 5.1). Since vegetation replaced bare ground in these simulations, we prescribed leaf area index with summer values reaching as high as 3.0 for shrublands and 1.5 for grasslands. We accounted for increases in Arctic rainfall and plant available moisture that led to replacement of tundra by boreal forest (*5*, *15*, *17–20*) with another sensitivity experiment entitled "*9ka*$_{GS+ARC}$" and "*6ka*$_{GS+ARC}$." This experiment added greening of the Arctic, through replacement of all C_3 grass north of 50°N with boreal forest, to the previously mentioned Saharan greening (Figure S5.6b; green boxes in Figure S5.1 and green circles in Figure 5.1). Lastly, we accounted for increases in NH mid-latitude rainfall and plant available moisture that expanded temperate deciduous forest cover (*5*, *15–17*) with a sensitivity experiment entitled "*9ka*" and "*6ka*." This experiment added NH mid-latitude greening, through replacement of C_3 grass between 30–60°N with deciduous forest, to the previously mentioned Saharan and Arctic greening (Figure S5.6c; dark green boxes in Figure S5.1 and dark green circles in Figure 5.1).

At 3 ka BP, pollen records (*18*, *50*) suggest a slight increase in moisture that may have shifted the boundary between the African Sahel and Sahara north by ~3–5° of latitude (*51*), while the extent of temperate deciduous forest expanded (*15*). A sensitivity experiment entitled "*3ka*" accounted for these changes by shifting the Sahara/Sahel boundary north by 5° of latitude through prescription of shrub from ~10–16°N and replacing 50% of C_3 grassland between 40 and 60°N with deciduous forest (Figure S5.6d; tan box in Figure S5.1 and tan circle in Figure 5.1).

5.5.4 Dust experiments

Two additional sensitivity experiments were performed at 6 ka BP to isolate the impact of reduced dust emissions with and without NH vegetation change (Figure 5.3). The simulation entitled "*6ka*$_{PI\_VEG\_LOWDUST}$" contained a PI vegetational extent with dust emissions lowered to 6 ka BP levels, in accordance with reconstructions (*34*, *35*, *52*, *53*), and the simulation entitled "*6ka*$_{HIGHDUST}$" contained identical prescribed NH vegetation as *6ka* but allowed for dust mobilization as if the vegetation were the PI extent (Table S5.1). While *6ka*$_{HIGHDUST}$ increased dust

aerosol optical depth by nearly 400% compared to $6ka_{PI\_VEG}$, it enabled us to calculate an extreme high endmember contribution of reduced dust to global temperature change. This was not meant to be a realistic simulation but rather provided for quantification of the maximum possible contribution of dust in increasing global temperatures. In CESM1.2, the dust model prohibits dust from mobilizing when leaf area index exceeds 0.3 (*39*); however, these two 6 ka BP sensitivity experiments were modified to not follow this rule. $6ka_{PI\_VEG\_LOWDUST}$ did not mobilize dust even in areas with leaf area index less than 0.3 and $6ka_{HIGHDUST}$ mobilized dust in areas where leaf area index exceeded 0.3. All other 9 and 6 ka BP experiments that included increased NH vegetation followed this rule and, as a result, had greatly reduced dust aerosol loading relative to $PI_{CONTROL}$ (Table S5.1).

5.5.5 APRP feedback analysis

To calculate the shortwave radiative effects of NH vegetation change at 6 ka BP, we used the approximate partial radiative perturbation (APRP) method (*38*). This method isolated the top-of-atmosphere shortwave radiative responses of surface albedo, cloud, and non-cloud atmospheric constituents to vegetation change in 6 ka BP sensitivity experiments relative to $6ka_{PI\_VEG}$ (Table S5.2). SW forcing has been shown to play the predominant role in vegetation-induced warming (*21*, *37*, *54*, *55*), so we neglected longwave forcing, which requires more extensive calculation (*56*). For this analysis, we used a climatology of the last 100 years of model output for the 6 ka BP sensitivity experiments and last 50 years for $6ka_{PI\_VEG}$.

5.5.6 T12K temperature proxy composites

We utilized temperature proxy records from the T12K database (*57*) to compare with our CESM1.2 simulations. All model-data comparisons in this study are presented as temperature anomalies with respect to the PI (1850 CE). For our global model-data comparison (Figure 5.1), we compared our simulated annual global mean surface temperature anomalies against the median value of three T12K statistical reconstructions of global mean surface temperature anomalies over the Holocene (DCC: Dynamic Calibrated Composite, GAM: General Additive Model, SCC: Standard Calibrated Composite) (*1*). Each of these three reconstructions utilized a different statistical approach to aggregate annual and seasonally biased T12K proxies from 679 sites into a

single time series of global temperature anomalies. We excluded PAI (Pairwise Comparison) and CPS (Composite Plus Scale) from our analysis due to their unrealistically high temperature anomalies. We calculated our global average temperature anomalies by weighting each 30° zonal value by its proportion of global area in accordance with (*1*). In our regional comparison (Figure 5.2), we showed the three statistical reconstructions (DCC, GAM, and SCC) individually and also compared against a composite of 580 publicly available annually-calibrated records from the T12K database (referred to in this study as $T12K_{ANN}$) (*1*, *2*). In order to compare directly between our modeling results and proxy records, we calculated zonal mean surface temperatures from CESM1.2 by only including model grid cells corresponding to the $T12K_{ANN}$ composite.

We highlighted the time evolution of the median value from T12K individual reconstructions and the simulated global mean temperature anomalies from CESM1.2 to show as close to a global like-for-like comparison as possible in Figure 5.1. When instead calculating the CESM1.2 mean from only model grid cells associated with the annually calibrated proxy reconstructed temperatures from the $T12K_{ANN}$ composite, our simulated temperature anomalies at the HTM were ~0.2°C colder (compare Figures 5.1 and S5.4), showcasing that the uneven sampling distribution of $T12K_{ANN}$ records likely leads to a cold bias in global temperature.

For our spatial comparisons of North America, Greenland, Europe, South America, Africa, and Asia-Pacific, we calculated $T12K_{ANN}$ proxy ΔT as 9 ka BP–PI and 6 ka BP–PI by averaging proxy values between 9.5–8.5 ka BP or 6.5–5.5 ka BP and subtracting from them the PI average of 0.5 ka BP–present. When more than one proxy record was located spatially within the same model grid cell, we averaged the proxy ΔT values to produce a single ΔT value for that grid cell.

5.5.7 Quantification of improvements in model-data agreement

We utilized three distinct methods to quantify the improvement in model-data agreement due to increased NH vegetation at 9 and 6 ka BP (see 5.8 Supplementary Information for more detailed explanations of each method).

First, we assessed the change in the weighted Cohen's κ statistic (*58*, *59*) as a result of increased vegetation. This method has been shown to be a robust measure of model-data agreement (*60*), and we use it here to quantify how well the model and data results agree in sign of ΔT, relative

to their agreement by random chance, by using two distinct categories: "warmer" and "colder." If the model and data are in complete agreement, then $\kappa = 1$, and if there is no agreement between the model and data other than is expected by chance, $\kappa = 0$. Positive values in Table 5.1 indicate higher Cohen's κ values as a result of NH vegetation change and improved model-data agreement.

Second, we calculated the percentage of nearest-neighbor grid cells where both the model and proxy record agreed in sign of ΔT. This method controls for uncertainty in the spatial locations of proxies and their corresponding grid cells in the model by allowing positive matches to occur in adjacent grid cells.

Third, we calculated the change in root-mean-square error (RMSE) normalized by the regional numbers of proxy records, which effectively measured the average difference in ΔT (°C) between each proxy record and its corresponding grid cell in the model. This method is useful for understanding the agreement in overall magnitude of change in model and proxy ΔT.

While inherent uncertainties may exist within the calculation of any one of these methods, analysis of them as a whole provides valuable insight into the regional improvements in model-data agreement brought about by increased NH vegetation and accounts for uncertainties relating to agreement by random chance, alignment of spatial locations in models and proxies, and the overall magnitude of change in ΔT.

5.6 Acknowledgments

The authors thank P. DiNezio for providing initial and boundary condition files for some of the CESM1.2 simulations. **Funding:** This work was supported by National Science Foundation (NSF) award 1602956 to C.J.P. and NSF award AGS-160223 and Heising Simons Foundation award #2016-015 to J.E.T. The CESM project is supported primarily by the NSF. This material is based upon work supported by the National Center for Atmospheric Research, which is a major facility sponsored by the NSF under Cooperative Agreement No. 1852977. Computing and data storage resources, including the Cheyenne supercomputer (doi:10.5065/D6RX99HX), were provided by the Computational and Information Systems Laboratory (CISL) at NCAR. **Author contributions:** A.J.T., J.Z., and C.J.P. designed the study. C.J.P. and J.E.T. secured funding. A.J.T. and J.Z. performed the numerical experiments. A.J.T. performed model-proxy comparison analyses. All authors contributed to the writing and editing of the manuscript. **Competing**

interests: The authors declare that they have no competing interests. **Data and materials availability:** All data needed to evaluate the conclusions in the paper are present in the paper and/or the Supplementary Materials. Additional data related to this paper will be available in a Zenodo repository that can be accessed after this work is published. Further data related to this paper may be requested from A.J.T.

5.7 References

1. D. S. Kaufman, N. McKay, C. Routson, M. Erb, C. Dätwyler, P. S. Sommer, O. Heiri, B. Davis, Holocene global mean surface temperature, a multi-method reconstruction approach. *Sci. Data*. **7**, 201 (2020).
2. D. S. Kaufman, N. P. McKay, C. C. Routson, M. Erb, B. A. S. Davis, O. Heiri, S. Jaccard, J. E. Tierney, C. Dätwyler, Y. Axford, T. Brussel, O. Cartapanis, B. M. Chase, A. Dawson, A. de Vernal, S. Engels, L. Jonkers, J. Marsicek, P. Moffa-Sánchez, C. Morrill, A. Orsi, K. Rehfeld, K. Saunders, P. S. Sommer, E. Thomas, M. Tonello, M. Tóth, R. Vachula, A. Andreev, S. Bertrand, B. Biskaborn, M. Bringué, S. Brooks, M. Caniupán, M. Chevalier, L. Cwynar, J. Emile-Geay, J. Fegyveresi, A. Feurdean, W. Finsinger, M.-C. Fortin, L. Foster, M. Fox, K. Gajewski, M. Grosjean, S. Hausmann, M. Heinrichs, N. Holmes, B. Ilyashuk, E. Ilyashuk, S. Juggins, D. Khider, K. Koinig, P. Langdon, I. Larocque-Tobler, J. Li, A. Lotter, T. Luoto, A. Mackay, E. Magyari, S. Malevich, B. Mark, J. Massaferro, V. Montade, L. Nazarova, E. Novenko, P. Pařil, E. Pearson, M. Peros, R. Pienitz, M. Płóciennik, D. Porinchu, A. Potito, A. Rees, S. Reinemann, S. Roberts, N. Rolland, S. Salonen, A. Self, H. Seppä, S. Shala, J.-M. St-Jacques, B. Stenni, L. Syrykh, P. Tarrats, K. Taylor, V. van den Bos, G. Velle, E. Wahl, I. Walker, J. Wilmshurst, E. Zhang, S. Zhilich, A global database of Holocene paleotemperature records. *Sci. Data*. **7**, 1–34 (2020).
3. Z. Liu, J. Zhu, Y. Rosenthal, X. Zhang, B. L. Otto-Bliesner, A. Timmermann, R. S. Smith, G. Lohmann, W. Zheng, O. E. Timm, The Holocene temperature conundrum. *Proc. Natl. Acad. Sci.* **111**, E3501--E3505 (2014).
4. A. Berger, M. F. Loutre, Insolation values for the climate of the last 10 million years. *Quat. Sci. Rev.* **10**, 297–317 (1991).
5. P. J. Bartlein, S. P. Harrison, S. Brewer, S. Connor, B. A. S. Davis, K. Gajewski, J. Guiot,

T. I. Harrison-Prentice, A. Henderson, O. Peyron, I. C. Prentice, M. Scholze, H. Seppä, B. Shuman, S. Sugita, R. S. Thompson, A. E. Viau, J. Williams, H. Wu, Pollen-based continental climate reconstructions at 6 and 21 ka: a global synthesis. *Clim. Dyn.* **37**, 775–802 (2011).

6. S. Bova, Y. Rosenthal, Z. Liu, S. P. Godad, M. Yan, Seasonal origin of the thermal maxima at the Holocene and the last interglacial. *Nature*. **589**, 548–553 (2021).
7. J. Marsicek, B. N. Shuman, P. J. Bartlein, S. L. Shafer, S. Brewer, Reconciling divergent trends and millennial variations in Holocene temperatures. *Nature*. **554**, 92–96 (2018).
8. C. Martin, G. Ménot, N. Thouveny, O. Peyron, V. Andrieu-Ponel, V. Montade, N. Davtian, M. Reille, E. Bard, Early Holocene Thermal Maximum recorded by branched tetraethers and pollen in Western Europe (Massif Central, France). *Quat. Sci. Rev.* **228** (2020), doi:10.1016/j.quascirev.2019.106109.
9. R. S. Smith, J. Gregory, The last glacial cycle: transient simulations with an AOGCM. *Clim. Dyn.* **38**, 1545–1559 (2012).
10. O. Timm, A. Timmermann, Simulation of the Last 21 000 Years Using Accelerated Transient Boundary Conditions*. *J. Clim.* **20**, 4377–4401 (2007).
11. Y. Liu, M. Zhang, Z. Liu, Y. Xia, Y. Huang, Y. Peng, J. Zhu, A Possible Role of Dust in Resolving the Holocene Temperature Conundrum. *Sci. Rep.* **8**, 1–9 (2018).
12. H. S. Park, S. J. Kim, A. L. Stewart, S. W. Son, K. H. Seo, Mid-Holocene Northern Hemisphere warming driven by Arctic amplification. *Sci. Adv.* **5** (2019), doi:10.1126/sciadv.aax8203.
13. P. Hoelzmann, D. Jolly, S. P. Harrison, F. Laarif, R. Bonnefille, H. Pachur, Mid-Holocene land-surface conditions in northern Africa and the Arabian Peninsula: A data set for the analysis of biogeophysical feedbacks in the climate system. *Global Biogeochem. Cycles*. **12**, 35–51 (1998).
14. D. Jolly, I. C. Prentice, R. Bonnefille, A. Ballouche, M. Bengo, P. Brenac, G. Buchet, D. Burney, J. Cazet, R. Cheddadi, T. Edorh, H. Elenga, S. Elmoutaki, J. Guiot, F. Laarif, H. Lamb, A. Lezine, J. Maley, M. Mbenza, O. Peyron, M. Reille, I. Reynaud-Farrera, G. Riollet, J. C. Ritchie, E. Roche, L. Scott, I. Ssemmanda, H. Straka, M. Umer, E. Van Campo, S. Vilimumbalo, A. Vincens, M. Waller, Biome reconstruction from pollen and plant macrofossil data for Africa and the Arabian peninsula at 0 and 6000 years. *J.*

Biogeogr. **25**, 1007–1027 (1998).

15. H. Binney, M. Edwards, M. Macias-Fauria, A. Lozhkin, P. Anderson, J. O. Kaplan, A. Andreev, E. Bezrukova, T. Blyakharchuk, V. Jankovska, I. Khazina, S. Krivonogov, K. Kremenetski, J. Nield, E. Novenko, N. Ryabogina, N. Solovieva, K. Willis, V. Zernitskaya, Vegetation of Eurasia from the last glacial maximum to present: Key biogeographic patterns. *Quat. Sci. Rev.* **157**, 80–97 (2017).
16. I. C. Prentice, S. P. Harrison, D. Jolly, J. Guiot, The climate and biomes of Europe at 6000 yr BP: Comparison of model simulations and pollen-based reconstructions. *Quat. Sci. Rev.* **17**, 659–668 (1998).
17. P. E. Tarasov, T. Webb, A. A. Andreev, N. B. Afanas'eva, N. A. Berezina, L. G. Bezusko, T. A. Blyakharchuk, N. S. Bolikhovskaya, R. Cheddadi, M. M. Chernavskaya, G. M. Chernova, N. I. Dorofeyuk, V. G. Dirksen, G. A. Elina, L. V. Filimonova, F. Z. Glebov, J. Guiot, V. S. Gunova, S. P. Harrison, D. Jolly, V. I. Khomutova, E. V. Kvavadze, I. M. Osipova, N. K. Panova, I. C. Prentice, L. Saarse, D. V. Sevastyanov, V. S. Volkova, V. P. Zernitskaya, Present-day and mid-Holocene biomes reconstructed from pollen and plant macrofossil data from the former Soviet Union and Mongolia. *J. Biogeogr.* **25**, 1029–1053 (1998).
18. COHMAP Members, Climatic Changes of the Last 18,000 Years: Observations and Model Simulations. *Science (80-.).* **241**, 1043–1052 (1988).
19. N. H. Bigelow, L. B. Brubaker, M. E. Edwards, S. P. Harrison, I. C. Prentice, P. M. Anderson, A. A. Andreev, P. J. Bartlein, T. R. Christensen, W. Cramer, J. O. Kaplan, A. V. Lozhkin, N. V. Matveyeva, D. F. Murray, A. D. McGuire, V. Y. Razzhivin, J. C. Ritchie, B. Smith, D. A. Walker, K. Gajewski, V. Wolf, B. H. Holmqvist, Y. Igarashi, K. Kremenetskii, A. Paus, M. F. J. Pisaric, V. S. Volkova, Climate change and Arctic ecosystems: 1. Vegetation changes north of 55°N between the last glacial maximum, mid-Holocene, and present. *J. Geophys. Res. D Atmos.* **108** (2003), doi:10.1029/2002jd002558.
20. I. C. Prentice, D. Jolly, Mid-Holocene and glacial-maximum vegetation geography of the northern continents and Africa. *J. Biogeogr.* **27**, 507–519 (2000).
21. A. L. Swann, I. Y. Fung, S. Levis, G. B. Bonan, S. C. Doney, Changes in arctic vegetation amplify high-latitude warming through the greenhouse effect. *Proc. Natl. Acad. Sci. U. S. A.* **107**, 1295–1300 (2010).

22. A. L. S. Swann, I. Y. Fung, Y. Liu, J. C. H. Chiang, Remote vegetation feedbacks and the mid-Holocene Green Sahara. *J. Clim.* **27**, 4857–4870 (2014).
23. F. S. R. Pausata, G. Messori, Q. Zhang, Impacts of dust reduction on the northward expansion of the African monsoon during the Green Sahara period. *Earth Planet. Sci. Lett.* **434**, 298–307 (2016).
24. J. E. Tierney, F. S. R. Pausata, P. B. DeMenocal, Rainfall regimes of the Green Sahara. *Sci. Adv.* **3**, e1601503 (2017).
25. A. J. Thompson, C. R. Tabor, C. J. Poulsen, C. B. Skinner, Water isotopic constraints on the enhancement of the mid-Holocene West African monsoon. *Earth Planet. Sci. Lett.* **554**, 116677 (2021).
26. P. O. Hopcroft, P. J. Valdes, W. Ingram, Using the Mid-Holocene "Greening" of the Sahara to Narrow Acceptable Ranges on Climate Model Parameters. *Geophys. Res. Lett.* **48**, 1–20 (2021).
27. S. P. Harrison, P. J. Bartlein, K. Izumi, G. Li, J. Annan, J. Hargreaves, P. Braconnot, M. Kageyama, Evaluation of CMIP5 palaeo-simulations to improve climate projections. *Nat. Clim. Chang.* **5**, 735–743 (2015).
28. S. a. Marcott, J. D. Shakun, P. U. Clark, A. C. Mix, A Reconstruction of Regional and Global Temperature for the Past 11,300 Years. *Science (80-.).* **339**, 1198–1201 (2013).
29. C. M. Brierley, A. Zhao, S. P. Harrison, P. Braconnot, C. J. R. Williams, D. J. R. Thornalley, X. Shi, J. Peterschmitt, R. Ohgaito, D. S. Kaufman, M. Kageyama, J. C. Hargreaves, M. P. Erb, J. Emile-Geay, R. D. D'Agostino, D. Chandan, M. Carré, P. J. Bartlein, W. Zheng, Z. Zhang, Q. Zhang, H. Yang, E. M. Volodin, R. A. Tomas, C. Routson, R. Peltier, B. Otto-Bliesner, P. A. Morozova, N. P. McKay, G. Lohmann, A. N. Legrande, C. Guo, J. Cao, E. Brady, J. D. Annan, A. Abe-Ouchi, Large-scale features and evaluation of the PMIP4-CMIP6 midHolocene simulations. *Clim. Past Discuss.* (2020), doi:10.5194/cp-2019-168.
30. Z. Liu, B. L. Otto-Bliesner, F. He, E. C. Brady, R. Tomas, P. U. Clark, A. E. Carlson, J. Lynch-Stieglitz, W. Curry, E. Brook, D. Erickson, R. Jacob, J. Kutzbach, J. Cheng, Transient Simulation of Last Deglaciation with a New Mechanism for Bolling-Allerod Warming. *Science (80-.).* **325**, 310–314 (2009).
31. F. He, J. D. Shakun, P. U. Clark, A. E. Carlson, Z. Liu, B. L. Otto-Bliesner, J. E.

Kutzbach, Northern Hemisphere forcing of Southern Hemisphere climate during the last deglaciation. *Nature*. **494**, 81–85 (2013).

32. X. Liu, D. S. Battisti, The influence of orbital forcing of tropical insolation on the climate and isotopic composition of precipitation in South America. *J. Clim.* **28**, 4841–4862 (2015).
33. J. A. Badgeley, E. J. Steig, G. J. Hakim, T. J. Fudge, Greenland temperature and precipitation over the last 20 000 years using data assimilation. *Clim. Past*. **16**, 1325–1346 (2020).
34. S. Egerer, M. Claussen, C. Reick, T. Stanelle, The link between marine sediment records and changes in Holocene Saharan landscape: Simulating the dust cycle. *Clim. Past*. **12**, 1009–1027 (2016).
35. S. Albani, N. M. Mahowald, G. Winckler, R. F. Anderson, L. I. Bradtmiller, B. Delmonte, R. François, M. Goman, N. G. Heavens, P. P. Hesse, S. A. Hovan, S. G. Kang, K. E. Kohfeld, H. Lu, V. Maggi, J. A. Mason, P. A. Mayewski, D. McGee, X. Miao, B. L. Otto-Bliesner, A. T. Perry, A. Pourmand, H. M. Roberts, N. Rosenbloom, T. Stevens, J. Sun, Twelve thousand years of dust: The Holocene global dust cycle constrained by natural archives. *Clim. Past*. **11**, 869–903 (2015).
36. A. L. S. Swann, I. Y. Fung, J. C. H. Chiang, Mid-latitude afforestation shifts general circulation and tropical precipitation. *Proc. Natl. Acad. Sci. U. S. A.* **109**, 712–716 (2012).
37. W. Zhang, P. A. Miller, C. Jansson, P. Samuelsson, J. Mao, B. Smith, Self-Amplifying Feedbacks Accelerate Greening and Warming of the Arctic. *Geophys. Res. Lett.* **45**, 7102–7111 (2018).
38. K. E. Taylor, M. Crucifix, P. Braconnot, C. D. Hewitt, C. Doutriaux, A. J. Broccoli, J. F. B. Mitchell, M. J. Webb, Estimating shortwave radiative forcing and response in climate models. *J. Clim.* **20**, 2530–2543 (2007).
39. K. W. Oleson, D. M. Lawrence, B. Gordon, M. G. Flanner, E. Kluzek, J. Peter, S. Levis, S. C. Swenson, E. Thornton, A. Dai, M. Decker, R. Dickinson, J. Feddema, C. L. Heald, J. Lamarque, G. Niu, T. Qian, S. Running, K. Sakaguchi, A. Slater, R. Stöckli, A. Wang, L. Yang, X. Zeng, X. Zeng, "Technical description of version 4.0 of the Community Land Model (CLM)" (2010), , doi:10.5065/D6FB50WZ.
40. Y. Axford, E. C. Osterberg, A. de Vernal, Past warmth and its impacts in Greenland

during the Holocene Thermal Maximum. *Annu. Rev. Earth Planet. Sci.*, 279–307 (2020).

41. B. L. Otto-Bliesner, P. Braconnot, S. P. Harrison, D. J. Lunt, A. Abe-Ouchi, S. Albani, P. J. Bartlein, E. Capron, A. E. Carlson, A. Dutton, H. Fischer, H. Goelzer, A. Govin, A. Haywood, F. Joos, A. N. LeGrande, W. H. Lipscomb, G. Lohmann, N. Mahowald, C. Nehrbass-Ahles, F. S. R. Pausata, J.-Y. Peterschmitt, S. J. Phipps, H. Renssen, Q. Zhang, The PMIP4 contribution to CMIP6 – Part 2: Two interglacials, scientific objective and experimental design for Holocene and Last Interglacial simulations. *Geosci. Model Dev.* **10**, 3979–4003 (2017).
42. M. Claussen, S. Bathiany, V. Brovkin, T. Kleinen, Simulated climate–vegetation interaction in semi-arid regions affected by plant diversity. *Nat. Geosci.* **6**, 954–958 (2013).
43. L. G. Rodriguez, A. L. Cohen, W. Ramirez, D. W. Oppo, A. Pourmand, R. L. Edwards, A. E. Alpert, N. Mollica, Mid-Holocene, Coral-Based Sea Surface Temperatures in the Western Tropical Atlantic. *Paleoceanogr. Paleoclimatology*. **34**, 1234–1245 (2019).
44. H. Renssen, H. Seppä, X. Crosta, H. Goosse, D. M. Roche, Global characterization of the Holocene Thermal Maximum. *Quat. Sci. Rev.* **48**, 7–19 (2012).
45. J. W. Hurrell, M. M. Holland, P. R. Gent, S. Ghan, J. E. Kay, P. J. Kushner, J. F. Lamarque, W. G. Large, D. Lawrence, K. Lindsay, W. H. Lipscomb, M. C. Long, N. Mahowald, D. R. Marsh, R. B. Neale, P. Rasch, S. Vavrus, M. Vertenstein, D. Bader, W. D. Collins, J. J. Hack, J. Kiehl, S. Marshall, The community earth system model: A framework for collaborative research. *Bull. Am. Meteorol. Soc.* **94**, 1339–1360 (2013).
46. W. R. Peltier, D. F. Argus, R. Drummond, Space geodesy constrains ice age terminal deglaciation: The global ICE-6G_C (VM5a) model. *J. Geophys. Res. Solid Earth*. **120**, 450–487 (2015).
47. P. J. Bartlein, S. L. Shafer, Paleo calendar-effect adjustments in time-slice and transient climate-model simulations (PaleoCalAdjust v1.0): impact and strategies for data analysis. *Geosci. Model Dev.* **12**, 3889–3913 (2019).
48. J. E. Tierney, J. Zhu, J. King, S. B. Malevich, G. J. Hakim, C. J. Poulsen, Glacial cooling and climate sensitivity revisited. *Nature*. **584**, 569–573 (2020).
49. J. Zhu, C. J. Poulsen, Last Glacial Maximum (LGM) climate forcing and ocean dynamical feedback and their implications for estimating climate sensitivity. *Clim. Past*. **17**, 253–267

(2021).

50. S. Kröpelin, D. Verschuren, A.-M. Lézine, H. Eggermont, C. Cocquyt, P. Francus, J.-P. Cazet, M. Fagot, B. Rumes, J. M. Russell, F. Darius, D. J. Conley, M. Schuster, H. von Suchodoletz, D. R. Engstrom, Climate-driven ecosystem succession in the Sahara: the past 6000 years. *Science (80-.).* **320**, 765–8 (2008).
51. A. Dallmeyer, M. Claussen, S. J. Lorenz, T. Shanahan, The end of the African humid period as seen by a transient comprehensive Earth system model simulation of the last 8000 years. *Clim. Past*. **16**, 117–140 (2020).
52. J. Adkins, P. DeMenocal, G. Eshel, The "African humid period" and the record of marine upwelling from excess 230Th in Ocean Drilling Program Hole 658C. *Paleoceanography*. **21**, 1–14 (2006).
53. D. McGee, P. B. DeMenocal, G. Winckler, J. B. W. Stuut, L. I. Bradtmiller, The magnitude, timing and abruptness of changes in North African dust deposition over the last 20,000 yr. *Earth Planet. Sci. Lett.* **371**–**372**, 163–176 (2013).
54. G. B. Bonan, D. Pollard, S. L. Thompson, Effects of boreal forest vegetation on global climate. *Nature*. **359**, 716–718 (1992).
55. J. A. Foley, J. E. Kutzbach, M. T. Coe, S. Levis, Feedbacks between climate and boreal forests during the Holocene epoch. *Nature*. **371**, 52–54 (1994).
56. R. Colman, A comparison of climate feedbacks in general circulation models. *Clim. Dyn.* **20**, 865–873 (2003).
57. D. Kaufman, N. McKay, C. Routson, M. Erb, B. Davis, O. Heiri, S. Jaccard, A global database of Holocene paleo-temperature records. *figshare*. **Collection** (2020), doi:10.6084/m9.figshare.c.4705478.v3.
58. J. Cohen, A Coefficient of Agreement for Nominal Scales. *Educ. Psychol. Meas.* **20**, 37–46 (1960).
59. J. Cohen, Weighted kappa: Nominal scale agreement provision for scaled disagreement or partial credit. *Psychol. Bull.* **70**, 213–220 (1968).
60. P. N. DiNezio, J. E. Tierney, The effect of sea level on glacial Indo-Pacific climate. *Nat. Geosci.* **6**, 485–491 (2013).

5.8 Supplementary Information

We utilized three distinct methods for quantifying the improvement in model-data agreement as a result of NH vegetation change at 9 and 6 ka BP: weighted Cohen's κ statistic, the percentage of nearest-neighbor grid cells where both the model and proxy record agree in sign of ΔT, and root-mean-square error (RMSE) normalized by the regional number of proxy records.

To calculate the weighted Cohen's κ statistic for each region, we quantified agreement between the CESM1.2 and $T12K_{ANN}$ using the following categories:

		CESM1.2	
		warmer	colder
$T12K_{ANN}$	warmer	a	c
	colder	b	d

The value of κ was determined by the following equation:

$$\kappa = \frac{p_o - p_e}{1 - p_e}$$

where p_o is defined as the agreement between models and proxies, calculated by:

$$p_o = \frac{a + d}{N}$$

where N is the sum of all elements in each category (i.e., a to d) and p_e is the probability that the models and proxies agree by chance, calculated by:

$$p_e = \left[\frac{a + c}{N} * \frac{a + b}{N}\right] + \left[\frac{b + d}{N} * \frac{c + d}{N}\right]$$

We weight the κ value to penalize for total misses (e.g., if warmer should be colder) by multiplying the matrix above by the following weight matrix:

1	0
0	1

To determine the percentage of nearest-neighbor grid cells where both the model and proxy record agree in sign of ΔT, we defined two categories of model-data agreement ("warmer" or "colder") and calculated the total number of grid cells that exhibit model-data agreement with at least one adjacent model grid cell. The following is an example of adjacent cell agreement:

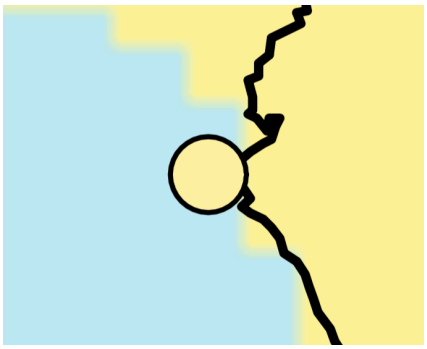

To determine RMSE normalized by the regional number of proxy records, we first calculated the difference (CESM1.2–T12K$_{ANN}$) at each grid cell. The sum of this difference across all regional grid cells was then divided by the total number of proxy records present within the region.

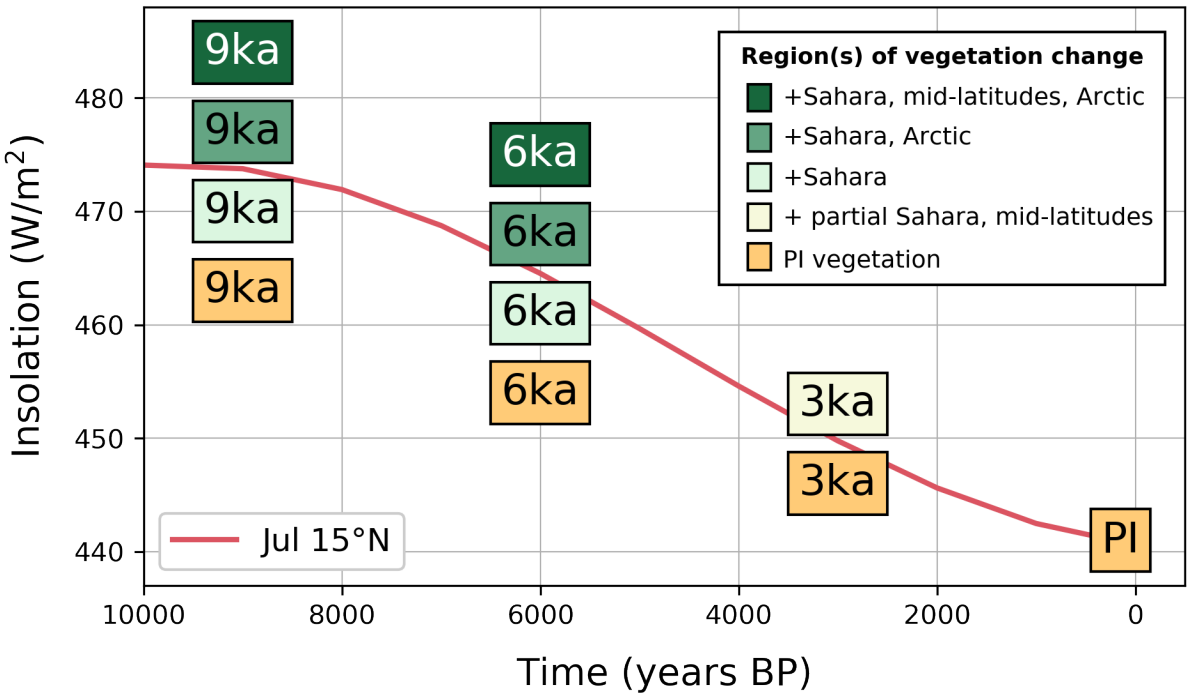

Figure S5.1. Suite of CESM1.2 simulations and respective vegetation modifications performed at each orbit year. Colors represent specified vegetation for each simulation: PI vegetation (orange; used in simulations $PI_{CONTROL}$ and $*_{PI\_VEG}$), 3 ka BP partial Saharan and mid-latitude greening (tan; used in *3ka*), greening of the Sahara (light green; used in $9ka_{GS}$ and $6ka_{GS}$), both Saharan and Arctic greening (green; used in $9ka_{GS+ARC}$ and $6ka_{GS+ARC}$), and Saharan, mid-latitude, and Arctic greening (darkest green; used in *9ka* and *6ka*). See Table S5.1 for details on prescribed vegetation in the Sahara, NH mid-latitudes, and Arctic and Figure S5.6 for details regarding the spatial modification of plant functional types. July insolation at 15°N (red line) is shown for reference (*4*).

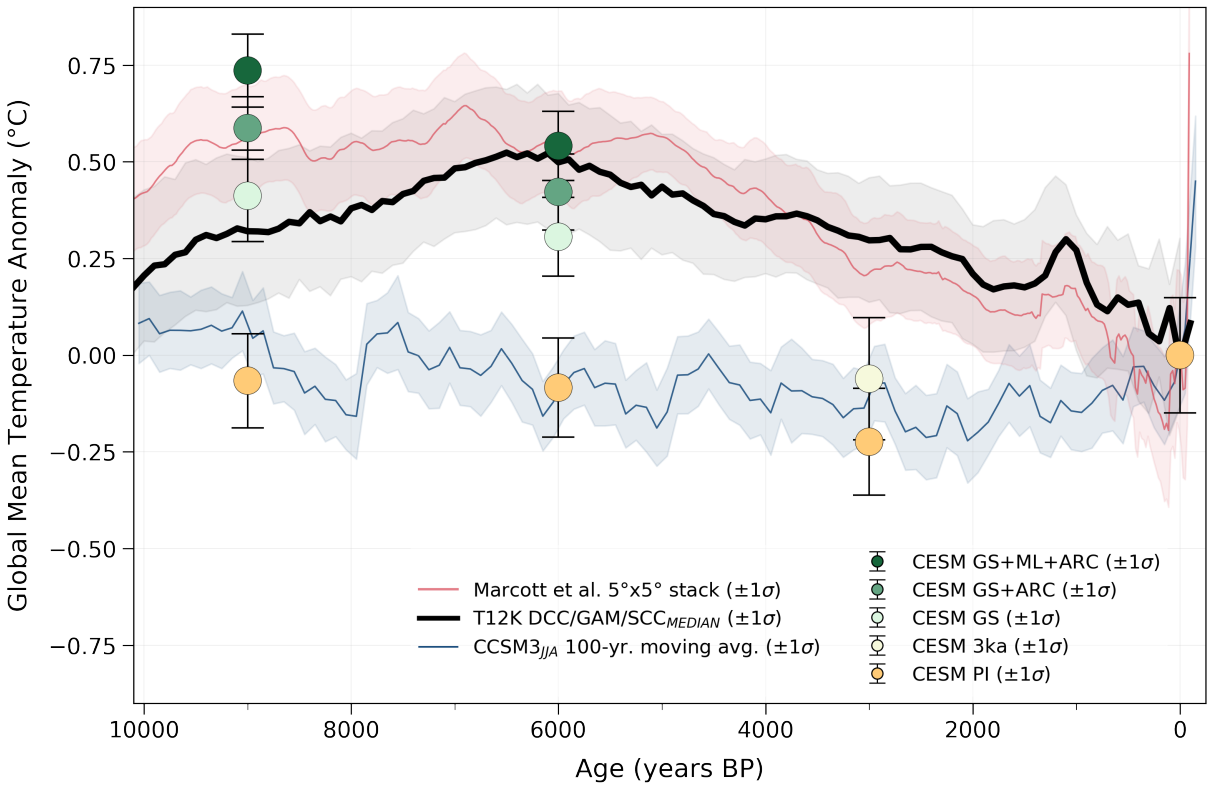

Figure S5.2. Model-proxy comparison of JJA global mean surface temperature anomalies relative to 1850 CE. This plot is identical to Figure 5.1 in the main text, but displays boreal summer (JJA: June, July, August) average CESM1.2 and CCSM3 temperature anomalies.

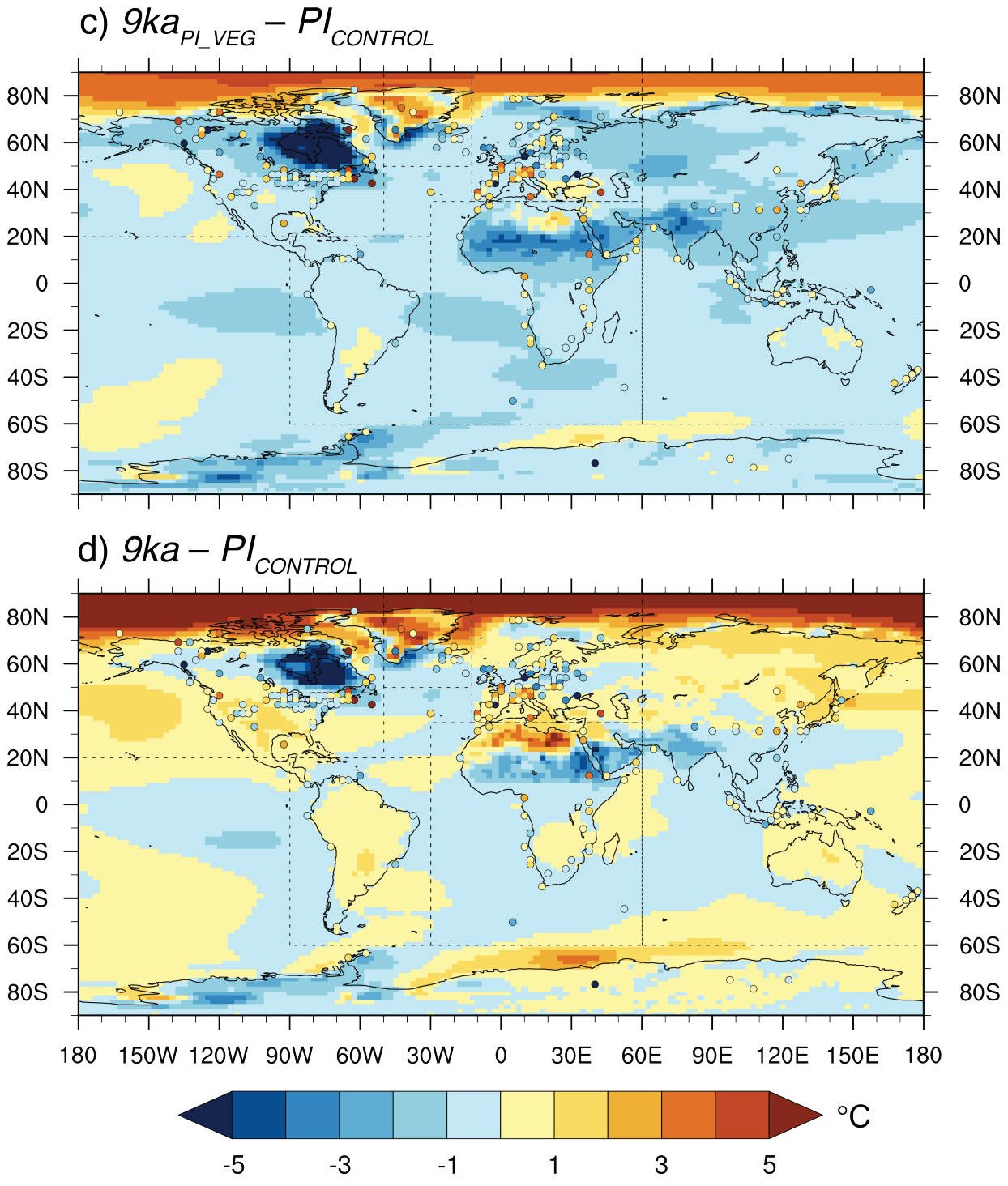
c) 9ka PI_VEG – PI CONTROL
d) 9ka – PI CONTROL
80N
60N
40N
20N
0
20S
40S
60S
80S
180
150W
120W
90W
60W
30W
0
30E
60E
90E
120E
150E
180
°C
-5
-3
-1
1
3
5

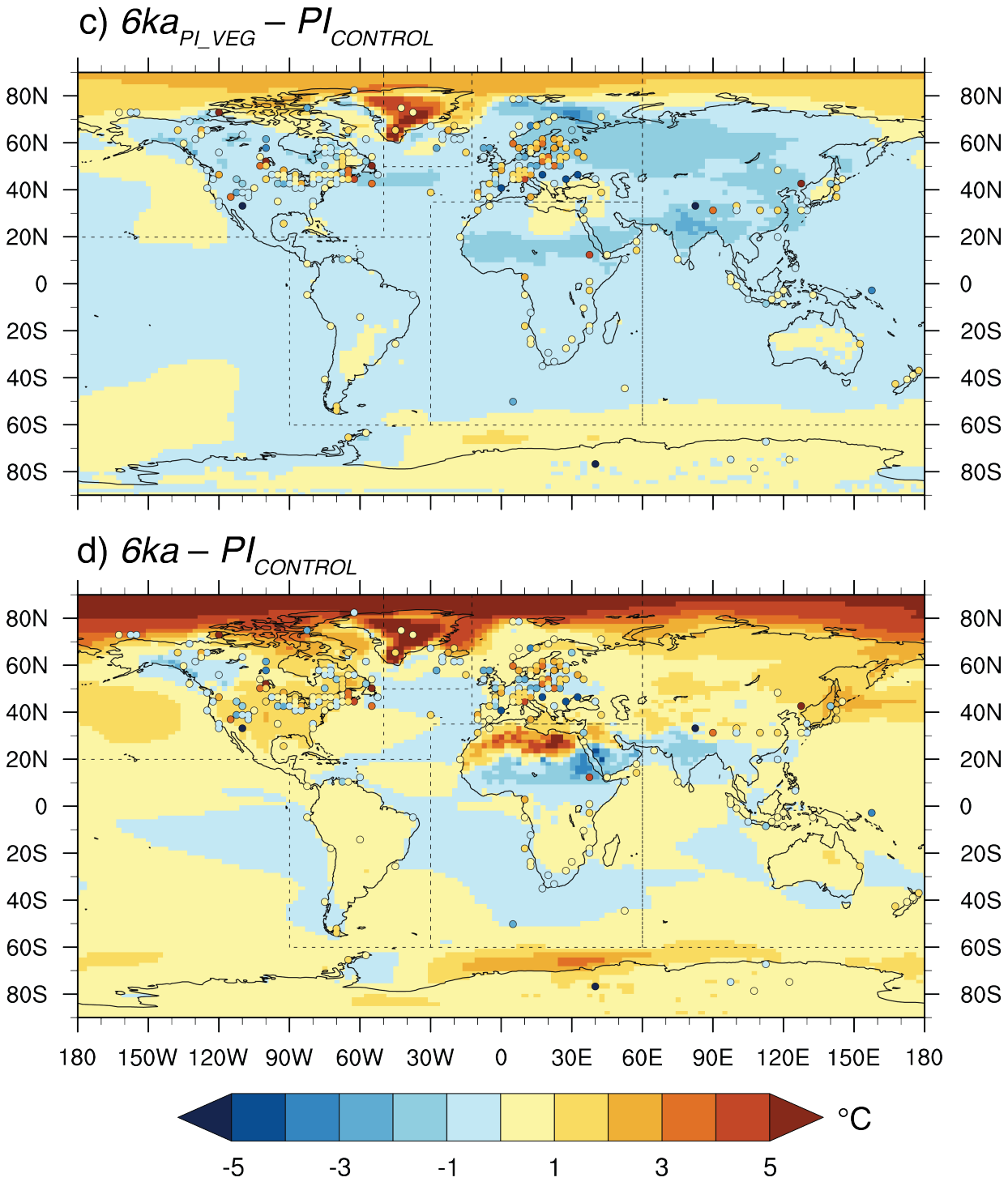

Figure S5.3. Global comparison of annual ΔT between CESM1.2 and the T12K$_{ANN}$ composite. The colors of dots (shading) correspond to a) 9 ka BP – 1850 CE (*9ka$_{PI_VEG}$–PI$_{CONTROL}$*), b) 9 ka BP – 1850 CE (*9ka–PI$_{CONTROL}$*), c) 6 ka BP – 1850 CE (*6ka$_{PI_VEG}$–PI$_{CONTROL}$*), and d) 6 ka BP – 1850 CE (*6ka–PI$_{CONTROL}$*). Regions defined for spatial analysis are shown by dashed black lines. The lone record in the Atlantic Ocean at ~40°N and ~30°W is included with proxies from Europe.

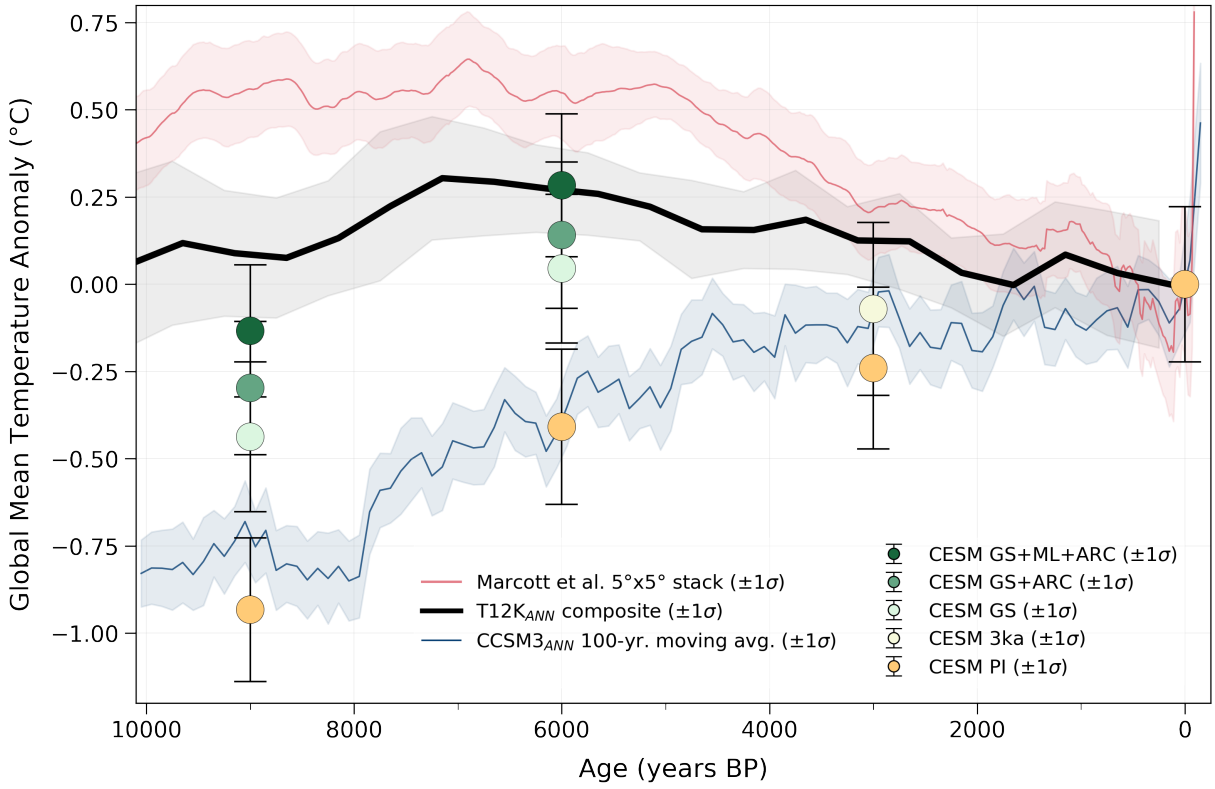

Figure S5.4. Model-proxy comparison of T12K$_{ANN}$ location mean surface temperature anomalies relative to 1850 CE. This plot is identical to Figure 5.1 in the main text but calculates CESM1.2 temperature anomalies as the mean of only grid cells corresponding to the T12K$_{ANN}$ composite (*2*). Comparison between Figure 5.1 and this figure indicates that the global mean temperature anomalies in CESM1.2 are higher than the anomalies from the average of sampled locations in the T12K$_{ANN}$ composite.

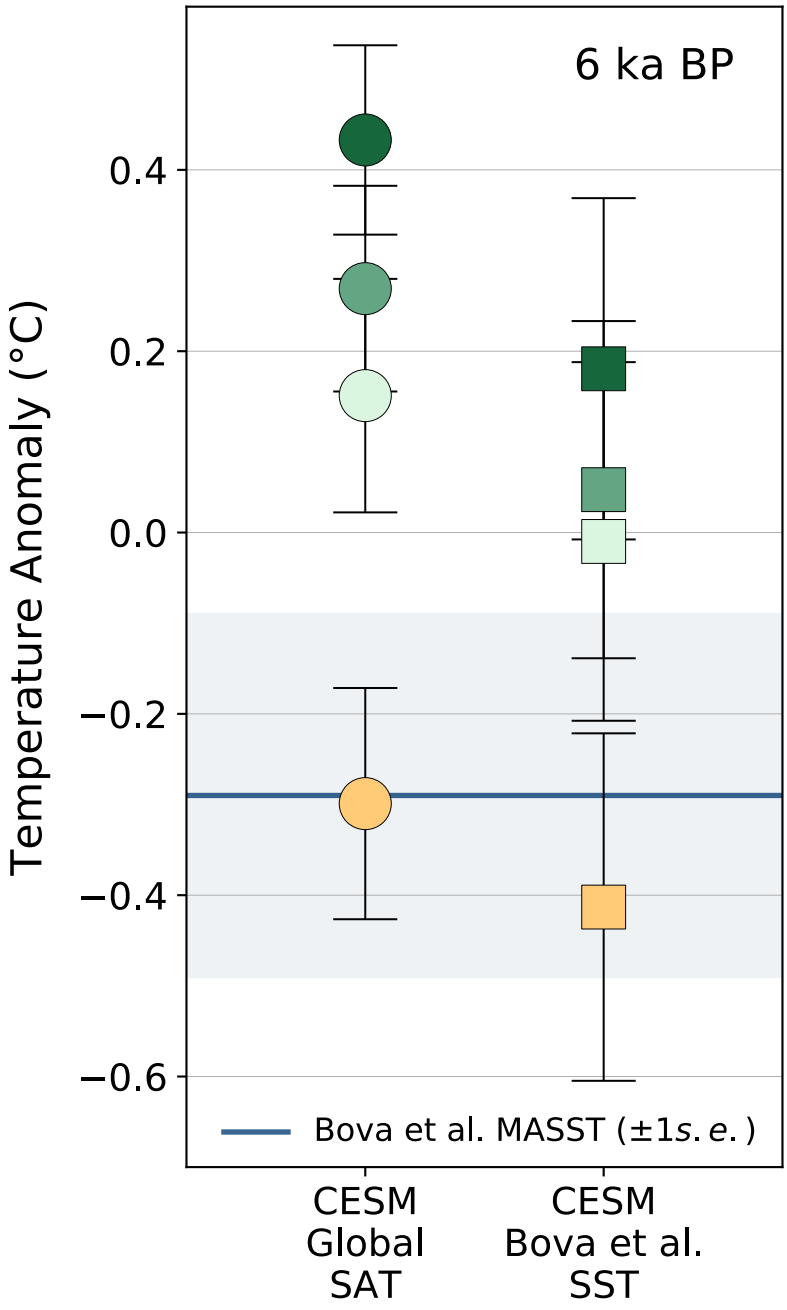

Figure S5.5. Comparison of simulated sea surface temperature at Bova et al. grid cells with global mean air temperature. Simulated CESM1.2 annual anomalies at 6 ka BP of global mean surface air temperature (SAT, circles; left) and mean sea surface temperature (SST, squares) of grid cells corresponding to Bova et al. (*6*) locations (right). The blue line signifies the 6 ka BP mean value ± one standard error from the SST reconstruction by Bova et al. (*6*). Colors are same as Figure 5.1. The differences shown here between global mean SAT and Bova et al. (*6*) grid cell mean SST anomalies demonstrate that the Bova et al. (*6*) reconstruction is not representative of, and is colder than, global mean surface air temperature anomalies.

a) ***6ka*** and ***9ka***: In the African Sahara, shrub/C_4 grass replaces bare ground

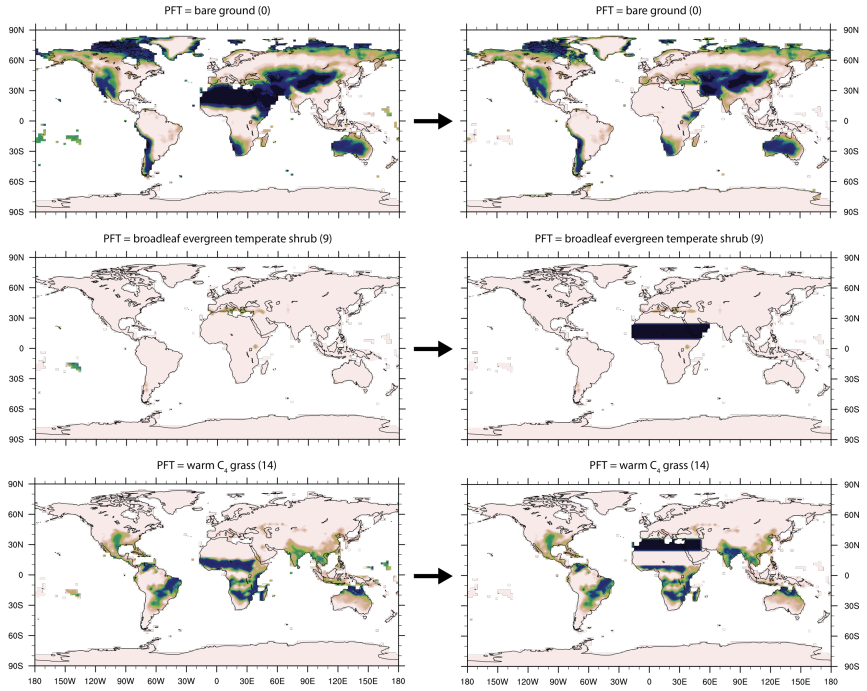

b) ***6ka*** and ***9ka***: In the Arctic north of 50°N, boreal forest replaces C_3 grass

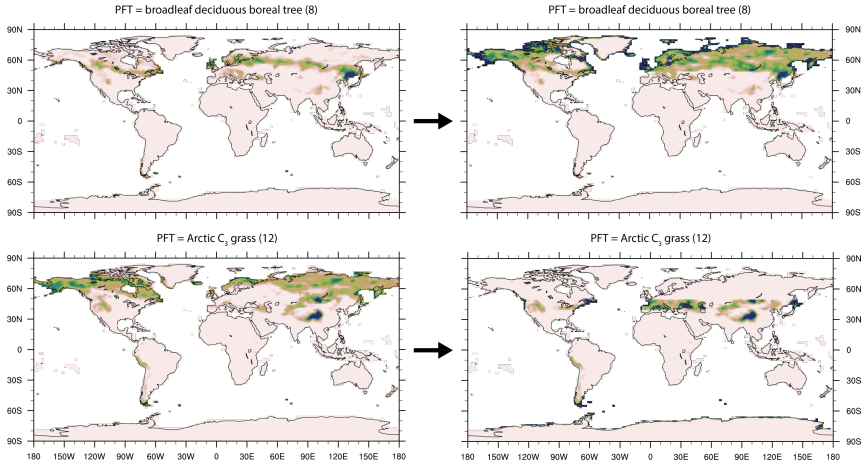

c) ***6ka*** and ***9ka***: In the mid-latitudes between 30°N and 60°N, deciduous forest replaces C_3 grass

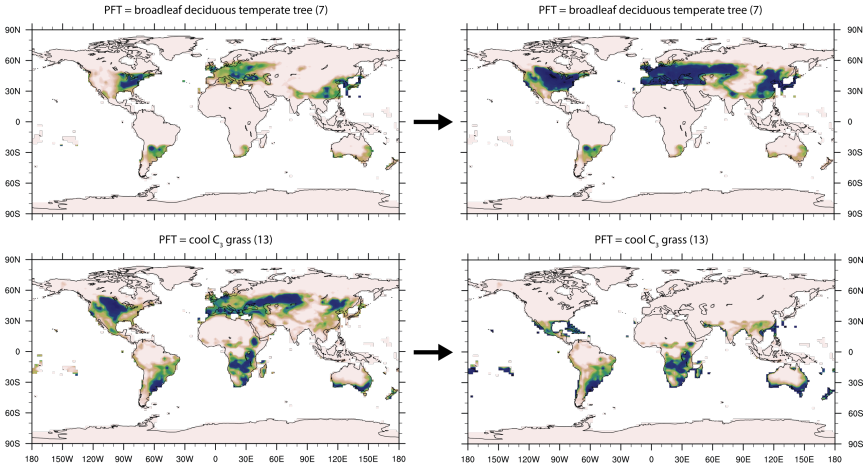

d) ***3ka***: Sahara/Sahel transition shifts ~5° north; between 40 and 60°N, deciduous forest replaces 50% of C_3 grass

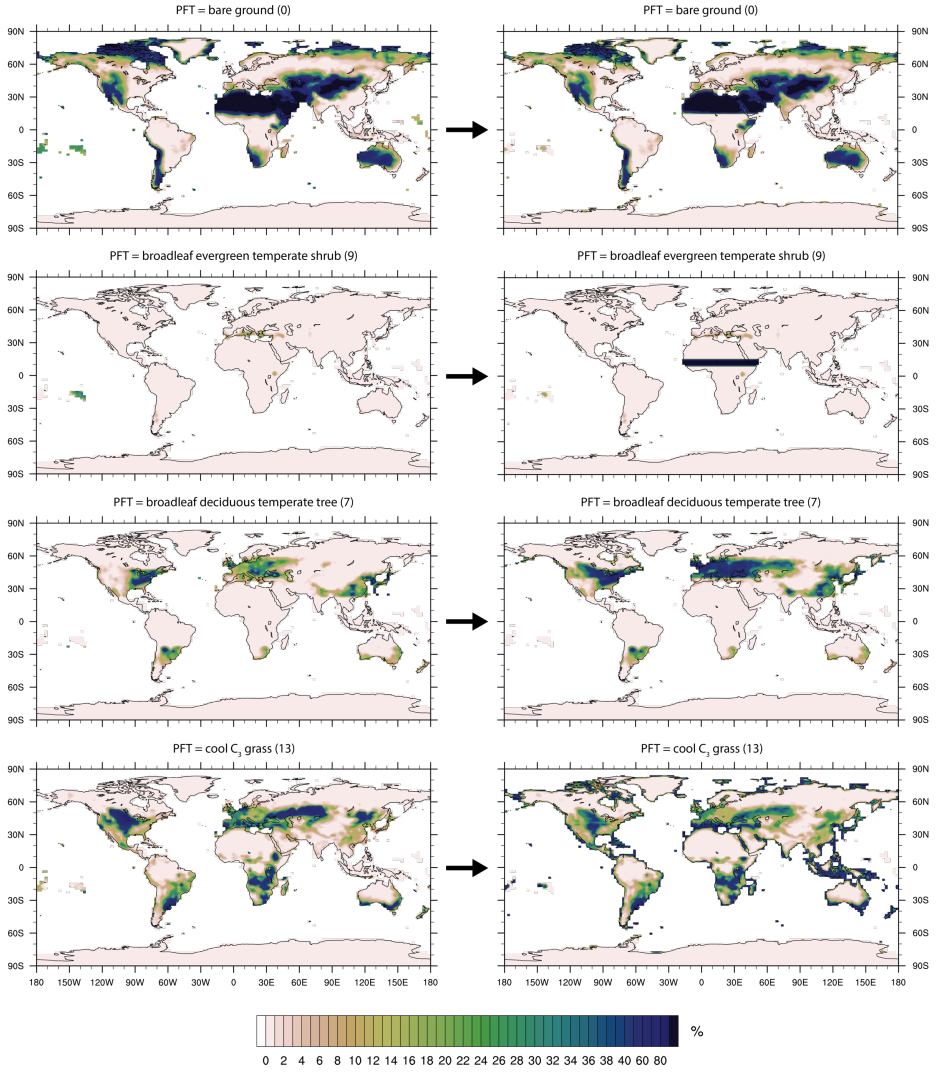

Figure S5.6. Modifications made to plant functional type. (a-c) *9ka* and *6ka* and (d) *3ka*. Numbers correspond to index for the specific plant functional type in CLM4.

Table S5.1. List of all CESM1.2 simulations used in this study. Included are the corresponding colors used for each simulation, details regarding length and branch history, and specifications of orbit year, greenhouse gases, dust loading, and vegetation type in the Northern Hemisphere.

Simulation	*Years Run*	*Branched From*	*Orbit Year*	*CO_2 (ppm)*	*CH_4 (ppb)*	*N_2O (ppb)*	*Global dust (AOD* 10^{-3})*	*Northern Hemisphere Vegetation*		
								Sahara	*Mid-latitudes*	*Arctic*
$PI_{CONTROL}$	900	N/A	1850 CE	284.7	791.6	275.7	23.3	Bare ground	C_3 grass	C_3 grass
$3ka_{PI\_VEG}$	900	N/A	3 ka BP	275.0	580.0	270.0	21.0	Bare ground	C_3 grass	C_3 grass
3ka	200	$3ka_{PI\_VEG}$	3 ka BP	275.0	580.0	270.0	20.4	Shrub to 16°N	50% deciduous forest	C_3 grass
$6ka_{PI\_VEG}$	400	$6ka_{GS+ARC}$	6 ka BP	264.4	597.0	262.0	20.1	Bare ground	C_3 grass	C_3 grass
$6ka_{PI\ VEG\ LOWDUST}$	200	$6ka_{PI\_VEG}$	6 ka BP	264.4	597.0	262.0	5.7	Bare ground	C_3 grass	C_3 grass
$6ka_{GS}$	200	$6ka_{GS+ARC}$	6 ka BP	264.4	597.0	262.0	4.1	Shrub/ C_4 grass	C_3 grass	C_3 grass
$6ka_{GS+ARC}$	900	N/A	6 ka BP	264.4	597.0	262.0	4.1	Shrub/ C_4 grass	C_3 grass	Boreal forest
6ka	200	$6ka_{GS+ARC}$	6 ka BP	264.4	597.0	262.0	4.9	Shrub/ C_4 grass	Deciduous forest	Boreal forest
$6ka_{HIGHDUST}$	200	*6ka*	6 ka BP	264.4	597.0	262.0	99.9	Shrub/ C_4 grass	Deciduous forest	Boreal forest
$9ka_{PI\_VEG}$	300	$9ka_{GS}$	9 ka BP	260.2	658.5	255.0	51.8	Bare ground	C_3 grass	C_3 grass
$9ka_{GS}$	900	N/A	9 ka BP	260.2	658.5	255.0	4.1	Shrub/ C_4 grass	C_3 grass	C_3 grass
$9ka_{GS+ARC}$	250	$9ka_{GS}$	9 ka BP	260.2	658.5	255.0	4.2	Shrub/ C_4 grass	C_3 grass	Boreal forest
9ka	250	$9ka_{GS+ARC}$	9 ka BP	260.2	658.5	255.0	4.9	Shrub/ C_4 grass	Deciduous forest	Boreal forest

Table S5.2. Top-of-atmosphere shortwave radiative responses to vegetation change. Changes are W/m^2 relative to $6ka_{PI\_VEG}$ calculated with the approximate partial radiative perturbation (APRP) method (*38*). α: surface albedo radiative response to vegetation change (Eq. 16a); *cld*: cloud radiative response to vegetation change (Eq. 16b); and *clr*: non-cloud atmospheric constituent radiative response to vegetation change (Eq. 16c).

Experiment	α	*cld*	*clr*
6ka	+2.41	–0.61	–0.02
$6ka_{GS+ARC}$	+2.11	–0.71	–0.04
$6ka_{GS}$	+1.91	–0.79	–0.05

Chapter 6 Conclusion

6.1 Summary of conclusions

This dissertation is a compilation of four chapters that use Earth system models to directly identify the responses of regional and global climate to Holocene land surface change. Comparison of these results with geochemical proxy data highlights the importance of changes to the land surface in the African Sahara and Northern Hemisphere mid- and high latitudes in resolving challenges related to Holocene climate change. This section summarizes the most important findings and implications presented by this dissertation.

6.1.1 Enhancement of the mid-Holocene West African monsoon

Previous modeling studies have underestimated the enhancement of the mid-Holocene West African monsoon inferred from geochemical proxy data (Braconnot et al., 2012; Brierley et al., 2020; Tierney et al., 2017). In past attempts to simulate the monsoonal enhancement, many modeling studies have neglected land surface changes, but concluded that the incorporation of changes in other climate forcings, such as orbital insolation or greenhouse gas concentrations, did not adequately enhance the mid-Holocene West African monsoon (Joussaume et al., 1999; Perez-Sanz et al., 2014). Only recently have some studies accounted for the greening of the African Sahara through changes in vegetation and soil properties, but while their simulations improved alignment of models with proxy data, they did not resolve the many challenges related to reconstructing the response of the West African monsoon to Holocene land surface changes (Hopcroft et al., 2021; Pausata et al., 2016; Skinner and Poulsen, 2016; Tabor et al., 2020).

The collection of Chapters 2 and 3 provide further insight into how African hydroclimate, predominantly the West African monsoon, responds to a variety of land surface changes related to the greening of the Sahara. The most important findings from these chapters help us better quantify the competing effects of dust and vegetation on the mid-Holocene West African monsoon and better constrain its northernmost limit with stable water isotopic analysis. Chapter 2 shows that the

direct radiative effects associated with reduced dust aerosols in the mid-Holocene strongly enhance West African monsoon convective rainfall, but that the indirect aerosol-cloud effects suppress the overall increase in monsoonal rainfall by reducing stratiform rainfall. The direct impacts of vegetation, however, exert a stronger influence on the mid-Holocene West African monsoon than the overall effects of dust aerosols. Chapter 3 highlights a simulated positive anomaly in the isotopic composition of precipitation, due to Saharan greening, that is at odds with interpretations of monsoonal enhancement from leaf wax *n*-alkane and speleothem records. Results from this chapter inform the leaf wax *n*-alkane interpretation in northwestern Africa as likely representing soil water, rather than rainfall, and improve constraints on the northernmost limit of the mid-Holocene West African monsoon, demonstrating that it reached ~23–28°N, in agreement with interpretations from dust and pollen records.

6.1.2 Isotopic signature of the North American monsoon

The opposing signature of isotopic proxy reconstructions representing the North American monsoon, when compared with reconstructions from other Northern Hemisphere land monsoons, contributes to challenges in our understanding of how the North American monsoon evolved since the Last Glacial Maximum and how it responded to various climate forcings (Asmerom et al., 2007; Cai et al., 2012; Dong et al., 2010; Metcalfe et al., 2015; Tierney et al., 2017). Further uncertainty exists because there are only a few continuous isotopic proxy records from this region and no model-data comparisons have been performed thus far that utilize water isotope-enabled models (Hermann et al., 2018; Metcalfe et al., 2015). Chapter 4 addresses these challenges in reconstructing the evolution of the North American monsoon with the hypothesis that positive isotopic anomalies in southwestern North American proxy records during the early and mid-Holocene, in opposition to negative anomalies from African and Asian records, may be due to local Walker circulation impacts associated with the greening of the African Sahara. Without the Green Sahara, the model instead simulates isotopic anomalies that do not match reconstructions from proxy records. Through systematic evaluation of summer and winter hydroclimate, the results of this chapter demonstrate a gradual increase in North American monsoon rainfall in its coastal core region and a potentially large impact on the northern fringe of the monsoon by the Green Sahara. Future work will further address the remaining uncertainties regarding NAM evolution

from the LGM to the PI and strengthen the link between southwestern North American isotopic changes and the greening of the African Sahara.

6.1.3 Holocene thermal maximum and temperature conundrum

The Holocene thermal maximum has been a topic of recent controversy. Temperature proxies generally show the maximum in the early to mid-Holocene, with cooling thereafter, but models have instead simulated gradual warming and some studies have suggested the maximum is a result of seasonal bias in proxy records (Bova et al., 2021; He et al., 2013; Kaufman et al., 2020b, 2020a; Liu et al., 2014). Yet, no modeling studies to date have directly investigated the impact of large pollen-inferred changes in Northern Hemisphere vegetation on annual global mean temperature. Chapter 5 highlights these vegetation changes in the African Sahara and Northern Hemisphere mid- and high latitudes, demonstrating that they directly drive a maximum in Holocene global temperatures. The results from this chapter suggest that the model-data disagreement in temperature reconstructions, known as the Holocene Temperature Conundrum, is largely resolved in global and regional temperatures when the increases in vegetation are included in model simulations. Conclusions from this chapter highlight that Earth system models can simulate a realistic temperature response to external climate forcings, but only when all relevant forcings, including changes to the land surface, are included.

6.2 Synthesis and implications

The most important contributions from this dissertation are highlighting that land surface changes have profound impacts on Holocene climate and their inclusion in Earth system model simulations helps to resolve a variety of challenges relating to hydroclimate in Africa (Chapters 2 and 3) and North America (Chapter 4) and relating to global temperature (Chapter 5). The work presented in this dissertation showcases three overarching conclusions related to understanding how Holocene land surface changes impacted the climate system and can help address several paleoclimate challenges in reconciling model and proxy reconstructions.

1. *Holocene land surface changes have widespread impacts on hydroclimate*. The work presented in this dissertation highlights how the land surface changes associated with the Green Sahara impacted both the West African and North American monsoons. The chapters in this

dissertation are among the first studies to showcase the direct impacts of these land surface changes by explicitly including them in Earth system model simulations.

2. *Holocene land surface changes significantly impacted global temperature*. Reconstruction of global temperature evolution throughout the Holocene has important implications for placing modern anthropogenic global warming in context with the recent past. This dissertation shows that Holocene increases in Northern Hemisphere vegetation impacted global temperature and drove a mid-Holocene thermal maximum.

3. *Models must incorporate land surface changes in order to accurately predict changes in climate*. The chapters in this dissertation demonstrate that Earth system models can simulate realistic climate responses to external climate forcings, but only when all forcings, including land surface changes, are included. This suggests that past and future climate simulations that incorporate changes to the land surface are likely to produce more trustworthy predictions of climate change.

6.3 Future research directions

This dissertation presents important findings for constraining the responses of regional and global climate to Holocene land surface change and further reconciling model simulations with geochemical proxy data. Yet, this work also highlights further disagreements that remain unresolved at the regional and global scale in simulating Holocene climate. The remainder of this section explores potential avenues for future research and proposes several broad questions related to further resolving these challenges in reconstructing past climate change.

1. Are critical mechanisms or feedbacks missing from Earth system models in their simulation of Holocene climate change? The chapters in this dissertation have demonstrated that inclusion of land surface changes, such as vegetation cover or dust aerosol emissions, greatly improves agreement between models and proxies in their reconstruction of regional and global Holocene climate. However, previous Earth system model experiments have lacked several additional mechanisms or feedbacks, likely due to large uncertainties involved with their representation in models. Therefore, it remains unknown whether or not these factors are critical for reconciling models and proxies. For instance, local modifications to Saharan soil properties or the extent of lakes, as well as the human impact on the African land surface through pastoralism, can provide a better understanding of the degree to which the Saharan land surface changed during

the Holocene (Chandan and Peltier, 2020; Wright, 2017) and may provide potential answers for further improving agreement between models and proxies. Additionally, remote teleconnections, potentially through land surface changes in other regions of the world (Swann et al., 2014), may produce large regional climate impacts that are presently unknown.

2. Are important climate processes represented correctly in Earth system models? Alternatively, Earth system model simulations may not align with proxy data in their reconstruction of Holocene climate because of incorrect representation of atmospheric and land surface processes. A range of convective parameterizations, which are critical for simulating a realistic early and mid-Holocene enhancement of Northern Hemisphere land monsoons, have been shown to better align simulated hydroclimate with proxy data (Hopcroft et al., 2021). Therefore, the large uncertainties that exist in the representation of these critical atmospheric processes suggest that further analysis must investigate the range of acceptable parameterizations and how these differences may impact simulation of Holocene climate. The resolution of the model grid may also play a large role in further aligning models with proxy data. This is evidenced by the northernmost African monsoon limit in Chapter 2 (~1° resolution) that reached farther north than in Chapter 3 (~2° resolution). Future work may simulate regional paleoclimate with variable grid resolution, using the method of Huang et al. (2016), to pinpoint the finer local details and potentially resolve outstanding model-data disagreements.

In addition to questions directly related to the representation of climate processes in Earth system models, future work may also focus on a more complete understanding of the transient land surface changes in Holocene climate. This may be done with newly developed dynamic vegetation modeling components, such as the Functionally Assembled Terrestrial Ecosystem Simulator (FATES) model (Fisher et al., 2015), which can simulate the temporal evolution of vegetation demographic changes. Alternatively, additional proxy data, particularly isotopic, should be collected in critical regions, such as the African Sahara or southwestern North America, to improve our understanding of the regional climate and land surface changes that occurred throughout the Holocene.

3. Does incorporation of land surface changes in Earth system model simulations improve model-data disagreements during other past time periods? The research presented in this dissertation highlights the importance of land surface change, through model experiments with prescribed vegetation, in reconciling model-data disagreements in Holocene climate. These

findings potentially imply that this same methodology may be impactful for resolving additional paleoclimate challenges in other past time periods. For example, large model-data disagreements exist in North America during the Last Glacial Maximum (Lora and Ibarra, 2019) and in northern Africa during the last interglacial (Eemian; ~122 to 128 ka BP) (Larrasoaña et al., 2013). Future work can explore the extent to which incorporation of land surface change in Earth system model simulations of these past time periods can resolve these outstanding disagreements.

6.4 References

Asmerom, Y., Polyak, V., Burns, S., Rassmssen, J., 2007. Solar forcing of Holocene climate: New insights from a speleothem record, southwestern United States. Geology 35, 1–4. https://doi.org/10.1130/G22865A.1

Bova, S., Rosenthal, Y., Liu, Z., Godad, S.P., Yan, M., 2021. Seasonal origin of the thermal maxima at the Holocene and the last interglacial. Nature 589, 548–553. https://doi.org/10.1038/s41586-020-03155-x

Braconnot, P., Harrison, S.P., Kageyama, M., Bartlein, P.J., Masson-Delmotte, V., Abe-Ouchi, A., Otto-Bliesner, B., Zhao, Y., 2012. Evaluation of climate models using palaeoclimatic data. Nat. Clim. Chang. 2, 417–424. https://doi.org/10.1038/nclimate1456

Brierley, C.M., Zhao, A., Harrison, S.P., Braconnot, P., Williams, C.J.R., Thornalley, D.J.R., Shi, X., Peterschmitt, J., Ohgaito, R., Kaufman, D.S., Kageyama, M., Hargreaves, J.C., Erb, M.P., Emile-Geay, J., D'Agostino, R.D., Chandan, D., Carré, M., Bartlein, P.J., Zheng, W., Zhang, Z., Zhang, Q., Yang, H., Volodin, E.M., Tomas, R.A., Routson, C., Peltier, R., Otto-Bliesner, B., Morozova, P.A., McKay, N.P., Lohmann, G., Legrande, A.N., Guo, C., Cao, J., Brady, E., Annan, J.D., Abe-Ouchi, A., 2020. Large-scale features and evaluation of the PMIP4-CMIP6 midHolocene simulations. Clim. Past Discuss. https://doi.org/10.5194/cp-2019-168

Cai, Y., Zhang, H., Cheng, H., An, Z., Lawrence Edwards, R., Wang, X., Tan, L., Liang, F., Wang, J., Kelly, M., 2012. The Holocene Indian monsoon variability over the southern Tibetan Plateau and its teleconnections. Earth Planet. Sci. Lett. 335–336, 135–144. https://doi.org/10.1016/j.epsl.2012.04.035

Chandan, D., Peltier, W.R., 2020. African Humid Period Precipitation Sustained by Robust Vegetation, Soil, and Lake Feedbacks. Geophys. Res. Lett. 47, 1–12.

https://doi.org/10.1029/2020GL088728

Dong, J., Yongjin Wang, Hai Cheng, Hardt, B., Edwards, R.L., Xinggong Kong, Jiangying Wu, Shitao Chen, Dianbing Liu, Xiuyang Jiang, Kan Zhao, 2010. A high-resolution stalagmite record of the Holocene East Asian monsoon from Mt Shennongjia, central China. The Holocene 20, 257–264. https://doi.org/10.1177/0959683609350393

Fisher, R.A., Muszala, S., Verteinstein, M., Lawrence, P., Xu, C., McDowell, N.G., Knox, R.G., Koven, C., Holm, J., Rogers, B.M., Spessa, A., Lawrence, D., Bonan, G., 2015. Taking off the training wheels: The properties of a dynamic vegetation model without climate envelopes, CLM4.5(ED). Geosci. Model Dev. 8, 3593–3619. https://doi.org/10.5194/gmd-8-3593-2015

He, F., Shakun, J.D., Clark, P.U., Carlson, A.E., Liu, Z., Otto-Bliesner, B.L., Kutzbach, J.E., 2013. Northern Hemisphere forcing of Southern Hemisphere climate during the last deglaciation. Nature 494, 81–85. https://doi.org/10.1038/nature11822

Hermann, N.W., Oster, J.L., Ibarra, D.E., 2018. Spatial patterns and driving mechanisms of mid-Holocene hydroclimate in western North America. J. Quat. Sci. 33, 421–434. https://doi.org/10.1002/jqs.3023

Hopcroft, P.O., Valdes, P.J., Ingram, W., 2021. Using the Mid-Holocene "Greening" of the Sahara to Narrow Acceptable Ranges on Climate Model Parameters. Geophys. Res. Lett. 48, 1–20. https://doi.org/10.1029/2020GL092043

Huang, X., Rhoades, A.M., Ullrich, P.A., Zarzycki, C.M., 2016. An evaluation of the variable-resolution <scp>CESM</scp> for modeling California's climate. J. Adv. Model. Earth Syst. 8, 345–369. https://doi.org/10.1002/2015MS000559

Joussaume, S., Taylor, K.E., Braconnot, P., Mitchell, J.F.B., Kutzbach, J.E., Harrison, S.P., Prentice, I.C., Broccoli, A.J., Abe-Ouchi, A., Bartlein, P.J., Bonfils, C., Dong, B., Guiot, J., Herterich, K., Hewitt, C.D., Jolly, D., Kim, J.W., Kislov, A., Kitoh, A., Loutre, M.F., Masson, V., McAvaney, B., McFarlane, N., de Noblet, N., Peltier, W.R., Peterschmitt, J.Y., Pollard, D., Rind, D., Royer, J.F., Schlesinger, M.E., Syktus, J., Thompson, S., Valdes, P., Vettoretti, G., Webb, R.S., Wyputta, U., 1999. Monsoon changes for 6000 years ago: Results of 18 simulations from the Paleoclimate Modeling Intercomparison Project (PMIP). Geophys. Res. Lett. 26, 859–862. https://doi.org/10.1029/1999GL900126

Kaufman, D.S., McKay, N., Routson, C., Erb, M., Dätwyler, C., Sommer, P.S., Heiri, O., Davis,

B., 2020a. Holocene global mean surface temperature, a multi-method reconstruction approach. Sci. Data 7, 201. https://doi.org/10.1038/s41597-020-0530-7

Kaufman, D.S., McKay, N.P., Routson, C.C., Erb, M., Davis, B.A.S., Heiri, O., Jaccard, S., Tierney, J.E., Dätwyler, C., Axford, Y., Brussel, T., Cartapanis, O., Chase, B.M., Dawson, A., de Vernal, A., Engels, S., Jonkers, L., Marsicek, J., Moffa-Sánchez, P., Morrill, C., Orsi, A., Rehfeld, K., Saunders, K., Sommer, P.S., Thomas, E., Tonello, M., Tóth, M., Vachula, R., Andreev, A., Bertrand, S., Biskaborn, B., Bringué, M., Brooks, S., Caniupán, M., Chevalier, M., Cwynar, L., Emile-Geay, J., Fegyveresi, J., Feurdean, A., Finsinger, W., Fortin, M.-C., Foster, L., Fox, M., Gajewski, K., Grosjean, M., Hausmann, S., Heinrichs, M., Holmes, N., Ilyashuk, B., Ilyashuk, E., Juggins, S., Khider, D., Koinig, K., Langdon, P., Larocque-Tobler, I., Li, J., Lotter, A., Luoto, T., Mackay, A., Magyari, E., Malevich, S., Mark, B., Massaferro, J., Montade, V., Nazarova, L., Novenko, E., Pařil, P., Pearson, E., Peros, M., Pienitz, R., Płóciennik, M., Porinchu, D., Potito, A., Rees, A., Reinemann, S., Roberts, S., Rolland, N., Salonen, S., Self, A., Seppä, H., Shala, S., St-Jacques, J.-M., Stenni, B., Syrykh, L., Tarrats, P., Taylor, K., van den Bos, V., Velle, G., Wahl, E., Walker, I., Wilmshurst, J., Zhang, E., Zhilich, S., 2020b. A global database of Holocene paleotemperature records. Sci. Data 7, 1–34. https://doi.org/10.1038/s41597-020-0445-3

Larrasoaña, J.C., Roberts, A.P., Rohling, E.J., 2013. Dynamics of Green Sahara Periods and Their Role in Hominin Evolution. PLoS One 8, e76514. https://doi.org/10.1371/journal.pone.0076514

Liu, Z., Zhu, J., Rosenthal, Y., Zhang, X., Otto-Bliesner, B.L., Timmermann, A., Smith, R.S., Lohmann, G., Zheng, W., Timm, O.E., 2014. The Holocene temperature conundrum. Proc. Natl. Acad. Sci. 111, E3501--E3505. https://doi.org/10.1073/pnas.1407229111

Lora, J.M., Ibarra, D.E., 2019. The North American hydrologic cycle through the last deglaciation. Quat. Sci. Rev. 226, 105991. https://doi.org/10.1016/j.quascirev.2019.105991

Metcalfe, S.E., Barron, J.A., Davies, S.J., 2015. The Holocene history of the North American Monsoon: “known knowns” and “known unknowns” in understanding its spatial and temporal complexity. Quat. Sci. Rev. 120, 1–27. https://doi.org/10.1016/j.quascirev.2015.04.004

Pausata, F.S.R., Messori, G., Zhang, Q., 2016. Impacts of dust reduction on the northward expansion of the African monsoon during the Green Sahara period. Earth Planet. Sci. Lett.

434, 298–307. https://doi.org/10.1016/j.epsl.2015.11.049

Perez-Sanz, A., Li, G., González-Sampériz, P., Harrison, S.P., 2014. Evaluation of modern and mid-Holocene seasonal precipitation of the Mediterranean and northern Africa in the CMIP5 simulations. Clim. Past 10, 551–568. https://doi.org/10.5194/cp-10-551-2014

Skinner, C.B., Poulsen, C.J., 2016. The role of fall season tropical plumes in enhancing Saharan rainfall during the African Humid Period. Geophys. Res. Lett. 43, 349–358. https://doi.org/10.1002/2015GL066318

Swann, A.L.S., Fung, I.Y., Liu, Y., Chiang, J.C.H., 2014. Remote vegetation feedbacks and the mid-Holocene Green Sahara. J. Clim. 27, 4857–4870. https://doi.org/10.1175/JCLI-D-13-00690.1

Tabor, C., Otto-Bliesner, B., Liu, Z., 2020. Speleothems of South American and Asian Monsoons Influenced by a Green Sahara. Geophys. Res. Lett. 1–11. https://doi.org/10.1029/2020gl089695

Tierney, J.E., Pausata, F.S.R., DeMenocal, P.B., 2017. Rainfall regimes of the Green Sahara. Sci. Adv. 3, e1601503. https://doi.org/10.1126/sciadv.1601503

Wright, D.K., 2017. Humans as Agents in the Termination of the African Humid Period. Front. Earth Sci. 5, 1–14. https://doi.org/10.3389/feart.2017.00004